Quantum walks of photons in disordered media

Hugo Defienne

THÈSE DE DOCTORAT
DE L'UNIVERSITÉ PIERRE ET MARIE CURIE

Spécialité : Physique

École doctorale : « Physique en Île-de-France »

réalisée

au Laboratoire Kastler Brossel

présentée par

Hugo DEFIENNE

pour obtenir le grade de :

DOCTEUR DE L'UNIVERSITÉ PIERRE ET MARIE CURIE

Sujet de la thèse :

Quantum walks of photons in disordered media

soutenue le 2 Décembre 2015

devant le jury composé de :

M.	Eric Lantz	Rapporteur
M.	Allard Mosk	Rapporteur
M^{me}	Nadia Belabas	Examinateur
M^{me}	Catherine Schwob	Examinateur
M.	Ian Walmsley	Examinateur
M.	Sylvain Gigan	Directeur de thèse

Contents

Introduction **5**

1 Quantum optics in linear optical systems **9**
1.1 Quantum light . . . 10
1.1.1 Quantum sources . . . 10
1.1.2 Photon-pairs generation by spontaneous parametric downconvertion (SPDC) . . . 11
1.1.3 Source configurations . . . 14
1.1.4 Observing quantum correlations on a beam-splitter . . . 16
1.1.5 Quantum interference interpretation . . . 21
1.2 Quantum walks of photons . . . 24
1.2.1 Photons propagating in linear optical networks . . . 25
1.2.2 From classical random walk to multi-photon quantum walk . . . 27
1.2.3 Application of quantum walks in quantum information processing: solving the Boson sampling problem . . . 31
1.3 Quantum walks in disordered media . . . 34
1.3.1 Properties of disordered media . . . 35
1.3.2 Quantum optics and disordered media . . . 37

2 Controlling light propagation in disordered media **41**
2.1 Wavefront shaping methods . . . 42
2.1.1 Spatial Light Modulator . . . 42
2.1.2 The optimization approach . . . 42
2.1.3 The Scattering Matrix approach . . . 43
2.2 The characterization step: transmission matrix measurement . . . 45
2.2.1 Linearity and matricial formalism . . . 45
2.2.2 Holographic measurement process . . . 48
2.2.3 Experimental setup using a layer of paint . . . 49
2.2.4 Experimental setup using a multimode fiber . . . 50
2.3 The inversion process: controlling light . . . 57
2.3.1 The inverse operator . . . 57
2.3.2 Focusing light through complex system . . . 59
2.4 Conclusion . . . 61

3 Single-photon quantum walk in a scattering medium **63**
3.1 A new optical platform for quantum walk experiments . . . 64
3.1.1 A layer of paint: a highly multimode coupling device . . . 65

3.1.2 Experimental constraints . . . 67
3.2 Characterization of the medium using a classical source . . . 68
3.2.1 Wavefront shaping setup . . . 68
3.2.2 Classical source properties . . . 69
3.3 Control of a single-photon quantum walk in a layer of paint . . . 69
3.3.1 Single-photon source . . . 70
3.3.2 Guiding of a single-photon in a specific output mode . . . 70
3.3.3 Deterministic control of the single-photon output state . . . 71
3.3.4 Conclusion . . . 76
3.4 Quantum walks with single-photons in a multimode fiber . . . 77
3.4.1 Mixing processes in multimode fibers . . . 77
3.4.2 Controlling single-photon propagation through a multimode fiber 79
3.5 Conclusion . . . 79

4 Two-photon scattering matrix 83
4.1 Single-photon propagation in a linear network . . . 84
4.1.1 Scattering and transmission matrix . . . 84
4.1.2 Single-photon formalism . . . 84
4.2 Photon-pairs propagation in a multimode linear system . . . 85
4.2.1 Perfectly indistinguishable or distinguishable photons . . . 85
4.2.2 Partially indistinguishable photons . . . 86
4.3 Two-photon transmission matrix . . . 88
4.3.1 Example of a balanced beam splitter . . . 88
4.3.2 Two-photon transmission matrix calculation . . . 89
4.3.3 Mathematical properties of the transformation process . . . 90
4.3.4 Multi-photon scattering matrix . . . 91
4.4 Scattering matrix approach to control photon-pairs . . . 92
4.4.1 Focusing classical light . . . 93
4.4.2 Single-photon focusing . . . 95
4.4.3 Two-photon focusing . . . 97
4.5 Focusing two-photon under experimental constraints . . . 98
4.5.1 Reduced form of the input states due to experimental constraints 100
4.5.2 The focusing fidelity . . . 101
4.5.3 Two practical methods to focus photon-pairs . . . 102
4.6 Numerical optimization approach . . . 102
4.6.1 The optimization process . . . 102
4.6.2 Towards an analytical solution . . . 103
4.7 Analytical approach . . . 103
4.7.1 Two-photon transmission matrix decomposition . . . 103
4.7.2 Analytical expression of the focusing fidelity . . . 106
4.7.3 Analytical expression of the experimental input state . . . 107
4.7.4 Practical method to use the analytical approach . . . 111
4.8 Conclusion . . . 112

5 Two-photon quantum walk in a multimode fiber 115
5.1 Photon-pairs propagation in a multimode fiber . . . 116

5.1.1 Photon-pairs source . . . 117
5.1.2 Experimental reconstruction of the two-photon transmission matrix . . . 117
5.2 Characterization of the MMF using a classical source . . . 122
5.2.1 Classical source . . . 122
5.2.2 TM measurement process . . . 124
5.2.3 Two-photon transmission matrix reconstruction . . . 124
5.3 Controlling photon-pairs propagation through a MMF . . . 126
5.3.1 Focusing photon-pairs using the analytical approach . . . 127
5.3.2 Deterministic manipulation of the quantum interferences . . . 129
5.4 Conclusion . . . 134

General conclusion **135**

Appendix A **139**
A.1 Photon-pair source . . . 139
A.2 Stability curves of a layer of paint and a multimode fiber . . . 140

Appendix B **143**
B.1 Technical constraints of the SLM . . . 143
B.2 Calibration of the *Fourier* basis . . . 143

Appendix C **147**
C.1 Reduced density matrix and concurrence measurement . . . 147
C.1.1 Measurements of the elements of $\hat{\rho}_r$ . . . 148
C.1.2 Concurrence measurement . . . 151
C.2 Statistical data analysis of data presented in Chapter 3 . . . 151

Appendix D **153**
D.1 Spectral dispersion in a MMF . . . 153
D.2 Method to find the zero delay optical path difference . . . 155
D.3 Statistical data analysis of data presented in Chapter 5 . . . 156

Introduction

Almost all optics experiments can be explained using classical electromagnetic theory [1]. The classical wave theory describes the fundamental properties of light - spatial and spectral distributions, polarization - and enables to understand effects such as diffraction, interferences or non-linear optics phenomena. However, quantum theory of light has emerged during the last century to give a more complete description of light phenomenon.
At the beginning of the 20th century, interpretation of the Black Body radiation by Plank [2] and study of the photoelectric effect by Einstein [3] raised the concept of photon [1] to describe light: emission or absorption of light by atoms requires the assumption that light is made up of discrete energy units. Depending on the experiment performed, light can be treated either as a wave or a particle flow. First experiments realized with very low light intensities investigated the dual structure of light:

- In 1909, G.I Taylor reproduced the Young's double slit experiment [5] with a very low energy flux. To interpret his results, he proposed to make the probability of counting a photon proportional to the intensity of the corresponding classical field. In this case, the classical theory of interference, based on electromagnetic waves, and the quantum explanation, based on probability amplitude interferences, can be made to coincide, and the experiment can not distinguish these two interpretations.
- In 1956, R.Hanbury-Brown and R.Twiss observed an enhancement of the intensity correlation function between two detectors illuminated by a thermal source [6]. This effect is also named the *photon bunching effect*. It has been shown later that this effect can not be reproduced using laser light because of its particular photon statistics. While these results were still predictable without distinction by both classical and quantum model, the Hanbury-Brown-Twiss experiment proved for the first time the existence of correlations between photons and that these correlations are preserved in the process of photoelectric emission.
- Physicists had to wait until 1977 to observe an optical effect that can not be derived from the classical theory of light. Predicted by R.J Glauber in 1963 using quantized electromagnetic field theory [7], the *photon anti-bunching* phenomenon was experimentally observed by H.J Kimble, M.Dagenais and L.Mandel [8]. This experiment validated the use of a quantum description light rather than a classical model to predict all optical phenomena. With this experiment, Quantum optics entered in a new era.

1. The term *photon* was only suggested in 1926 by G.N.Lewis in [4]

Experimental quantum optics has offered an interesting playground to confirm quantum physics predictions: photons are quantum particles that can be generated at room temperature, they can propagate with a high degree of coherence and do not interact with each other. Starting with the founding experiments performed by A.Aspect, P.Grangier and G.Roger [9] and later by A.Zeilinger [10], non-classical concepts such as wave-particle duality, entanglement, indistinguishability [11], non-locality [12] or teleportation [13] have been intensively investigated and tested during last decades. The most convincing experiments that have changed the way we understand nature, such as the inadequacy of local hidden variable models [9] or more recently the correspondence between reality and its description [14], have been demonstrated using quantum light. Quantum optics has become a reference scientific platform to test foundations of physics and an inspiration to other quantum domains [15, 16].

While light allows exploring curiosities of nature, its easily accessible quantum characteristics have also made quantum light a promising platform for emerging technologies. Rapid progresses made in photonics - such as the development of integrated optical structures or highly efficient detectors - and in quantum sources open perspectives for thirty years developing new modes of information processing based on quantum physics. Laboratories have already started to make inroads into technological challenges like communications, computation, sensing and imaging [17].
Photonic devices have originally been developed to study classical light propagation and are generally not adapted to carry quantum light. In particular, losses represent an important issue associated to quantum light propagation: although photons retain their information well, they are easily absorbed or scattered. Moreover, a photon can not only be used to transmit the information, but also to process it [18]. In consequence, design of photonic optical systems need to be rethought taking into account special properties of quantum light and fully exploit their capacities.
Linear optical networks - taking the form of integrated optical circuits, fiber arrays or array of conventional free space optical devices - have appeared in the past years as very promising optical systems to study and take advantage of non-classical properties of light. In particular, they allow the implementation of quantum walk of photons which has deep implications for quantum computing [19, 20, 21], including the possibility of universal computing [22, 23].
The attention of physics community has recently focus on another type of system: *disordered media*. White paint layers, pieces of paper, multimode fibers, biological tissues, all these disordered systems scatter light in a very complex manner. Thanks to the linearity of the elastic scattering processes, coherence is maintained during scattering, but light is scrambled during its propagation and the modes become highly complex. These natural systems allow access up to a number of modes well beyond what is possible using current photonic devices [24]. This large increase in the number of available modes suggest that these media could represent a valid platform for implementing more computationally complex optical networks. Figure 0.1 represents this new type of experimental implementation from an artistic point of view.

In the work presented in this thesis, we propose a radically novel solution for the implementation of multi-photon quantum walks by using disordered systems as highly multimode optical platforms. This solution has arisen from a multidisciplinary collabo-

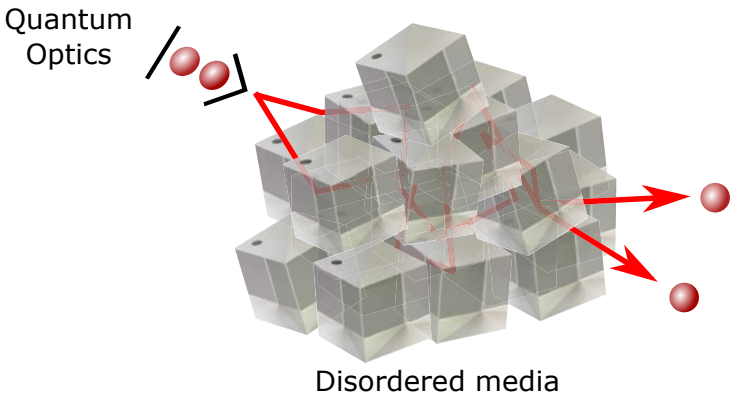

Figure 0.1: **Artistic view of using a disordered medium as a mutimode platform for quantum optics**. The use of beam-splitters in this representation highlights the fact that some complex photonic systems, such as layer of white paints or multimode fibers, are almost non absorptive and are therefore suitable for quantum optics experiments. A high number of this symbolic optical device, used in almost all quantum optics experiments, is drawn here to emphasize the important modal capacities of a disordered medium. Their random distribution accentuates also the complexity of the mixing process.

ration that combines quantum optics with the control of light propagation in disordered media. In this work, we have succeed in controlling and programming quantum walks of photons - single-photon and photon-pairs - in complex systems by using wavefront shaping. Our study opens up many new possibilities for the development of reconfigurable highly multimode optical network and, as it was originally predicted by J.Ott and coworkers in their work in [25], paves the way for the next generation of quantum information processing photonic instruments.

Chapter 1

Quantum optics in linear optical systems

Taking advantage of the quantum nature of light is a promising avenue to develop new technologies dedicated to information processing, quantum simulation and computation. In this respect, quantum walks of photons have emerged as a powerful tool, which has recently received a great interest by the scientific community [26, 17]. The turning point in these realizations has been the introduction of integrated optical structures that allowed to extend the abilities far beyond what was possible before. However, this recent technology suffers from serious limitations arising from the constraints of the fabrication process, which enables to couple only a few dozens of modes for the photons to walk through.
Disordered systems, such as layer of paints, biological tissues or multimode fibers, can be considered as optical platforms offering an efficient coupling between a huge number of spatial, spectral and polarization modes. Due to their inherent random and lossy nature, these systems have always been considered unpractical for quantum optics experiments. Wavefront shaping methods, developed in the last decade to control light propagation in complex media, allow moving beyond these limitations and make these media exploitable with non-classical light.

In this chapter, non-classical features of quantum light are first introduced (1.1) by describing its propagation through the most simple linear multimode optical network: the *balanced beam-splitter* (BS). The use of more complex photonic platforms offer a richer interference structures that can be exploited to implement *quantum walks* of photons. Such systems are then investigated both from a fundamental and applied physics point of views (1.2). Finally, recent works studying non-classical light propagation in disordered media are presented (1.3). These studies reveal the high potential of combining quantum optics with disordered media, but also its strong experimental complexity.

1.1 Quantum light

Photons are fundamental excitations of the electromagnetic field and the energy building blocks of any light radiation. Presence of a photon can only be characterized through its interaction with matter. From an experimental point of view, a photon is often represented as a *click* on a detector: a photon interacts with an atom and ejects an electron. The resulting electrical signal is detected after avalanche amplification. While recent improvements of photo-counting techniques have enabled to detect a photon - or several photons - with a very high efficiency, generate photons with well-controlled properties is not a trivial process.
Photons are produced using different types of light source. Depending on the generation process, photons are created with different characteristics and define the *quantum state* of the radiation field. A state of the field regroups information about spectral, spatial, and polarization properties of the photons as well as about their emission statistics. For instance, a laser working well above its threshold emits a *coherent state*: photons are created in a well defined optical mode and the photons flux follows a *Poissonian statistics*[1] [7]. Two other important classes of states are *the squeezed states* and the *Fock states* [27]. Squeezed states can be seen as modified coherent states that follow *sub-Poissonnian statistics* (amplitude squeezed state) or *super-Poissonnian statistics* (phase squeezed state). On the contrary, the number of photon contained in a *Fock states* is well-defined: photons statistics is delta distributed.
In the scope of this thesis, we only consider quantum states containing a precise number of photons: *single-photon Fock states* and *two-photon Fock states*. In this situation, non-classical light properties are really explored at the level of a few isolated particles and not through their collective behavior.

This section describe single-photon and photon-pairs generation processes used in this thesis. Non-classical properties of the quantum states created are studied and compared to a classical sources characteristics.

1.1.1 Quantum sources

Quantum photonic applications require sources capable to generate photons with well-controlled properties. An ideal single-photon source would deliver on-demand single-photon with a complete control over all its degrees of freedom - frequency distribution, emission time, spatial structure and polarization. However, there are many experimental obstacles in its realization. The many different methods of generating photons can be divided in two categories: sources using a *single-emitter* and those consisting of *many-emitters*.

Single-emitter sources

Single-emitter sources use for instance a single atom or a quantum dot to generate single-photons by spontaneous emission. Photon properties are adjusted by controlling

1. When the photon flux is intense, the relative fluctuation of the photon number becomes negligible and the classical limit is reached: amplitude and phase are well defined and the radiation can be simply described using classical electromagnetic theory.

the environment surrounding the emitter. For example, coupling the emitter to a cavity change the spatial distribution and the spectrum of the emitted photon. While the generation of a photon with these sources is close to deterministic (almost on-demand), collection efficiencies are poor which reduces the chance of having an exploitable photon at the output. Atoms trapped in cavities [28], quantum dots [29] or lattice defects in inorganic crystals [30, 31] are the most popular single-emitter sources, but they generally require a complex equipment (vacuum chamber, cryogenic equipment) to be implemented.

Multi-emitters sources

Multi-emitters sources consist of many emitters such as an atomic gas or a bulk medium. In this case, structure of the emission is determined by the relative phase of the emitters: *phase-matching* properties of the assembly determine preferential directions and spectrum of the photon emission. While laser-cooled atomic assembly methods [32] enable direct single-photon generation, multi-emitters assemblies are generally used to generate photon-pairs. Parametric Down Conversion (PDC) process in non-linear crystal is probably the most popular method to generate photon-pairs with well-defined properties [33].

1.1.2 Photon-pairs generation by spontaneous parametric downconvertion (SPDC)

In SPDC, a high frequency photon interacts with a non-linear crystal and is converted into a pair of lower energy photons [34, 35]. Optical properties of the generated photons are function of the pump mode and the crystal characteristics. SPDC sources are commonly used to produce correlated photon-pairs with well-defined frequency and spatial properties[36, 37].
A large range non-linear crystals can be pumped to generate photon-pairs. Beta Baryum Borate (BBO), Lithium Nobiate (LN) or Potassium Dihydrogen Phosphate (KDP) are examples of very commonly used non-linear crystals. To give a real example of a photon-pair generation process, we describe here an experimental implementation of a photon-pairs source using a periodically poled potassium titanyl phosphate (PPKTP) pumped with a blue laser (405nm).

Parametric downconversion (PDC)

PDC is a three-wave mixing process where a photon of the pump field decays into a pair of daughter photons known as *signal* and *idler* photons. Coupling between the fundamental and the sub-harmonic fields is ensured by the non-zeros second order susceptibility of the crystal. Both energy conservation of the parametric process and the phasematching condition in the crystal determines properties of the emitted light. The following equations describe these conditions:

$$w_p = w_s + w_i \tag{1.1.1}$$

$$\boldsymbol{k_p} = \boldsymbol{k_s} + \boldsymbol{k_i} \tag{1.1.2}$$

where w_α is the frequency of the photon, $\boldsymbol{k_\alpha}$ is wavevector, and $\alpha = p, s, i$ denote respectively pump, signal an idler.
PDC takes place in two regimes: *spontaneous* and *stimulated*. In spontaneous parametric down conversion, photon-pairs are only generated by spontaneous decay processes. In a stimulated regime, the fist pair is emitted spontaneously and then acts as a seed for the sub-harmonic field to stimulate generation of other pairs.
The probability of generating multiple photon-pairs at the same time is very low in the spontaneous regime. Photon-pairs sources then generally work in this regime to emit two-photon Fock states with high fidelity.

Example of photon-pairs generation using a PPKTP crystal

Photon-pair source using a PPKTP crystal is a typical example of a source exploiting a SPDC process to generate photons with very well-defined characteristics [38, 39, 40, 41, 42]. In this part we give a general description of the properties of this type of source.
Non-classical light is generated by pumping a PPKTP crystal using a continuous-wave blue laser centered at 405nm. This system allows generating infrared photon-pairs through a type II SPDC process. Type II phase matching conditions constrains down-converted photons to have orthogonal polarizations at the output: one daughter photon has a polarization parallel to the pump polarization and to the extraordinary axis of the crystal, and the other one is crossed polarized along the ordinary axis. A general scheme of the photon-pairs source is given on Fig 1.1 and more details can be found in Appendix A.

Spectral properties Phase-matching conditions in the PPKTP crystal allow generation of photons pairs with frequencies around 810nm when the crystal is pumped at 405nm. Due to energy and momentum conservations (Equation 1.1.2), photon-pairs frequencies are strongly correlated. Spectral correlations depend on spectral properties of the pump, temperature of the crystal and properties of spectral filters added to the setup. Following the theoretical approach detailed in [38], these different contributions to the joint density spectrum of the two-photon state are represented on Figure 1.2.

A precise control on the crystal temperature and the use of narrow-band filters permit to tune spectral properties of the emitted photons.

Spatial distribution The design of periodically poled crystals such as PPKTP establishes specific phase matching conditions (*quasi phase-matching conditions* [43]) and creates daughter photons in a spatial mode collinear to the pump mode. This effect enables an efficient collection of the pairs using single mode fibers (SMFs). SMFs play also the role of spatial filters and clean spatial distribution of the photons.

Polarization mode Type II SPDC is a process that generates crossed polarized photons. As a consequence, photons are easily split into two separated spatial modes using a polarizing beam-splitter (PBS), and each polarization is efficiently controlled using birefringence optical devices.

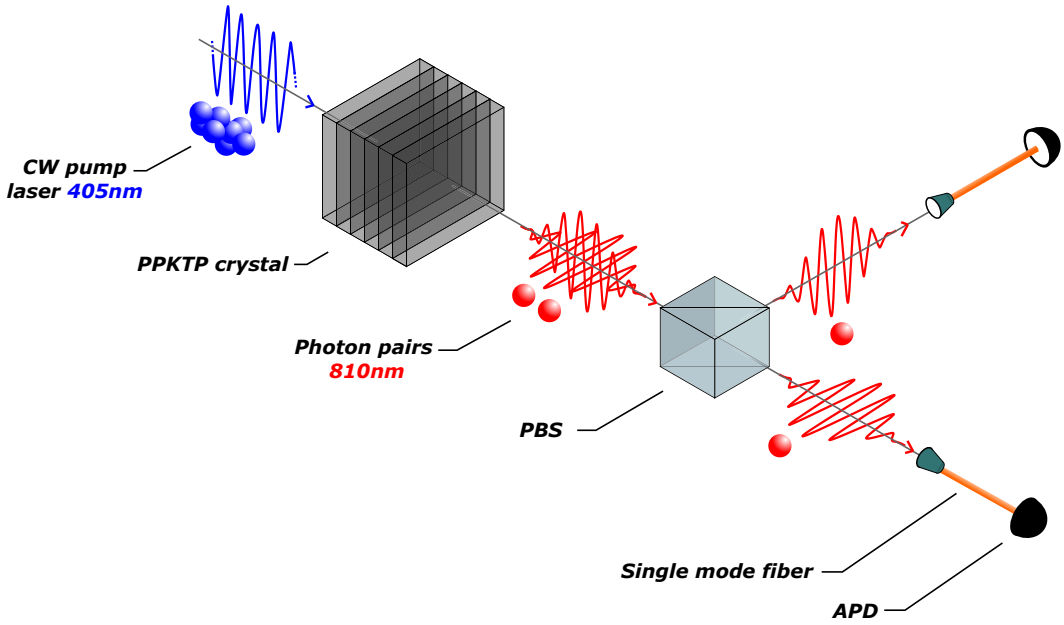

Figure 1.1: **Scheme of photon-pairs generation**. A periodically poled potassium titanyl phosphate (PPKTP) crystal is pumped by a continuous-wave blue laser centered at 405nm. Infrared photon-pairs are generated by type II SPDC in the crystal. Each photon of the pair is spatially separated using a polarizing beam-splitter (PBS) and injected in a single mode fiber (SMF). Avalanche photodiodes (APDs) detect photons at the two outputs.

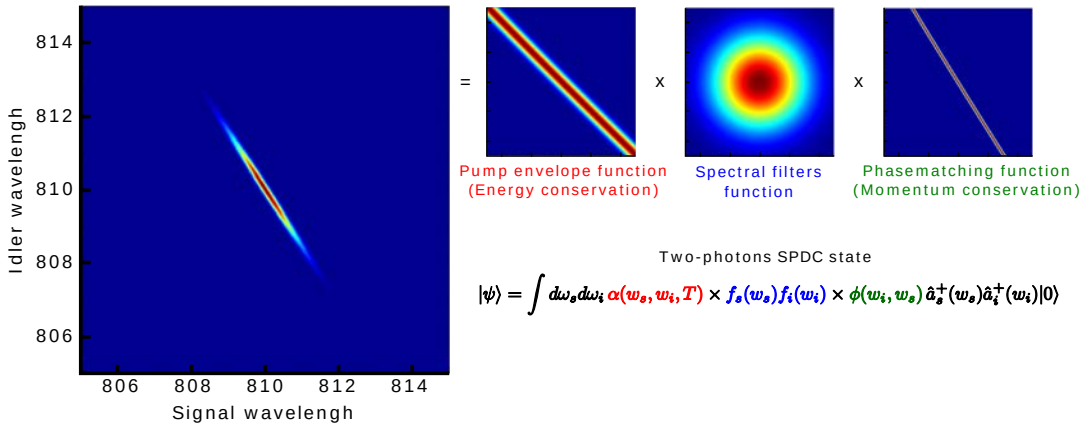

Figure 1.2: **Components of the joint spectral density of a two-photon state generated by type II SPDC**. The joint spectral density is the product of the pump envelope function (red), the spectral filters (blue) and the phasematching function (green). Results presented have been acquired by simulating a model detailed in [38]. Two-photon state generated by SPDC contains three important contributions: the pump envelope function α, the phase-matching function ϕ and the spectral shape of filters acting on each photons f_s and f_i. Subscripts s and i refer respectively to signal and idler photons ; $w_{s/i}$ are the corresponding frequencies and $\hat{a}^+_{s/i}(w_{s/i})$ the corresponding creation operators ; T is the temperature.

1.1.3 Source configurations

Depending on the experimental configuration of the source, properties of generated photons can be used in different ways. For instance, correlations between energy or spatial distribution of the emitted pairs can be exploited to generate *entangled state* of light [44]. Based on the example of a photon-pairs source using a PPKTP crystal, we present here two configurations of the source allowing generation of *heralded single-photons* and *indistinguishable photon-pairs* (Figure 1.3).

Single-photon configuration

Single-photon are generated using a *heralding detection process* described on Figure 1.3.a [45]. photon-pairs are spatially separated using a PBS at the output of the crystal. One photon of the pair is used as a trigger photon and measured with an avalanche photodiode (APD). This detection reflects that pair-generation has occurred in the crystal and a single-photon is collected by a polarization maintaining single mode fiber (PMSMF) in the other arm of the apparatus. Experimentally, presence of a single-photon in the second arm is characterized by measuring a *coincidence* between this output and the trigger detector. Spectral properties of single-photons are adjusted by adding spectral filters on the corresponding output and tuning the crystal temperature.

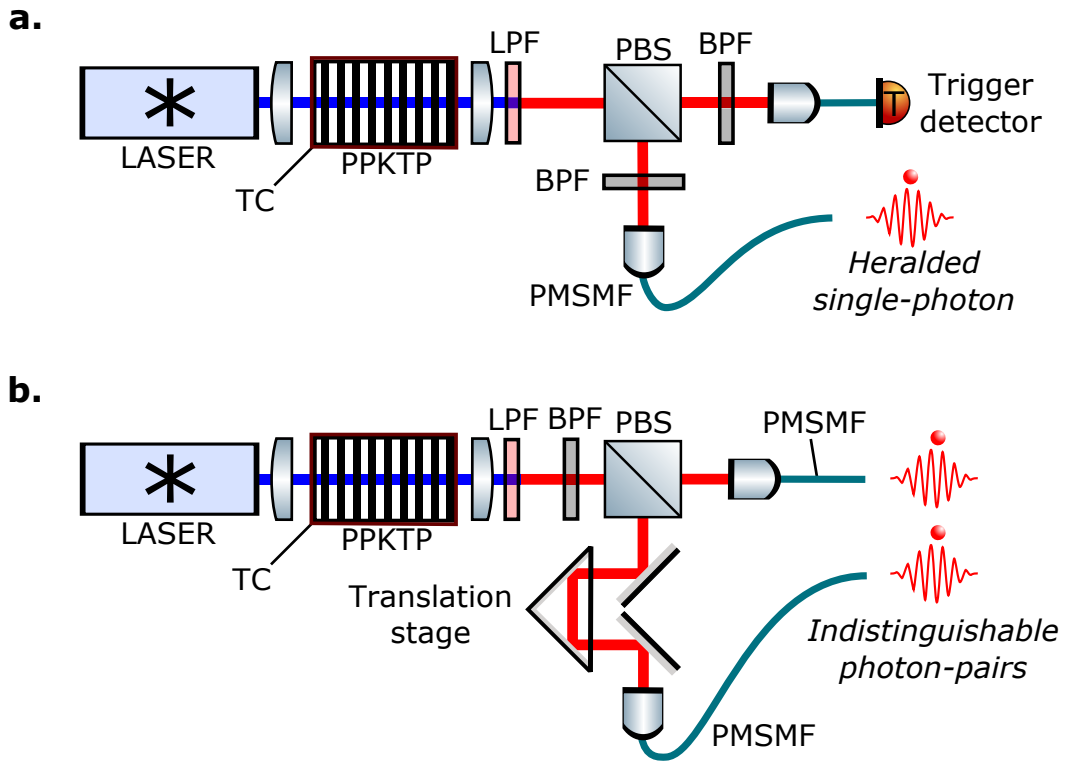

Figure 1.3: **Schematic of the two different configurations of the source**. **(a)** represents the *heralded single-photon configuration*. One photon of the pair is used as a trigger photon and the other one is collected by a polarization maintaining single-mode fiber (PMSMF). A low pass filter (LPF) is used to absorb pump photons after propagation through the crystal. Band pass filters (BPF) permit to adjust spectral properties of the heralded single-photon, as well as the crystal temperature controller (TC). **(b)** represents the configuration in which the source emits *indistinguishable photon-pairs*. PMSMF and spectral BPF ensure that both photons are collected in the same spectral, spatial and polarization mode. Relative time delay between photon can be adjusted with a picosecond precision using the translation stage positioned on one of the two arms.

Indistinguishable photon-pairs configuration

In this configuration, described on Figure 1.3.b, photon properties need to be well controlled: while detecting coincidences between the two outputs proves that photons are emitted by pairs, this does not ensure that they are indistinguishable i.e have identical properties. First, collecting photons in PMSMFs guarantees that their spatial distribution and polarizations are identical. Then, spectral properties are adjusted by controlling the crystal temperature and by adding spectral filters to the setup. In particular, the use of narrow-band spectral filters (with typical bandwidth of 1-3 nm) is an efficient method to overlap almost perfectly photon spectra, but it also decreases the brightness of the source. Finally, a translation stage positioned on one arm allows to modify the path length difference between the two photons and cancel their relative time delay [2]. This experimental configuration enables the realization of an Hong-Ou-Mandel (HOM) experiment [11]. This experiment allows at once to set the relative path delay between the photon with a high precision and to quantify the overlap of photon properties.
A HOM experiment exploits a quantum interference phenomenon occurring when photon-pairs are sent through a balanced BS and coincidences are measured between the two outputs. As presented on Figure 1.4, this phenomenon is identified by a dip in the output coincidence rate when scanning the relative path delay. The center of the HOM dip corresponds to a relative path delay perfectly reduced to zero. Its contrast relies to the overlap of optical properties of the photons and gives a measurement of their maximum indistinguishability. This quantum interference phenomenon is discussed in details in part 1.1.5. A HOM experiment performed to analyze the photon-pair source implemented in this thesis is detailed in Appendix A.

1.1.4 Observing quantum correlations on a beam-splitter

Single-photon and indistinguishable photon-pairs exhibit non-classical properties that are at the heart of most quantum optics experiments. Such properties have been first investigated as quantum physics curiosities [46, 11, 47] and later exploited as new resources for developing new applications [48, 22, 23]. These properties can be revealed using the most simple optical multimode system: the *balanced beam-splitter*.
Two non-classical concepts are introduced in this section: *wave-particle duality* and *two-photon quantum interferences*.

Single-photon interferences: wave-particle duality

Photons display both particle and wave-like properties. In particular, a single-photon is the simplest object that can be used to verify wave-particle duality. In the last decades, experiments have been implemented to demonstrate this non-classical concept ; they are now inversely used as tools to characterize wave-particle structure of quantum sources.

2. Considering the frequency-time equivalence picture, a time delay in the temporal picture corresponds to a spectral phase ramp. Just as spectral filters modify the amplitude shape of the spectrum, a modification in time is actually correcting the complex phase of the spectrum.

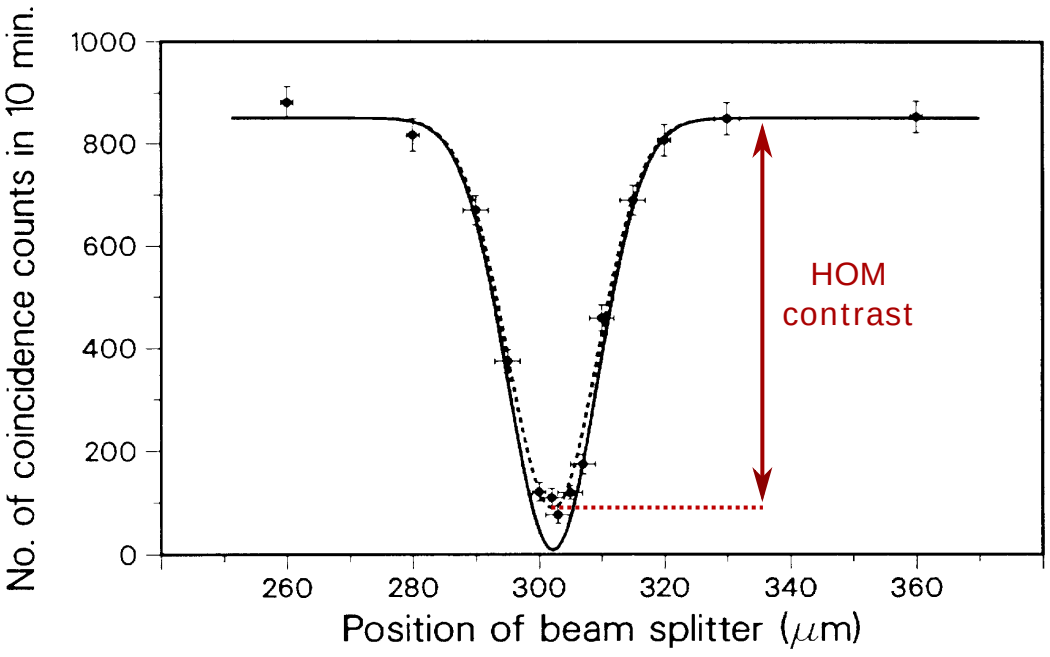

Figure 1.4: **Hong-Ou-Mandel experiment**. In this experiment, coincidences are recorded between the outputs of a balanced BS when each photon of a pair is sent through a different input. The curve shown here is extracted from the publication associated to the historical experiment first implemented by C.K.Hong, Z.Y.Ou and L.Mandel in 1987 [11]. The HOM curve shows evolution of the coincidence rate when scanning the relative path delay between the photons. In their experimental configuration, the relative delay corresponds to the 'position of beam splitter'. The dip observed is due to a quantum interference effect between photons occurring when the delay is reduced to zero. Center of the HOM dip identifies then precisely a zero time delay between the photons. Its contrast relies to the similarity of photon properties and gives a measurement of their maximum indistinguishability.

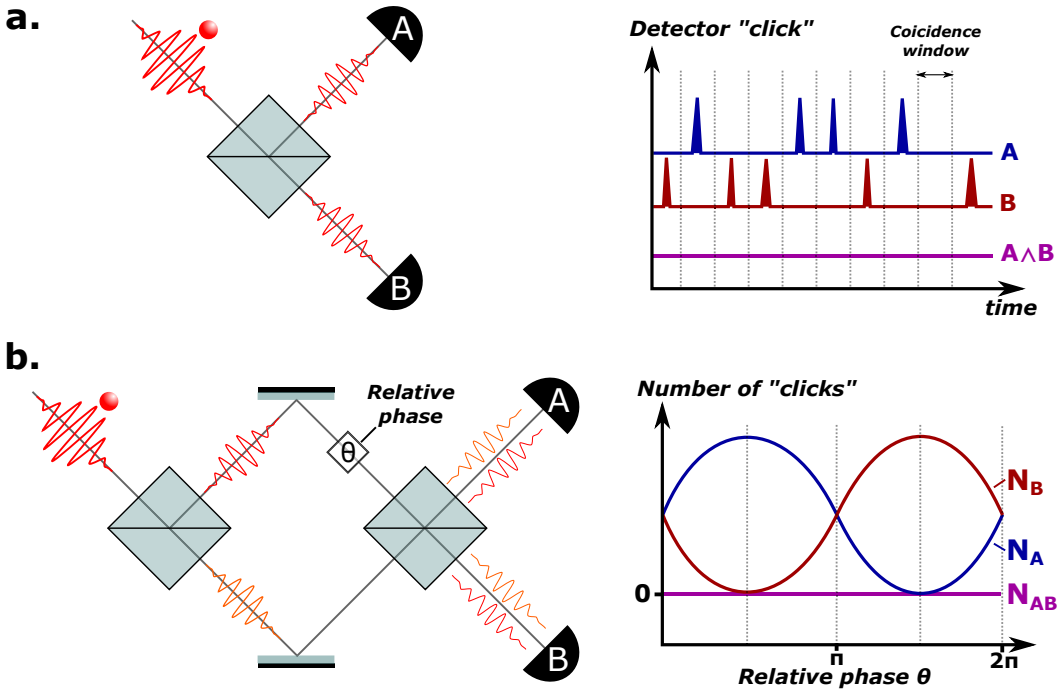

Figure 1.5: **Schematics of experiments characterizing single-photon wave-duality**. **(a)** represents a single-photon propagating through a balanced BS. While its associated wave-packet propagates as a classical wave, the single-photon is detected either by detector A or detector B: no $A \wedge B$ coincidence are registered . **(b)** describes a single-photon Mach-Zender experiment. Waves interfere after the second BS. The number of photons detected N_A or N_B by output detectors changes according to the relative phase θ, but the number of coincidences N_{AB} stays equal to zero because of the particle nature of a single-photon.

Beam-splitter experiment As detailed on Figure 1.5.a, when a single-photon propagates through a balanced BS, the photon as a particle is either transmitted or reflected while its associated wave is split between the two output paths. Experimentally, single measurements (*clicks* on detectors A and B) record a photon rate divided by two after propagation through the BS. The same result is obtained using a classical source. Coincidence measurements (*coincidence click* between detector A and B) show that the probability of joint detection falls to zero when using a single-photon state while it is non-zero with a classical source. This result demonstrates the particle-like behavior of a single-photon and the failure of classical electromagnetic theory. As detailed in [46], a parameter named $g^{(2)}$ can be extracted from this simple experiment to quantify the purity of the single-photon source.

Mach-Zender experiment Wave-particle duality can also be observed by implementing a Mach-Zender experiment with a single-photon source as described on Figure 1.5.b. In this experiment, the wave associated to the single-photon takes both paths simultaneously and interferes on the second BS while the photon as a particle can only be detected on one of the two arms. Depending on the relative phase between the two paths, probabilities of detecting the photon at the outputs are unbalanced. At the same time, coincidence detection is close to zero and independent of the relative phase value [3]. This experiment shows that a photon propagates like a wave and can therefore interfere with itself: the electromagnetic wave coincides with the probability amplitude wavefunction introduced in quantum theory.

Hong-Ou-Mandel experiment

Although wave-particle duality is fully described by the quantum theory of light, previous theories (such as the M.DeBroglie *pilot wave theory* [49]) interpreted correctly this phenomenon using radically different approaches. An important step towards the understanding of quantum theory of light has been made by the emergence of indistinguishable photon-pair sources.
Indistinguishability is a fundamental difference between quantum and classical physics. While classical particles can always be labeled by their position and momentum during their propagation, it is not possible to track indistinguishable particles and determine which path is taken by which particle: an assembly of indistinguishable particles has to be considered as a single object and not as a collection of distinct particles. As a consequence, detection probabilities show correlations that can not be reproduced by replacing photon with uncorrelated classical particles or using classical electromagnetic theory.
The first experimental demonstration of this effect was performed by C.K.Hong, Z.Y.Ou and L.Mandel in 1987 [11]: each photon of a pair is sent through different mode of a balanced BS and coincidences are measured between the two outputs. This experimental setup is reproduced on Figure 1.6 and analyzed with several type of input: classical uncorrelated particles, indistinguishable photons and classical light.

3. In the Mach-Zender experiment, a relative phase set to $\pi/2$ decreases the coincidence rate to zero with both classical and non-classical sources because there is no light in one of the two outputs. This case is taken into account when calculating the parameter $g^{(2)}$

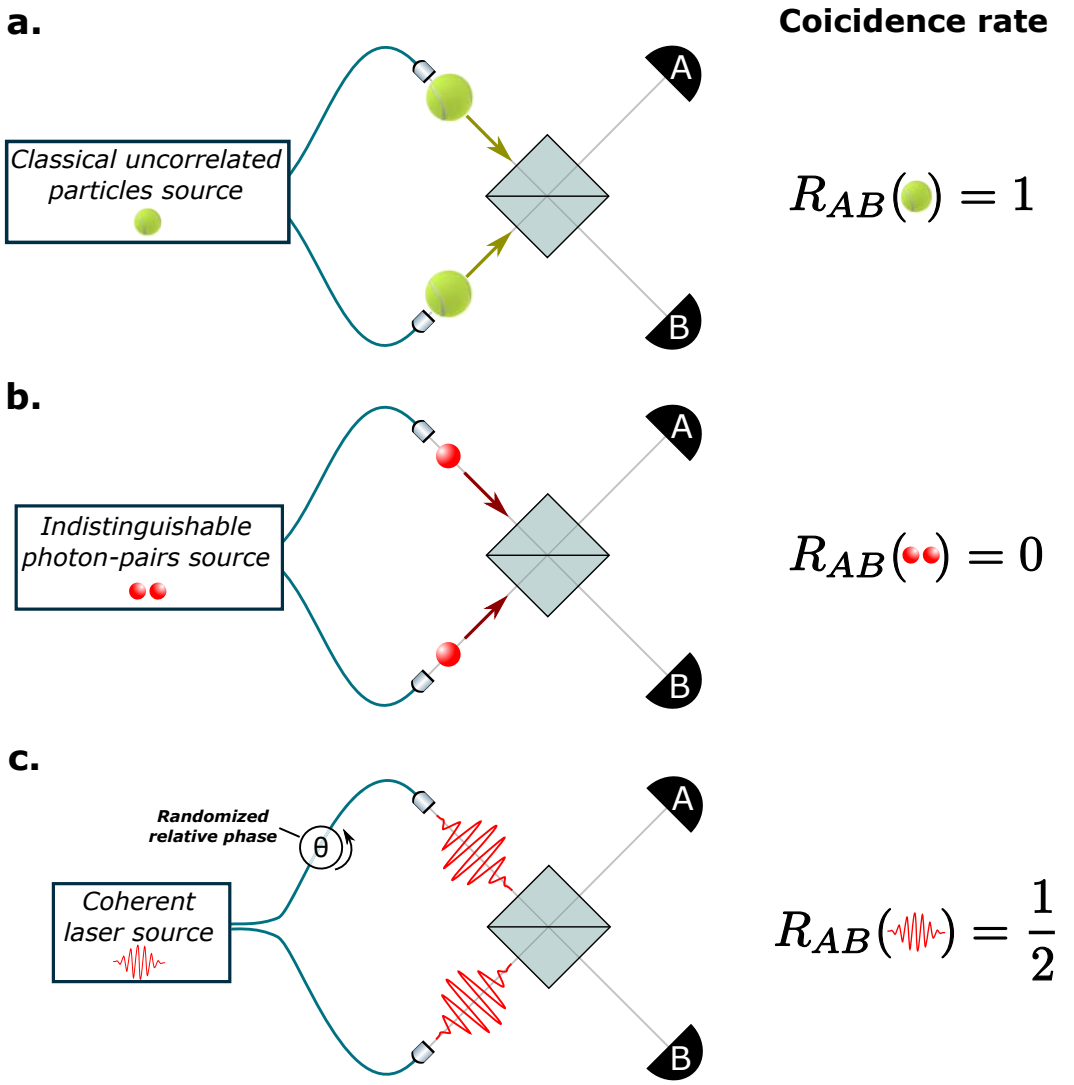

Figure 1.6: **Hong-Ou-Mandel-like experiments with different types of source**. **(a)** Classical uncorrelated particles propagating through a balanced BS. A coincidence is detected at the output half of the time. The corresponding coincidence rate is fixed to one and serves as a reference. **(b)** Indistinguishable photon-pairs launched through a balanced BS. The probability to detect coincidences falls to zero. **(c)** Classical coherent light propagation through a BS. The coincidence rate can be decreased down to 1/2 when the relative phase θ between the two arms is randomized rapidly compared to detector acquisition time.

Classical uncorrelated particles When photons are replaced by classical uncorrelated particles (Figure 1.6.a), the BS acts independently on each particle and the probability of detecting a coincidence at the output is calculated directly from the output probabilities of each photon (equations 1.1.4).

$$\begin{aligned} P_{AB} &= P(1 \to A \wedge 2 \to B) + P(2 \to A \wedge 1 \to B) \\ &= P(1 \to A)P(2 \to B) + P(2 \to A)P(1 \to B) \\ &= 1/2 \times 1/2 + 1/2 \times 1/2 = 1/2 \end{aligned} \tag{1.1.3}$$

where P_{AB} is the probability of measuring a coincidence between detectors A and B, $P(i \to I \wedge j \to J)$ the joint probability of photon i being detected by I and photon j by J and $P(i \to I)$ the probability of photon i being detected by I. The associated coincidence rate $R_{AB}(\text{cla})$ - number of coincidences detected within a coincidence window divided by the coincidence window duration - is arbitrary taken equal to one $R_{AB}(\text{cla}) = 1$ to serve as a reference in the other experimental situations.

Indistinguishable photon-pairs Contrary to classical uncorrelated particles, no coincidences are measured when indistinguishable photons propagate through the BS (Figure 1.6.b). This result characterizes the presence of correlations between the photons: $P(i \to I \wedge j \to J) \neq P(i \to I)P(j \to J)$. This *bunching effect* - characterized by a coincidence rate equal to zero - can not be observed using classical sources or interpreted with classical theory of light [4] .

Classical light Reproducing the same experiment with incoherent classical sources show either no-correlations (two incoherent laser beams) or positive correlations (filtered thermal source). The only way to reproduce negative coincidences is to launch a coherent laser source in both inputs of the BS (Figure 1.6.c). By randomizing the relative phase between the two input beams much faster than the acquisition time of the detectors, the corresponding coincidence rate is decreased down to $R_{AB} = 1/2\text{in}$ [50, 51, 52]. As a consequence, a photon source exhibits *quantum correlations* when the limit $R_{AB} < 1/2$ is broken.

1.1.5 Quantum interference interpretation

A physical interpretation of photon correlations observed in experiments detailed in the previous section is given by extending the notion of classical interferences to *quantum interferences* [7]. The corresponding mathematical formalism is constructed by analogy to the classical interference formalism:

4. Photon correlations observed in an HOM experiment do not break any non-locality theorem because results can be reproduced using correlated classical particles. Let's suppose that particles carry a *hidden property* unknown from physicists that can take two values denoted T or R. The BS acts on each particle depending on its hidden value: it reflects the particle when the value is R and transmits it when the value is T. Particles are then generated with anti-correlated hidden values - when particule 1 takes the value T (R), then particle 2 takes R (T) - but keeping a random proportion of T and R values for each particle. Under these constraints, classical particles reproduce the results obtained with indistinguishable photons propagating through a BS.

- Propagation of n-indistinguishable photons is described by introducing a n-photon field
- The probability to detect the photons simultaneously at particular space-time positions is proportional to the square of the field

This formalism applied in the particular case of photon-pairs uses the notion of *two-photon field* [7, 53, 54] and gives a physical interpretation of the HOM experiment described in the previous section.

Classical interference

To show the analogy between classical and two-photon interferences, we first review some important properties of the classical interference formalism.
Classical fields propagating through a balanced BS (Figure 1.7) are distributed between the outputs following Equations 1.1.4.

$$\begin{aligned} E_1 &\longrightarrow \frac{1}{\sqrt{2}}(E_3 + iE_4) \\ E_2 &\longrightarrow \frac{1}{\sqrt{2}}(iE_3 + E_4) \end{aligned} \tag{1.1.4}$$

where E_i (E_j) represents the complex field at input $i \in \{1, 2\}$ (output $j \in \{3, 4\}$). Fields are considered here monochromatic and in the same polarization mode.

Considering classical light propagating through the BS, light that outcomes for instance at output 3 has two possible origins: light comes from input 1 and has been reflected by the BS or light comes from input 2 and has been transmitted by the BS. The corresponding intensity is easily calculated by:

- summing the two classical fields corresponding to each two-photon paths taken and calculating the overall intensity if input fields are *coherent*: $I_3 \propto |E_1 + iE_2|^2$
- summing intensities of the two classical fields if input fields are *incoherent*: $I_3 \propto |E_1|^2 + |E_2|^2$

Symmetric results are obtained for output 4: $I_4 \propto |E_2 + iE_1|^2$ for coherent fields and $I_4 \propto |E_2|^2 + |E_1|^2$ for incoherent fields.

Two-photon interference

In an HOM experiment [11], each photon of the pair is sent through a different input of the BS. Photons of the pairs can be made either *distinguishable* or *indistinguishable* by moving the translation stage. Considering two-photon propagation, photons that outcome in coincidence at the outputs have two possible origins: photon from input one and photon from input two both reflected or both transmitted. The resulting coincidence rate is calculated by:

- summing the two two-photon fields corresponding to each path taken and calculating the overall coincidence intensity if input photons are *indistinguishable*: $R_{34} \propto |E_1E_2 + iE_1iE_2|^2 = 0$

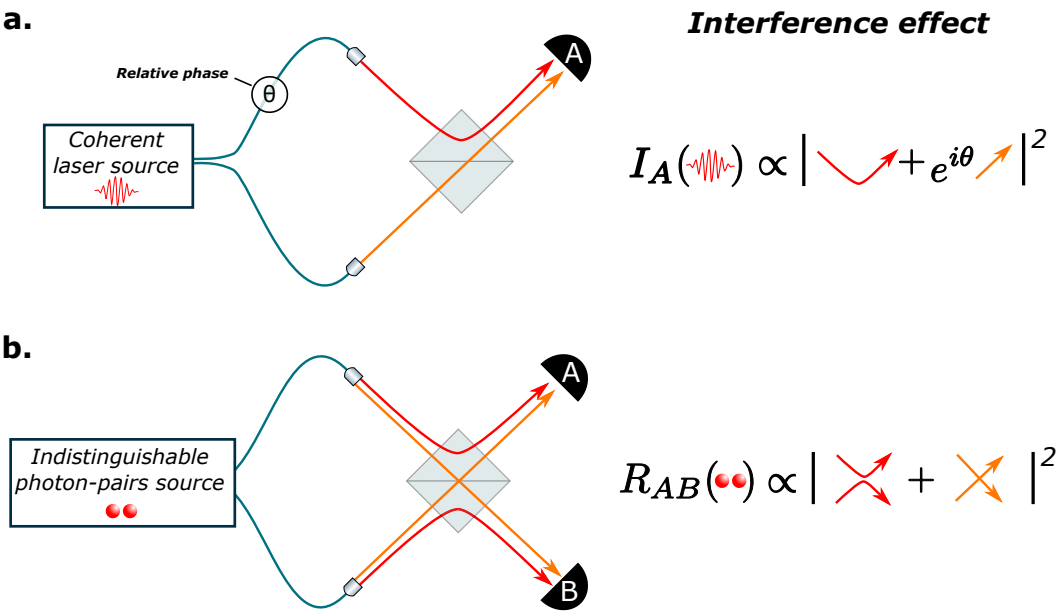

Figure 1.7: **Classical and two-photon interferences on a beam-splitter**. **(a)** Classical interferences of a coherent laser source on a BS with a relative phase θ. Output intensity I_A is calculated adding complex amplitudes corresponding to each path taken by light. **(b)** Two-photon interferences of an indistinguishable photon sources on a BS. Coincidence rate R_{AB} is evaluated similarly to a classical interference effect by adding two-photon paths amplitudes.

	Classical field	**Two-photons field**	**n-photons field**
Complex notation	$E_1(\boldsymbol{r_1}, t_1)$	$E_1(\boldsymbol{r_1}, t_1)E_2(\boldsymbol{r_2}, t_2)$	$\prod_{i=1}^{n} E_i(\boldsymbol{r_i}, t_i)$
Measurement type	Intensity I	Coincidences rate $R^{(2)}$	n-fold coincidences rate $R^{(n)}$
Measurement probability	$I(\boldsymbol{r}, t) \propto \lvert E_1 \rvert^2$	$R_{12}^{(2)} \propto \lvert E_1 E_2 \rvert^2$	$R_{1..n}^{(n)} \propto \lvert \prod_{i=1}^{n} E_i \rvert^2$
Coherence notion	Coherence	Indistinguishability	Indistinguishability

Table 1.1: **Classical and non-classical field analogies**. Notions introduced by extending concept of interferences to non-classical light are listed here. The theoretical approach allows good understanding of the optical phenomenon studied in this thesis. A formal theory can be found in [7].

– summing intensities of the two two-photon fields if input photons are *distinguishable*[5]: $R_{34} \propto |E_1E_2|^2 + |iE_1iE_2|^2$

Table 1.1 summarizes analogies between classical and non-classical fields when considering the propagation of n-indistinguishable photons.

This formalism can be extended to experimental implementations that involve more complex optical systems than simple BSs. In particular, multimode linear networks provide rich and complex interferometric structures for light. When indistinguishable photons are injected in these coherent platforms, classical and quantum interferences occur during propagation: they perform a *quantum walk*.

1.2 Quantum walks of photons

While classical random walks have been successfully used in a lot of domains modeling complex phenomena [55, 56, 57, 58, 59, 60], quantum walks are expected to provide new resources to solve many problems more effectively [61]. They have already inspired efficient algorithms with applications in graph theory [62, 63] or element distinctness [19] and are capable of acting as universal computational primitives [22, 23]. Developing the physical hardware permitting to implement quantum walk in the laboratory is now an important challenge for many physicists. In particular, such system is expected to be highly flexible, enabling to deal with a large range of practical problems. Over the past decade, a large variety of systems have been suggested to implement quantum walk, including atomic systems [64] or Nuclear Magnetic Resonance [65]. Because quantum features of photons are easily accessible at room temperature, photonics have provided a very promising architecture to implement quantum walk with photons. Linear optical networks, permitting nearest neighbor coupling across a certain number of optical modes, have been the key technology so far allowing for a fast growing number of explorations of quantum walk of photons [66].

5. The notion of indistinguishability for photons-pairs is analogue to notion of coherence for classical fields in a sense that if this property is validated, then interference effect can be observed

This section introduces the notion of quantum walk of photons in linear optical networks, describes their physical properties and focuses on their potential for computing and information processing.

1.2.1 Photons propagating in linear optical networks

Linear optical networks are passive structures composed of linear optical components, such as BSs, phase shifters or mirrors. Their potential use for quantum walk implementation was originally introduced by Z.Zhao and coworkers in 2002 [67]. Light propagation in such networks strongly depends on their architecture. By using structures in which coupling parameters are either deterministically adjusted or totally randomly set, light is guided through the system by taking several optical paths from the source to the detectors. All optical paths interfere at the output and create a complex interference pattern.

Properties of linear optical networks

One of the first experimental implementation of quantum walks in a linear network was performed by B.Do and coworkers [68] building an array of half-wave plate (HWP) and PBS. The corresponding experimental setup is described on Figure 1.8a.
HWPs associated to PBSs play the role of controlled BSs and divide the input field at each step of the walk. Optical path lengths between two successive PBS are adjusted during implementation of the setup to fix the relative phase of interfering fields. In this work, an incoming photon interferes with itself while traversing all possible paths from the source to the detector. Due to the wave-like property of a photon, output statistics are different from those resulting from a classical particle propagating in a similar Galton's board network [69].
This experiment highlights three important properties required by linear optical networks to host quantum walks experiments: *linearity, coherence and stability.*

Linearity A linear optical network is only composed of linear optical components. Therefore, output field of the system results from linear combinations of all input fields. In case of discrete networks, a *transmission matrix* links the complex amplitudes of all input modes to outputs modes and thus characterizes light propagation through the system.

Coherence Interference effect can only be observed if path length differences are shorter than the coherence length of the source. If optical paths distribution of a network is wider than the coherence length of the source, interference contrasts will be reduced at the output. Finally, the output field results from coherent but also incoherent contributions. Consequently, optical networks have to be designed or selected depending on spectral properties of the source.

Stability Optical components are generally sensitive to mechanical vibrations and temperature changes. An optical network becomes practicable only if it is stable

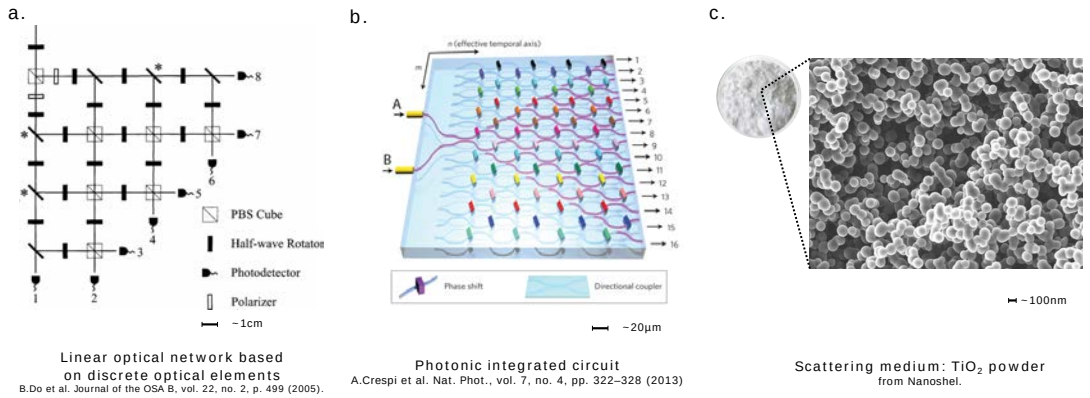

Figure 1.8: **Examples of experimental linear optical networks**. **(a)** Scheme of a linear optical network built with conventional linear optical components with a characteristic size of a milliliter. **(b)** Photonic integrated circuit designed using a femto-laser writing process on a silicon chip. The characteristic size is about a micrometer. **(c)** Sketch of a scattering medium constituted of densely packed dielectric nano-particles. Characteristic size is about a nanometer.

during the acquisition time. Otherwise, its configuration evolves with time and output measurements are averaged.

Photonic integrated structures have recently proven a versatile architecture to implement quantum walks of photons (example on Figure 1.8b). They allow optical systems to be made more compact than when using discrete optical components. Various fabrication processes - as for instance laser writing methods used to design silica waveguides on silicon chip [70] - permit a high-fidelity control over coupling coefficients and length of optical paths. Moreover, a good stability is ensured by the monolithic structure of the device. Photonic integrated technology has enabled the implementation of several quantum walks experiments in the last decades, ranging from multi-particle [66] and multi-dimentional walks [71], to analogues of Anderson localization in condensed matter systems [72], to the implementation of the boson sampling problem [73, 74, 75, 76]. While this technology has improved performance of existing quantum circuits, increasing the size of these waveguide structures - which currently allow access up only to twenty modes - remains an important challenge to develop quantum information processing applications.

A promising alternative to photonic integrated circuits is the use of complex linear systems. Disordered media - such as thick layers of densely packed dielectric particles (example on Figure 1.8c)- scatters light in a complex manner. Thanks to the linearity of the elastic scattering processes, coherence is maintained during multiple scattering but the modes become highly complex. These natural linear systems allow access up to a number of modes well beyond what is possible using waveguides. An important motivation of this thesis is that these systems should represent a valid platform for implementing more computationally complex optical networks.

Modal characterization of a linear optical network

For classical light, a linear optical network acts as a linear application transforming an input field of the system into the corresponding output field. After decomposition over sets of spatial, spectral and polarization modes, this transformation is mathematically represented by a matrix which contains complex coefficients connecting inputs to outputs. Complex field at the output can then be written as a linear combination of all the input fields (Equation 1.2.1)

$$E^{\text{out}}_{j\in[1,M]} = \sum_{j=1}^{N} T_{ji} E^{\text{in}}_{i} \tag{1.2.1}$$

where N (M) is the number of input modes (output modes) of the network, and $T = T_{ji\in[1,M]\times[1,N]}$ its associated matrix.

In this general approach, a mode of the system refers to a spatial, spectral or polarization mode without distinction. However, experimental constraints generally reduce the real number of modes to be taken into account. For example, the use of input light with shorter enough spectral bandwidth avoids spectral mixing effects during propagation. In this case, the spectral mode is preserved between input and output and does not need to be taken into account in the matrix. As another example, photonic integrated structure generally maintain polarization of the input signal and the same polarization is observed at the output.

If the medium does not absorb light and has been characterized over all the existing optical modes, its associated matrix is unitary because of energy conservation [6]. In this case, the complete matrix is called *the scattering matrix* of the system.

Optical properties of a linear network are fully characterized once its associated matrix has been measured. Several measurement methods have been recently proposed to characterize photonic integrated circuits [78, 79]. Another method adapted to disordered media [80] is presented in Chapter 2.

1.2.2 From classical random walk to multi-photon quantum walk

Non-classical concepts of wave-particle duality - allowing one photon to interfere with itself - and quantum interferences - allowing several photons to interfere with each other - are of fundamental interest not only for obtaining a deeper understanding of quantum mechanics, but also to explore the field of quantum information science. Quantum walks of photons in optical networks involve these interference effects which can be exploited to process information or solve certain types of problem.

This section highlights the differences between the dynamics of the walks performed by classical particles and photons. This comparative approach is carried out studying the propagation of single-photon or particle and pairs of photons or particles through regular multimode linear networks.

6. The operator associated to a lossless linear optical network is represented by a unitary matrix. It has been shown in [77] that a unitary matrix can be reduced to a matrix decomposed in BS and phase shifter submatrices. As a result, any lossless optical system can be reproduced in a laboratory by assembling BSs, phase shifters and mirrors. For instance, optical properties of a white paint layer - in which absorption is negligible - can be mimicked by conventional linear optical components positioned on an optical table.

Single-photon quantum walk

Dynamics of a single-photon quantum walk depends only upon the interference of waves evolving during the propagation. As a consequence, outcome statistics of a single-photon propagating in a given linear network (Figure 1.9.a) are different from those obtained by classical particle propagating in a similar network (Figure 1.9.b). These difference is quantified by studying spreading properties of each probability distributions. While probability to find the classical particle after N steps takes a Gaussian shape with a variance $\sigma^2 \sim N$, probability distribution of the quantum object shows a variance scaling in $\sigma^2 \sim N^2$.
A single-photon launched in a linear optical network does not employ any quantum resources - such as entanglement or quantum interferences - to propagate and relies instead only on the wave-like interferences of probability amplitudes. As demonstrated by [81], single-photon quantum walk can therefore be simulated in a purely classical regime, using a classical coherent source, classical linear optics and a classical measurement scheme.

Two-photons quantum walk

Multi-photon quantum walks can offer potential advantages over the single-photon walk when considering the possibility of incorporating more exotic quantum behavior, such as entanglement as well as various forms of inter-particle interaction. Here we describe the implementation of quantum walks using photon-pairs. The case of indistinguishable photons is then distinguished from walks performed with uncorrelated photons or non-interacting particles because of the presence of two-photon interference during their propagation. One of the first work that studied photon-pairs propagation through simple multimode networks was reported by K.Mattle and coworkers in [82]. In this study, these systems are simply named *multiport beam splitters*.

A simple and ordered linear optical array is represented on Figure 1.10. Particle-pairs are injected in the system and detected at the output by ten photon counting modules used to measure coincidence events. When two uncorrelated and non-interacting classical particles propagates through a Galton's network [69] (Figure 1.10.a), two-photon coincidence probability distribution is directly calculated from Gaussian distribution of each particle taken independently. Indeed, a classical particle does not interfere with itself - leading to the Gaussian probability distribution - and two particles do not interact with each other - leading to a coincidence probability equals to the product of probabilities of each particle. In case of photon-pairs propagating through a similar system (Figure 1.10.b.c), projections of coincidence probabilities along both axis differ from the Gaussian shapes and reveal wave-like property of each individual particle. However, while joint probability distribution of distinguishable photon-pairs can be retrieved from probability distribution of each photon (Figure 1.10.b), quantum interferences occurring when indistinguishable photons propagate in the system modify output coincidence detections (Figure 1.10.c).
The difference observed at a given coincidence mode $\{i, j\}$ is quantified by calculating the *non-classical interference contrast* from coincidence probabilities in both distinguishable Q_{ij} and indistinguishable R_{ij} cases (Equation 1.2.2)

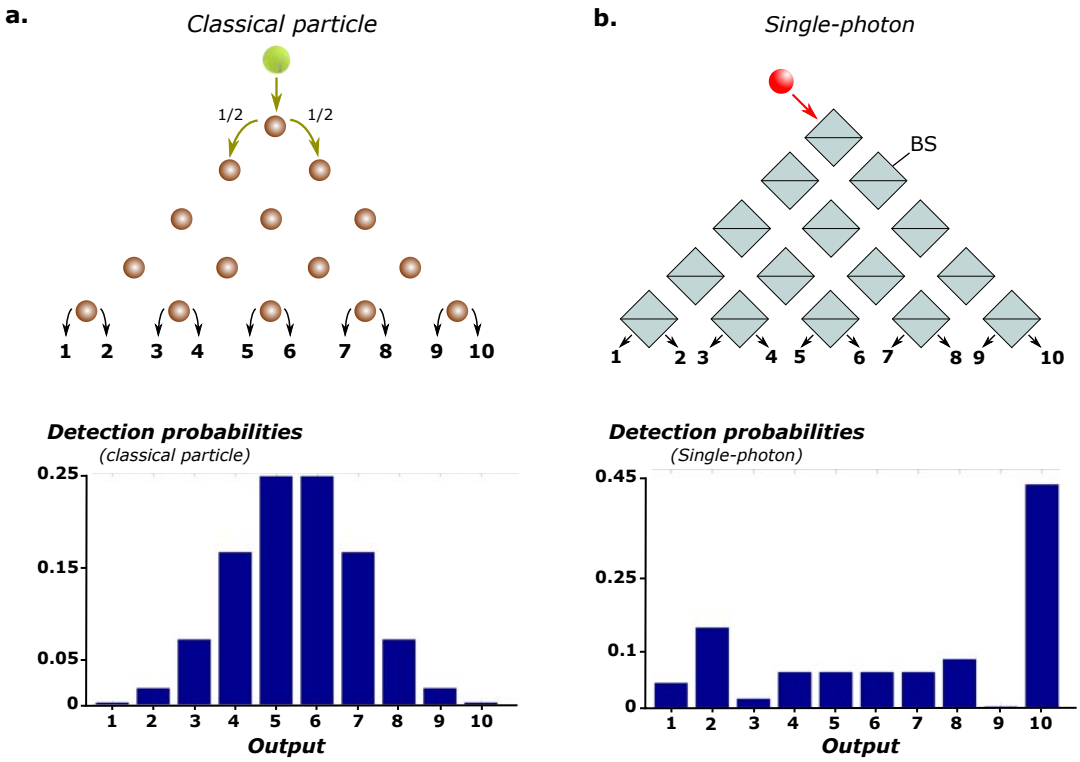

Figure 1.9: **Classical particle and single-photon walks**. **(a)** Classical particle propagating in a Galton's board structure [69] performing a classical unbiased random walk. At each node of the structure, the probability for the particle to go left or right is half. Output probability distribution takes a Gaussian form with a variance σ^2 proportional to the number of steps N of the walk: $\sigma^2 \sim N$. **(b)** Single-photon propagating in an array of balanced BSs. When a photon passes through a BS, its associated wave-function is split in two. Due to its wave-like property, output statistics are different from those obtained with a classical particle propagating in a similar network **(a)**: probability distribution has a variance scaling in $\sigma^2 \sim N^2$.

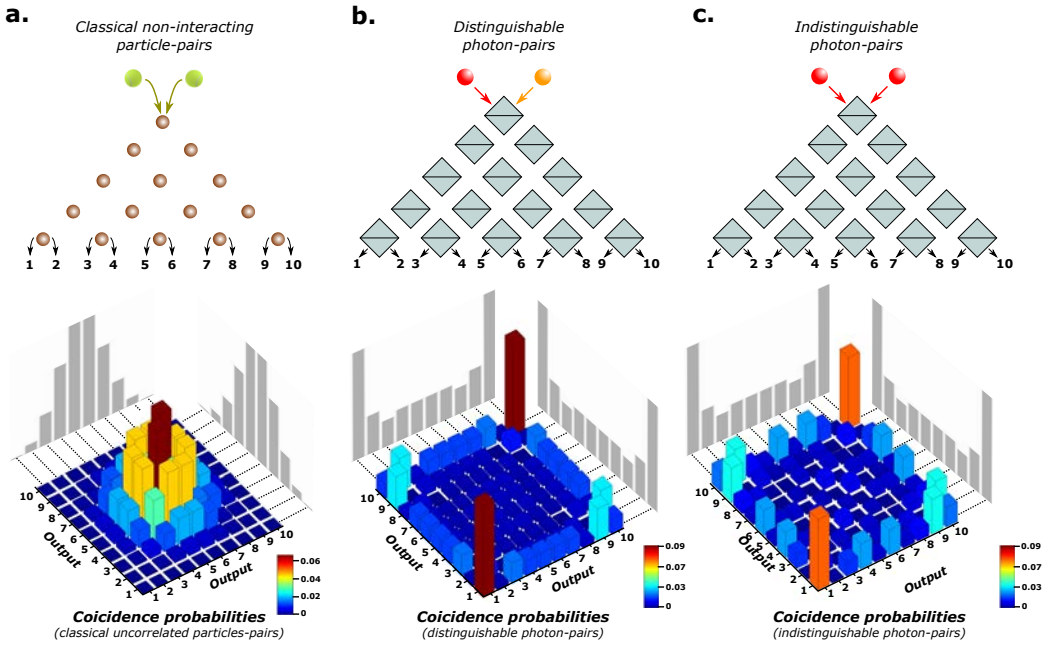

Figure 1.10: **Two-particles walk with classical non-interacting particles and photons**. **(a)** Classical non-interacting particles propagating in a Galton's board network. Because particles do not interact, joint probability distribution is simply equal to the product of probability distribution of each particle taken independently. **(b)** Distinguishable photon-pairs propagating in an array of balanced BSs. As shown by projections along both axis of the coincidence probability distribution, each photon interferes with it self leading to an individual probability distribution different from this of a classical particle. Distinguishable photons do not interact with each other and the corresponding coincidence probability distribution is the product of each individual probability distribution. **(c)** Indistinguishable photon-pairs propagating in an array of balanced BSs. Quantum interference leadd to a coincidence probabilities distribution different from this of distinguishable photons. However, coincidence probability matrix projections along both axis demonstrate that the behavior of each individual photon remains the same.

$$V_{ij} = \frac{R_{ij} - Q_{ij}}{Q_{ij}} \tag{1.2.2}$$

Non-classical contrasts quantify quantum interferences occurring in the system. For instance, the destructive interference effect observed when performing a HOM experiment [11] is characterized by a contrast value of minus one.

Unlike the single-photon, where the walk can be simulated using coherent light [81], two-photon quantum walk gives uniquely rise to quantum interference effects. These walks enrich the quantum walk evolution and lead to a new class of applications [26].

1.2.3 Application of quantum walks in quantum information processing: solving the Boson sampling problem

The *Boson sampling problem* (BSP) has both a well-defined computational complexity class and a clear physical implementation [83]. The problem has been raised by studying linear transformations applied to bosonic particles.

A sampling problem

We consider a physical system made of photons injected in a linear multimode optical device. Photons are distributed over the input modes following an arrangement denoted I. During their propagation, the linear network rearranges the particles and leads to a certain output probabilities distribution. Each output arrangement of the photons, denoted S, has a certain probability $P_{I\to S}$ to be measured.
The goal of the BSP is to sample the distribution of probabilities $P_{I\to S}$ using a finite number of measurements [7].

Describing photon propagation with matrix permanents

Propagation of indistinguishable photons through a multimode system can be predicted using the knowledge of its transmission matrix T. In particular, the probability $P_{I\to S}$ of observing a certain arrangement S at the output assuming a certain input distribution I is directly given by calculating the *permanent* of a submatrix of T [84]. The permanent of a complex square matrix $A = (a_{ij})_{i,j\in[1,n]}$ of size $n \times n$ is defined as

$$\mathrm{Per}(A) = \sum_{\sigma\in S_n} \prod_{i=1}^{n} a_{i\sigma(i)} \tag{1.2.3}$$

where the sum here extends over all elements σ of the symmetric group S_n i.e. over all permutations of the numbers $1, 2, \ldots, n$.
As an example, we first consider the simple case of photon-pairs propagating through a balanced BS. The BS is represented by a 2×2 matrix denoted T_{BS}. When indistinguishable photon-pairs are injected into each input of a BS, the output coincidence

7. This distribution verifies $\sum_S P_{I\to S} = 1$ if the system is unitary.

probability vanishes because of destructive two-photon interference effects. As presented on Figure 1.11.a, this result can be directly obtained by computing the permanent of T_{BS}.
Another example is given on Figure 1.11.b. This scheme represents the propagation of three identical photons through a 5×5 linear network characterized by its transmission matrix $T_{5\times5}$. Photons are injected at inputs 1, 2 and 4 and threefold coincidence are detected between output ports b, d and e. Following the generalized quantum interferences approach presented in section 1.1.4, the resulting coincidence probability is calculated by taking the absolute square value of the sum of all possible three-photons paths. As demonstrated on Figure1.11.b, this result is directly predicted by computing the permanent of a 3×3 submatrix of $T_{5\times5}$. This submatrix regroups coefficients linking the input modes $\{1, 2, 4\}$ to output modes { b,d,e } .

Computational complexity of a matrix permanent

If the transmission matrix T of the linear network is known, it is also possible to calculate directly all possible output distributions using a classical computer. As we have seen before, this calculation requires computation of a matrix permanents. However, calculating a permanent is a demanding task that becomes rapidly intractable with classical computer when the matrix is too large. The definition of a permanent given by equation 1.2.3 is very similar to the familiar definition of the matrix *determinant*:

$$\mathrm{Det}(A) = \sum_{\sigma\in S_n} \epsilon_\sigma \prod_{i=1}^{n} a_{i\sigma(i)} \tag{1.2.4}$$

where ϵ_σ denotes the signature of permutation σ. Despite this apparent similarity, computing the permanent of a matrix using a classical computer is a more difficult problem than calculating a determinant.
The *Gaussian elimination method* is one of the most efficient algorithm used to calculate a determinant. It allows computing a determinant of a square matrix of size N using a *polynomial* number of arithmetic operations on the order of N^3. However, this method can not be used to compute the permanent of a matrix. This impossibility relies in the fact that the property: $\mathrm{Det}(A \times B) = \mathrm{Det}(A)\mathrm{Det}(B)$, where A and B are square matrices, is not verified in the general case for the permanent: $\mathrm{Per}(A \times B) \neq \mathrm{Per}(A)\mathrm{Per}(B)$. In consequence, computing a permanent in the general case is based on another algorithm [85] that requires an *exponential* number of arithmetic operations on the order of $2^N N^2$. A permanent becomes then intractable with a current classical computer when matrix size exceeds approximately 50×50.

Solving the Boson sampling problem with an optical setup

As described previously, computing a matrix permanent is a difficult task for a classical computer but it is naturally performed by photons propagating in a linear network. However, the number of measurements required to reconstruct efficiently a

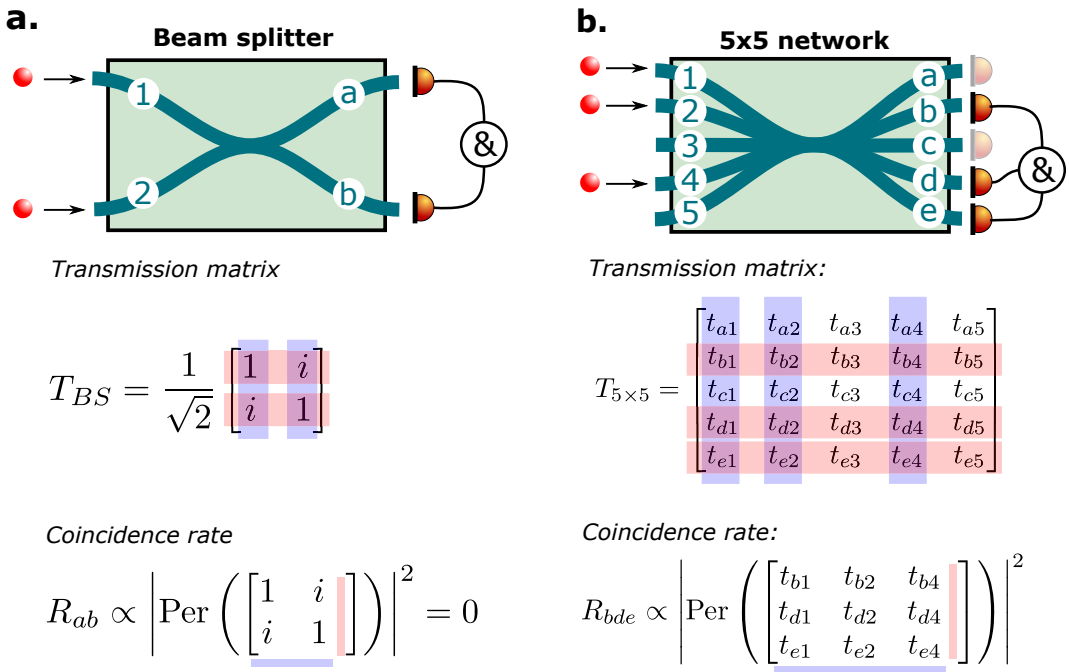

Figure 1.11: **Coincidence probability distributions predicted by permanent calculations**. **(a)** A balanced BS is characterized by a 2×2 transmission matrix. When two identical photons are injected into each input ports 1 and 2, output coincidence between ports A and B is given by computing the permanent of the submatrix containing these coefficients, which in this case is the complete matrix. **(b)** A 5×5 optical network is characterized by a 5×5 transmission matrix. Three identical photons are injected in input modes 1, 2 and 4. Coincidences are measured between output ports b,d and e. The corresponding coincidence rate is calculated using the permanent of a submatrix grouping matrix coefficients of the concerned inputs { 1,2,4 } and outputs { b,d,e }.

matrix permanent in a linear network also scales exponentially [8] with the number of photons. It is then impossible to calculate a given permanent $P_{I\to S}$ with sufficient precision when using a polynomial number of trials. In consequence, a BSP experiment does not help to calculate a matrix permanent.
The boson sampling problem relies more precisely on estimating the distribution of the probabilities $P_{I\to S}$. This problem remains very hard when using a classical computer because it requires the calculation of the permanents corresponding to all the possible output distributions. However, this problem can be solved efficiently with an optical setup using a polynomial number of measurements, even if all the individual permanents can not be precisely determined [83].
From a practical point of view, the problem would become really intractable for a classical computer for systems larger than 20 photons injected in a 200×200 mutimode device.

Experimental implementation of the Boson Sampling Problem

The BSP have been recently implemented using photonic integrated technologies [73, 74, 75, 76, 86, 87]. Experiments have been performed with three to five photons using linear networks mixing up to twelve modes. In particular, protocols have been shown to be robust over undesirable effect of photon loss, partial indistinguishably, and imperfect detection [88, 89, 90]. Considering the rapid development of quantum optical techniques, these optical experiments may enable to demonstrate for the first time a quantum speed-up that exceeds capacities of classical computers.
The BSP is a new model of quantum computation using passive linear optical elements. In contrast with computational models that provide well-defined answers to well-defined questions [91, 92, 48, 93, 94, 95, 96], the BSP carries out effectively a specific problem of sampling. This approach is then really varies from the usual quantum computer idea.

As of now, such a device is not universal and does not solve a problem of practical interest. Nevertheless, it seems plausible that more complicated systems may be useful to solve diverse problems that have practical applications. For instance, the use of disordered systems as multimode optical networks would offer a major increase of the platform size, moving from the dozens of modes currently offered by integrated circuits to the thousands of a layer of paint.

1.3 Quantum walks in disordered media

Transport of waves through complex media is a very active research topic that has been intensively explored during the last decades. Study of light propagation in disordered media such as fog, clouds, white paint, optical fibers, biological tissues is of interest to develop communication technologies and imaging applications. The light that outcomes from a scattering medium carries information both on the coherence

8. The number of configurations in the output modes scales as $\begin{pmatrix} n+m+1 \\ n \end{pmatrix}$ where n is the number of photons and m the number of output.

properties of the radiation and on microscopic details of the system. Only recently, a handfull of teams have started investigating the strong potential of combining disordered media with quantum optics.

1.3.1 Properties of disordered media

Despite a wide variety of complex media, the community has mainly focused its attention on systems with *negligible absorption* where the scattering process is *linear*. Two standard systems are concerned in the work of this thesis: *white paint layers* and *multimode fibers*. Thanks to the linearity of the scattering process [97] in these systems, coherence is maintained during multiple scattering but the modes become highly complex. When classical light travels through these systems, the multiple possible paths interfere at the output, creating a complex spatio-temporal distribution of light called a *speckle pattern*, represented on Figure 1.12. In consequence, a speckle pattern does not have a random structure because it results from the complex but deterministic propagation of optical waves through the medium.

Characteristic lengths

The macroscopic scattering properties of such systems are described by some characteristic quantities.

Mean free path l_s The *mean free path* is defined as the characteristic length of optical index fluctuations of the medium. In a layer of paint, the *mean free path* corresponds to the average distance traveled by a photon between two scattering events. When light propagates on a distance smaller than the mean free path, photons are either scattered once or not scattered at all: it is the *ballistic regime*. This distance is then associated with the extinction of ballistic light (not-scattered light).

Transport Mean free path l_t The *transport mean free path* is the characteristic length over which the direction of a photon is randomized. It corresponds to a redefinition of the mean free path taking into account the non-isotropic property of a scattering event. If particles of the medium scatter light isotropically (typically when the wavelength is much smaller than the particle size), the initial photons direction is randomized after a single event and $l_s = l_t$. However, if a photon is more likely scattered in the forward direction (when the wavelength is much larger than the particle size), memory of the initial direction is conserved after a few scattering events and $l_s < l_t$. After propagation over a distance on the order of the transport mean free path, light totally losses the memory of its initial direction and enters into the *diffusive regime*. In this regime, light intensity propagation is described by a *diffusive equation* with a diffusive constant proportional to l_p [98].

Medium bandwidth and modal dispersion

A speckle pattern carries both a temporal and spatial complex structures. As presented on Figure 1.12, when light with a limited *coherence length* l_c - equivalent to a limited bandwidth - propagates through scattering medium, pulses that have taken

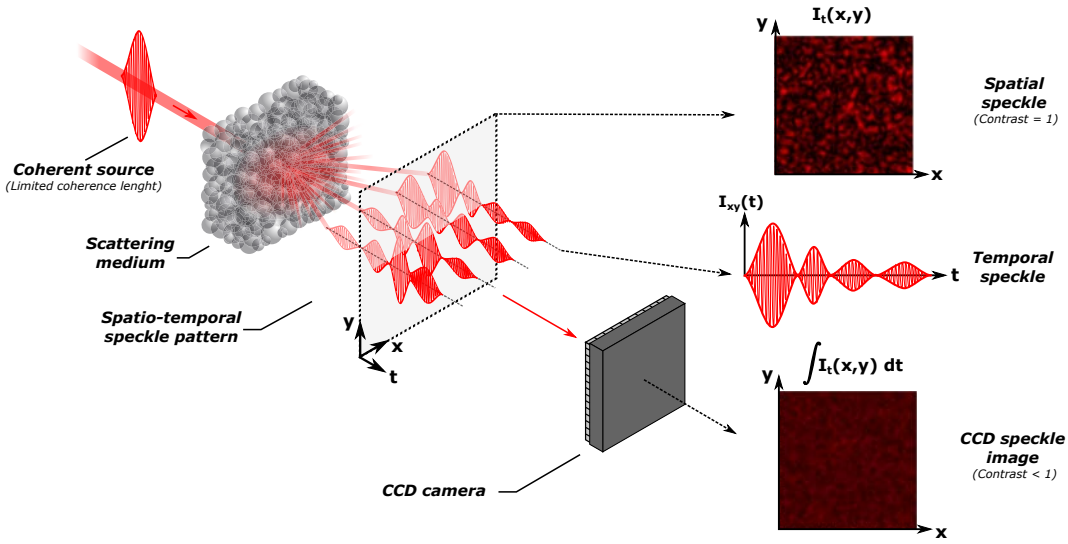

Figure 1.12: **Speckle pattern structures**. A coherent source with a limited coherence length propagates through a scattering medium creating a so-called speckle pattern. A speckle pattern displays a complex spatial and temporal structure. When output signal is integrated using a standard CCD camera, the effect of *temporal elongation* or *modal dispersion* reduces speckle contrast of the captured image.

different paths do not interfere perfectly in coherence and the output pulse becomes elongated. The corresponding speckle image captured by a CCD camera - a time-integrated detection device - records a speckle image with reduced contrast.

Pulse elongation phenomenon can also be interpreted from a spectral point of view introducing notion of *spectral bandwidth* $\delta\omega_m$ [9] of a disordered medium. This quantity is defined as the minimum frequency shift to apply at the input light to induce a complete decorrelation of the output speckle pattern [100, 99]. As a result, a source with a spectral bandwidth of $\Delta\omega$ larger than $\delta\omega_m$ generates an independent speckle pattern for each $\delta\omega_m$-width part of its spectrum. The incoherent sum of each speckle pattern explains the contrast reduction observed on CCD camera images [100]. This *modal dispersion* effect - or similarly *pulse elongation* effect - has been studied for different types of sources and media [101, 102].
In experiments conducted in this thesis, the condition $\Delta\omega << \delta\omega_m$ is always respected and ensures that there is no spectral mixing effects: the illumination can thus be considered as quasi-monochromatic [10].

9. The spectral bandwidth $\delta\omega_m$ of a scattering medium is inversely proportional to the confinement time of light in the medium [99]

10. While the *mean free path* and the *transport mean free path* are well-defined quantities for a white paint layer, they do not have a precise sense for a multimode fiber. However, spectral bandwidth of a multimode fiber is well-defined and can be estimated from fiber properties (core size diameter, fiber type, length, numerical aperture) [103]

Stability

Complex media community distinguishes *dynamic* and *static* disorder systems. In a dynamic medium, scatterers move and the output speckle pattern evolves with a characteristic time smaller or on the order of the acquisition time of the detection device. Observation of light dispersion by milk or fog with a standard camera are typical examples of dynamic media experiments. On the contrary, a medium is considered *static* if scatterers and speckle patterns are stable during the time of an experiment.
Stability of a complex system can be characterized by measuring decorrelation of output speckle pattern keeping a constant illumination. Stability curves relative to a layer of paint and a multimode fiber are given in Appendix A. In experiments conducted in a lab environment, a multimode fiber has been found to be less sensitive to temperature changes and vibrations than a layer of paint ; its use has then enabled to conduct experiments with longer acquisition times.
When their properties are chosen adapted to those of the sources, disordered systems fulfill the three necessary conditions to be exploited as quantum walk platforms: *linearity, coherence and stability.*

1.3.2 Quantum optics and disordered media

While disordered media naturally provide a coherent coupling between a huge number of modes, their association with quantum light raises new experimental challenges: weak intensities of currently available quantum sources combined with the impossibility to collect all output light severely reduce detection efficiencies. In consequence, disordered media are generally considered unpractical for quantum applications. During the past fifteen years, only few teams in the complex media community have investigated propagation of quantum light through complex systems.

Non-classical light propagating in disordered media

Theoretical models of non-classical light traveling through disordered systems were first developed to study propagation of squeezed radiation [104, 105, 106], quantum noise [107], spatially entangled state [108] or two-photons state [109, 110, 111, 112]. Such mathematical approaches have inspired several experimental works exploring the evolution of non-classical properties of light through complex systems. Squeezed light [113] and especially photon-pairs [114, 115, 116, 117, 118, 119, 120] were the first non-classical states of light under study. Among all these works, the paper of W.H.Peeters and coworkers in [116] reports the first observation of a *two-photon speckle pattern* obtained by measuring coincidences after photon-pairs propagation through a weakly scattering medium.
All these studies have highlighted the high potential of quantum light propagation in complex systems for fundamental and applied physics, but they have also revealed new experimental constraints set by the use of quantum light.

Controlling non-classical light propagation in disordered systems

As it is described with more details in Chapter 2, the development of wavefront shaping methods has led to a surge in activity dedicated to the control of light propagation through complex media [121]. These methods are widely used to image or focus classical light through disordered photonic structures of biological tissues. Recently, they have been combined with quantum optics for the first time to solve detection efficiency problems. Huisman and coworkers used an optimization method [122] to enhance the probability of detecting a single-photon at the output of a white paint layer [123]. As presented on Figure 1.13, the output signal in the targeted mode has been enhanced by a factor thirty.

Wavefront shaping techniques have also the potential to transform a disordered medium into a versatile platform for creating programmable speckle patterns [124, 125]. The *Scattering Matrix* approach, developed in our group as a alternative method to the optimization technique [126], allows a deterministic control of light propagating through a complex linear system once it has been characterized i.e. once its scattering matrix has been measured. As presented in Chapter 3, this approach has been applied to a single-photon propagating in a white paint layer to design deterministically the single-photon state collected at the output [127]. This method was then extended to photon-pairs by introducing the novel concept of *Two-photon scattering matrix*. Theoretical aspects of the two-photon scattering matrix are discussed in Chapter 4. Finally, this technique is applied in Chapter 5 to guide photon-pairs launched in a multimode fiber [128] by controlling both quantum and classical interferences, turning a multimode fiber into an efficient reconfigurable multimode optical device.

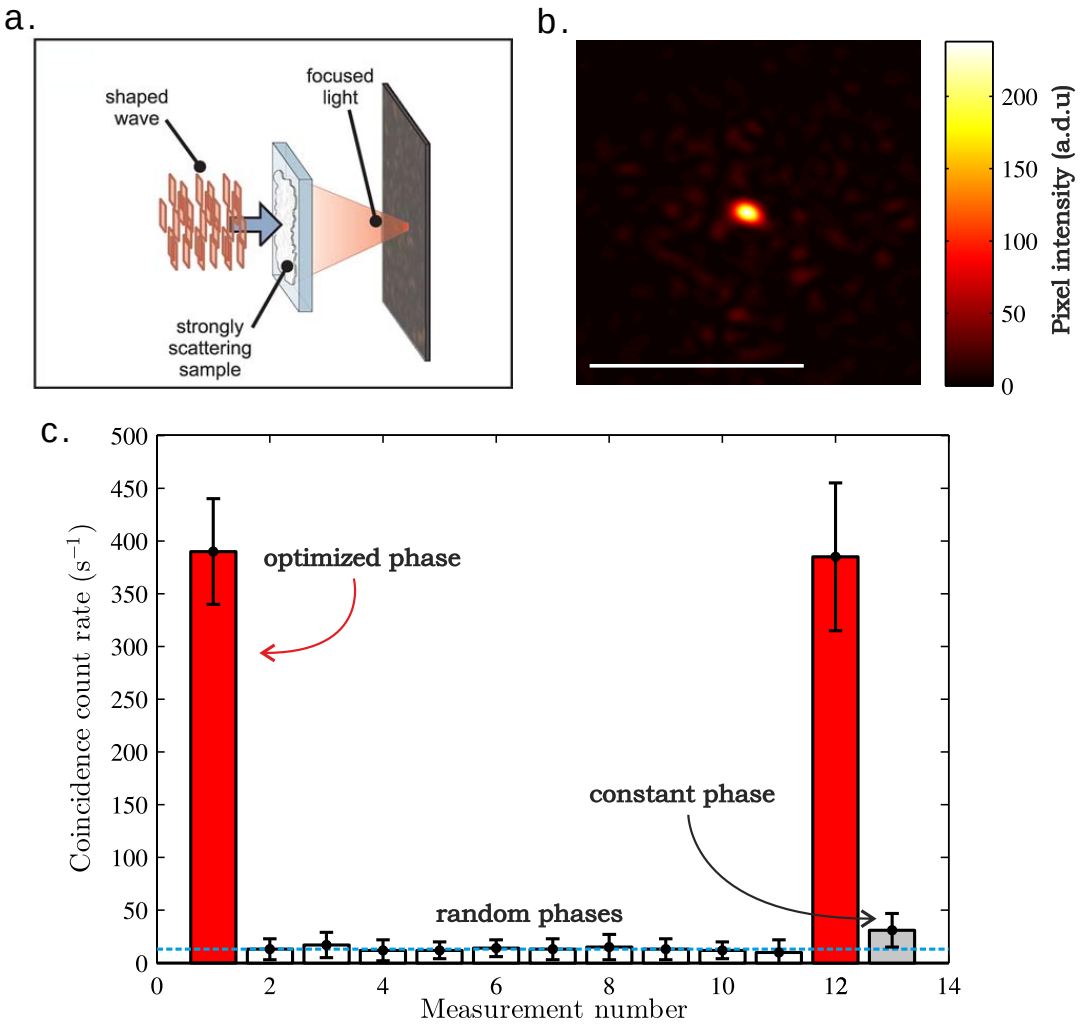

Figure 1.13: **Controlling a single-photon Fock state through opaque scattering media using an optimization algorithm**. **(a)** Design of the experiment when the wavefront of the incident light is shaped so that scattering makes the light focus at a defined target. **(b)** Speckle pattern with a single enhanced mode imaged on a CCD camera obtained with classical light and the optimized pattern. The white line represents 0.5mm. **(c)** Coincidence count rate at the position of the bright spot in **(c)** when a heralded single-photon source replaces the classical source. Coincidence measurements are performed for an optimized (red), constant (gray) and random phase pattern (white). The blue dashed line represents the average coincidence rate measured for random phase patterns. The errors are taken as two times the standard deviations. All figures are extracted from publications of T.J.Huisman, I.M.Vellekop and coworkers [123, 122] .

Chapter 2

Controlling light propagation in disordered media

During the last century, the development of medical imaging techniques - ultrasounds, X-ray radiation, MRI ... - revolutionized the field of medical sciences. These methods are used to reveal internal structures of the body and have deep applications in human medicine. All these methods have one thing in common: they do not use *visible light* in their imaging process.
Visible light properties are intensively exploited in the field of microscopy because optical wavelength strongly interacts with organic molecules. Because of these strong interactions, photons traveling in a biological sample carry a lot of information on very small structures of the sample, such as cellular anomalies or biochemical changes. Images acquired with visible light then generally have a much better resolution that it would be with other medical imaging methods. However, these strong light-matter interactions also make a photon prone to be *scattered* or *absorbed* during its propagation. Imaging *inside* a biological tissue then only relies on the possibility to collect *ballistic light* at the output which limits the penetration depth to a few number of transport mean free paths (approximately 1mm for most of the biological structures) [129]. This constraint makes light-based techniques generally unpractical for biomedical imaging. Absorption is an irreversible process - an absorbed photon is lost with the carried information and can not be retrieved by any means - but scattered light can still be detected at the output. The carried information has then just been scrambled during propagation. In a positive way, the message can be received but it is unreadable.

The study of light propagation in complex systems aims at finding a way to retrieve information hidden in scattered light [130, 131, 132]. Recent works have for example made important progresses in this direction demonstrating the possibility to reconstruct the image of an object positioned behind an opaque layer [133, 134]. Inspired from adaptive optics, *Wavefront Shaping methods* have recently emerged in the community [121, 24]. These techniques allow studying light propagation in a complex medium and can be used to partially cancel the scattering effects.
This chapter introduces different wavefront shaping methods that can be used to study and control light propagation in a complex system. In particular, the technique named

Scattering Matrix approach is more precisely discussed because it is at the heart of all experiments conducted in this thesis. Two experimental cases are particularly investigated: light propagation control in a layer of paint 2.2.3 and through a multimode fiber 2.2.4.

2.1 Wavefront shaping methods

When a photon propagates in a disordered medium, it bounces on its inhomogeneities and can often be described as a particle performing of random walk. Such probabilistic approach of light propagation in complex system has enabled to reach remarkable results about light transport and average intensity distributions [98, 135]. But this particle-diffusion theory neglects all interferences effects which, in spite of their complexity, are deterministic and can be described using Maxwell's equation.

Wavefront shaping methods exploit the deterministic nature of elastic light scattering to study and control its propagation through complex systems. When light propagates through a layer of paint, light gets scattered and all optical paths interfere at the output creating a complex interference pattern: *a speckle pattern* [136]. By modulating the wavefront of the incoming light, one can change how optical waves interfere into the system and modify accordingly the output field. Spatial Light Modulators (SLMs) offer the possibility to address thousands of spatial degrees of freedom of the incident wavefront. They have been the key technology that enabled light manipulation in disordered media.

2.1.1 Spatial Light Modulator

The term SLM regroups different types of optical devices: deformable mirrors, digital micromirrors (DMDs) and liquid crystal displays (LCDs) [137]. Due to their high resolution, LCDs are not only used as displays but can also operate as wavefront modulators. The so-called Liquid Crystal SLMs (LC-SLMs) are miniaturized LCDs which can address the amplitude or the phase of light transmitted or reflected by the device .

For instance, the SLM used in this thesis is a LC-SLM with an active area of about $16 \times 9\,mm$ which offers a very high resolution of 1920×1080 pixels. In a typical Wavefront Shaping setup, this device is positioned just before the complex system and allows controlling the incoming illumination with a very good precision. Nevertheless, its 50% reflectivity is one important weakness of this technology, especially when the SLM is combined with very weak intensity sources such as quantum light sources. The use of an SLM introduces also some other technical constraints that are listed in Appendix B.

2.1.2 The optimization approach

An SLM has been used for the first time to control light propagating through a layer of paint in 2008 by I.Vellekoop and A.P.Mosk [122]. In their experiment, presented on Figure 2.1, coherent light is launched through a layer of paint after being reflected by a

SLM. Output light is collected by CCD camera. Each input mode - SLM pixel - gives rise to a different field at the output: when the incident wavefront is uncontrolled, all those fields interfere in a complex manner and create a speckle pattern (Figure 2.1a). By programming dynamically the SLM, the incident wavefront can be optimized with respect to a targeted intensity signal on the camera. This feedback creates a linear combination of modes at the input that makes the output fields interfering constructively at the targeted position (Figure 2.1b).

This optimization method is very simple to implement: it only requires a detector at the targeted output position connected to a computer programming the SLM accordingly. Different types of optimization algorithms can be used depending on the experimental conditions such as the level of noise or the system stability [138, 139]. If the system is stable enough, the optimization technique enhances the intensity by a factor proportional to the number of freedom degrees controlled by the SLM [122, 140]. This technique can also be extended to multiple output targets. However, an important weakness of this approach relies on the fact that a complete optimization process needs to be performed each time a new target is defined.

This technique demonstrated for the first time the strong potential of using Wavefront Shaping methods to control light propagation in complex systems. This procedure has been subsequently used in a lot of influential works in the complex media community, such as non-linear signal optimization [101], photo-acoustics [141, 142] or second harmonic generation signals [143], to cite a few.
Another approach to control light propagation in complex media has been proposed in 2010 by S.Popoff and co-workers [144]. This method allows a more complete control over the output field using an experimental reconstruction of the *transmission matrix* of the medium.

2.1.3 The Scattering Matrix approach

The *Scattering matrix approach* has first been introduced as an alternative method to the optimization technique. Inspired by works realized in acoustics [145], this approach allows characterizing the mixing properties of a complex linear medium and uses its knowledge to control light propagation through the system. The experimental procedure is then divided in two steps:

- The *characterization step*: the transmission matrix of the medium is measured (2.2).
- The *inversion process*: knowledge of the matrix is exploited to control light propagation (2.3).

This approach has been applied to a large variety of linear systems, ranging from layers of paint [144] to multimode fibers [146, 147] passing by photonic integrated strutures [79, 78]. It has also been extended to more complicated situations that exploit linearity of the scattering process. For instance, a photo-acoustic transmission matrix has been recorded using acoustic detectors at the output [148]. In this case, an acoustic absorber positioned in the output speckle plane emits an acoustic signal proportional

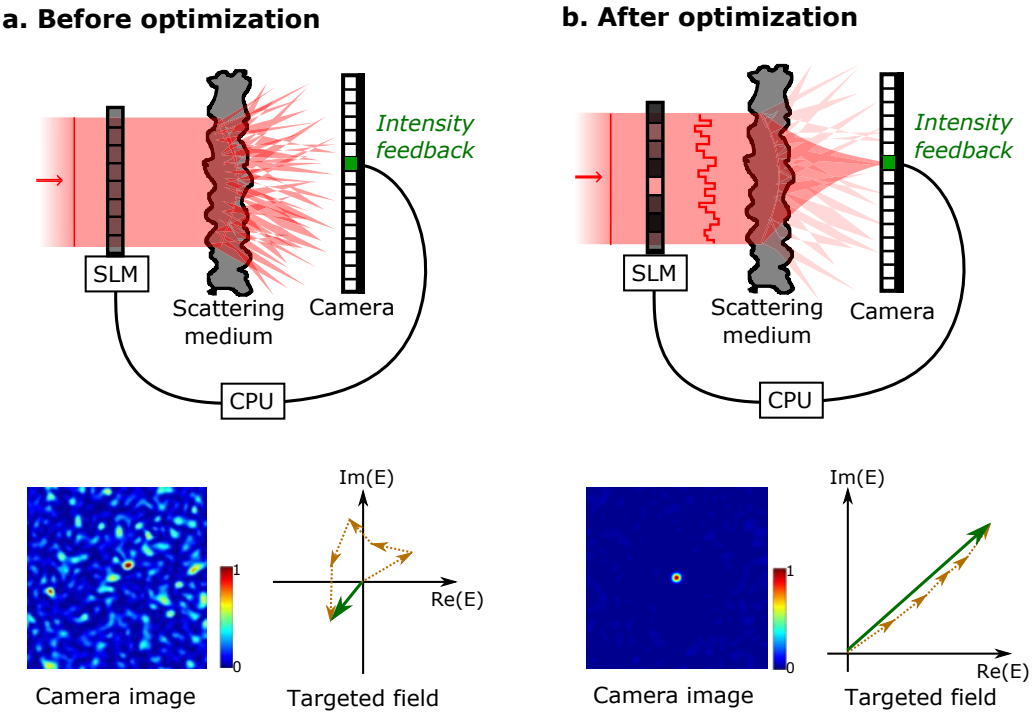

Figure 2.1: **Optimization process to focus light through a scattering medium (a.)** A SLM is positioned on one side of a scattering medium to shape the illumination. Intensity value of a targeted CCD camera pixel is used as a feedback signal. Before optimization, the SLM pattern is flat. , As represented in the complex plane, all the fields created by each SLM pixel add up to the targeted camera pixel with uniformly distributed phase components due to the multiple scattering process. **(b.)** After the optimization process, intensity of the targeted camera pixel is strongly enhanced. As represented in the complex plane, phase components of all the fields contributing to the targeted field are now aligned along a common direction. The global interference effect is then constructive which increase the intensity of the field in the targeted output.

to the intensity it receives. There is a linear relationship between the input optical amplitude and the output acoustic amplitude, that can therefore be described by a "generalized" matrix formalism. Another example is the multi-spectral transmission matrix [99]. In this experiment, a broadband light source propagates through a disordered medium and a spatio-temporal speckle is observed at the output (see Figure 1.12 of chapter 1). By measuring the spatial speckle for each wavelength composing the incoming pulse, one can retrieved a spatio-spectral transmission matrix that describes both the spatial mixing and the temporal spreading of the pulse.
In the scope of this thesis, light and medium properties are chosen to avoid any temporal mixing effects: light propagation can be considered quasi-monochromatic. The scattering matrix approach is then used to investigate the evolution of spatial and polarization properties of quasi-monochromatic light when it propagates through a disordered medium. In this chapter, the matrix measurement process is described using examples of light propagation in a layer of paint and through a multimode fiber.

2.2 The characterization step: transmission matrix measurement

The transmission matrix characterizes the mixing properties of a complex linear system. Mathematically, it is represented by a complex matrix linking a set of optical spatial input modes to a set of optical spatial output modes at a given wavelength. This matrix is a subpart of the complete scattering matrix (SM) involving all the existing optical modes. In particular, this SM is unitary if the system is non-absorptive. Knowledge of the TM brings fundamental insights of the medium. It allows extracting some relevant information on the scattering process such as single and multiple scattering contributions [149, 150], the backscattering cone or the singular values distribution [151]. As presented in section 2.3, its knowledge can be used to control light propagation.
In the characterization step, the TM of a complex linear system is experimentally measured using an holographic technique to access the amplitude of the field.

2.2.1 Linearity and matricial formalism

When coherent light propagates through a complex system, a speckle pattern is created at the output. This speckle pattern represents a signature of the medium disorder under a certain illumination. If the input illumination changes, the corresponding speckle pattern also changes. Thanks to the linearity of the scattering processes, the output speckle field is directly linked to the input field by a linear operator denoted $\mathcal{L}$:

$$\boldsymbol{E}^{\boldsymbol{out}} = \mathcal{L}(\boldsymbol{E}^{\boldsymbol{in}}) \tag{2.2.1}$$

In consequence, once output fields have been recorded for a certain number of input illuminations, the propagation of any linear combinations of these inputs can be predicted.
As presented on Figure 2.2, the characterization step is implemented experimentally using a SLM to shape the input illumination and detection devices - such as CCD

camera of fibers - to collect the output light. All these devices are based on a multi-elements technology: SLM or CCD camera are divided in pixels and an APD integrates signals detected on a certain area. In consequence, these optical systems impose a natural decomposition of the field over discrete sets of input and output modes. A simple representation is to associate one pixel of a device to one mode of the system. Under this constraint, the linear operator L is represented by a matrix T:

$$E^{out} = T \times E^{in} \tag{2.2.2}$$

where E^{out} and E^{in} are input and output fields decomposed on the modes.
Because an SLM or a camera can not control or collect all the existing modes of a given system, T is only a subpart of the complete scattering matrix S.

Input basis

Liquid crystal cell technology of the SLM introduces a natural discretization of the input field where SLM pixels - or macropixels - represent independent modes of the system. As represented on Figure 2.2, the input field takes then the form of a complex vector. The set of modes that associates one SLM pixel to one input mode is called the *X-Y canonical* basis.
Depending on experimental constraints, it is also possible to use other types of basis in the measurement process. In this thesis, two other basis are employed:

- The *X-Y Hadamard* basis: this basis is used in the experiment described in part 2.2.3 which investigates light propagation in a layer of paint.
- The *Fourier* basis: this basis is used the experiment using the multimode fiber and described in part 2.2.4.

Once the matrix has been measured in a certain basis, it is always possible to express it back in the *X-Y canonical* basis or in any basis using basis transformation matrices.

An input mode is defined by the properties of the disordered medium and those of the optical setup. For instance, two SLM pixels very close to each other generally create very similar speckle patterns at the output. One speckle pattern can then be partially expressed using the other speckle and the system is oversampled. In consequence, a vector of the *X-Y canonical* basis is usually defined by a group of correlated pixels forming a macropixel.

Output modes

In experiments conducted in this thesis, output detections are performed using a CCD camera or single mode fibers (SMFs). SMFs are connected to avalanche photodiodes (APDs) and act sensibly as a camera pixel. As represented on Figure 2.2, the output field takes then the form of a complex vector where output modes are associated to camera pixels or SMF cores.

An output mode of the system is defined by a *speckle grain*. As represented on Figure 2.1, a speckle pattern has a granular structure where the size of a grain is

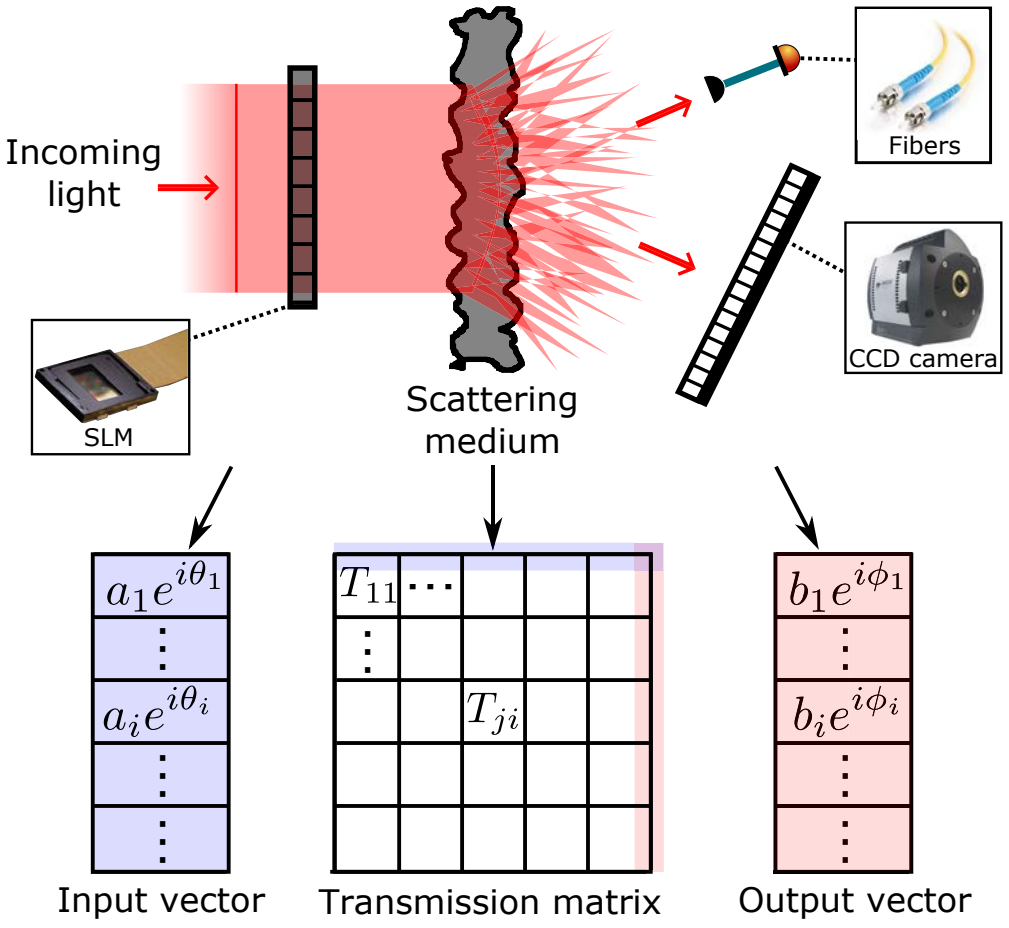

Figure 2.2: **Experimental scheme of the characterization step**. Different illuminations of the scattering medium are generated by programming the SLM. Output light is recorded using detection devices such as a CCD camera pixels or single-mode fibers (SMFs). The transmission matrix links an input field to an output field decomposed on a discrete input and output set of spatial modes.

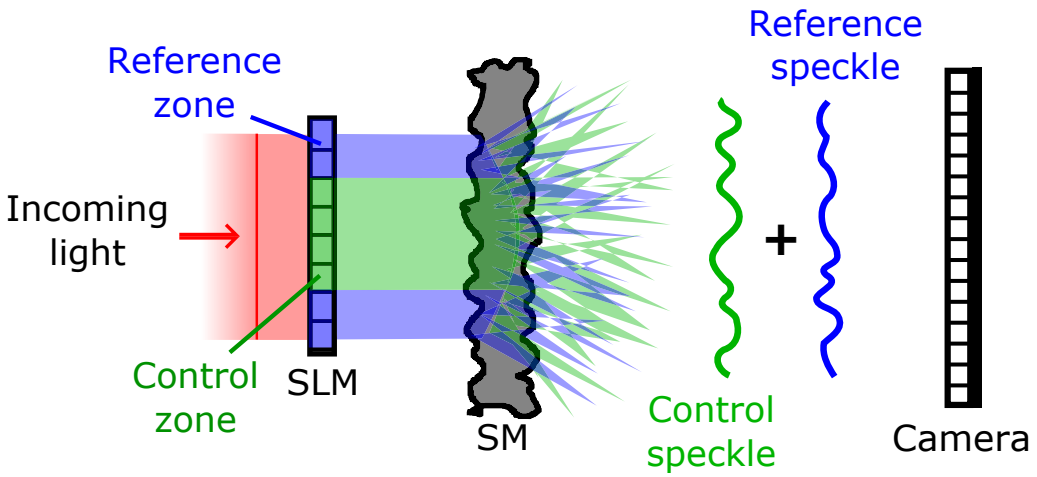

Figure 2.3: **Phase-stepping holographic technique with a speckle field as reference**. The SLM is divided in a *control part* and a *reference part*. After propagation through the medium, light reflected by each part creates two speckle patterns that interfere at the output. The speckle created by the reference part plays the role of reference field in the phase-stepping holographic process.

determined by the medium properties and the experimental configuration. If a camera pixel is much smaller than a speckle grain, pixels close to each other are strongly correlated and can be grouped in macropixels to match the mode size. In the case of SMFs, the imaging configuration is generally adapted to match the size of a speckle grain to the mode field diameter of the SMF [1].

2.2.2 Holographic measurement process

Field measurement in optics raises several difficulties because conventional devices are only sensitive to its intensity. One can generally have access to the complex output field by using an holographic method.
Output fields are then measured using a *phase-stepping holographic method*. As presented on Figure 2.3, the SLM is divided in two parts: a *control part* is programmed to modulate the input illumination and a *reference part* is kept flat during the measurement process. As presented on Figure 2.3, light reflected by each part of the SLM creates two different speckle fields that interfere at the output. In this configuration, the speckle field created by the reference part plays the role of reference field in the holographic process [80].

1. The granular structure of a speckle pattern offers another way to understand how an input mode of a system is defined. Let's imagine that the camera used in Figure 2.2 is replaced by a phase conjugate mirror. In this situation, if a random pattern is programmed on the SLM, it creates a speckle pattern at the output that is reflected by the camera-mirror. This speckle re-propagates backwards in time through the medium and regenerate the phase pattern in the SLM plane. Similarly to the output speckle pattern, this phase pattern also shows a specific granular structure with a typical grain size defined by the properties of the medium and the imaging system. This grain size then defines the typical size of an input mode - or macropixel.

When the reference part is shifted by a global phase θ, the corresponding speckle is shifted by the same amount of phase. The output intensity I_{ji} measured in the output mode j for an input mode i becomes

$$\begin{aligned} I_{ji}^{\theta} &= |r_j e^{i\theta} + E_{ji}|^2 \\ &= |r_j|^2 + |E_{ji}|^2 + 2\cos(\phi_j^r - \phi_{ji}^c + \theta) \end{aligned} \tag{2.2.3}$$

where r_j denotes the complex reference speckle field in output mode j, E_{ji} the complex field at the j^{th} output mode created by the control part generating input mode i. ϕ_{ji} and ϕ_j^r are the phases components of the fields E_{ji} and r_j.
For a fixed input mode i, measurements performed with four different phase values $\theta = \{0, \pi/2, \pi, 3\pi/2\}$ allows reconstructing the complex coefficient M_{ji}

$$\begin{aligned} M_{ji} &= \frac{I_{ji}^0 - I_{ji}^{\pi}}{4} - i\frac{I_{ji}^{3\pi/2} - I_{ji}^{\pi/2}}{4} \\ &= E_{ji} r_j^* \\ &= |E_{ji}||r_j| e^{i(\phi_{ji} - \phi_j^r)} \end{aligned} \tag{2.2.4}$$

M_{ij} is a complex coefficient containing the desired output field value E_{ji} multiplied by the conjugate of reference speckle field. M is called the *unfiltered transmission matrix.*

This unfiltered transmission matrix works efficiently to control light propagation when performing a focusing process (part 2.3). However, this matrix fails in more advanced controlling tasks and the reference amplitude terms $|r_j|$ need to be compensated. A method to retrieve the reference speckle amplitudes directly from the knowledge of M is proposed by S.Popoff and coworkers in [126]. Another technique well adapted to the experimental setup using a multimode fiber is introduced in section 2.2.4.
Once the amplitudes of the reference speckle are known, the transmission matrix coefficients T_{ji} linking input mode i to output mode j can be retrieved by dividing M_{ij} by the reference amplitudes

$$\begin{aligned} T_{ji} &= \frac{M_{ji}}{|r_j|} \\ &= |E_{ji}^{out}| e^{i(\phi_{ji}^c - \phi_j^r)} \end{aligned} \tag{2.2.5}$$

where ϕ_j^r is the phase component of the reference field in output mode j. This remaining phase distortion of the output field does not modify the information contained in the matrix because only the relative phases between the input modes are relevant.

2.2.3 Experimental setup using a layer of paint

We now describe an experimental setup implemented in this thesis that allows characterizing and controlling light propagation through a layer of paint. The setup is

presented on Figure 2.4.a.
In this experiment, vertically polarized monochromatic light is reflected by the SLM and focused into the scattering medium using a microscope objective (MO). Back-reflected light is collected using two types of detection devices: a CCD camera and SMFs connected to avalanche photo-diode (APDs). The combination of a half-wave plate (HWP) and a polarizing beam splitter (PBS) allows selecting one linear polarization at the output. In this configuration, the transmission matrix is measured between N input and M output spatial modes.
Note that the same experimental configuration is also used to perform the experiment of single-photon propagation described in chapter 3.

Input modes

The control part is sampled into N macropixels forming the *X-Y canonical* basis. However, a vector of this set can not be experimentally generated because a macropixel controls only the phase and can not set the field amplitude to zero. As presented on Figure 2.4.b, a *X-Y Hadamard* basis is used instead of the canonical basis during the measurement process [144]. This basis contains N vectors made of combinations of 1 (e^{i0}) and -1 ($e^{i\pi}$). The transmission matrix is first measured using the *X-Y Hadamard* basis and then expressed in the *X-Y canonical* basis by performing a change of basis.

Output modes

In a back-scattering configuration, the output plane corresponds to the surface of the medium. The surface is then imaged on three conjugated planes where a CCD camera and two SMFs are positioned. Direct speckle images are recorded using the camera, and both SMFs can be translated along one axis of the plane to record cross-sections of the speckle pattern (Figure 2.4.c). Lenses magnifications are chosen to ensure a good match between a speckle grain and a SMF core. A rotating half-wave plate (HWP) associated to a polarizing beam splitter (PBS) positioned before the detection devices enable the measurement of both polarizations at the output.

At the end of the process, the unfiltered TM measured links the SLM macropixels to the camera pixels and SMF cores. Then, it is possible to retrieve the transmission matrix T directly from matrix M using the method described in [126]. While this step is not crucial if the matrix is only used to perform focusing tasks, it becomes important for more advanced processes like image reconstruction [126] or singular-value decomposition [80].

2.2.4 Experimental setup using a multimode fiber

The experimental setup described on Figure 2.5 allows characterizing and controlling light propagating through a multimode fiber (MMF). In this experiment, the SLM is divided in two zones denoted SLM H and SLM V. The two incoming beams reflected and controlled by zones H and V are recombined on a PBS just before injection in the MMF. The two shaped illuminations are then crossed polarized at the input which allows acting on both polarization and spatial modes. Output light is collected using

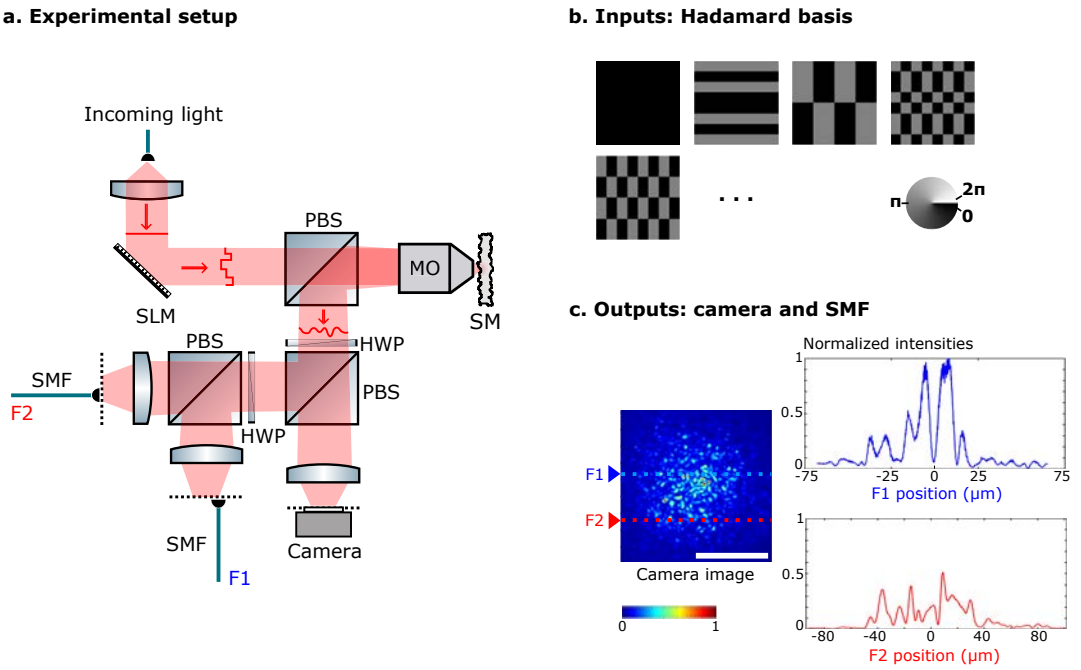

Figure 2.4: **Experimental setup of light propagating in a layer of paint. (a.)** Apparatus to study and control of light propagating in a layer of paint. Light from a single-mode fiber (SMF) is collimated and reflected by a phase-only Spatial Light Modulator (SLM). The SLM plane is Fourier imaged on the input face of the scattering medium using a microscope objective (MO) with a numerical aperture of 0.95. The scattering medium (SM) is an opaque layer of paint (TiO_2) with a mean free path $l_s \approx 1\mu m$ to $2\mu m$. The same MO is used to collect back-scattered light from the medium. This configuration gives a higher collection efficiency of the scattered light and allows a broader effective bandwidth of the medium than is possible in transmission. A polarizing beam splitter (PBS) associated to an half-wave plate selects one of the two output linear polarizations. The light is then collected either with an (a) electron multiplied charged coupled device camera (EMCCD) or with (b) two SMFs. The amplitude ratio between each path is controlled combining a half wave plate (HWP) with a PBS. In the first path the output plane of the medium is imaged on the EMCCD. In the other path, the output field is imaged onto two conjugated planes using two lenses, each containing one of the two output PMSMFs mounted on translation stages. Both fibers and the EMCCD camera are positioned in optical planes conjugated to the surface of the scatterer. Lenses magnification are chosen to match the speckle grain diameter to the mode field diameter of the fibers ($5.3\mu m$). **(b.)** Input modes used during the measurement process. All pattern of the *X-Y Hadamard* basis are successively programmed on the control part of the SLM and the corresponding output field is measured by holography. **(c.)** Camera and both SMFs are positioned in three conjugated output planes. Direct speckle images are acquired using the camera, and SMF can be translated along one plane axis to record cross-section of the speckle pattern. The white scale bar represents 1.5mm in the camera plane.

a CCD camera and two SMFs positioned in output planes conjugated to the output face of the MMF.
Contrary to the experimental setup described in the previous section (2.2.3), the present configuration enables the reconstruction of a TM of the MMF taking into account polarization and spatial modes. In this situation, the TM measurement process needs to be performed following a series of steps detailed in part 2.2.4. At the end of the process, the measured TM links N spatial and polarization modes to M spatial modes at the output.
Note that this experimental setup is also used to perform the experiment of photon-pairs propagation described in chapter 5.

Spatial input modes

We first consider the case where only one input polarization (H or V) is injected into the MMF. The corresponding SLM zone (SLM H or SLM V) is then separated in control and reference parts that allow the TM to be reconstructed by phase-stepping holography.
In this experiment, the measurement process is performed using a *Fourier* basis at the input. As detailed on Figure 2.6.a, the SLM is positioned in a Fourier plane of the input face of the MMF. The basis is then composed by a set of phase ramps programmed on the SLM (Figure2.6.b). Each SLM pattern generates a focused spot on the input face of the MMF characterized by a radius r and an angular parameter α (Figure 2.6.a). A calibration step detailed in Appendix B allows selecting only non-redundants modes to constitute the input basis. Once output fields have been measured for all SLM patterns of the basis, the TM associated to this specific input polarization is reconstructed.

Matrix measurement process

In the experimental setup presented on Figure 2.4, light is reflected simultaneously by both zones of the SLM and is injected into the MMF where spatial and polarization modes get mixed. The resulting output speckle pattern is then a coherent combination of speckles created by both inputs polarizations.
The monochromatic light that enters into this wavefront shaping setup is connected to the source using SMFs. Because these fibered connections are very sensitive to temperature changes and vibrations, the relative path delay between the two input polarizations fluctuates. In consequence, the output speckle pattern is very unstable and this configuration does not enable a direct measurement of the TM (the typical stability time is on the order of the second).
To solve this problem of stability, the matrix measurement process is decomposed in three different steps:

Step 1: Measurement of M_V M_V denotes the part of the unfiltered matrix relative to vertical input polarization. The measurement process is performed using SLM V and blocking light reflected by SLM H. The matrix M_V is then reconstructed using the spatial input basis previously described in 2.2.4. The speckle field used as a reference in the holographic process is denoted r^V.

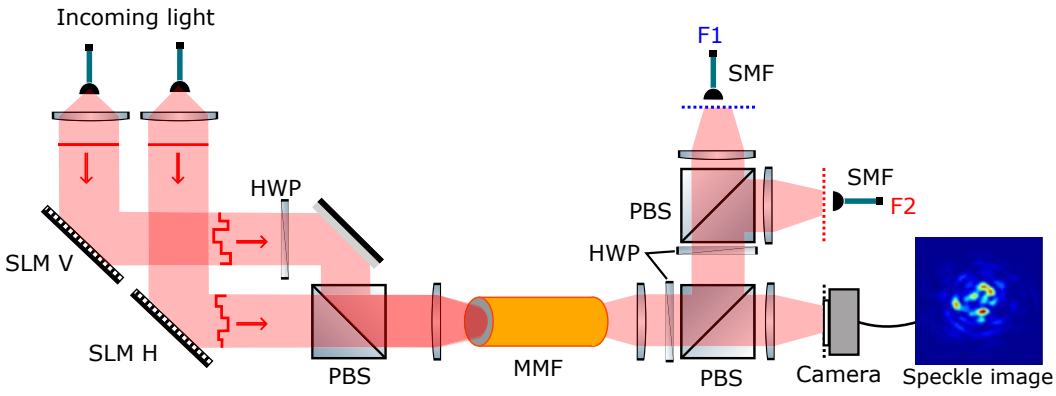

Figure 2.5: **Apparatus to control light propagation through a multimode fiber.** This optical setup allows measuring the TM of a MMF on both polarization and spatial modes. For this purpose, the SLM is divided in two zones denoted SLM H and SLM V. The two incoming beams reflected and controlled by zones H and V are recombined on a PBS just before injection into the MMF. The two shaped illuminations are crossed polarized at the input which allows acting on both polarization and spatial modes. After propagation through the MMF, output light is monitored by an CCD camera and two SMFs F1 and F2 connected to APDs all imaging the output plane of the MMF. The HWP and PBS positioned just after the MMF allows selecting one specific polarization of the output speckle pattern. The second HWP and PBS are used as a beam splitter to duplicate the image plane on the two SMFs.

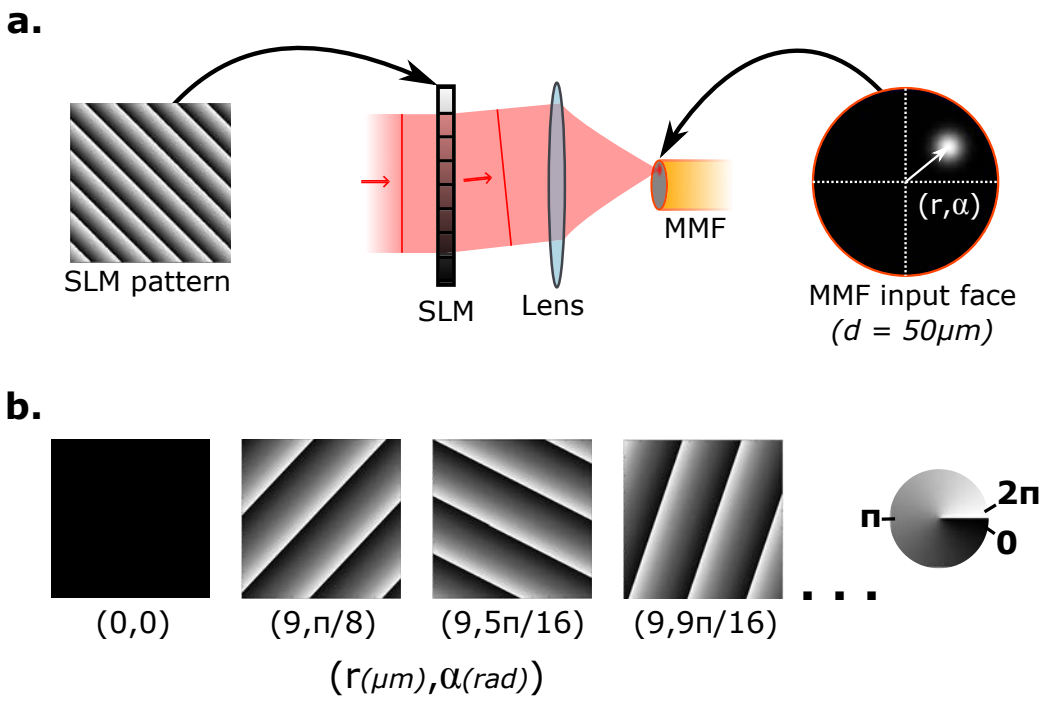

Figure 2.6: ***Fourier* basis used in the matrix measurement process. (a.)** Each vector of the basis refers to a focused light spot onto the input face of the fiber denoted by parameters (r,α). The corresponding SLM pattern tilts the reflected beam by displaying a phase ramp on its surface. **(b.)** The full vector set is then composed of SLM patterns tilting the reflected incoming beam to adjust the different parameters (r,α).

As an additional measurement, we also record the intensity of the reference speckle field. To do so, a SLM pattern corresponding to $r \gg 25\,\mu m$ is programmed on the control part of SLM V. In this situation, light reflected by the control part does not enter in the MMF because its radius is about $25\,\mu m$. In consequence, only the reference part remains injected and its resulting speckle can be directly measured at the output. The quantities M_V and $|r^V|^2$ are known after this step.

Step 2: Measurement of M_H The other part M_H relative to horizontal input polarization is reconstructed using SLM H and blocking light reflected by SLM V. This matrix is also recorded using the spatial input basis described in 2.2.4. The speckle field used as a reference in the holographic process is denoted r^H and its intensity is directly monitored using the same method than the one used with SLM V. The quantities M_V and $|r^H|^2$ are known after this step.
Figure 2.7 shows (a.) typical speckle images obtained by blocking successively SLM H and SLM V and (b.) SMFs scans performed at the output.

Step 3: Measurement of the relative phase between r^H and r^V A reference speckle pattern corresponding to a $r \gg 25\,\mu m$ is now programmed on both SLM zones simultaneously. The two input polarizations are injected simultaneously to make r^H and r^V interfering at the output. A phase-stepping holographic process between the two reference fields is performed for a short time during which the system remains stable. This holographic process allows access to the quantity: $r_j^V r_j^{H*} = |r_j^V||r_j^H|e^{i(\phi_j^{Vr} - \phi_j^{Hr})}$.

Matrix reconstruction process The transmission matrices T_V and T_H relative to the two input polarizations are first calculated using the quantities measured in step 1 and step 2:

$$T_V(ji) = M_V(ji)/|r_j^V| = |E_{ji}^V|e^{i(\phi_{ji}^V - \phi_j^{Vr})} \tag{2.2.6}$$

$$T_H(ji) = M_V(ji)/|r_j^H| = |E_{ji}^H|e^{i(\phi_{ji}^H - \phi_j^{Hr})} \tag{2.2.7}$$

where E_{ji}^V (E_{ji}^H) is the complex value of the output speckle field generated by the i^{th} mode of SLM V (SLM H) measured in output mode j and ϕ_{ji}^V (ϕ_{ji}^H) its phase value.

Then, the matrix T_V is reduced to the same reference than T_H using the relative phase measured in step 3:

$$T_V(ji) \times e^{i(\phi_j^{Vr} - \phi_j^{Hr})} = |E_{ji}^V|e^{i(\phi_{ji}^V - \phi_j^{Hr})} \rightarrow T_V(ji) \tag{2.2.8}$$

Finally, T_V and T_H are concatenated to form the matrix T. An example of a reconstructed matrix is given on Figure 2.8. This TM has been measured in a MMF between $N_V = 69$ plus $N_H = 65$ ($N = N_H + N_V = 134$) input modes (SLM V + SLM H) and 1140 camera pixels.

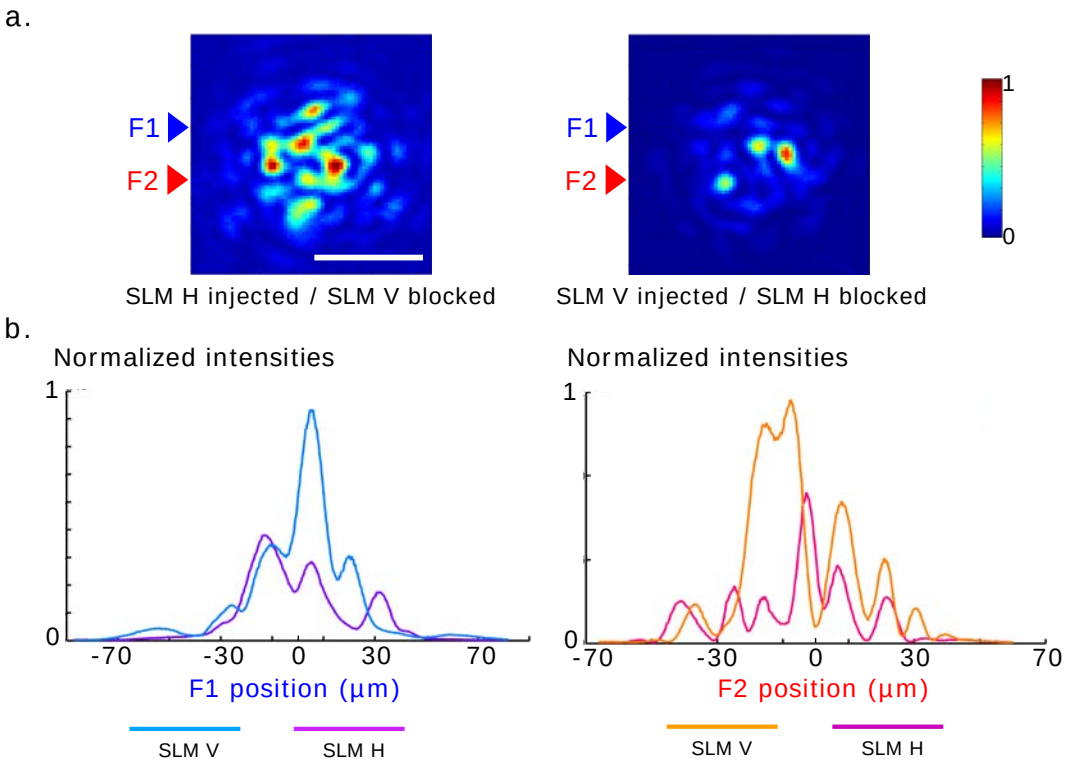

Figure 2.7: **Output images acquired with CCD camera or SMFs**. **(a.)** Typical speckle patterns acquired with the CCD camera when light is injected into the MMF only from SLM V and only from SLM H. **(b.)** SMF scans performed with fibers F1(blue) and F2(red) when light is injected in the MMF only from SLM V and only from SLM H. The blue and red marks on the camera images indicate the positions of the scans. The white scale bar refers to 0.4mm in the camera plane.

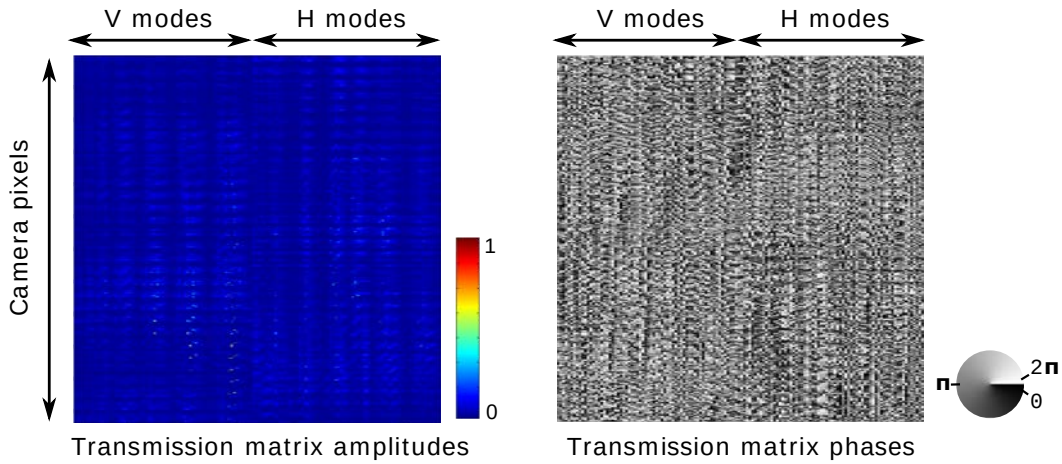

Figure 2.8: **Experimentally reconstructed transmission matrix**. The figure represents amplitudes and phases components of a measured transmission matrix. This matrix has been measured by generating 69 vertically polarized input modes (V input modes) and 65 horizontally polarized input modes (H input modes) and by collecting light on 1140 camera pixels.

2.3 The inversion process: controlling light

Once the TM of a linear medium has been measured, it can be used to control light propagating in the complex system. This step is called the *inversion step* because it requires calculation of an "inverse" of T.
The inverse denoted $T^{"-1"}$ is defined as the matrix linking any output mode of the system to its corresponding input mode:

$$E^{in}_{\text{shape}} = T^{"-1"} \times E^{out}_{\text{target}} \tag{2.3.1}$$

Using the previous equation, it becomes possible to calculate the input field that corresponds to any desired output field of the system. The corresponding field can then be generated at the input by programming the SLM accordingly and the targeted field should be measured at the output.
This process requires both a proper definition of $T^{"-1"}$ and the possibility to shape perfectly the input field. However, experimental constraints do not allow these conditions to be verified and the ideal inversion process given by equation 2.3.1 needs to be adapted .

2.3.1 The inverse operator

In experiments conducted in this thesis, the inversion process is mainly used to concentrate light into specific output modes of the system. As presented in this section, the transpose conjugate operator is the most efficient inverse operator that can be used for energy concentration. It is then exploited here to perform the focusing task under our experimental constraints (2.3.1). This operator has been employed to focus light

through a layer of paint and a multimode fiber. The results obtained confirm the theoretical predictions (2.3.2).

Pseudo-inverse operator

The pseudo-inverse matrix is a generalization of the inverse of a matrix [152]. This inverse exists from any complex matrix and verifies $T \times T^{-1} = \mathbb{1}$. In consequence, it appears as the most suitable operator for the inversion process. Assuming that the input field is perfectly shaped, the desired output field should be perfectly retrieved after re-propagation through the system:

$$\begin{aligned} \text{Input field calculation: } & E^{in}_{\text{shape}} = T^{-1} \times E^{out}_{\text{target}} \\ \text{Re-propagation: } & E^{in} = T \times T^{-1} \times E^{out}_{\text{target}} = E^{out}_{\text{target}} \end{aligned} \tag{2.3.2}$$

However, two experimental constraints prevent using this operator in a real experiment:

- Experimental noise is always introduced during the measurement process of T. During the pseudo-inverse calculation of T, a small noise introduced in T gets strongly amplified in T^{-1}. This operator is then very sensitive to noise. As a result, it becomes very unstable and totally inefficient in a real experiment.
- The SLM can only shape the phase of the input field. Under this experimental limit, the efficiency of the operator decreases very quickly with the complexity of the targeted field.

The pseudo-inverse operator can also be modified for instance using the Tikhonov regularization method [153]. This method enhances the efficiency of this operator for a specific types of inverse problems, such as image reconstruction problems [126].

Transpose conjugate operator

The transpose conjugate operator T^+ offers a good alternative to the pseudo-inverse. When certain conditions on the matrix coefficients are verified (see chapter 4 for more details), the product $T \times T^+$ shows strong amplitude of its diagonal coefficients compared to the the off-diagonal coefficients. Re-propagation of an input field determined by T^+ then reconstructs efficiently the targeted field at the output:

$$\begin{aligned} \text{Input field calculation: } & E^{in}_{\text{shape}} = T^{+} \times E^{out}_{\text{target}} \\ \text{Re-propagation: } & E^{in} = \underbrace{T \times T^{+}}_{\approx \mathbb{1}} \times E^{out}_{\text{target}} \approx E^{out}_{\text{target}} \end{aligned} \tag{2.3.3}$$

This operator is very stable regarding the noise level: a small noise introduced in T remains a small noise in T^+. Moreover, its efficiency is less impacted by the phase only character of the SLM when performing a focusing process. In a focusing process, the targeted output field is very simple: a small number of modes contain the value of one, and the others are set to zero. Because the shaping is imperfect, none can expect to retrieve perfectly this output field. However, a good approximation is to have the

greatest difference of intensity between the modes set to one and the others. The transpose conjugate operator is exactly achieving this: it forces the multiple interferences to be constructive in the targeted modes and does not act on the others [154]. In this case, the possibility to shape also the amplitude of the input field would only decrease the total intensity in the target outputs because a SLM is a passive device [155].
The transpose conjugate operator is then an ideal operator when combined with a phase only SLM to perform focusing tasks.

2.3.2 Focusing light through complex system

Experiments using the transpose conjugate operator T^+ to focus light into several output modes of the system confirm its efficiency [80]. This section presents two examples of focusing processes realized in layer of paint and a multimode fiber.

Focusing light on a camera pixel

Figure2.9 shows results of light focusing through a layer of paint (**a.**) and through a MMF (**b.**). The corresponding experimental setups are presented on Figures 2.4 and 2.5.
An enhancement η is defined as the value of intensity of the targeted pixel in the focusing case divided by the average intensity of speckle pattern surrounding it. In these examples, η is about 100 in both cases when using a basis of 256 modes for the layer of paint and a basis of 180 modes for the MMF.
Under the hypothesis that the system is characterized by a TM composed of random independent complex numbers following a Gaussian statistics [138], the theoretical model gives an expected enhancement value of $\eta_{th} = \frac{N\pi}{4}$ where N is the number of modes controlled. Enhancements predicted for the layer of paint $\eta_{th} \approx 200$ and the MMF $\eta_{th} \approx 140$ are in good adequacy with our experimental results.

Focusing light in an output SMF

Figure 2.10 represents a focusing process performed through a layer of paint using an output SMF as a target. The corresponding experimental setup is presented on Figures 2.4.
In this case, the transmission matrix has been measured by collecting light only with the SMF fixed at a certain position in the output plane. The resulting matrix is then a simple complex line. During the inversion process, knowledge of this matrix-vector is used to focus light into the SMF and an enhancement $\eta_{SMF} \approx 100$ is observed (Figure 2.4a).
Keeping the same SLM pattern on the SLM, a complete image of the output speckle pattern is acquired with the camera and shown on Figure 2.4b. The focused spot is also clearly visible on the image, but the enhancement η_C measured is much smaller than the enhancement measured on the SMF scan: $\eta_C \approx 10 \ll \eta_{SMF}$. Note that in this configuration the surface of a camera pixel ($16 \times 16\,\mu m$) was perfectly matched to the diameter of the SMF ($5.3\,\mu m$ diameter) in the conjugated observation planes. The difference observed relies on the fact that the spatial mode collected by the SMF is filtered by its small numerical aperture ($NA = 0.12$). The spatial mode measured

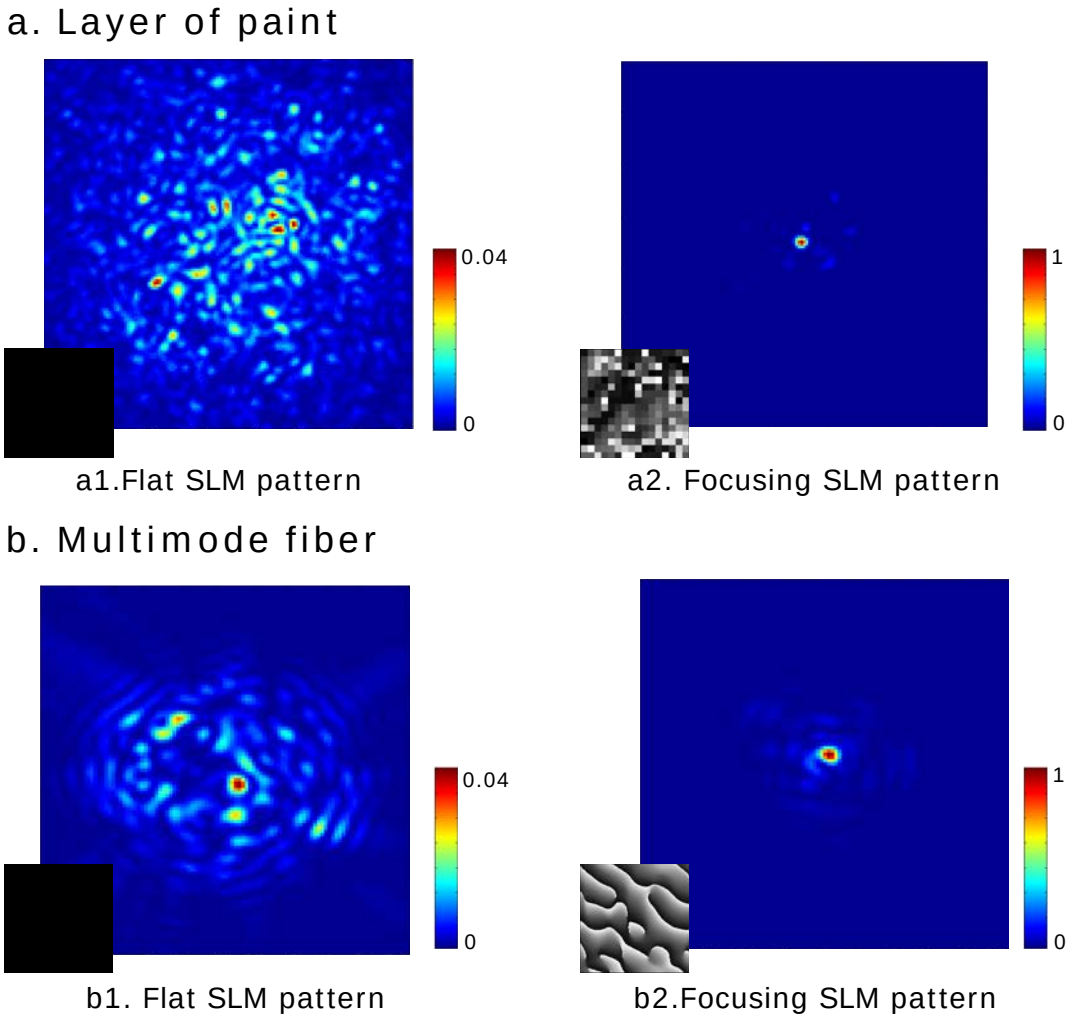

Figure 2.9: **Focusing processes using the transpose conjugate operator in a layer of paint and a multimode fiber**. **(a1.)** and **(b1.)** represent speckle patterns acquired when the control part of the SLM is maintained flat at the input and do not shape the illumination. **(a2.)** and **(b2.)** represent output speckles when focusing masks are calculated with the transpose conjugate operator and programmed on the SLM. The intensity enhancement η is defined as the maximum intensity of the focusing target divided by the average speckle intensity. η is about 100 in both cases. Transmission matrices have been measured using 256 input modes in the layer of paint setup and with 180 modes in the MMF setup (only using SLM V). Images in inset show the SLM patterns corresponding to each speckle.

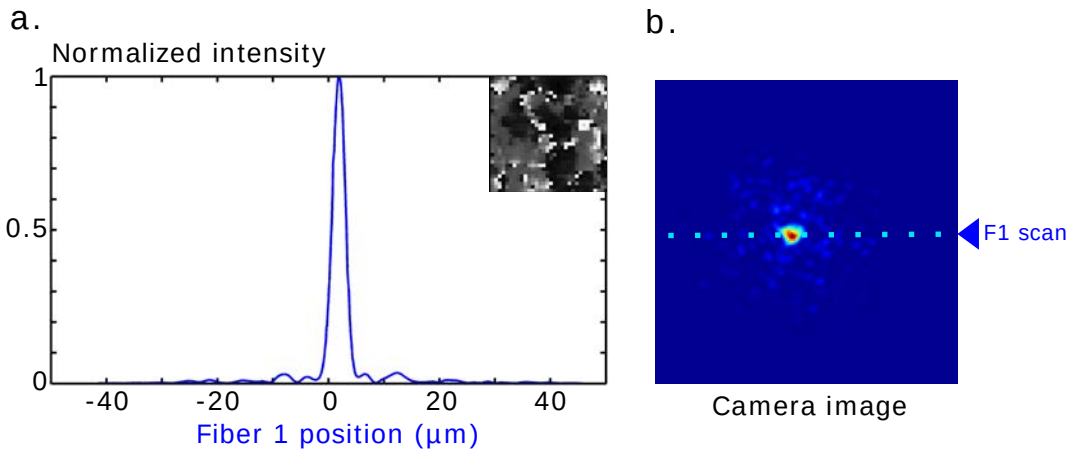

Figure 2.10: **Focusing process through a layer of paint using a SMF target**. The transmission matrix has been measured using a SMF as output mode of the system. Using the transpose conjugate of the measured matrix, an enhancement of $\eta_{SMF} \approx 100$ is observed on the SMF scan at the targeted position **(a.)**. However, the corresponding camera image shows a smaller enhancement of about $\eta_c \approx 10$ **(b.)**.

with the corresponding camera pixel does not exactly correspond to the spatial mode measured with the SMF. In consequence, the SLM mask that focuses light in the SMF is not perfectly adapted to focus light on the corresponding SLM pixel.

These results demonstrate the efficiency of the transpose conjugate operator to perform focusing tasks independently of the type of detector used. However, we have seen previously that matrices measured using a camera pixel or a SMF core are not perfectly identical: the focusing enhancement is not the same when the matrix is reconstructed with one device and observed with the other. A focusing process performed on a certain detection device is thus more efficient when using its corresponding matrix.

2.4 Conclusion

At first glance, a speckle pattern appears as an image composed of bright and dark spots randomly distributed. It was therefore normal that statistical methods have been used first to describe speckle properties and more generally to study light propagation in disordered media [136]. However, a speckle pattern is generated by complex but *deterministic* interference phenomena: if the medium is stable, two speckle patterns observed at different times under the same illumination are identical. Wavefront shaping methods have exploited the deterministic aspect of wave interference phenomena and have introduced a new concept to study light propagation in complex systems. In particular, the scattering matrix approach allows characterizing how light is scrambled during propagation through a disordered medium by reconstructing its transmission matrix. Moreover, the TM reveals information on the scattering process that can be

exploited to control light propagation [80]. In particular, we have seen that the use of the transpose conjugate operator allows focusing light efficiently in several output modes of the system.

The scattering matrix technique has been employed for different types of systems ranging from biological tissues [156] to multimode fibers [146, 147] passing by photonic integrated circuits [79, 78]. Disordered media have also been investigated with different types of light such as short light pulses [101, 157, 99] or incoherent light [133, 134]. An important goal of this thesis was to apply the scattering matrix approach presented previously with classical light to the control of non-classical light. This goal has been achieved for two different type of sources: a *single-photon source* and a *photon-pairs source*.

In chapter 3, the scattering matrix approach is used to control of single-photons propagating in a layer of paint. After the characterization step performed with a classical source, the source is replaced by a single-photon source with the same optical properties (spectrum, polarization, spatial mode). Knowledge of the transmission matrix can then be directly used to manipulate single-photon propagation.
An theoretical extension of this wavefront shaping approach to photon-pairs propagation is presented in chapter 4. In this chapter, we introduce for the first time the concept of *two-photon transmission matrix* that describes propagation of indistinguishable photon-pairs in a complex multimode system. As for classical light, the knowledge of the two-photon matrix can also be used to control photon-pairs propagation. In chapter 5, this method is implemented to focus photon-pairs into a specific output mode of a multimode fiber.

Chapter 3

Single-photon quantum walk in a scattering medium

This first part of this work explores the possibility of using multiple-scattering media as highly multimode platforms to implement quantum walks with single-photons. We aim at using wavefront shaping to control the propagation of the single-photon through the medium. In this experiment, propagation of the single-photon in a layer of paint is investigated with a fully characterized transmission matrix (TM). We show that, similarly to [123], we can control the incident wavefront of the single-photon and deliver it with enhanced efficiency to a chosen set of positions. In a second step, this allows us to demonstrate the controlled manipulation of a single-photon state delocalized between two output modes after propagation in multiple-scattering medium. This work is reported in the letter [127].

In the first part of this chapter (3.1), we assess the advantages and the drawbacks of using a layer of paint as an optical platform for quantum optics. In particular, we discuss the various solutions that we suggested to overcome some important experimental issues.
The control of a single-photon propagating in a layer of paint is then described in two steps. In a first part (3.2), we present the characterization step where the TM of the scattering medium is measured with a classical source. This section reuses some results that have already been introduced in part 2.2.3 of chapter 2. Then, the classical source is replaced by a single-photon source and the knowledge of the TM is used to manipulate single-photon propagation. As described in section 3.3, this method allows deterministic guiding of a single-photon into several outputs of the system. A simplified scheme of the experiment is presented on Figure 3.1.
In the last part of this chapter (3.4), we propose another implementation of a single-photon quantum walk but using a multimode fiber (MMF). We present some experimental results similar to those obtained with the layer of paint and analyze the advantages provided by this new platform.

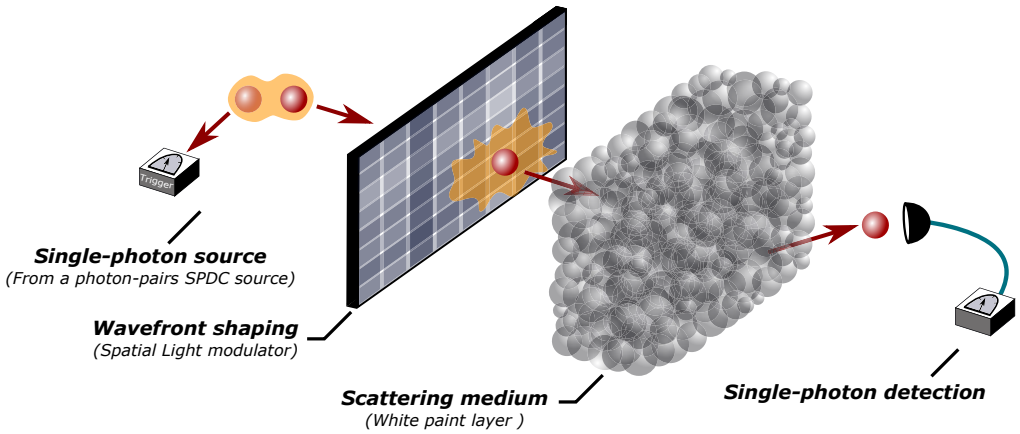

Figure 3.1: **Single-photon quantum walk in a layer of paint**. Single-photons are generated using a heralded single-photon source. They are distributed over the different input modes of a layer of paint using a spatial light modulator (SLM). Output light is collected by single mode fibers (SMFs). Coincidences measured with the trigger detector certify the detection of a single-photon. For the sake of simplicity, this scheme represents a photon being transmitted through the medium, while in our experimental setup we collect in fact the back-reflected photons.

3.1 A new optical platform for quantum walk experiments

As it has been described in chapter 1, quantum walks provide a simple and powerful model of quantum dynamics and have found a broad range of practical applications. For instance, they have been used to model natural quantum phenomena, such as photosynthesis [158] or exciton dynamics [159], and form the basis of a large variety of quantum algorithms developed for problems including graph search [160, 161, 162] or computation of a broad class of general formulas [163].

The scientific relevance of quantum walks and the computational advantages of their applications are strongly related to the capacities of the platform where the walk occurs [83]. In the last decade, photonic integrated circuits have been the key technology that has enabled the implement of a large variety of quantum walk experiments. This is mainly explained by the stability and the simple fabrication process of these platforms [164]. However, they show two important weaknesses: they only connect a *limited number of modes* (up to ~ 10) and they are not easily *reconfigurable*.
On the one hand, the number of optical modes involved during photons propagation play an important role in the complexity of the process because it fixes the size of the Hilbert space to consider [83] [1]. On the other hand, a reconfigurable linear optical

1. Some works studying for instance the boson sampling problem [73, 74, 75, 76, 86, 87] or Anderson localization effects [165, 72, 166] have demonstrated the importance of working with large interferometric platforms.

system would allow replacing a multitude of existing devices of the same size and may help the development of new algorithms for information processing [167, 168].

In the first of this section (3.1.1), we explain why scattering media such as layers of paint can be considered as multimode optical devices. And even more, as multimode optical devices with modal capacities that overperform those offered by current photonic integrated circuits.
Nevertheless, these systems are very difficult to combine with quantum optics because losses and scattering severely reduce the detection efficiencies. The solution proposed in this chapter is to use wavefront shaping methods [122, 80] to control single-photon propagation and then enhance signal intensities over certain modes. However, to implement these techniques, we have to take into account some specific properties of a layer of paint and build the optical setup accordingly. The specific configuration chosen is detailed in part 3.1.2.

3.1.1 A layer of paint: a highly multimode coupling device

The term *scattering medium* is generally associated to a multitude of systems ranging from biological tissues to ground glass diffusers passing by plasmonic systems. In this study, it simply refers to a densely packed layer of TiO_2 particles: a *white paint layer*. The particles of our sample have an average diameter of 100 nm and the layer has a thickness on the order of $L \sim 10\,\mu$m. Our medium is also characterized by a mean free path on the order of $l_s \sim 1\mu m$ (see part 1.3.1 of chapter 1 for more details).

The number of optical modes connected by this device can be evaluated by considering the simple situation where light is focused on the surface of the sample. Photons then propagate through the medium and become either back-reflected or transmitted [2].
In transmission, light propagation reaches the multiple-scattering regime ($L \gg l_t$) and the diffusive hallow has an area A_T proportional to the square of the medium thickness: $A_T \sim L^2$. The number of modes then scales as $N_T \sim L^2/\lambda^2$.
In reflection, the area of the diffusive hallow A_R is much smaller and depends only on the transport mean free path: $A_R \sim l_t^2$. In consequence, the number of modes is reduced and scales as $N_T \sim l_t^2/\lambda^2$ [136].

The experimental setup used in this experiment is the same than the one presented on Figure 2.4 in chapter 2. Due to some reasons detailed in the next part (3.1.2), we work here in a *reflection configuration*. The back-reflected light is collected by a high numerical aperture (NA= 0.95) microscope objective (MO) and the surface of the medium is imaged with a CCD camera. A typical back-reflected speckle pattern measured when incoming light is focused on the surface is shown on Figure 3.2.a. The speckle image shows about 200 speckle grains which correspond to independent optical modes. The number of modes involved is much larger than the tens of modes offered by photonic integrated structures [164].

2. The part of light that outcomes from the sides of the system is negligible [169] because of the quasi-planar geometry.

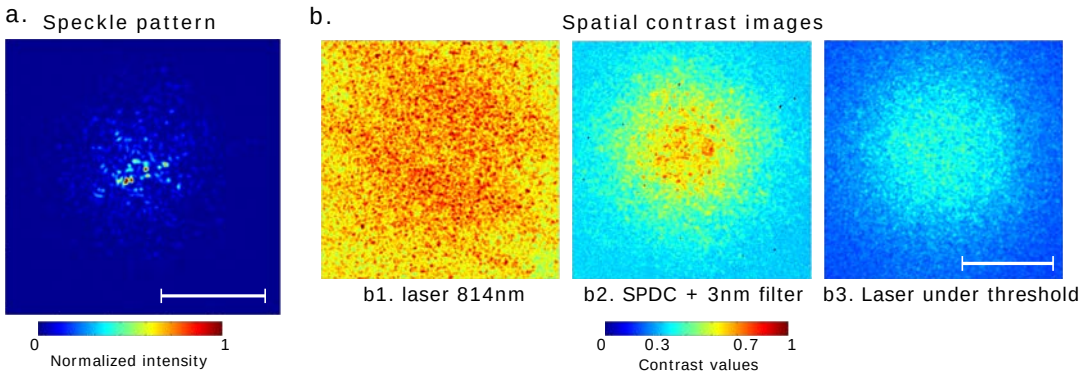

Figure 3.2: **Speckle pattern and spatial contrast images of back-scattered light from a layer of paint**. **(a.)** Back-scattered speckle pattern acquired with the CCD camera when light is focused on the surface of the medium. The number of speckle grains - or optical modes - is about 200. **(b.)** Spatial contrast images recorded with different types of incoming light for the same scattering medium. To calculate the contrast value at a specific pixel of the camera, we first estimate the standard deviation of the intensity measured on this pixel for 100 independent speckle realizations. A contrast value ranging from 0 to 1 is then obtained by dividing this standard deviation by the mean intensity. One specific speckle realization is obtained by programming a random phase pattern on the SLM. As expected, we observe contrast values close to 1 when using a laser centered at 814nm (b1). Contrasts are decreased to an average value close to 0.3 when the laser is working under the threshold because the light has a broader spectrum in this regime (b3). When using light generated by a SPDC process filtered with a 3 nm bandwidth filter centered at 810nm, we observe an important increase of the contrast at the center of the speckle (b2). It is difficult to perform a quantitative analysis because the measurements are very noisy due to the weak intensity of the source. More accurate acquisitions performed using a bright classical source with the same spectrum have shown an average contrast value of 0.71. This ensures that light propagation can be considered as quasi-monochromatic. The white scale bars correspond to approximately $8\,\mu m$ on the surface of the layer.

3.1.2 Experimental constraints

In spite of their important modal capacities, scattering media raise important issues when they are implemented in a real optical setup working with non-classical light.

The first important challenge is related to the very weak intensity of the quantum source and the insufficient stability of the medium. The quantum source that we use in this experiment is approximately 10^{10} times less intense than a simple 1 mW laser source. In consequence, all detection measurements require very long integration time to collect relevant data. However, the integration time is limited by the stability of the medium. For instance, the layer of paint that we use is very sensitive to vibrations or temperature fluctuations and remains stable only during few hours under our laboratory conditions (Appendix B). We need then to pay particular attention to the stability of our medium and the intensity of the light that we want to measure.
The second issue relies on the spectral properties of the photons emitted by the quantum source. In this type of source, photons spectrum is determined by the generation process as well as potential additional filters and can not be considered monochromatic. When polychromatic light propagates through a scattering medium, spectral dispersion effects can be observed [170, 171] [3]. While these effects can be investigated using well-adapted detection systems [157, 99], they reduce the quality of interferences occurring during light propagation. In our experiment, we only study and control the spatial properties of light, and therefore we want to avoid all spectral effects.

The solution that has been found to partially solve these problems is to work in a *reflection configuration*. A complete description of the experimental setup is represented on Figure 2.4 in chapter 2. In this experiment, the same MO is used to focus light on the surface and to collect back-scattered light.
On the one hand, the "Ohm's" law for light stipulates that the transmitted intensity is inversely proportional to the sample thickness [172]. In our thick layer of paint ($L \gg l_s$), most of the light is then back-reflected and working in a reflection configuration allow maximizing the number of photons that can be collected. Moreover, the number of optical modes to consider in this configuration is smaller than in the transmission configuration (3.1.1), which enables to collect more photons by mode for the same total intensity. On the other hand, this configuration reduces the spectral dispersion phenomenon because the distribution of optical paths that contribute to the back-reflected speckle is narrower than in the transmission configuration [173]. As presented on Figure 3.2.b, we can evaluate the modal dispersion effects by measuring the spatial contrast of the speckle pattern [100]. Using our quantum light source with the 3nm narrowband filter, we find a contrast value close enough to unity which ensures that light propagation can be considered quasi-monochromatic [4].
In addition, we also point out that a polarizing beam splitter (PBS) positioned at the output selects an orthogonal linear polarization relatively to the input field. While

3. A similar dispersion problem is detailed in Appendix D in the case of a multimode fiber.

4. The image on Figure 3.2.b2 is very noisy and do not gives a very good estimation of the contrast. Complementary experiments realized with a more intense source with the same spectrum have permitted to estimate more precisely an average contrast value of approximately 0.71.

direct reflections and single scattering events conserve polarization, multiple scattering events generate complex polarization states. In this configuration, we thus collect exclusively photons that have been multiply scattered [174].

The next sections of this chapter describe the method implemented to control single-photon propagation in a layer of paint using the setup described on Figure 2.4 in chapter 2. For the sake of simplicity, all the schemes of the experiment (Figures 3.3,3.4 and 3.5) are drawn in a transmission configuration, but we have to keep in mind that the real experiment is implemented in reflection.

3.2 Characterization of the medium using a classical source

When a photon propagates through a disordered medium, it bounces off the medium inhomogeneities and has a certain probability to exit in a specific output mode of the system. While the detection of one photon in a certain mode is a *probabilistic* phenomenon, we can determine the complete output probability distribution by considering the propagation of its associated field, which is a *deterministic* process (see part 1.1.4 of chapter 1 for more details). The probability distribution can be retrieved by accumulating many measurements working with single-photons, but also directly by using an intense classical field, provided that it is in the same optical mode - spatial, spectral and polarization - than the single-photons. Once light propagation has been characterized with a classical source, we can predict the probabilities of detecting single-photons at the output of the same system. The TM measured with classical light remains thus valid to describe propagation of single-photons. In this chapter, we exploit this result to predict and control the propagation of single-photon through a layer of paint. This section describes the first step of the experiment: measuring the TM with a classical source.

As reported in chapter 2, light propagation in a complex system can be characterized by measuring the TM of the medium [5]. The measurement process performed in this experiment is based on the method described in part 2.2.3 of chapter 2. In particular, the experimental setup used here is the same than the one described on Figure 2.4. In this section, we simply remind some important aspects of this process (part 3.2.1) and gives more precisions on the classical source that we use (part 3.2.2).

3.2.1 Wavefront shaping setup

As described in part 2.2.3 of chapter 2, the TM measurement process allows retrieving a complex matrix T that connects an input field decomposed on SLM macro-pixels to an output field collected by camera pixels and polarization maintaining single-mode fibers (PMSMFs). In this experiment, the control part of the SLM is split into 32×32 macro-pixels which represent $N = 1024$ input modes. Output modes are collected simultaneously with 512×512 pixels of the camera and with two PMSMFs which leads to a total number of output modes of $M = 512 \times 512 + 2$. The two spatial modes

5. Taking into account the fact that we work in a reflection configuration in this experiment, this matrix could also be called the *reflection matrix*.

locally injected in the output PMSMFs during the measurement process are denoted A and B.
During the measurement process, the acquisition time is set to a minimum of 300ms and the TM is then recorded over about 20min. The procedure is fast relatively to the typical stability time of the medium because we use a bright classical source. The same measurement would have not been possible in our experimental conditions by directly using the single-photon source.

3.2.2 Classical source properties

The classical source used in this characterization step is a continuous-wave infrared diode laser with a central wavelength of 814 nm. When working in the laser regime, the source does not fit the spectral properties of the quantum source, which emits single-photons with a spectrum centered at 810nm and a bandwith of 3nm (see part 3.3.1). In consequence, we decrease the laser pump intensity to work bellow the laser threshold. The source thus emits light with a broad spectrum (FWHM $\simeq$ 13 nm). This light is then filtered using a 3nm narrowband filter centered at 810nm to perfectly match the spectral properties of the quantum source.
Under these conditions, the speckle contrast of the reflected light is close to unity (Figure 3.2.b2) and ensures that there is no spectral dispersion during light propagation [100]. Polarization and spatial properties of light are well-controlled by using PMSMFs to connect the source to the wavefront shaping setup. Moreover, these fiber connections facilitate the interchange between the classical and the quantum source required in the next step of the experiment.

After the characterization step, we use the transpose conjugate of the TM to control light propagation following the method given in part 2.3 of chapter 2. In the next section, this technique is applied to control single-photon propagation.

3.3 Control of a single-photon quantum walk in a layer of paint

The classical source is now replaced by a single-photon source with the same optical properties. We then exploit the knowledge of the TM to program the SLM and manipulate single-photons propagation using exactly the same approach than the one described in part 2.3 of chapter 2 with classical light. As mentioned in the previous sections, the only requirement to success here is to make the single-photons properties (spectrum, spatial distribution and polarization) perfectly matching those of the classical source that has been used in the TM measurement process.

In this section, we first provide some clarifications on the single-photon source that replaces the classical source (3.3.1). Then, we demonstrate that the scattering matrix approach is very effective to focus single-photons into an arbitrary output mode of the system (3.3.2). Finally, we show that this method can be used to manipulate more complex single-photon states at the output where the photon is delocalized between several modes (3.3.3).

3.3.1 Single-photon source

In this experiment, single-photons are generated using a heralded single-photon source. The general properties of this source are given in section 1.1.2 of chapter 1 and some additional details can also be found in Appendix A. Here we simply remind some important characteristics of this source.

The source is implemented by pumping a periodically poled potassium titanyl phosphate (PPKTP) crystal with a 50mW continuous-wave laser diode at 405nm. Photon-pairs are produced around 810nm and are filtered using the same narrowband filter centered at 810 nm (FWHM $\simeq$ 3nm) than the classical source which ensures a very good overlap of the spectra. In an heralded single-photon source configuration, one photon of the pair is used as a trigger photon and is measured with a trigger detector denoted T. Its twin is injected in a PMSMF which certifies well-defined spatial and polarization modes. The coincidence rate - corresponding to the amount of single-photon effectively generated by the source - is about $10^5 s^{-1}$ which corresponds to 0.1pW. The purity of the source is characterized by the parameter $g^{(2)} \approx 0.07 \ll 1$ [46].

3.3.2 Guiding of a single-photon in a specific output mode

During the TM measurement process described in part 3.2, the two PMSMFs F1 and F2 are positioned in the output speckle plane and define two spatial output modes of the system denoted A and B (3.2.1). To demonstrate our capacity to guide single-photons, we first calculate the phase pattern that focuses light into mode A using the transpose conjugate of the TM (part 2.3 of chapter 2). Then, by displaying this phase pattern on the SLM, single-photons are focused into the targeted output mode A. A simplified scheme of the single-photon focusing process is shown in Figure 3.3.a.

After programming the SLM, two fiber scans are performed with fiber F1. One scan is realized with a random phase pattern displayed on the SLM, and the other one with the optimized phase pattern for focusing (Figure 3.3.b). Because we use an heralded single-photon source (3.3.1), all counting events detected by the APD connected to F1 are measured in coincidence with the trigger photon of the source. This coincidence detection process is performed using a field-programmable gate array (FPGA) coincidence counter with a coincidence window time set to 2.5 ns. These coincidence events are called *heralded single-photon* events (hsp).
We observe on the blue curve of Figure 3.3.b an important enhancement of the intensity located exactly at position $0\,\mu m$ which corresponds to the position of mode A. The enhancement ratio can not be precisely quantified because the speckle patterns generated without the focusing mask are too noisy (purple curve). However, we can estimate the efficiency of the focusing process by comparing the intensity measured in the targeted output mode R_f to the total speckle intensity R_s. For this purpose, we first estimate the losses η in our experimental setup using a classical source. η takes into account the absorption in the different optical devices crossed by the photons, the collection efficiency of the microscope objective and the amount of light lost in transmission. We measure $\eta \approx 5\%$. Starting from a source with a rate of 10^5 hsp/s,

the total speckle intensity is found to be about $R_s = 5000$ hsp/s. The efficiency of the focusing process is then estimated to be:

$$\frac{R_f}{R_s} \approx \frac{350}{5000} \approx 7\% \tag{3.3.1}$$

Because the fiber can be moved to any position in the output plane, the mode injected in the target SMF is arbitrary chosen within all the output modes of the diffusive halo. Finally, this single-photon focusing process using he TM enhances the probability amplitude of the state $\hat{a}_A^+|0\rangle$. This state becomes then experimentally measurable and exploitable.

3.3.3 Deterministic control of the single-photon output state

In the second part of the experiment, we adopt the TM method to focus a single-photon state into the two output modes A and B simultaneously with a controlled relative phase ϕ. A and B denote the two spatial modes that are locally injected in the two output PMSMFs during the TM measurement process (3.2.1). In this situation, we then attempt to enhance the probability of detecting at the output a single-photon state of the form:

$$|\phi_{out}\rangle \approx (\hat{a}_A^+ + \hat{a}_B^+ e^{i\phi})|0\rangle \tag{3.3.2}$$

Simultaneous focusing on two targeted modes

Knowledge of the TM is now used to determine the input pattern that allows focusing light simultaneously in A and B with a controlled relative phase ϕ. By displaying the corresponding phase pattern on the SLM, single-photons are then focused simultaneously onto the two targeted output modes. A simplified scheme of the single-photon focusing process is shown in Figure 3.4.a.

As shown on Figure 3.4, we observe intensity enhancement in the two targeted modes by scanning both PMSMFs in the speckle plane. The heralded single-photon rates are optimized up to 40 hsp/s in both targeted modes. Position of the targeted modes can also be directly visualized in the image plane acquired by the camera (Figure 3.4.b).

Coherence properties of the optimized state

Coherence properties of the optimized output state are investigated by reconstructing its reduced density matrix $\hat{\rho}_r$ [175, 176]. In this part, we give a simple description of the matrix and we focus our attention on the measurement techniques used to determine its elements. A more complete description of this matrix can be found in Appendix C.

Diagonal elements of this matrix are denoted P_{ij} $(i, j \in \{0, 1\})$. They represent the probability of finding i photons in mode A and j in mode B. The P_{ij} can be directly estimated by photon counting on both modes. The non-zero off-diagonal element denoted d is called the coherence term. Contrary to the diagonal-elements, its value

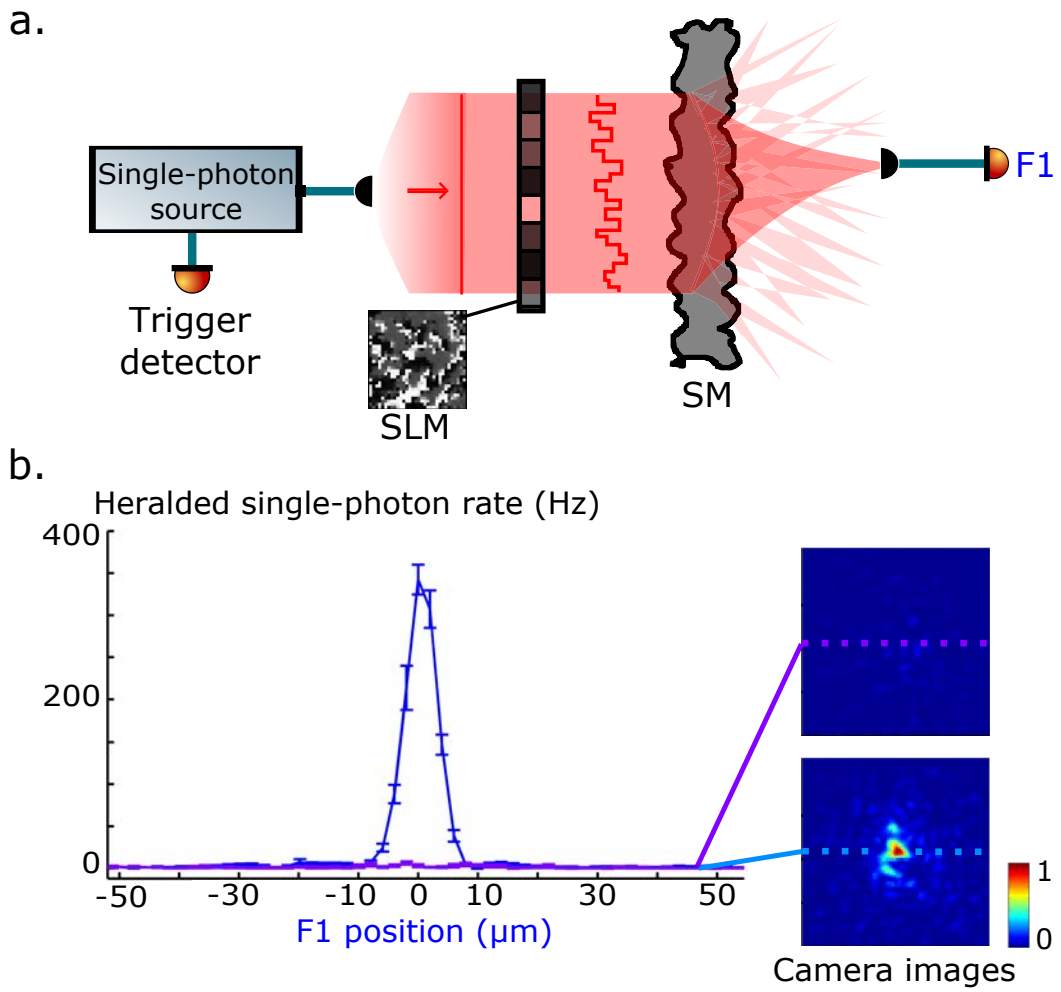

Figure 3.3: **Single-photon focused on a targeted output mode of a layer of paint** **(a.)** Scheme of the single-photon focusing process using the TM approach. **(b.)** 1D scans of the output PMSMF realized with a random phase pattern (purple curve) and the focusing phase pattern (blue curve) displayed on the SLM. Output plane images are recorded with the CCD camera for the same random phase pattern and the same focusing pattern displayed on the SLM. Purple and blue dashed lines represent the position of the scans produced with the output fiber. Contrary to the fiber output signal, measured in coincidences with the trigger photon of the non-classical source, intensity images recorded with the camera are not triggered and therefore correspond to looking at attenuated coherent states.

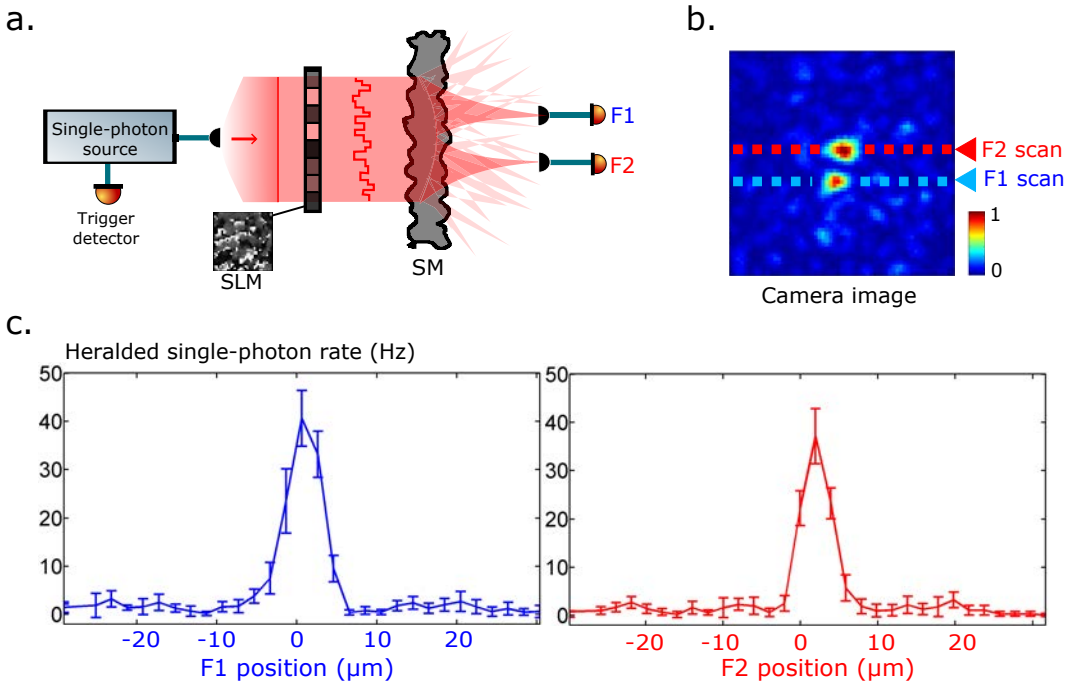

Figure 3.4: **single-photon focused simultaneously in two output modes of a layer of paint (a.)** Experimental configuration of simultaneous focusing single-photons in two modes. The focusing process is performed using the two PMSMFs as output targets. **(b.)** Image of the output plane acquired with the camera displaying position of the two targeted modes. **(c.)** Fiber scans performed with both output PMSMFs showing single-photon intensity enhancement at the two targeted output positions. Heralded single-photon rates go up to approximately 40 ph/s in both modes.

is not directly accessible, but can be estimated by interfering the two output modes. More details on these measurement techniques are given in Appendix C.
Single-photon interference is observed by combining the two output signals on a beam splitter (BS) as represented on Figure 3.5a. To record interference fringes shown on Figure 3.5b, a set of SLM phase patterns is first calculated using the TM. Each phase pattern corresponds to an output field focused simultaneously onto the two output PMSMFs with equal amplitude and a relative phase $\phi \in [0, 2\pi]$. Interference fringes are then reconstructed by displaying successively on the SLM the different phase patterns with a relative phase varying from 0 to 2π. The interference visibility is evaluated from Figure 3.5a to be $V = 0.78 \pm 0.04$. This gives an estimation of $|d| \approx (3.3 \pm 0.6) \times 10^{-5}$ and allows experimental reconstruction of the reduced density matrix presented on Figure 3.5c (Appendix C).

This analysis confirms that the scattering matrix approach provides a complete control over the amplitude and phase properties of the output single-photon state. In the next part, we use the knowledge of the reduced density matrix measured here to characterize entanglement in the optimized state.

Characterizing entanglement in the optimized state

Uniform coherent superpositions of a single-photon across several modes are called quantum optical W-states [177, 178, 179]. These states exhibit multipartite entanglement properties that can be exploited in quantum information science. In this experiment, the optimized state $|\phi_{out}\rangle$ tends to approach a very simple W-state involving only two modes.
Non-classical features of $|\phi_{out}\rangle$ are strongly attenuated due to the imperfection of the focusing process, as it is proved by the strong value of P_{00} in the density matrix. Nevertheless, the amount of non-classicality contained in the optimized state can be characterized by evaluating its level of entanglement.

The level of entanglement in the measured state has a lower bound given by the concurrence [175, 176]. The concurrence, C, is a monotonic measure of bipartite entanglement that is zero for any separable state and positive for all entangled states. The concurrence is calculated from the equation:

$$C = \max(2|d| - 2\sqrt{P_{00}P_{11}}, 0) \tag{3.3.3}$$

where d, P_{00} and P_{11} are elements of the reduced density matrix presented on Figure 3.5c. The C value provides a strict lower bound to the entanglement.
With no correction for detection efficiencies or propagation losses, and without substraction of any background, we find a lower bound for the concurrence: $C = (4.6 \pm 1.2) \times 10^{-5} > 0$ with a 99% confidence level [6].
This conclusively demonstrates a non-zero degree of entanglement [7] in the optimized

6. The statistical analysis is presented in Appendix C

7. Note that the notion of entanglement in a quantum state involving only one particle is still under discussion in the community [180, 181].

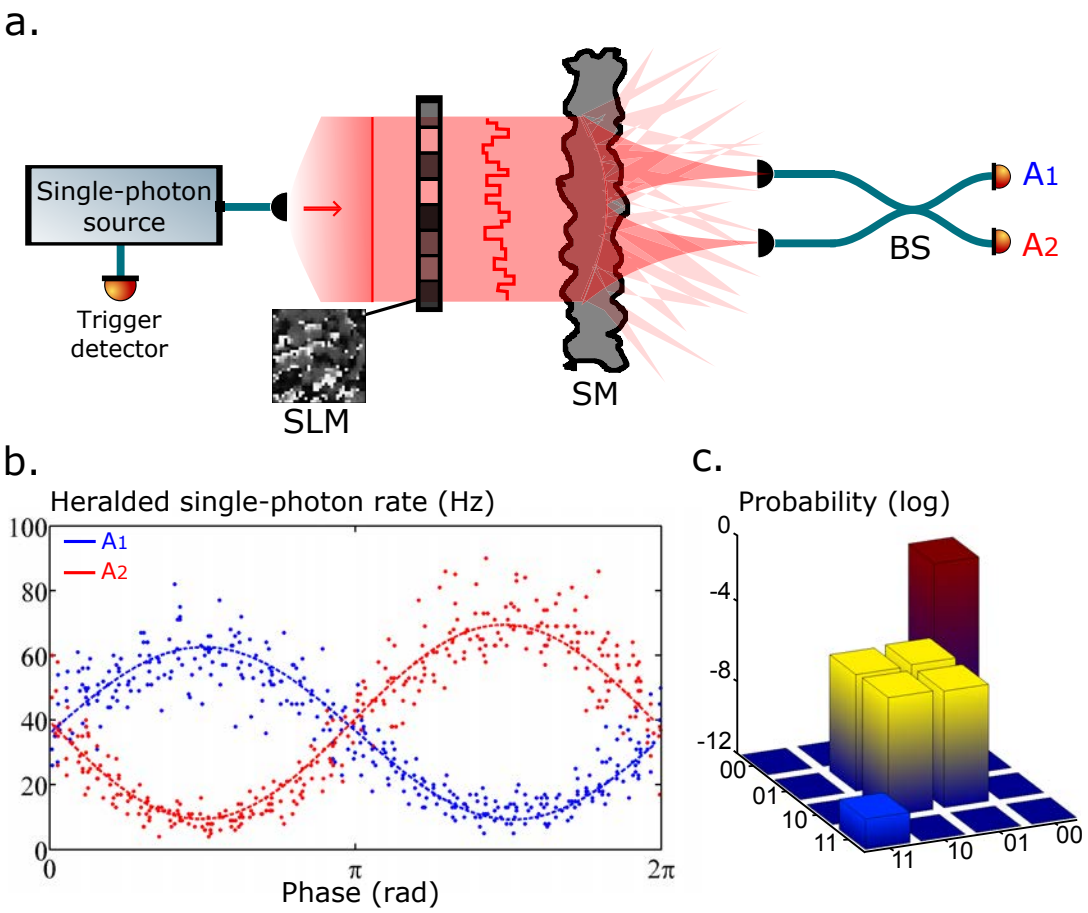

Figure 3.5: **Coherence properties of the optimized state a.** Experimental configuration of focusing single-photon simultaneously on two output modes both recombined on a beam splitter (BS). **b.** Single-photon interference fringes observed by combining the two output PMSMFs on a beam splitter. The relative phase ϕ is driven between 0 and 2π by programming the SLM accordingly. Interference visibility is estimated to be $V = 0.78 \pm 0.04$. **c.** Reduced density matrix of the generated state. The matrix elements are measured running a 3 hours acquisition with a coincidence window time of 2.5 ns. The diagonal elements are: $P_{00} = 1 - 8.4 \times 10^{-5}, P_{01} = (4.1 \pm 0.7) \times 10^{-5}, P_{10} = (4.3 \pm 0.7) \times 10^{-5}, P_{11} = 1/(1.1 \times 10^{10})$. The off-diagonal elements are: $|d| = (3.3 \pm 0.6) \times 10^{-5}$. More details on the reduced density matrix are given in Appendix C.

single-photon state. Quantum resources of the optimized therefore remain exploitable.

3.3.4 Conclusion

This experiment demonstrates that a multiple scattering system, such as a layer of paint, can be used as a multimode optical platform to implement single-photon quantum walks. Moreover, it proves that wavefront shaping methods - originally developed to manipulate classical light propagation - can be directly transposed to the control of non-classical states of light propagating in a disordered system, here a single-photon Fock state.
After characterization of the system, the TM approach allows focusing single-photons onto several output modes of the system. By delocalizing the single-photon between two output modes, we can also optimize a coherent superposition of single-photon state at the output whose non-classical features remains exploitable. More generally, this experiment shows that the control of the light in a scattering medium allows a coherent superposing of a non-classical state of light between several spatial modes.

This work which uses complete knowledge of the TM of a multiple scattering medium opens a number of potential routes to implement quantum information processing. While we have demonstrated control over two independent spatial modes, the complexity of the scattering process could allow access to a significantly larger number of modes (easily on the order of $N = 10^4$), hence a much larger Hilbert space. The scattering process could therefore be seen as a complex mode converter, potentially allowing the generation of large W-state of the form $|W\rangle = |10..0\rangle + e^{i\phi_2}|01..0\rangle + ... + e^{i\phi_N}|00..1\rangle$, possibly in a simpler and more scalable way than using interferometers [182, 179] or photonic lattices [183].

This experiment represents a first important step towards implementation and the control of multi-photon quantum walk in complex systems. However, while a layer of paint has very important modal capacities, it has also some disadvantages compare to systems such as photonic integrated structures. The very complex mixing process in the paint layer and the optical devices that are required to exploit it introduce important losses which considerably reduced the detection efficiencies. Moreover, these losses can not really be compensated by increasing the integration time because it is limited by the stability of medium (3.1.2). In particular, we have shown in this study that it is almost impossible to detect photons that emerge from the medium without controlling them (purple curve on Figure 3.3.b). This problem is even more worrisome when we want to use multi-photon states which require *coincidence* detections at the output.

New complex multimode systems have recently focus the attention of the complex media community: *multimode optical fibers* (MMFs). When light propagates through a MMF, it is distributed over the different optical modes. These modes then interfere during light propagation and a speckle pattern is created at the output. MMFs share with layers of paint this capacity to strongly mix a high number of optical modes, but they also have some particular properties that could be interesting in the context of

quantum optics. To complete this chapter, we then investigate the ability of the MMFs to be used as complex multimode platforms for photonic quantum walks.

3.4 Quantum walks with single-photons in a multimode fiber

Optical fibers have been created at the beginning of the twentieth century [184]. This technology has played a fundamental role in the development of light based communications techniques [185]. Contrary to single-mode fibers (SMFs), which support the propagation of only one spatial transverse mode of light, multimode fibers (MMFs) allow guiding a few optical modes [186].
The extra degrees of freedom provided by MMFs have been first exploited in the communication context to increase the amount of transmitted information using for instance space-division multiplexing techniques [187, 188]. Wavefront shaping methods, that were first developed to control light propagation in scattering media [122, 80], have recently been transposed to MMFs [189, 190]. These works have opened new opportunities for example in imaging [191, 192] and optical trapping [190]. While MMF technology has already been combined with quantum optics to *transmit* information [193], from our knowledge there are no works that exploit MMFs to *process* information, for instance by implementing quantum walk of photons.

In the last section of this chapter, we highlight the fact that a MMF is also a very promising optical platform to implement quantum walk of photons. We first discuss the characteristics of MMFs by reviewing some important studies conducted in the domain (3.4.1). In this part, we also discuss the advantages provided by these systems compared to the layer of paint studied previously.
Then, we describe one of the first manipulation of single-photons through a MMFs using the scattering matrix approach (3.4.2). This experiment demonstrates the strong potential of using MMFs as optical platforms to implement quantum walks and paves the way for the two-photon quantum walk experiment described in chapter 5.

3.4.1 Mixing processes in multimode fibers

In this part, we analyze the progresses made during the last decades on the study and the control of light propagation in MMFs. In particular, we point out the main differences between the mode mixing process of a MMF and the one occurring in a scattering medium such as a layer of paint. Finally, we compare properties of MMFs to those of scattering media from an experimental point of view.

Light propagation control technique developed with scattering media such as layer of paints have recently been transposed to MMFs. Focusing light into a specific output mode of a MMF has been performed by optimization [189, 194], digital phase conjugation [195, 196, 191] or by measuring the TM of the fiber [190, 197]. These results have been used to develop new imaging techniques with application for instance in fluorescence [198] or photoacoustic microscopy [192]. These investigations have also been extended to polychromatic light because spatio-temporal coupling occurs in a MMF like in a scattering medium. Temporal focusing of a short-pulse propagating through a

MMF has then been demonstrated by E. Morales-Delgado and coworkers in [199] and an original application has also been proposed by B.Redding and coworkers [102, 200]: the use of a MMF as a high resolution spectrometer.

While many of the methods used in scattering media can be directly applied to MMFs, MMFs also exhibit some unique features due to their particular geometry. The mixing properties of a MMF strongly depends on the characteristics of the fiber (core diameter, length, refractive indexes, numerical aperture) [103, 147] and on its configuration [195, 197]. Such properties can be investigated by measuring and studying the TM of these systems [201, 202, 147, 203].
Among these investigations, the recent work of M.Plöschner and coworkers [147] provides a very precise study of the mode mixing process. In this study, they have demonstrated the possibility to find a basis of optical input-output modes where the TM is almost amplitude diagonal (if the MMF is not too much bended). The choice of this basis would then cancel the mixing process and light would propagate like in a transparent medium. Because phase components of the diagonal are not identical, a basis change allows retrieving a matrix that is sparse, but partially correlated [8]. For instance, the basis described in section 2.2.4 of chapter 2 allows retrieving a very sparse matrix shown on Figure 2.8. Even if these sparse matrices are similar to those measured with a scattering medium, the statistics of their elements are totally different. In addition, the limited number of mode supported by a MMF enables to measure almost a complete and unitary TM [147]. In this case, the focusing processes become very efficient and it is possible to near-perfectly control the output pattern using an SLM [206].

From an experimental point of view, MMFs have several advantages compare to layers of paint. Because absorption and backscattering are generally negligible [207], almost all the light injected in the MMF emerges at the output. Moreover, light that exits the MMF has limited directions because of the finite numerical aperture of the fiber, which makes its collection more efficient.
A large range of parameters (core diameter, length, refractive indexes, numerical aperture) can also be set during the fabrication process and enable to select a MMF well-adapted to the light that we use. In particular, the number of modes carried by the fiber can be chosen small enough to increase the number of photons per mode and its length can be selected short enough to neglect any spectral dispersion effects (Appendix D). Another important property is the stability of the MMF. As presented in Appendix B, a MMF stays very stable during a few days in our laboratory conditions, which allow detecting photons using very long integration times.

All these characteristics suggest that MMFs are very suitable to implement quantum walk of photons. Before increasing the number of photons and therefore the complexity of the walk (chapter 5), we first reproduce the same experiment of single-photon focusing as in the previous section to test this new platform [9].

8. These correlations are clearly visible when a plane wave is injected in the MMF with a certain angle because it gives rise to a ring shape at the output of the fiber [204, 205].

9. Note that very similar results on single-photon propagation in MMF have been reported in the same time by J.Carpenter and coworkers in [193]

3.4.2 Controlling single-photon propagation through a multimode fiber

In this experiment, we consider the experimental setup described on Figure 2.5 of chapter 2, but we only keep one of the two SLMs (SLM V).
In this configuration, we first reconstruct the vertically polarized part of the fiber TM using the same classical source than in the previous experiment (3.2.2). This matrix links a set of input modes (part 2.2.4 of chapter 2) to camera pixels and SMFs at the output. Similarly to the previous experiment (3.3.2), the SMF is placed at a specific position denoted A during the measurement process. The matrix is then used to calculate the SLM pattern that concentrates light into output mode A. A simplified scheme of the focusing process is shown on Figure 3.6.a.

Once the pattern is programmed on the SLM, the classical source is replaced by the same single-photon source than the one used in the previous experiment (3.3.2). As presented on Figure 3.6.b, we then perform two scans in the output plane: one scan is realized with a random phase pattern displayed on the SLM (purple curve) and the other one with the optimized phase pattern for focusing (blue curve).
Similarly to the previous experiment, we observe on the blue curve of Figure 3.6.b an important enhancement of the intensity exactly at position $0\,\mu m$ which corresponds to the position of mode A. In this case, the maximum heralded single-photon rate is increased up to 1350 hsp/s. When this result is compared to the result obtained in the previous experiment (Figure 3.3), we observe that the optimized intensity is now 10 times higher [10].
Thanks to the stability of the MMF, we are also able to integrate the detections over 10min for each position of F1. This allows reconstructing with a good precision the output speckle created when a random SLM pattern is programmed (purple curve).

From an experimental point of view, we conclude that a MMF is more suitable than a layer of paint to implement quantum walk of photons for several reasons:
- We have access to more modes at the input relatively to the total number of modes supported by the MMF.
- We collect almost all the output light because of the finite numerical aperture of the fiber.
- The optical setup required to control light through the MMF is less lossy, mainly because we do not need to use the microscope objective.
- The stability of the fiber allows increasing the integration times up to a few days.

3.5 Conclusion

Although this experiment represents a first important step towards implementation of quantum walk in complex systems, we must introduce more photons in the system to observe quantum walk behavior not explained by a classical wave model (1.2.2 in chapter 1). Quantum interferences involved during multi-photon state propagation enrich the quantum walk's evolution which become more interesting both from

10. We take also into account that when this experiment was performed, the heralded single-photon source was emitting a lower rate of about 3.10^4 heralded single-photons per second (hsp/s).

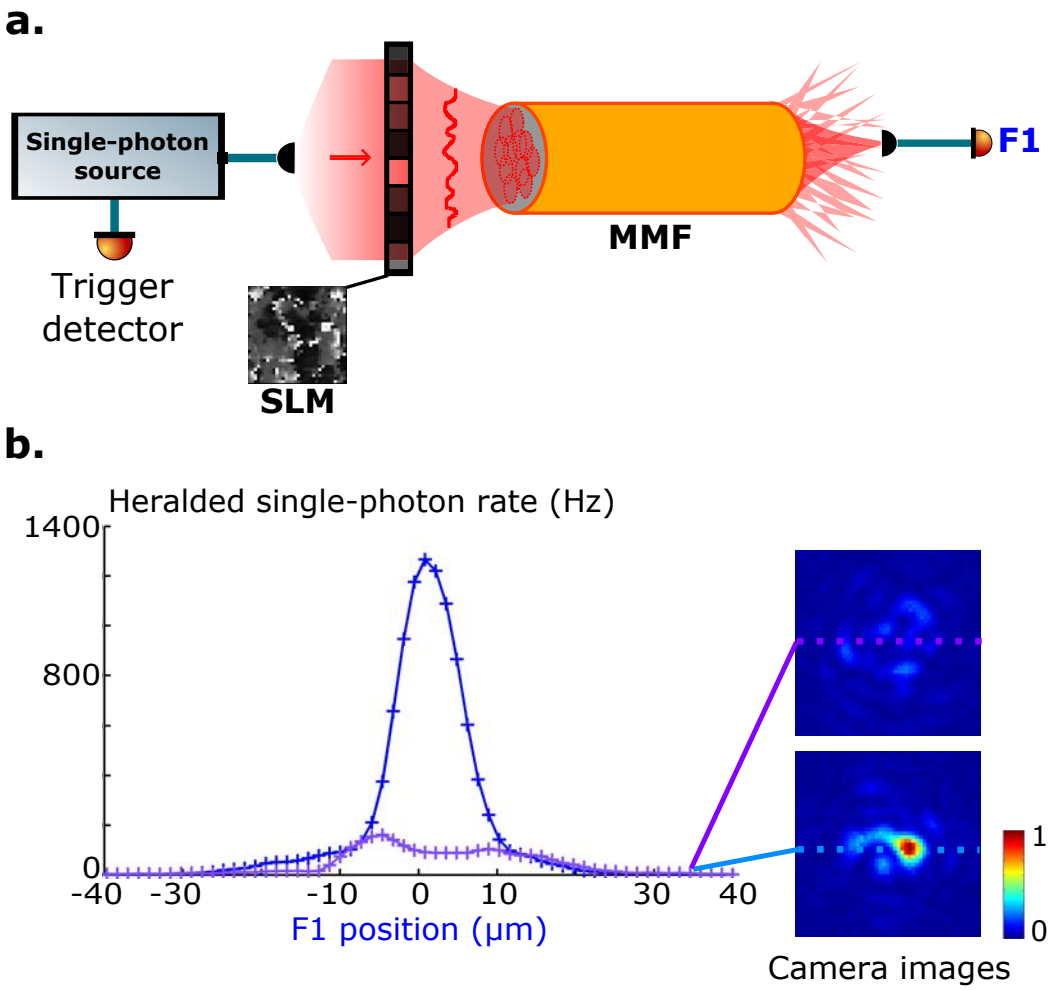

Figure 3.6: **Single-photon focusing in a targeted output mode through a MMF (a.)** Scheme of the single-photon focusing process using the TM approach. **(b.)** 1D scans of the output PMSMF realized with a random phase pattern (purple curve) and the focusing phase pattern (blue curve) displayed on the SLM. Output plane images are recorded with the CCD camera. Purple and blue dashed lines represent the position of the scans realized with the output fiber. Contrary to the fiber output signal measured in coincidences with the trigger photon of the source, intensity images recorded with the camera are not triggered.

a fundamental and applied physics point of view [17].
In the last chapters on this thesis, we investigate propagation of photon-pairs in a multimode system. Chapter 4 presents a theoretical extension of the scattering matrix approach to investigate and control propagation of photon-pairs in a multimode platform. Finally, chapter 5 describes the first experimental implementation of two-photon quantum walk in a MMF.

Chapter 4

Two-photon scattering matrix

This chapter describes the theoretical tools that enable the study of non-classical light propagation in multimode systems. It introduces the notion of two-photon transmission matrix that characterizes photon-pairs propagation and explains its utilization to guide the photons by wavefront shaping. In particular, this theoretical work takes into account some experimental constraints that can be found in the optical setup described in chapter 3 and 5.
In the first sections the present chapter (4.1 and 4.2), we introduce the formalism that allows describing propagation of a single-photon and photon-pairs through a multimode network. These results paves the way to the subsequent calculations.
The concept of two-photon transmission matrix (TTM) is then explained in section 4.3. TTM matrix is an analogous to the classical transmission matrix (TM) for photon-pairs propagation. In this section, we gives a method to compute the TTM directly from the measured TM and analyze some relevant properties of the transformation.
In chapter 2, we have shown that knowing the TM allows the control light propagation in a complex system. A similar approach is now developed in section 4.4 in order to control photon-pairs propagation using the TTM.
Finally, the two-photon control method is used in the framework of a real optical experiment. To this end, we consider an optical implementation based on the experiment presented in chapter 5. The experimental constraints introduced here are first detailed in section 4.5. Then, the two-photon wavefront control method is adapted to these limitations and two practical methods emerge: a numerical optimization approach (4.6) and an analytical approach (4.7).

Notations
- The scattering matrix (SM) of a lossless multimode linear system is denoted S. S is an unitary matrix of size $P \times P$. Its associated two-photon scattering matrix (SSM) is denoted $S^{(2)}$ and has a size of $P_2 \times P_2$.
- The transmission matrix (TM) is denoted T. T is a $M \times N$ submatrix of S grouping only the measurable and controllable modes of the system. Its associated two-photon transmission matrix (TTM) is denoted $T^{(2)}$ and has a size of $M_2 \times N_2$.
- We use the second quantization formalism, where $\hat{a}_i^+$ denotes the operator that creates a photon in input mode i and $\hat{b}_j^+$ the operator that creates a photon in output mode j. Modes i or j denote either a polarization or a spatial mode. Light propagating in the system is considered monochromatic.

4.1 Single-photon propagation in a linear network

This section introduces the formalism used to describe propagation of single-photons in multimode linear optical networks. The goal of the present section is to define some relevant mathematical notations that will be used in the other sections. This formalism is partially derived from [82, 87].

4.1.1 Scattering and transmission matrix

A lossless optical multimode linear system is characterized by a *scattering matrix* (SM) denoted S. S is a $P \times P$ complex unitary matrix linking input modes to output modes of the system. Due to experimental constraints, we generally do not have access to all the modes of the system. T defines thus a submatrix of S that contains only these accessible modes. T has a size $M \times N$ with $N < P$ and $M < P$:

$$T = \begin{bmatrix} T_{11} & \dots & T_{1N} \\ \cdots & \cdots & \cdots \\ T_{M1} & \dots & T_{MN} \end{bmatrix} \tag{4.1.1}$$

T is named the *transmission matrix* (TM) of the system. Knowing T enables to determine the output field E^{out} (decomposed on M output modes) for a given input field E^{in} (decomposed on N input modes):

$$E^{out} = T \times E^{in} \tag{4.1.2}$$

4.1.2 Single-photon formalism

Propagation of single-photon states through a given system is also described by its TM. Input and output modes are now formally written as:

$$\text{Inputs:}\{|1_i\rangle\}_{i\in[1,N]} = \{|1,0,\dots,0\rangle, |0,1,\dots,0\rangle, \dots, |0,\dots,1\rangle\} \tag{4.1.3}$$

$$\text{Outputs:}\{|1_j\rangle\}_{j\in[1,M]} = \{|1,0,\dots,0\rangle, |0,1,\dots,0\rangle, \dots, |0,\dots,1\rangle\} \tag{4.1.4}$$

Using the second quantization formalism, the transformation rule for photonic operators in a system described by a matrix T takes the form:

$$\hat{a}_i^+ \rightarrow \sum_{j=1}^{M} T_{ji} \hat{b}_j^+ \tag{4.1.5}$$

where $\hat{a}_i^+$ is the operator creating a photon into the input mode i and $\hat{b}_j^+$ the operator creating an photon in the output mode j. A coefficient of the TM is then expressed as:

$$T_{ji} = \langle 1_j | T | 1_i \rangle \tag{4.1.6}$$

For example, we consider a input state $|\phi_{in}\rangle$ of the form:

$$|\phi_{in}\rangle = \sum_{i=1}^{N} \alpha_i \hat{a}_i^+ |0\rangle = \sum_{i=1}^{M} \alpha_i |1_i\rangle \tag{4.1.7}$$

where α_i is a complex coefficient associated to the input mode i. After propagation though the system, this state is transformed into an output state $|\phi_{out}\rangle$ which can be expressed using TM coefficients:

$$|\phi_{out}\rangle = T|\phi_{in}\rangle = \sum_{j=1}^{M} \sum_{i=1}^{N} T_{ji} \alpha_i |1_j\rangle \tag{4.1.8}$$

4.2 Photon-pairs propagation in a multimode linear system

When optical properties of two photons are made identical, they become *indistinguishable*: it is not possible to track them and determine the path taken by each photon [208, 209]. As described in part 1.1.5 of chapter 1, indistinguishable photons exhibit non-classical behaviors that can be interpreted when introducing the notion of quantum interferences [11, 210, 211]. Photon-pairs propagation through linear multimode networks involve these interference effects. Their propagation can be directly predicted from classical TM coefficients [87].
In this section, we introduce some important results of photon-pairs propagation through a multimode system in two different cases. We first describe simple situation when photons are either perfectly indistinguishable or totally distinguishable (4.2.1). Then we explore a more general case when photons are only partially indistinguishable and discuss some analogies between classical and quantum interferences in this case (4.2.2).

4.2.1 Perfectly indistinguishable or distinguishable photons

We consider propagation of photon-pairs in a multimode system characterized by a TM denoted T. When two *indistinguishable* photons enter the system through input modes i and j, quantum interference occur during propagation and the probability for coincidence detection at output ports k and l is given by [84]:

$$P_{kl}^{ij} = \frac{|T_{ki}T_{lj} + T_{kj}T_{li}|^2}{(1+\delta_{kl})(1+\delta_{ij})} \tag{4.2.1}$$

If the photons are totally distinguishable, they behave like two independent single-photons and the coincidence detection probability becomes

$$Q_{kl}^{ij} = \frac{|T_{ki}T_{lj}|^2 + |T_{kj}T_{li}|^2}{1+\delta_{kl}} \tag{4.2.2}$$

In a realistic case, photon-pairs are never perfectly identical: they are *partially indistinguishable*. In the next part, we define the notion of degree of indistinguishability of photons and derive the formula describing their propagation.

4.2.2 Partially indistinguishable photons

The relevant mathematical function to characterize indistinguishability is an overlap integral, which accounts for the photons properties such as the spectral shape, polarization, spatial mode and relative temporal delay. Any type of distinguishability can be considered as mode mismatch, which reduces non-classical interference contrast according to this mode overlap integral [87].

Example of partial indistinguishability induced by temporal mode mismatch

Indistinguishably of two photons can for instance be affected by their relative temporal delay. As presented in [11], tuning of the relative temporal delay of photon-pairs launched on a balanced beam splitter is a well established technique to characterize photon-pairs indistinguishability. When temporal delay is perfectly adjusted, a unitary contrast is measured only if all other properties perfectly overlap. Otherwise, interference visibility measured is used to quantify the degree of partial indistinguishability.
In the approach presented bellow, the continuous temporal component is processed separately than other degrees of freedom which are considered to perfectly overlap. The corresponding two-photon state can be written:

$$|\phi_{in}\rangle = \hat{a}^+_{1,t_1}\hat{a}^+_{2,t_2}|0\rangle \tag{4.2.3}$$

where $\hat{a}^+_{i,t_i}$ creates a photon in mode i (grouping spatial, polarization and spectral shape modes) with the temporal wave-function $|t_j\rangle$. The wave-function $|t_2\rangle$ of the photon in the second mode can be decomposed into both an indistinguishable and a distinguishable contributions

$$|t_2\rangle = |t_1\rangle\langle t_1|t_2\rangle + |t_2'\rangle\sqrt{1-|\langle t_1|t_2\rangle|^2} \tag{4.2.4}$$

where $|t_2'\rangle$ is the projection of $|t_2\rangle$ orthogonal to $|t_1\rangle$

$$|t_2'\rangle = \frac{|t_2\rangle - \langle t_1|t_2\rangle|t_1\rangle}{\sqrt{1-|\langle t_1|t_2\rangle|^2}} \tag{4.2.5}$$

The initial state then becomes

$$\begin{aligned}|\phi_{in}\rangle &= \hat{a}^+_{1,t_1}\hat{a}^+_{2,t_2}|0\rangle \\ &= \hat{a}^+_{1,t_1}(\langle t_1|t_2\rangle\hat{a}^+_{2,t_1} + \sqrt{1-|\langle t_1|t_2\rangle|^2}\hat{a}^+_{2,t'_2})|0\rangle \\ &= (\chi\hat{a}^+_{1,t_1}\hat{a}^+_{2,t_1} + \sqrt{1-\chi}\hat{a}^+_{1,t_1}\hat{a}^+_{2,t'_2})|0\rangle\end{aligned} \tag{4.2.6}$$

The term $\hat{a}^+_{1,t_1}\hat{a}^+_{2,t_1}|0\rangle$ refers to perfectly indistinguishable photons and its weight is given by the overlap integral [1] $|\chi|^2 = |\langle t_1|t_2\rangle|^2$.
Linearity of the time evolution operator enables to consider indistinguishable and distinguishable terms separately. In consequence, the resulting event probabilities R for partially distinguishable photons can be calculated from probabilities P and Q relative to perfectly indistinguishable and totally distinguishable photons:

$$R = |\chi|^2 P + (1-|\chi|)^2 Q \tag{4.2.8}$$

In the next sections, χ represents a general overlap integral between properties of the photons and do not necessarily refers to a time difference.

Propagation of partially distinguishable photons

We now consider partially indistinguishable photons characterized by an overlap integral χ that propagate in a multiport device [212]. As detailed in the previous part, the coincidence probability R^{ij}_{kl} detection at the output ports k and l for photons entering at inputs i and j is simply given by:

$$R^{ij}_{kl} = |\chi|^2 P^{ij}_{kl} + (1-|\chi|)^2 Q^{ij}_{kl} \tag{4.2.9}$$

where P^{ij}_{kl} (Q^{ij}_{kl}) is the output coincidence rates for indistinguishable photons given by equation 4.2.1 (distinguishable photons given by equation 4.2.2).

Physical interpretation

We now give a physical interpretation of the previous equation. When considering two photons injected in different inputs $i \neq j$ and detected in different output ports $k \neq l$, equation 4.2.9 simplifies in:

$$R^{ij}_{kl} = |T_{ki}T_{lj}|^2 + |T_{kj}T_{li}|^2 + 2\Re(T_{ki}T_{lj}T^*_{kj}T^*_{li})|\chi|^2 \tag{4.2.10}$$

Two-photon interference phenomenon clearly appear in equation 4.2.10. Using the analogy to classical interference, $|T_{ki}T_{lj}|^2$ and $|T_{kj}T_{li}|^2$ refer to direct coincidence intensities of each *two-photon fields* taken separately and $2\Re(T_{ki}T_{lj}T^*_{kj}T^*_{li})$ is the interference term. $|\chi|^2$ then corresponds to a contrast that weights the interference term depending on the degree of indistinguishability of the photons.

1. In case of a two-photon state as produced by SPDC, the time-overlap integral can be simply modeled by

$$\chi = e^{i(t_2-t_1)\omega}e^{-\frac{\delta l^2\Delta\omega}{4c^2}} \tag{4.2.7}$$

where $\Delta\omega$ is the filter bandwidth, ω the central frequency, c the speed of light and δl the length difference between the optical paths of the two-photons on their way to the multimode system.

Two-photon propagating without interfering

Another interesting result can be derived from equation 4.2.9: two photons injected in the same input ports $i = j$ and detected at two different output ports $k \neq l$. In this case, equation 4.2.10 becomes:

$$R_{kl}^{ii} = 2|T_{ki}T_{li}|^2 \tag{4.2.11}$$

This equation shows that the output coincidence probability does not depend on the overlap integral χ of the photons. As a result, output coincidence distribution observed when both photons are injected in a common input mode remains the same if photon are identical or not. Photon-pairs propagation in this specific configuration only involve classical interference effects, even if the photons are perfectly indistinguishable.

Results of this part show that partially indistinguishable photons can be viewed as two sets of independent particles: (a) a set of perfectly indistinguishable photons and (b) a set totally indistinguishable photons. Once the proportion of each type of photons has been measured - for instance by performing an HOM experiment - these two sets propagate with their own laws and the same proportionality rule is simply applied between the probabilities at the end of the process.
In the experiment conducted in this thesis, initial indistinguishably degree of photons goes up to 86% (see Appendix A). The correction to apply, related to the presence of distinguishable photons, is then relatively small. If we want to be more precise, the propagation of distinguishable photons is still easy to predict because it can be directly calculated from the propagation of each photon of the pair taken independently. In the following sections of the present chapter, we will thus focus on the propagation of indistinguishable photons through complex systems considering that the impact of partial distinguishability is negligible.

4.3 Two-photon transmission matrix

The scattering matrix formalism introduced in chapter 2 for classical light can be extended to the case of non-classical light. In the present section, we focus our attention on a system composed of two indistinguishable photons injected in a N-input M-outputs multiport system characterized by a TM T. We first use the example of the simplest multiport system - the balanced beam-splitter - in order to introduce the method (4.3.1). The general method that allows calculating the TTM directly from the TM of any linear multimode system is presented in part 4.3.2 and we discuss its mathematical properties in 4.3.3. Finally, we provide a generalization of this process to the case of multi-photon fock states (4.3.4).

4.3.1 Example of a balanced beam splitter

We first use the example of the simplest multimode system: the balanced beam-splitter (BS) [213, 214]. A BS is characterized by a 2×2 matrix:

$$T_{BS} = \frac{1}{\sqrt{2}} \begin{bmatrix} 1 & e^{i\pi/2} \\ e^{i\pi/2} & 1 \end{bmatrix} \tag{4.3.1}$$

When considering propagation of indistinguishable photon-pairs, the size of the corresponding Hilbert space enlarges compared to the single-photon case. For a BS, all possible input states are:

- $\frac{\hat{a}_1^+ \hat{a}_1^+}{\sqrt{2}}|0\rangle = |2,0\rangle$: both photons in the input 1 of the BS.
- $\hat{a}_1^+ \hat{a}_2^+|0\rangle = |1,1\rangle$: one photon on the input 1 and the other in the input 2.
- $\frac{\hat{a}_2^+ \hat{a}_2^+}{\sqrt{2}}|0\rangle = |0,2\rangle$: both photons in the input 2 of the BS.

Similarly, all possible output states can be written: $|2,0\rangle, |1,1\rangle, |0,2\rangle$.
As a result, the TTM of the BS is a 3×3 matrix decomposed on the following sets of modes:

$$\begin{array}{rl} \text{Inputs: } \{|1_{i_1} 1_{i_2}\rangle\}_{\{i_1 \leq i_2\} \in [1,2]} = & \{|2,0\rangle, |1,1\rangle |0,2\rangle\} \\ \text{Outputs: } \{|1_{j_1} 1_{j_2}\rangle\}_{\{j_1 \leq j_2\} \in [1,2]} = & \{|2,0\rangle, |1,1\rangle |0,2\rangle\} \end{array} \tag{4.3.2}$$

Coefficients of the TTM are calculated using the transformation rule for photonic amplitude operators given by equation 4.1.5. The TTM of a BS is finally expressed as:

$$T_{BS}^{(2)} = \frac{1}{2} \begin{bmatrix} 1 & \sqrt{2}i & -1 \\ \sqrt{2}i & e^{i\pi} + 1 = 0 & \sqrt{2}i \\ -1 & \sqrt{2}i & 1 \end{bmatrix} \tag{4.3.3}$$

A remarkable point of this matrix is that its central element is null. This result is directly observed in a HOM experiment [11] where an input state of the form $|1,1\rangle$ is injected through the BS and an output state $|1,1\rangle$ is measured. The *bunching effect* of indistinguishable photon-pairs on a BS is then well interpreted by the TTM.

4.3.2 Two-photon transmission matrix calculation

The TTM is now derived for a general $N \times M$ multimode system characterized by its TM T. Because the Hilbert space associated a two-photon state is larger than for a single-photon, the TMM is larger than the TM [84]. The TTM has a size of $M_2 \times N_2$ with:

$$N_2 = \frac{(N+1)N}{2} \tag{4.3.4}$$

$$M_2 = \frac{(M+1)M}{2} \tag{4.3.5}$$

In the present work, we decide to organize input and output sets of modes in the following way [2]

2. The state $|1_{i_1} 1_{i_2}\rangle$ is set at the i^{th} position of the basis by the formula:

$$\begin{aligned}
\text{Inputs: } \{|1_{i_1}1_{i_2}\rangle\}_{\{i_1\leq i_2\}\in[1,N]} =&\{|2,0,\ldots,0\rangle,|1,1,\ldots,0\rangle,\ldots,|1,0,\ldots,1\rangle,\\
&|0,2,\ldots,0\rangle,|0,1,1,\ldots,0\rangle,|0,1,\ldots,1\rangle,\\
&|0,0,2,\ldots,0\rangle,\ldots\}\\
\text{Outputs: } \{|1_{j_1}1_{j_2}\rangle\}_{\{j_1\leq j_2\}\in[1,M]} =&\{|2,0,\ldots,0\rangle,|1,1,\ldots,0\rangle,\ldots,|1,0,\ldots,1\rangle,\\
&|0,2,\ldots,0\rangle,|0,1,1,\ldots,0\rangle,|0,1,\ldots,1\rangle,\\
&|0,0,2,\ldots,0\rangle,\ldots\}
\end{aligned} \tag{4.3.7}$$

Using results given by equations 4.1.7 and 4.2.1, the formula that expresses a TTM coefficient from TM coefficients for indistinguishable photons is:

$$\begin{aligned}
&\forall\{i_1\leq i_2\}\in[1,N] \text{ and } \forall\{j_1\leq j_2\}\in[1,M]\\
&\langle 1_{j_1}1_{j_2}|T^{(2)}|1_{i_1}1_{i_2}\rangle = \frac{T_{j_1,i_1}T_{j_2,i_2}+T_{j_2,i_2}T_{j_1,i_2}}{\sqrt{(1+\delta_{i_1,i_2})(1+\delta_{j_1,j_2})}}
\end{aligned} \tag{4.3.8}$$

The previous expression enable the calculation of the TTM for any linear multimode network of which the TM is known.

4.3.3 Mathematical properties of the transformation process

We denote L the application that maps a classical TM onto its corresponding two-photon matrix. L is formally defined as :

$$L : \left| \begin{array}{ccc} M_{MN}(\mathbb{C}) & \longrightarrow & M_{M_2N_2}(\mathbb{C}) \\ T & \longmapsto & T^{(2)} \end{array} \right. \tag{4.3.9}$$

where $M_{MN}(\mathbb{C})$ ($M_{M_2N_2}(\mathbb{C})$) is the assembly of complex matrices of size $M\times N$ ($M_2\times N_2$). In this section, we introduce some important properties of L that will be useful for calculations in the next parts of this chapter.
First, this application is not linear relative to the sum operator:

$$\forall\{A,B\}\in M_{M,N}(\mathbb{C})\ ,\ L(A+B)\neq L(A)+L(B) \tag{4.3.10}$$

but it is linear relative to the matricial product [3]

$$\forall\{A,B\}\in M_{M,N}(\mathbb{C})\times M_{N,R}(\mathbb{C})\ ,\ L(A\times B)=L(A)\times L(B) \tag{4.3.11}$$

Another remarkable property of L is that its transpose conjugate operation is preserved under L :

$$\forall A\in M_{M,N}(\mathbb{C})\ ,\ L(A^+)=[L(A)]^+ \tag{4.3.12}$$

$$\forall i_1\leq i_2\ ,\ i=1+(i_1-1)N-\frac{(i_1-1)(i_1-2)}{2}+i_2-i_1 \tag{4.3.6}$$

3. This property is obvious when considering a physical implementation of two multimode networks associated in cascade.

In particular, the previous result has two other important consequences:

$$L(\mathbb{1}) = \mathbb{1} \tag{4.3.13}$$

$$\forall A \in M_N(\mathbb{C}) \ , \ A^+ = A^{-1} \Rightarrow L(A)^+ = L(A)^{-1} \tag{4.3.14}$$

Finally, we demonstrate also that an element E_{ij} of the canonical basis of $M_{M,N}(\mathbb{C})$ is transformed under L into an element of the canonical basis of $M_{M_2,N_2}(\mathbb{C})$:

$$L(E_{ij}) = E_{i'j'} \tag{4.3.15}$$

where

$$i' = 1 + (i-1)(N - 1 - \frac{i}{2}) \tag{4.3.16}$$

$$j' = 1 + (j-1)(M - 1 - \frac{j}{2}). \tag{4.3.17}$$

4.3.4 Multi-photon scattering matrix

This previous mathematical approach can be extended to the general case of $p > 2$ indistinguishable photons. We briefly show here how a p-photon transmission matrix denoted $T^{(p)}$ can be calculated from the classical TM T.

When p photons operate between N optical modes, an input state of the system takes the general form $|k_1, k_2, \ldots, k_N\rangle$ where $k_1 + k_2 + \ldots + l_N = p$ and k_i are integers between 0 and p. The number of input and output state accessible for p photons propagating in a $M \times N$ network are denoted N_p and M_p and can be calculated using the formulas:

$$N_p = \begin{pmatrix} N+p-1 \\ p \end{pmatrix} \tag{4.3.18}$$

$$M_p = \begin{pmatrix} M+p-1 \\ p \end{pmatrix} \tag{4.3.19}$$

A coefficient of $T^{(p)}$ - linking an input state $|\psi_I\rangle = |i_1, i_2, \ldots, i_N\rangle$ to an output state $|\psi_O\rangle = |j_1, j_2, \ldots, j_M\rangle$ - is determined using the general formula:

$$\langle\psi_O|T^{(p)}|\phi_I\rangle = \frac{\mathrm{Per}(T_{I,O})}{\sqrt{i_1!i_2!\ldots i_N!j_1!j_2!\ldots j_M!}} \tag{4.3.20}$$

where $T_{I,O}$ is a $p \times p$ submatrix of T and $\mathrm{Per}(T_{I,O})$ its permanent [4].

Matrix $T_{I,O}$ is constructed from matrix T in two steps:

4. The permanent of a complex square matrix $A = (a_{ij})_{i,j\in[1,n]}$ of size $n \times n$ is defined as :

$$\mathrm{Per}(A) = \sum_{\sigma \in S_n} \prod_{i=1}^{n} a_{i\sigma(i)} \tag{4.3.21}$$

where the sum here extends over all elements σ of the symmetric group S_n i.e. over all permutations of the numbers $1, 2, \ldots, n$ [84].

1. A matrix denoted T_I of size $M \times p$ is first reconstituted by taking i_k copies of the k^{th} column of T for each $k \in [1, N]$
2. The matrix $T_{I,O}$ is then formed by taking j_k copies of the k^{th} row of T_I for each $k \in [1, M]$

As an example, we consider $p = 3$ photons propagating in a 4×5 modes of a linear network described by its transmission matrix T

$$T = \begin{bmatrix} a_1 & b_1 & c_1 & d_1 & e_1 \\ a_2 & b_2 & c_2 & d_2 & e_2 \\ a_3 & b_3 & c_3 & d_3 & e_3 \\ a_4 & b_4 & c_4 & d_4 & e_4 \end{bmatrix} \tag{4.3.22}$$

We inject the state $|\psi_I\rangle = |1, 0, 0, 1, 1\rangle$ in the system containing 3 photons arranged in modes 1,4 and 5. Output detections are performed between ports 1 and 4 to measure the output state $|\psi_O\rangle = |1, 0, 0, 2\rangle$.
First, T_I is obtained by selecting columns of T with numbers 1,4 and 5

$$T_I = \begin{bmatrix} a_1 & d_1 & e_1 \\ a_2 & d_2 & e_2 \\ a_3 & d_3 & e_3 \\ a_4 & d_4 & e_4 \end{bmatrix} \tag{4.3.23}$$

Then, $T_{I,O}$ is obtained from T_I by selecting row number 1 and two times row number 4

$$T_{I,O} = \begin{bmatrix} a_1 & d_1 & e_1 \\ a_4 & d_4 & e_4 \\ a_4 & d_4 & e_4 \end{bmatrix} \tag{4.3.24}$$

Finally, a coefficient of the matrix $T^{(3)}$ linking input mode $|1, 0, 0, 1, 1\rangle$ to ouptut mode $|1, 0, 0, 2\rangle$ is given by

$$\langle 1, 0, 0, 2|T^{(3)}|1, 0, 0, 1, 1\rangle = \frac{\text{Per}\left(\begin{bmatrix} a_1 & d_1 & e_1 \\ a_4 & d_4 & e_4 \\ a_4 & d_4 & e_4 \end{bmatrix}\right)}{\sqrt{1!1!1!1!2!}} \tag{4.3.25}$$

4.4 Scattering matrix approach to control photon-pairs

Optical properties of a linear complex system can be characterized by measuring its TM T. As described in chapter 2, Popoff and coworkers [80] have implemented a method to measure the TM of a white paint layer and used it to control light propagating through the system. In the previous section, we have observed that the propagation of photon-pairs through a linear multimode network can also be described in a similar way using a TTM. This TTM can be directly calculated from the TM. In this section, we now develop an approach that allows controlling photon-pairs propagation knowing

the TTM. In particular, we describe the case where photon-pairs are focused into a specific output coincidence mode of the system.
We first summarize the important results concerning the scattering matrix approach introduced in chapter 2. In particular, we introduce some theoretical notations that are useful in the processes of classical light focusing (4.4.1) and single-photons focusing (4.4.2). In the last part 4.4.3, we propose an extension of this technique applied to photon-pairs propagation knowing the TTM. The particular case of photon-pairs focused on a targeted output mode is then discussed in details.

4.4.1 Focusing classical light

Classical light focusing is already described in chapter 2. The present section provides more theoretical details on this process and introduces new mathematical tools.

Ideal inversion process

The SM links an incoming field to an outgoing field [80]:

$$E^{out} = S \times E^{in} \tag{4.4.1}$$

The problem of controlling light propagating through the system goes back to find the input field that corresponds to a desired field at the output. Mathematically, this can be done by inverting equation 4.4.1:

$$E^{in} = S^{-1} \times E^{in} = S^{+} \times E^{in} \tag{4.4.2}$$

where the unitary property of S ensures that S^{-1} exists and $S^{-1} = S^{+}$.
Conjugate transpose of S is then the mathematical operator that takes place in the inversion process. It relies on the physical idea that taking the complex conjugate of a complex monochromatic field amounts to consider propagation *backward in time* [154, 80]. When a shaped input field of the form $E_s^{in} = S^{(+)} \times E^{in}$ repropagates through the system, the field is perfectly retrieved at the output:

$$\begin{aligned} S \times E_{shaped}^{in} &= S \times S^{+} \times E^{out} \\ &= \mathbb{1} \times E^{out} \\ &= E^{out} \end{aligned} \tag{4.4.3}$$

Realistic inversion process

This procedure is only appropriate if one has access to the complete SM S of the system. However, only a small number of input and output modes are experimentally accessible and the system is only characterized by a TM T.

Hypothesis 1
We suppose that the number of modes measured in T is small compare to the total number of modes contained in S: $N, M << P$. In this situation, we make the assumption that the elements of T are realizations of independent complex random variables following a complex normal distribution with the same variance σ^2. In this work, we use without confusion the same notation T_{ji} to denote either one specific random variable or one realization of this variable. This hypothesis has been studied in the case of scattering media in [80, 215] and for a multimode fiber [147]. The case of a multimode fiber is discussed in more details in part 5.3.1 of chapter 5.

Considering this hypothesis, we calculate the product $T \times T^+$. First, we estimate the mean amplitude of its diagonal and off-diagonal coefficients.
On the one hand, the mean value of the amplitude of the off-diagonal coefficients denoted $[T \times T^+]_{ij}$ with $i \neq j$ results from a sum of random phasors [136]:

$$\begin{aligned} \left\langle |[T \times T^+]_{ij}| \right\rangle &= \left\langle |\sum_{k=1}^{N} T_{ik} T_{jk}^*| \right\rangle \\ &= \sqrt{N}\sigma^2 \end{aligned} \tag{4.4.4}$$

where $\langle\rangle$ is the an average over different realizations of variables T_{ij} and $\sigma^2 = \langle |T_{ij}|^2 \rangle$ is their variance. For a given matrix T, σ^2 can be estimated by averaging over all its coefficients: $\sigma \approx \frac{1}{NM} \sum_{i,j} |T_{ij}|^2$, assuming that the matrix T is large enough. On the other hand, the mean value of the amplitude of the diagonal coefficients takes the form:

$$\begin{aligned} \left\langle |[T \times T^+]_{ii}| \right\rangle &= \left\langle \sum_{k=1}^{N} |T_{ik}|^2 \right\rangle \\ &= N\sigma^2 \end{aligned} \tag{4.4.5}$$

As a result, the diagonal and off diagonal elements do not scale likewise with N. More generally, we can demonstrate that the product $T \times T^+$ can be decomposed under the general form:

$$T \times T^+ = \sigma^2 N \left[\mathbb{1} + \frac{1}{\sqrt{N}} H \right] \tag{4.4.6}$$

where H is a complex hermitian matrix composed by realizations of complex random variables denoted H_{ij} that do not depend upon N. They are characterized by the same variance $\sigma_H^2 = 1$.
Assuming that the number of modes controlled by the SLM is large ($N \gg 1$), the desired output field is then efficiently retrieved with a good signal to noise ratio after propagation of the shaped input field:

$$\begin{aligned} T \times E_{shaped}^{in} &= T \times T^{(+)} \times E^{out} \\ &= \sigma^2 N \left[\mathbb{1} + \frac{1}{\sqrt{N}} H \right] \times E^{out} \\ &\approx \sigma^2 N E^{out} \end{aligned} \tag{4.4.7}$$

As detailed in section 2.3 of chapter 2, the transpose conjugate operator is well-adapted to perform focusing tasks. When light is concentrated in only one output mode, the targeted output field is E^{out} is simply replaced by a vector containing zeros everywhere and a one in the targeted mode. In this situation, the intensity enhancement η - defined as the intensity of the field measured in the targeted mode divided by the average intensity value of the speckle surrounding it - is proportional to the number of mode controlled at the input: of $\eta \approx N$ [5]

As an example, a numerical simulation of a focusing process is presented on Figure 4.1. In this simulation, the SLM shapes phase and amplitude of $N = 100$ modes of the input field. We observe an amplitude enhancement of about 11, which is in good agreement with the expected intensity enhancement of $\eta \approx 10^2 = N$.

4.4.2 Single-photon focusing

As demonstrated in section 4.1, propagation of a single-photon is directly described by the TM of the system. As a consequence, the method used to control its propagation is exactly the same than the one described previously with classical light. Then; this part does not bring new physical results but introduces some important mathematical notations.

Single-photon focusing state

Given a targeted output mode labeled X, the input state focusing on $\hat{a}_X^+|0\rangle$ takes the form:

$$\begin{aligned} |\psi(X)\rangle &= T^+ \hat{a}_X^+ |0\rangle \\ &= \sum_{i=1}^{N} T_{Xi}^* \hat{a}_i^+ |0\rangle \end{aligned} \tag{4.4.8}$$

where T_{Xi} is the X^{th} row - i^{th} column coefficient of T.

Focusing operator notations

The *focusing operator* in output mode j can be interpreted as the operator creating a photon focused in mode j. It is denoted $\hat{f}_j^+$ and defined from the matrix coefficients as

$$\hat{f}_j^+ = \sum_{i=1}^{N} T_{ji}^* \hat{a}_i^+ \tag{4.4.9}$$

With this definition, equation 4.4.8 simplifies in

5. The theoretical enhancement value expected when using a phase only SLM is also proportional to N but adding a pre-factor: $\eta = \frac{\pi N}{4}$ [138]

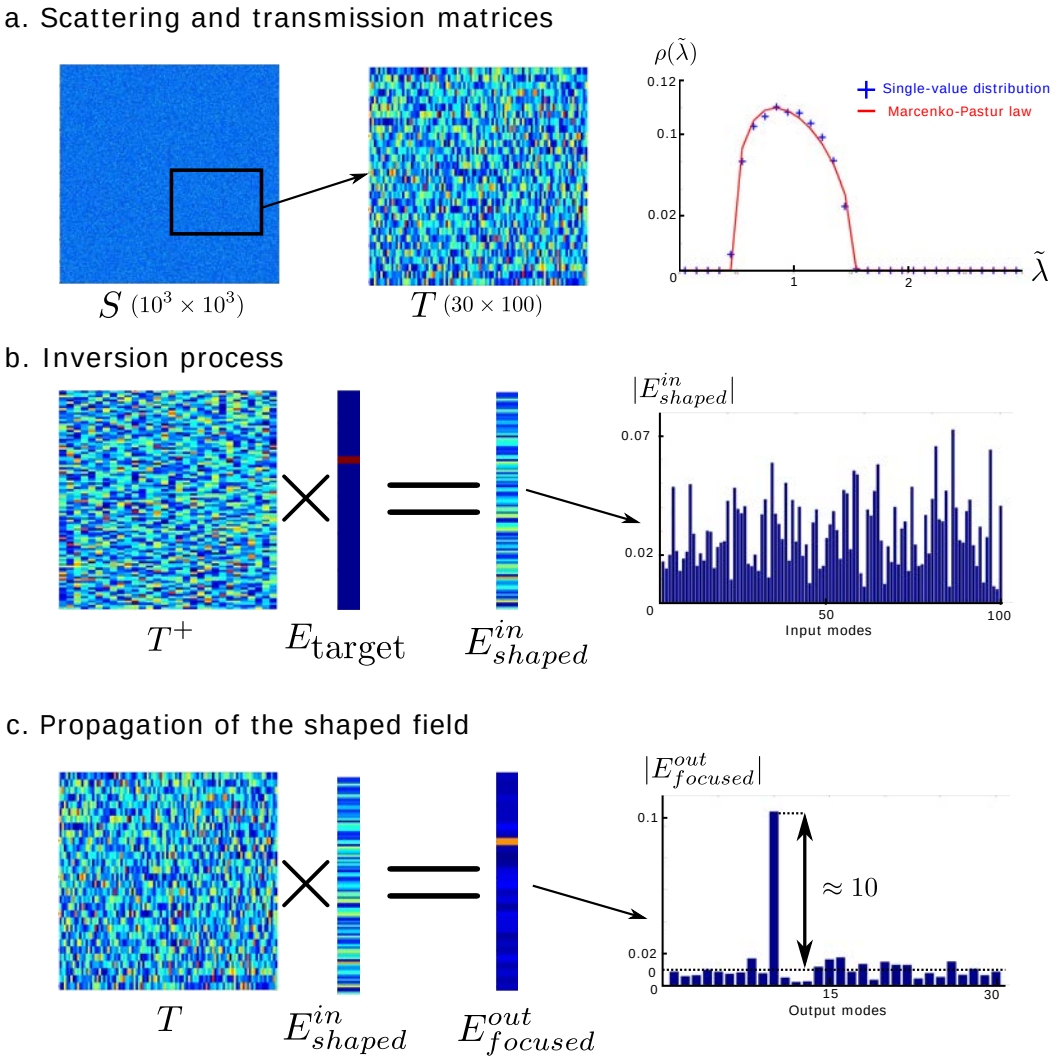

Figure 4.1: **Focusing classical light with the scattering matrix approach (a.)** The TM T of a multimode linear system is a submatrix of the complete unitary SM S. Randomness property of a TM is confirmed when studying the distribution $\rho(\tilde{\lambda})$ of its normalized singular values $\tilde{\lambda}$ [80]. The blue dot curve represents the statistical distribution of singular values calculated from TM of size 30×100 extracted from 100 different simulations of the unitary scattering matrices S. The plain red line corresponds to the Marcenko-Pastur law [216] that predicts the distribution expected with a perfect random matrix of the same size. **(b.)** The inversion process makes use of the transpose conjugate of the TM. By multiplying T^+ by the targeted output field E_{target} - here a field where light is concentrated in one specific mode - one can determine the correct shape of the input field E^{in}_{shaped} to retrieve efficiently the desired output field. **(c.)** The output field $E^{out}_{focused}$ is calculated by multiplying T by the shaped input field E^{in}_{shaped}. $E^{out}_{focused}$ shows a strong light spot exactly in the targeted output mode. We observed amplitude enhancement of the targeted mode, relative to the mean amplitude surrounding it, of about 10.

$$|\psi(X)\rangle = \hat{f}_X^+|0\rangle \tag{4.4.10}$$

The single-photon TM denoted also T can thus be formally written as an operator:

$$\hat{T} = \sum_{j=1}^{M} \hat{b}_j^+ \hat{f}_j \tag{4.4.11}$$

4.4.3 Two-photon focusing

The method used to focus light into a targeted output mode is now extended to the propagation of two-photon state of light.

Two-photon inversion process

In a ideal case where all input and output modes are accessible, the two-photon scattering matrix (SSM) $S^{(2)}$ derived from the unitary matrix S is also unitary (equation 4.3.14). The property $S^{(2)+} = S^{(2)-1}$ is then verified and the inversion process is perfect:

$$S^{(2)} \times E^{in}_{shaped} = \underbrace{S^{(2)} \times S^{(2)+}}_{=\mathbb{1}} \times E^{out} = E^{out} \tag{4.4.12}$$

In a realistic case, the two-photon transmission matrix (TTM) $T^{(2)}$ is calculated from the TM T. However, $T^{(2)}$ does not have the same properties than T. In particular, the complex coefficients of $T^{(2)}$ do not follow a normal distribution like the coefficients of T. The transformation L (equation 4.3.9) introduces correlations in $T^{(2)}$ because $M \times N$ elements are mapped onto a larger number $M_2 \times N_2 \approx M^2 \times N^2$ of elements. These correlations are for instance observed in the numerical simulation presented on Figure 4.2.a where the singular-values distribution of $T^{(2)}$ differs from the Marcenko-Pastur law [216]. Nevertheless, $T^{(2)}$ can be decomposed similarly to T (equation 4.4.7) using the property of L. The equation 4.3.11 enable to write the product $T^{(2)} \times T^{(2)+}$ as:

$$\begin{aligned} T^{(2)} \times T^{(2)+} &= L(T) \times L(T^+) \\ &= L(T \times T^+) \end{aligned} \tag{4.4.13}$$

Then, equation 4.4.6 is injected in the previous decomposition and this product takes then the form:

$$\begin{aligned} T^{(2)} \times T^{(2)+} &= L\left(\sigma^2 N \left[\mathbb{1} + \frac{1}{\sqrt{N}} H\right]\right) \\ &= \sigma^4 N^2 \left(\mathbb{1} + \frac{1}{\sqrt{N}} I + \frac{1}{N} J\right) \end{aligned} \tag{4.4.14}$$

where I and J are two complex hermitian matrices that do not depend upon N and verify the relations $\langle |J_{ij}|^2 \rangle \leq 2$ and $\langle |I_{ij}|^2 \rangle \leq 4$ (considering hypothesis 1). Assuming

that a large number of modes are controlled by the SLM ($N \gg 1$), a desired state $|\Psi_{out}\rangle$ is thus efficiently retrieved at the output when using the transpose conjugate operator $T^{(2)+}$:

$$\begin{aligned} T^{(2)} \times T^{(2)+} \times |\Psi_{out}\rangle &= \sigma^4 N^2 \left(\mathbb{1} + \frac{1}{\sqrt{N}} I + \frac{1}{N} J \right) \times |\Psi_{out}\rangle \\ &\approx \sigma^4 N^2 |\Psi_{out}\rangle \end{aligned} \tag{4.4.15}$$

This transpose conjugate operator can be used to focus photon-pairs in coincidence between two output modes X and Y. In this case, $|\Psi_{out}\rangle$ is simply replaced by $|1_X 1_Y\rangle$.

The numerical simulation presented in Figure 4.2 gives an example of a focusing process performed with $N = 100$ input modes. In this case, the SLM is supposed to shape perfectly in phase and amplitude the two-photon state at the input. Figure 4.2.c shows an amplitude enhancement of about 50. For large values of N, we expect an enhancement proportional to N for the two-photon field and N^2 for the coincidence rate.

Definition of the optimal two-photon focusing state

Given two output modes X and Y, the optimal state focusing on the state $|1_X 1_Y\rangle$ (or $|2_X\rangle$ if $X = Y$) is defined as:

$$|\Psi_{\text{opt}}(X, Y)\rangle = T^{(2)+} |1_X 1_Y\rangle \tag{4.4.16}$$

Actually, this optimal state can not be generated in a real optical setup using a SLM. Besides the technological limitations of SLM, some physical constraints appear and limit the shaping possibilities. In the next section, this result is thus adapted to take into account these restrictions.

4.5 Focusing two-photon under experimental constraints

The result given by equation 4.4.16 takes a different aspect when considering the constraints introduced by a real optical setup.
The experimental setup under consideration is depicted in Figure 2.5 of Chapter 2. In our investigation, the classical source is replaced by a source of indistinguishable photon-pairs. One photon of the pair is injected on the vertically polarized input and the other one on the horizontally polarized input. Each photon is then reflected and shaped by a different part of the SLM: SLM V or SLM H. In this chapter, the multimode fiber (MMF) that appears on Figure 2.5 is simply considered as a general complex linear system described by a random matrix T. In the experiment implemented in chapter 5, a MMF is really implemented in the experiment to mix photon-pairs. In particular, the theoretical results developed in this section are well adapted to describe this experiment.
In this section, we first discuss the different restrictions imposed by the use of an experimental setup similar to the one presented in Figure 2.5 (4.5.1). Once the framework

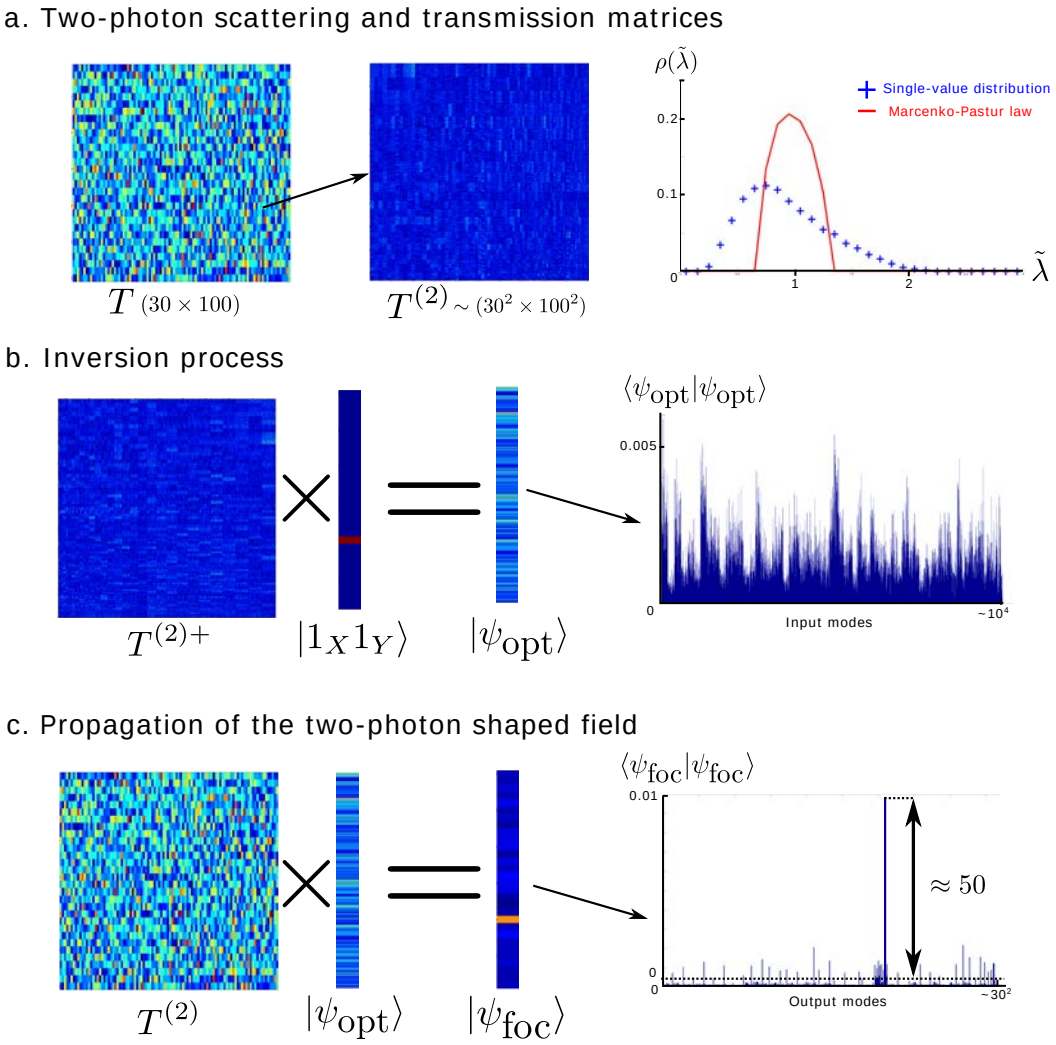

Figure 4.2: **Focusing two-photon state of light using the two-photon transmission matrix (a.)** The two-photon transmission matrix $T^{(2)}$ of a multimode linear system is directly derived from the classical transmission matrix T. The loss of the random property of T is confirmed when studying the distribution $\rho(\tilde{\lambda})$ of the normalized singular-values $\tilde{\lambda}$ of $T^{(2)}$. The blue dot curve represents the statistical distribution of singular-values calculated from $T^{(2)}$. The singular-value distribution is averaged over 100 two-photon matrices derived form transmission matrices of size 30×100 extracted from different simulations of the scattering matrices S. The plain red line corresponds to the Marcenko-Pastur law [216] predicting the distribution expected with a perfect random matrix of the corresponding size. **(b.)** The inversion process makes use of the transpose conjugate of the two-photon transmission matrix $T^{(2)}+$. By multiplying $T^{(2)}+$ by the targeted two-photon output $|1_X 1_Y\rangle$ - here a state where photon-pairs are concentrated in two specific modes X and Y - one can determine the corresponding input state $|\psi_{\text{opt}}\rangle$ that retrieves efficiently the desired output state. **(c.)** The output state denoted $|\psi_{\text{foc}}\rangle$ obtained after propagation of $|\psi_{\text{opt}}\rangle$ through the system can be predicted by multiplying $T^{(2)}$ by $|\psi_{\text{opt}}\rangle$. $|\psi_{\text{foc}}\rangle$ has a strong intensity exactly in the targeted output mode. We observe an enhancement of the amplitude of the targeted mode - relative to the mean amplitude surrounding it - of about 50.

has been placed, we focus our attention on the problem of focusing photon-pairs into a specific output mode of the system. The notion of *focusing fidelity* is introduced in part 4.5.2. This notion lays the basis of two practical methods that allows determining the best input state adapted to our experimental constraints (4.5.3). These techniques will be precisely investigated in the two next sections (4.6 and 4.7).

4.5.1 Reduced form of the input states due to experimental constraints

In our specific experimental configuration, adapted from the experiment of Figure 2.5, each photon of the pair has only access to a limited number of input modes: SLM V shapes one photon over the set of N_V vertical polarization modes (denoted Ω_V) and SLM H over the set of N_H horizontal polarization modes (denoted Ω_H). This situation raises three important limitations:

Limitation 1: Limited number of accessible modes

SLM H shapes one photon over a set of vertically polarized modes Ω_V of the MMF and SLM V over a set horizontally polarized modes Ω_H. In consequence, the two-photon states accessible at the input take the general form:

$$\{|1_{ih}1_{iv}\rangle\}_{\{ih,iv\}\in\Omega_H\times\Omega_V} = \{|\underbrace{0,\ldots,1_{ih},\ldots,0}_{\text{Modes H}}|\underbrace{0,\ldots,1_{iv},\ldots,0}_{\text{Modes V}}\rangle\} \tag{4.5.1}$$

In consequence, only $N_H \times N_V$ states within a total of $N(N+1)/2 \approx N^2$ are experimentally accessible. We then define $T^{(2)}_{HV}$ the subpart of $T^{(2)}$ that contains only the $N_H \times N_V$ possible modes of the system.

Limitation 2: Factorized form of the input state

This particular distribution of the photons at the input has also another consequence. Because one part of the SLM can not distribute the photon over the modes accessible to the other, the most general state that can be generated by the SLM at the input takes the factorized form:

$$|\Psi_{\text{exp}}\rangle = \left(\sum_{ih\in\Omega_H} \alpha_{ih}\hat{a}^+_{ih}\right)\left(\sum_{iv\in\Omega_V} \beta_{iv}\hat{a}^+_{iv}\right)|0\rangle \tag{4.5.2}$$

where coefficient $\alpha_i h$ ($\beta_i v$) represents the complex field value addressed by the SLM relative to input mode ih (input mode iv) of the horizontally (vertically) polarized photon.

Limitation 3: Phase only modulation

The SLM can only control the phase of the input modes. As a result, the shaping parameters α_{ih} and β_{iv} introduced in equation 4.5.2 take the form:

$$\begin{aligned}\beta_{iv} &= \frac{1}{\sqrt{N_V}} e^{i\phi_{iv}} \\ \alpha_{ih} &= \frac{1}{\sqrt{N_H}} e^{i\phi_{ih}}\end{aligned} \tag{4.5.3}$$

where the coefficients $\frac{1}{\sqrt{N_V}}$ and $\frac{1}{\sqrt{N_H}}$ are introduced as a normalization of the input field assuming that all the input modes contribute with the same intensity. This constraint is only valid if the matrix T is expressed in the X-Y *canonical* basis at the input. In this basis, one input mode i corresponds to one pixel - or macropixel - of the SLM.

General form of the input state

Under these limitations, the most general input state that can be generated by the SLM takes the form:

$$|\Psi_{\text{exp}}\rangle = \frac{1}{\sqrt{N_V N_H}} \left(\sum_{ih \in \Omega_H} e^{i\phi_{ih}} \hat{a}_{ih}^{+} \right) \left(\sum_{iv \in \Omega_V} e^{i\phi_{iv}} \hat{a}_{iv}^{+} \right) |0\rangle \tag{4.5.4}$$

where ϕ_{ih} (ϕ_{iv}) is the phase parameter of input mode ih (iv) set by the SLM. For the sake of simplicity, all the phase parameters are grouped in a N_V-components (N_H-components) vector denoted $\boldsymbol{\phi_V}$ ($\boldsymbol{\phi_H}$).

4.5.2 The focusing fidelity

In the next parts of this chapter, we describe methods that focus light into a specific output mode of the system taking into account all these experimental constraints. To achieve this task, these techniques tend to maximize the *focusing fidelity*. The focusing fidelity $\mathcal{F}_{XY}$ relative to the output mode $|1_X 1_Y\rangle$ is defined as:

$$\mathcal{F}_{XY} = |\langle \Psi_{\text{exp}} | T^{(2)+} | 1_X 1_Y \rangle|^2 \tag{4.5.5}$$

where $|\Psi_{\text{exp}}\rangle$ has the general form given by equation 4.5.4. This mathematical overlap has two physical meanings:

- $\mathcal{F}_{XY}$ can be seen as the overlap integral between (a) the experimental input state $|\Psi_{\text{exp}}\rangle$ and (b) the optimal focusing state $|\Psi_{\text{opt}}(X,Y)\rangle$ defined by equation 4.4.16
- $\mathcal{F}_{XY}$ can also be seen as the overlap integral between (a) the output state obtained after propagation of the experimental state through the system: $T^{(2)}|\Psi_{\text{exp}}\rangle$ and (b) the output targeted state $|1_X 1_Y\rangle$

When we consider the general form of $|\Psi_{\text{exp}}\rangle$ given at equation 4.5.4, the expression of the fidelity can be simplified by replacing $T^{(2)}$ by $T^{(2)}_{HV}$ since all other terms are null:

$$\mathcal{F}_{XY} = |\langle \Psi_{\text{exp}} | T^{(2)+}_{HV} | 1_X 1_Y \rangle|^2 \tag{4.5.6}$$

4.5.3 Two practical methods to focus photon-pairs

Two practical approaches that allow calculating $|\Psi_{\text{exp}}\rangle$ are now described. Their common goal is to find $|\Psi_{\text{exp}}\rangle$ that maximizes the focusing fidelity $\mathcal{F}_{XY}$.
In the first case, a *numerical optimization approach* is used to determine the best experimental input state. This method is very general and its efficiency relies on the capacities of the computer that performs the optimization process. In the second case, we provide an *analytical approach* that gives an expression of the input state as a function of the parameters of the system. This technique is only valid under specific assumptions. In particular, it requires to know completely the matrix T of the system, while the numerical optimization approach can be performed only when knowing its reduced two-photon matrix $T^{(2)}_{HV}$ [6].These techniques are described in details in the next two sections.

4.6 Numerical optimization approach

The numerical optimization approach allows calculating the best input state $|\Psi_{\text{exp}}\rangle$ that can be generated with the SLM (under the experimental constraints described in 4.5) to focus photon-pairs in the targeted state $|1_X 1_Y\rangle$ using an optimization technique. In this section, the system is supposed to be partially characterized: we only know its reduced two-photon matrix $T^{(2)}_{HV}$. The TM T or the complete TTM $T^{(2)}$ remain *unknown* and can not be retrieved from the knowledge of $T^{(2)}_{HV}$.

4.6.1 The optimization process

This approach allows finding $|\Psi_{\text{exp}}\rangle$ that maximizes the focusing fidelity $\mathcal{F}_{XY}$. Considering only that $T^{(2)}_{HV}$ is known, no analytical solutions for this maximization problem have been found. The method proposed here uses a relatively simple numerical optimization over the $N_V + N_H$ phase parameters of the input state (equation 4.5.4) inspired from the classical iterative algorithm in [122].
The optimization process is performed as follow: at a particular step of the optimization process, the computer calculates the focusing fidelity $\mathcal{F}_{XY}$ for a set of input states $|\Psi_{\text{exp}}\rangle$ generated with different values of one of its phase parameters. The phase value that gives a maximum for the fidelity is kept in memory. The optimization then continues iteratively for all the phase parameters. In all the numerical optimization that we have performed, the process has always converged.

As an example, we have performed a numerical simulation using this method presented in Figure 4.3. After the numerical calculation of $|\Psi_{\text{exp}}\rangle$, the input state is repropagated through the system and give a two-photon output speckle pattern shown

6. As described in part 4.3.2, $T^{(2)}_{HV}$ or $T^{(2)}$ can be fully predicted from T. In the inverse direction, the matrix T can also be retrieved from the two-photon matrix $T^{(2)}$ because some of its coefficients are directly proportional to those of T: $\langle 2_j|T^{(2)}|2_i\rangle = T^2_{ji}$ where i is an input mode and j an output mode of T. However, knowledge $T^{(2)}_{HV}$ is not sufficient to retrieve T. Note that it is also possible to retrieve T with a hybrid method described in [79] combining classical and two photon measurements.

on Figure 4.3.b. This output speckle confirms the important enhancement of the target output mode intensity $|1_X 1_Y\rangle$. The optimization process reaches a fidelity about $\mathcal{F}_{XY} \approx 2.01 \times 10^{-3}$. The two other modes that are also slightly enhanced correspond to $|2_X 0_Y\rangle$ and $|0_X 2_Y\rangle$. In Figure 4.3.c, we also present the two speckle patterns that would we be obtained with classical light injected either in input H or V keeping the same SLM pattern. These speckles give the intuition that each SLM part focuses each photon of the pair onto a superposition of modes X and Y with different weights.
In all the numerical optimizations performed, the SLM pattern found was enhancing the coincidence rate at the output. However, we need to study more precisely this technique to ensure that this solution is always optimal.

4.6.2 Towards an analytical solution

This optimization procedure is very general and can be performed even if we only know the reduced two-photon matrix $T^{(2)}_{HV}$ of the system. Its efficiency depends on the number of parameters to optimize in the process and could be limited by the capacities of the computer. Moreover, this approach does not bring any physical meanings on the focusing process and we can not guarantee this is the best solution. In the next part, we present an analytical solution of the problem. Contrary to the numerical optimization, this method requires to know completely T.

4.7 Analytical approach

The analytical approach offers the possibility to determine an analytical expression of $|\Psi_{\text{exp}}\rangle$ that focuses photon-pairs in $|1_X 1_Y\rangle$. In this section, we suppose that the TM T is known and we describe here the different steps that lead to an analytical solution of the problem.
In the first part 4.7.1, we derive the TTM $T^{(2)}$ associated to T and simplify its expression by decomposing it onto its different polarization components. This decomposition is useful for the future calculations. We then determine an analytical expression of the focusing fidelity (4.7.2). This expression gives an intuitive picture of the role played by quantum and classical interferences during the focusing process. All the calculation steps that lead to the analytical form of $|\Psi_{\text{exp}}\rangle$ are then detailed in part 4.7.3. Finally, we summarize our results in a step-by-step method that can be used practically (4.7.4).

4.7.1 Two-photon transmission matrix decomposition

In this part, the TTM is separated into its different polarization contributions. We introduce here new mathematical notations and detail the difference steps of this decomposition.

Focusing operator decomposition

The definition of a focusing operator is given by the equation 4.4.9. Using this definition, it can be easily split into two polarization parts:

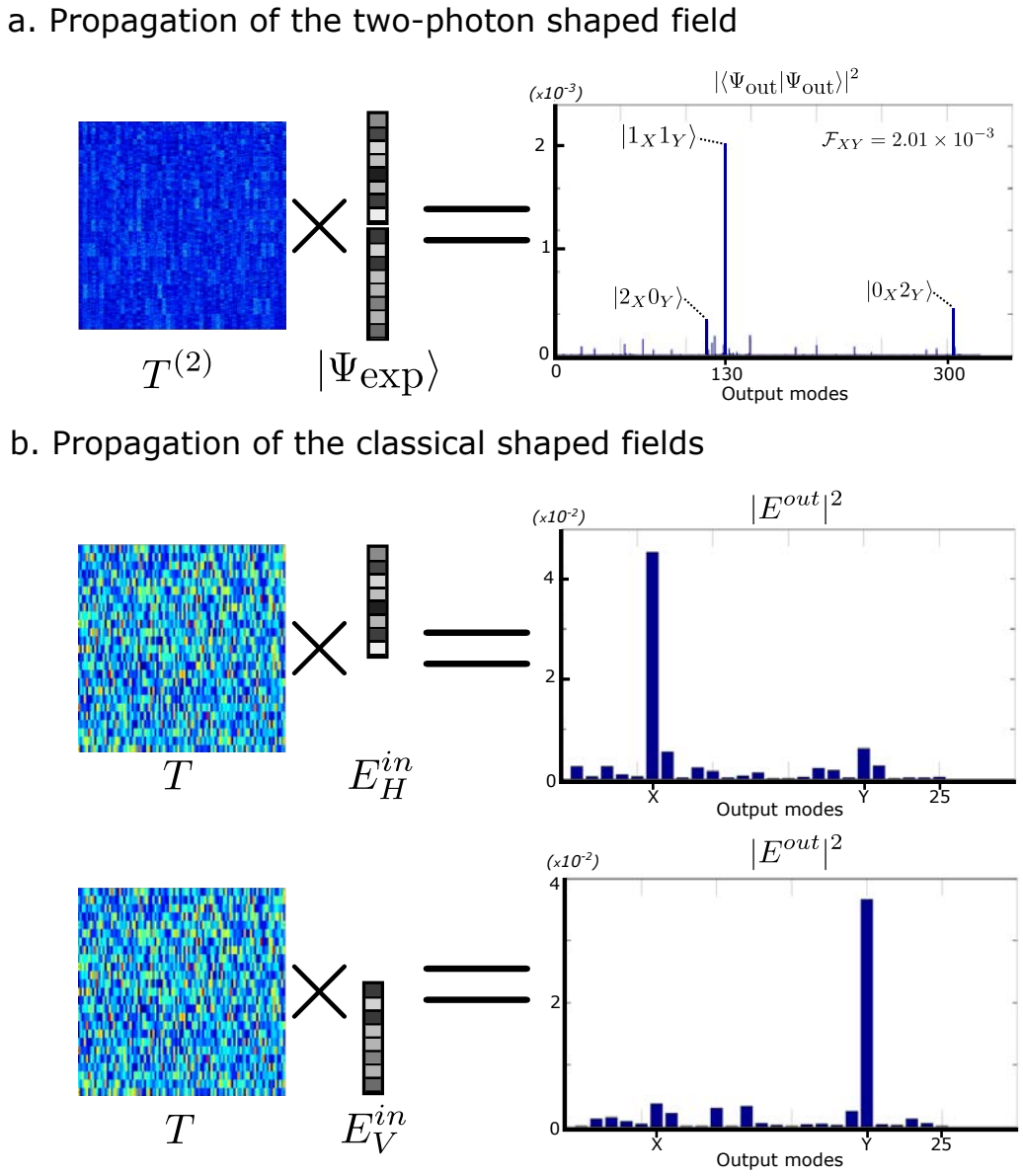

Figure 4.3: **Simulation of a numerical optimization approach focusing process** The transmission matrix generated in this simulation is a 200×30 extracted from a 1000×1000 unitary random scattering matrix. **a.** The experimental input state calculated with the numerical optimization procedure is re-propagated through the system and the corresponding two-photon speckle pattern is observed. Intensity of the targeted output mode $|1_X 1_Y\rangle$ is efficiently enhanced. $|2_X 0_Y\rangle$ and $|0_X 2_Y\rangle$ are also slightly optimized. The focusing fidelity is about $\mathcal{F}_{XY} \approx 2.01 \times 10^{-3}$. **c.** Classical speckles created by classical fields set alternatively on SLM V and SLM H are reconstructed. From these speckle patterns, an intuition is that each SLM focuses light into X and Y simultaneously with different weights.

$$\begin{aligned}\hat{f}_j^+ &= \sum_{i=1}^{N} T_{ji}^* \hat{a}_i^+ \\ &= \sum_{ih\in\Omega_H} T_{j,ih}^* \hat{a}_{ih}^+ + \sum_{iv\in\Omega_V} T_{j,iv}^* \hat{a}_{iv}^+ \\ &= \hat{f}_j^{H+} + \hat{f}_j^{V+}\end{aligned} \tag{4.7.1}$$

where $\hat{f}_j^{H+}$ ($\hat{f}_j^{V+}$) is defined as the horizontally polarized part (vertically polarized part) of the focusing operator $\hat{f}_j^+$.

Transmission matrix decomposition

The operator associated to the TM is described in equation 4.4.11. Similarly to the focusing operator, this TM operator can also be separated in two polarization components:

$$\begin{aligned}\hat{T} &= \sum_{j=1}^{M} \hat{b}_j^+ \hat{f}_j^V + \sum_{j=1}^{M} \hat{b}_j^+ \hat{f}_j^H \\ &= \hat{T}_V + \hat{T}_H\end{aligned} \tag{4.7.2}$$

where $\hat{T}_V$ ($\hat{T}_H$) is the operator associated to the vertical (horizontal) part of the TM.

TTM decomposition

We first define an operator associated the TTM. For this purpose, we follow a similar mathematical approach than the one used to define the TM operator in equation 4.4.11. The operator associated to $T^{(2)}$ takes then the form:

$$\hat{T}^{(2)} = \frac{1}{2} \sum_{j,j'\in[1,M]} \hat{b}_j^+ \hat{b}_{j'}^+ \hat{f}_j \hat{f}_{j'} \tag{4.7.3}$$

where $\hat{f}_j^+$ is a focusing operator in mode j.
At equation 4.7.1, we have shown that a focusing operator can be split into two different polarization parts. By injecting this decomposition in the previous equation, $\hat{T}^{(2)}$ is decomposed in three different components:

$$\hat{T}^{(2)} = \hat{T}_{VV}^{(2)} + \hat{T}_{HH}^{(2)} + \hat{T}_{HV}^{(2)} \tag{4.7.4}$$

where all these operators are formally expressed as:

$$\hat{T}^{(2)}_{VV} = \frac{1}{2} \sum_{j,j' \in [1,M]} \hat{b}^+_j \hat{b}^+_{j'} \hat{f}^V_j \hat{f}^V_{j'} \tag{4.7.5}$$

$$\hat{T}^{(2)}_{HH} = \frac{1}{2} \sum_{j,j' \in [1,M]} \hat{b}^+_j \hat{b}^+_{j'} \hat{f}^H_j \hat{f}^H_{j'} \tag{4.7.6}$$

$$\hat{T}^{(2)}_{HV} = \sum_{j,j' \in [1,M]} \hat{b}^+_j \hat{b}^+_{j'} \hat{f}^V_j \hat{f}^H_{j'} \tag{4.7.7}$$

$$\tag{4.7.8}$$

The operator $\hat{T}^{(2)}_{HV}$ introduced in the previous equation corresponds exactly to the operator associated to reduced TTM introduced in part 4.5.1. This operator can be finally decomposed in a product between horizontal and vertical part of TTM:

$$\hat{T}^{(2)}_{HV} = \hat{T}_V \times \hat{T}_H \tag{4.7.9}$$

This last result will be used in the next parts to derive analytical expressions of the focusing fidelity and the experimental input state.

4.7.2 Analytical expression of the focusing fidelity

The notations introduced in the previous section are now used to derive a simple expression of the focusing fidelity $\mathcal{F}_{XY}$.
First, we provide an expression of the output state obtained after propagation of an input state $|\Psi_{\text{exp}}\rangle$ through the system:

$$\begin{aligned} \hat{T}^{(2)}|\Psi_{\text{exp}}\rangle &= \hat{T}^{(2)}_{HV}|\Psi_{\text{exp}}\rangle \\ &= \frac{1}{\sqrt{N_V N_H}} \hat{T}_H \left(\sum_{ih \in \Omega_H} e^{i\phi_{ih}} \hat{a}^+_{ih} \right) \hat{T}_V \left(\sum_{iv \in \Omega_V} e^{i\phi_{iv}} \hat{a}^+_{iv} \right) |0\rangle \end{aligned} \tag{4.7.10}$$

By injecting the previous result in equation 4.5.6, we obtain then a simplified expression of the fidelity:

$$\mathcal{F}_{XY} = \left| \frac{([T_H \boldsymbol{\Phi_H}]_X [T_V \boldsymbol{\Phi_V}]_Y + [T_H \boldsymbol{\Phi_H}]_Y [T_V \boldsymbol{\Phi_V}]_X)}{\sqrt{1+\delta_{XY}}} \right|^2 \tag{4.7.11}$$

where $[T_H \boldsymbol{\Phi_H}]_j$ ($[T_V \boldsymbol{\Phi_V}]_j$) is a compact notation that represents the field value in mode output j after propagation of the horizontally (vertically) polarized field through the system. They are formally written as:

$$[T_H \boldsymbol{\Phi_H}]_j = \frac{1}{\sqrt{N_H}} \sum_{ih \in \Omega_H} T_{j,ih} e^{i\phi_{ih}} \tag{4.7.12}$$

$$[T_V \boldsymbol{\Phi_V}]_j = \frac{1}{\sqrt{N_V}} \sum_{iv \in \Omega_V} T_{j,iv} e^{i\phi_{iv}} \tag{4.7.13}$$

We now analyze the physical meaning of equation 4.7.11. This equation takes a form traducing a quantum interference phenomenon. The product $[T_H \mathbf{\Phi_H}]_X [T_V \mathbf{\Phi_V}]_Y$ represents the joint amplitude probability of photon H to reach X and photon V to reach Y. Inversely, $[T_H \mathbf{\Phi_H}]_X [T_V \mathbf{\Phi_V}]_Y$ represents the joint amplitude probability associated to photon H going to X and photon V going to Y. Same interference effect would appear considering propagation of two-photons in a lossy beam-splitter connecting inputs H and V to output X and Y. This system would be characterized by a 2×2 transmission matrix T_{eq} taking the form:

$$T_{\text{eq}} = \begin{bmatrix} [T_H \mathbf{\Phi_H}]_X & [T_V \mathbf{\Phi_V}]_X \\ [T_H \mathbf{\Phi_H}]_Y & [T_V \mathbf{\Phi_V}]_Y \end{bmatrix} \tag{4.7.14}$$

In our experimental configuration, the propagation of photon-pairs in a multimode system characterized by matrices T_V and T_H detected in two specific output ports X and Y is thus equivalent to propagation of photons in a 2×2 system characterized the matrix T_{eq}. In consequence, the maximization of the focusing fidelity is achieved by:

- manipulating classical interferences to adjust *amplitudes* of the two-photon paths
- manipulating quantum interferences to adjust *relative phase* of the two-photon paths

4.7.3 Analytical expression of the experimental input state

In this part, we derive an analytical expression of $|\Psi_{\text{exp}}\rangle$. For the sake of simplicity, the set of M output modes is now considered to be only composed of the two targeted modes X and Y where $X \neq Y$ [7]. In the following calculations, T is then considered as a $2 \times N$ matrix. This assumption has no consequences on the generality of the approach.

The energy conservation problem

We first make a new hypothesis concerning our capacity to focus light relatively to the problem of energy conservation.
When a SLM focuses classical light between several outputs of a non absorbing multimode system, energy conservation could impose some constraints on the relative phase of the targeted output modes. For instance, if light is focused into two output modes with an efficiency closed to one, the system works as a balanced beam splitter and energy conservation fixes the relative phase to π. In this situation, the relative phase can not be controlled by the SLM. This energy conservation effect is discussed in detail in [125].
In our configuration, we suppose that the hypothesis $N \ll P$ (Hypothesis 1) is verified *enough* to neglect any limitations on the control of the output field due to energy conservation. The existence of this unrestricted control regime for small enough N has been demonstrated for two targeted outputs in [125]. In our case, we then assume that the SLM can be programmed to control freely the intensity weights and the relative phase of the output modes.

7. The case $X = Y$ corresponds to focus photon-pairs in the output state $|2_X\rangle$. This focusing task is simply performed by directing each photon of the pair independently in the same output mode X.

The general factorized form of the input state

At equation 4.5.4, we have introduced the most general form of two-photon input state that can be produced by the SLM with our experimental constraints. This form has allowed to find an analytical form of the focusing fidelity with a very clear physical signification. However, this equation is not very convenient to continue our calculations. Using the notations introduced in part 4.7.1, we now investigate this problem of finding a more interesting expression of the experimental input state.
Thinking only about one photon, the most general output state involving the two modes X and Y takes the form:

$$|\phi_{out}\rangle = (\cos(\theta)\hat{b}_X^+ + e^{i\phi}\sin(\theta)\hat{b}_Y^+) \tag{4.7.15}$$

where θ and ϕ are two angular parameters. We can easily write its corresponding single-photon input state using the focusing operator notations introduced in equation 4.4.9:

$$\begin{aligned} |\phi_{in}\rangle &= \hat{T}^+|\phi_{out}\rangle \\ &= \left(\cos(\theta)\hat{f}_X^+ + e^{i\phi}\sin(\theta)\hat{f}_Y^+\right) \end{aligned} \tag{4.7.16}$$

where $\hat{f}_j^+$ is the focusing operator in output mode j. We apply this general decomposition of at each photon of the pair using the partial focusing operators introduced at equation 4.7.1. In consequence, the most general two-photon state that can be experimentally produced at the input to focus light in two output modes X and Y takes the general form:

$$\begin{aligned} |\Psi_{\text{exp}}(\boldsymbol{\theta})\rangle = &\left(\cos(\theta)\hat{f}_X^{V+} + e^{i\phi}\sin(\theta)\hat{f}_Y^{V+}\right) \\ &\left(\sin(\theta')\hat{f}_X^{H+} + e^{i\phi'}\cos(\theta')\hat{f}_Y^{H+}\right)|0\rangle \end{aligned} \tag{4.7.17}$$

where $\boldsymbol{\theta}$ is a vector that contains four free angular parameters $\boldsymbol{\theta} = [\theta, \theta', \phi, \phi']$ and $\hat{f}_j^V$ ($\hat{f}_j^H$) is the vertical (horizontal) part of the focusing operator in output mode j. This general form of the input state only depend on four phase parameters. The two-photon input state is now expressed using a very simple form that only involves four phases parameters [8].

A new matricial fomalism to write the input states

As presented in the previous part, any experimental input can be written as a linear combination of $\hat{f}_j^V$ and $\hat{f}_j^H$. In this part, we introduce a more compact notation adapted to this type of state. This compact notation will be useful to simply the future calculations.
Let's consider a general state of the form:

8. At this stage of the process, this new form of the input state respects the first two limitations introduced at parts 4.5.1 and 4.5.1. The third limitation - relative the the phase only control character of the SLM - will only be applied at the end of the calculation.

$$|\Psi\rangle = \sum_{j,j' \in [1,M]} A_{jj'} \hat{f}_j^{V+} \hat{f}_{j'}^{H+} |0\rangle \tag{4.7.18}$$

where $A_{jj'}$ are complex coefficients and $\hat{f}_j^{V+}$ and $\hat{f}_{j'}^{H+}$ are the focusing operators defined by equation 4.7.1. To simplify this expression, we define the matrix A composed of the coefficients $A_{jj'}$. This matrix completely defines the state $|\Psi\rangle$ [9]

$$|\Psi\rangle \rightarrow A \tag{4.7.19}$$

In our study, it is interesting to express the two states $|\Psi_{\text{exp}}(\boldsymbol{\theta})\rangle$ and $T_{HV}^{(2)+}|1_X 1_Y\rangle$ introduced previously using this matricial formalism:

1. The experimental state $|\Psi_{\text{exp}}(\boldsymbol{\theta})\rangle$ detailed equation 4.7.17 is then associated to a matrix $E(\boldsymbol{\theta})$ taking the form:

$$|\Psi_{\text{exp}}(\boldsymbol{\theta})\rangle \rightarrow E(\boldsymbol{\theta}) = \begin{bmatrix} \cos(\theta)\sin(\theta') & \cos(\theta)\cos(\theta')e^{i\phi'} \\ \sin(\theta)\sin(\theta')e^{i\phi} & \sin(\theta)\cos(\theta')e^{i(\phi+\phi')} \end{bmatrix} \tag{4.7.20}$$

2. Because the focusing fidelity also involved the state $T_{HV}^{(2)+}|1_X 1_Y\rangle$, we would like to express it using the same formalism. First, this state is expanded onto the form given by equation 4.7.18:

$$\begin{aligned} T_{HV}^{(2)+}|1_X 1_Y\rangle &= T^{(2)+}\frac{\hat{b}_X^+ \hat{b}_Y^+}{\sqrt{2}}|0\rangle \\ &= \sum_{j,j' \in [1,M]} \hat{b}_j \hat{b}_{j'} \hat{f}_j^{H+} \hat{f}_{j'}^{H+} \frac{\hat{b}_X^+ \hat{b}_Y^+}{\sqrt{2}}|0\rangle \\ &= \frac{\hat{f}_X^{H+}\hat{f}_Y^{V+} + \hat{f}_X^{V+}\hat{f}_Y^{H+}}{\sqrt{2}}|0\rangle \end{aligned} \tag{4.7.21}$$

   Then, we can easily identify the different matrix elements. Its associated matrix O is finally defined as:

$$T_{HV}^{(2)+}|1_X 1_Y\rangle \rightarrow O = \frac{1}{\sqrt{2}}\begin{bmatrix} 0 & 1 \\ 1 & 0 \end{bmatrix} \tag{4.7.22}$$

Mathematical proposition: scalar product between input states expressed in the matricial formalism

We continue to prepare the ground for the future calculations by giving here a simplified form of the scalar product between two states, using the matricial formalism

9. This matricial formalism is very well adapted to consider more complex problems of photons control. It can be easily generalized to problems involving:
   – a *higher number of targeted modes*: by increasing size of the matrices
   – a *higher number of photons*: by introducing tensors to describe the input state instead of matrices

.

previously introduced.
We consider two input states $|\Psi\rangle$ and $|\Phi\rangle$ written in the general form given by equation 4.7.18 and their associated matrices: $|\Psi\rangle \to A$ and $|\Phi\rangle \to B$. The scalar product $\langle\Psi|\Phi\rangle$ can be written under the compact form:

$$\langle\Psi|\Phi\rangle = \mathrm{Tr}\left[A^{+}T_V T_V^{+} B (T_H T_H^{+})^{*}\right] \tag{4.7.23}$$

Compact expression of the focusing fidelity

We now apply the result obtained in the previous part to the input states $|\Psi_{\mathrm{exp}}(\boldsymbol{\theta})\rangle$ and $T_{HV}^{(2)+}|1_X 1_Y\rangle$ that are both involved in the formula of the focusing fidelity $\mathcal{F}_{XY}$ (equation 4.5.6). These two states are associated with two matrices denoted $E(\boldsymbol{\theta})$ (4.7.20) and O (4.7.22). Using the previous mathematical result, the focusing fidelity given at equation 4.7.11 is then written under the compact form:

$$\mathcal{F}_{XY} = \left|\mathrm{Tr}\left[E(\boldsymbol{\theta})^{+} T_V T_V^{+} O (T_H T_H^{+})^{*}\right]\right|^2 \tag{4.7.24}$$

Calculation of the experimental input state

We keep working on this compact expression to determine the input state $|\Psi_{\mathrm{exp}}(\boldsymbol{\theta})\rangle$ - so in fact the angular parameters $\boldsymbol{\theta}$ - that maximizes the fidelity.
First, we simplify the products $T_V T_V^{+}$ and $T_H T_H^{+}$. Because T_H and T_V are subparts of the matrix T, the hypothesis 1 is also valid for them and their products $T_H T_H^{+}$ and $T_V T_V^{+}$ can be decomposed as:

$$T_H T_H^{+} = \sigma^2 N \left[\mathbb{1} + \frac{1}{\sqrt{N}} R'\right] \tag{4.7.25}$$

$$T_V T_V^{+} = \sigma^2 N \left[\mathbb{1} + \frac{1}{\sqrt{N}} R\right] \tag{4.7.26}$$

where R and R' are 2×2 random hermitian matrices whose entries do not depend [10] upon N. The elements of R (R') are denoted $R_{jj'}$ ($R'_{jj'}$) with $j = X$ or Y and $j' = X$ or Y.
These products are then injected into equation 4.7.24:

$$\begin{aligned}\mathcal{F}_{XY}(\boldsymbol{\theta}) = &\sigma^8 N^4 \Big|\mathrm{Tr}\left[E(\boldsymbol{\theta})^{+} O\right] \\ &+ \frac{1}{\sqrt{N}}\mathrm{Tr}\left[(E(\boldsymbol{\theta})^{+} R + R'^{*} E(\boldsymbol{\theta})^{+}) O\right] \\ &+ \frac{1}{N}\mathrm{Tr}\left[E(\boldsymbol{\theta})^{+} R O R'^{*}\right]\Big|^2\end{aligned} \tag{4.7.27}$$

Assuming that [11] $N \gg 1$, we can discard the term proportional to $1/N$ in the

10. Even if T_H (T_V) only contains N_H (N_V) and not N, the decomposition is possible because we can always write $N_H = \alpha N$ ($N_V = (1-\alpha)N$) where $\alpha \in [0,1]$. The variance of the elements of R and R' are then different in each case depending on the value of α, but they still do not depend upon N

11. To be more precise, we also need to assume that $N_V \gg 1$ and $N_H \gg 1$

previous expression. Up to the multiplicative factor $\sigma^8 N^4$, the expression under study becomes:

$$\mathcal{F}_{XY}(\boldsymbol{\theta}) \approx \left| \mathrm{Tr}\left[E(\boldsymbol{\theta})^{+} O\right] + \frac{1}{\sqrt{N}} \mathrm{Tr}\left[(E(\boldsymbol{\theta})^{+} R + R'^{*} E(\boldsymbol{\theta})^{+}) O\right] \right|^2 \tag{4.7.28}$$

By studying the derivative of this expression, one can find the angular entries $\boldsymbol{\theta} = [\theta, \theta', \phi, \phi']$ that maximize the focusing fidelity:

$$\phi - \phi' = 0 \tag{4.7.29}$$

$$\theta = \theta' = \frac{\pi}{4} + \frac{\arctan\left(\nu/|\lambda|\right)}{2} \tag{4.7.30}$$

where $\lambda = \Re(R_{XY} + R'_{XY})$ and $\nu = R'_{XX} - R_{XX} + R_{YY} - R'_{YY}$. Using the matricial formalism introduced at equation 4.7.23, the matrix associated to the state maximizing the focusing fidelity is denoted E_m and can be written as

$$E_m = \frac{1}{\sqrt{2}} \left(\frac{\sigma_x}{\sqrt{2}} + \frac{\sigma_x}{\sqrt{\lambda^2 + \nu^2}} \begin{bmatrix} \lambda & -\nu \\ \nu & \lambda \end{bmatrix} \right) \tag{4.7.31}$$

We observe that there are an infinite number of phase settings that verify the two conditions given at equations 4.7.30 i.e. an infinite number of input state that are optimal the focusing process. Each condition acts on a different type on interference:

- The condition involving θ and θ' constraints the classical interference processes to adjust the intensity weight in each output modes.
- The condition involving ϕ and ϕ' constraints the quantum interference processes to adjust the relative phase between each mode and make them constructive.

4.7.4 Practical method to use the analytical approach

This part summarizes the analytical approach and explains point by point the method to calculate the input state in any focusing situation. In this part, we suppose that the TM T is known and verifies the hypothesis: $1 << N << P$. T is expressed in the *X-Y canonical* basis (where the i^{th} pixel - or macropixel - of the SLM corresponds to the input mode i) and can be split in its horizontal T_H and vertical part T_V.
The goal here is to determine the SLM pattern that allows focusing photon-pairs into the output mode $|1_X 1_Y\rangle$ $(X \neq Y)$ and gives the highest coincidence rate. The step-by-step method is described bellow:

1. Two matrices denoted R^+ and R^- are first calculated from T_H and T_V:

$$\begin{aligned} R^+ &= T_H T_H^+ + T_V T_V^+ \\ &= \sqrt{N}\sigma^2 \begin{bmatrix} R_{XX} + R'_{XX} + \sqrt{N} & R_{XY} + R'_{XY} \\ R_{YX} + R'_{YX} & R_{YY} + R'_{YY} + \sqrt{N} \end{bmatrix} \end{aligned} \tag{4.7.32}$$

and

$$\begin{aligned} R^{-} &= T_V T_V^{+} - T_H T_H^{+} \\ &= \sqrt{N}\sigma^2 \begin{bmatrix} R_{XX} - R'_{XX} & R_{XY} - R'_{XY} \\ R_{YX} - R'_{YX} & R_{YY} - R'_{YY} \end{bmatrix} \end{aligned} \tag{4.7.33}$$

2. The parameter $\nu/|\lambda|$ is simply estimated using R^{+} and R^{-} as:

$$\frac{\nu}{|\lambda|} = \frac{R^{-}_{YY} - R^{-}_{XX}}{|\Re(R^{+}_{XY})|} \tag{4.7.34}$$

3. The angular parameter θ_m is given by:

$$\theta_m = \frac{\pi}{4} + \frac{\arctan\left(\nu/|\lambda|\right)}{2} \tag{4.7.35}$$

4. Finally, the input state becomes:

$$\begin{aligned} |\Psi_{\text{exp}}\rangle = &\left(\cos(\theta_m)\hat{f}_X^{V+} + \sin(\theta_m)\hat{f}_Y^{V+}\right) \\ &\left(\sin(\theta_m)\hat{f}_X^{H+} + \cos(\theta_m)\hat{f}_Y^{H+}\right) \end{aligned} \tag{4.7.36}$$

5. The corresponding SLM pattern is programmed by setting the value of the i^{th} pixel of SLM V (denoted $[\boldsymbol{\phi_V}]_i$) to:

$$[\boldsymbol{\phi_V}]_i = \arg\left(\cos(\theta_m)\sum_{ih\in\Omega_H} T^{*}_{X,ih} + \sin(\theta_m)\sum_{ih\in\Omega_H} T^{*}_{Y,ih}\right) \tag{4.7.37}$$

and pixel i of SLM H denoted $[\boldsymbol{\phi_H}]_i$ to the value

$$[\boldsymbol{\phi_H}]_i = \arg\left(\sin(\theta_m)\sum_{iv\in\Omega_V} T^{*}_{X,iv} + \cos(\theta_m)\sum_{iv\in\Omega_V} T^{*}_{Y,iv}\right) \tag{4.7.38}$$

For example, a numerical simulation of a focusing process is performed using the analytical approach. This simulation is presented on Figure 4.4. The transmission matrix generated here is the same than the one used in the simulation of the optimization process presented Figure 4.3. As shown on Figure 4.4.a, this method ensures a strong enhancement of the targeted mode intensity. The corresponding focusing fidelity reaches the value $\mathcal{F}_{XY} \approx 1.99 \times 10^{-3}$ very close to the value obtained in the optimization process, which confirms its efficiency.

4.8 Conclusion

In the first section of this chapter, we have introduced the theoretical tools that allow describing the propagation of non-classical light - single-photon state and photon-pairs - through a multimode system. In particular, we have demonstrated that the

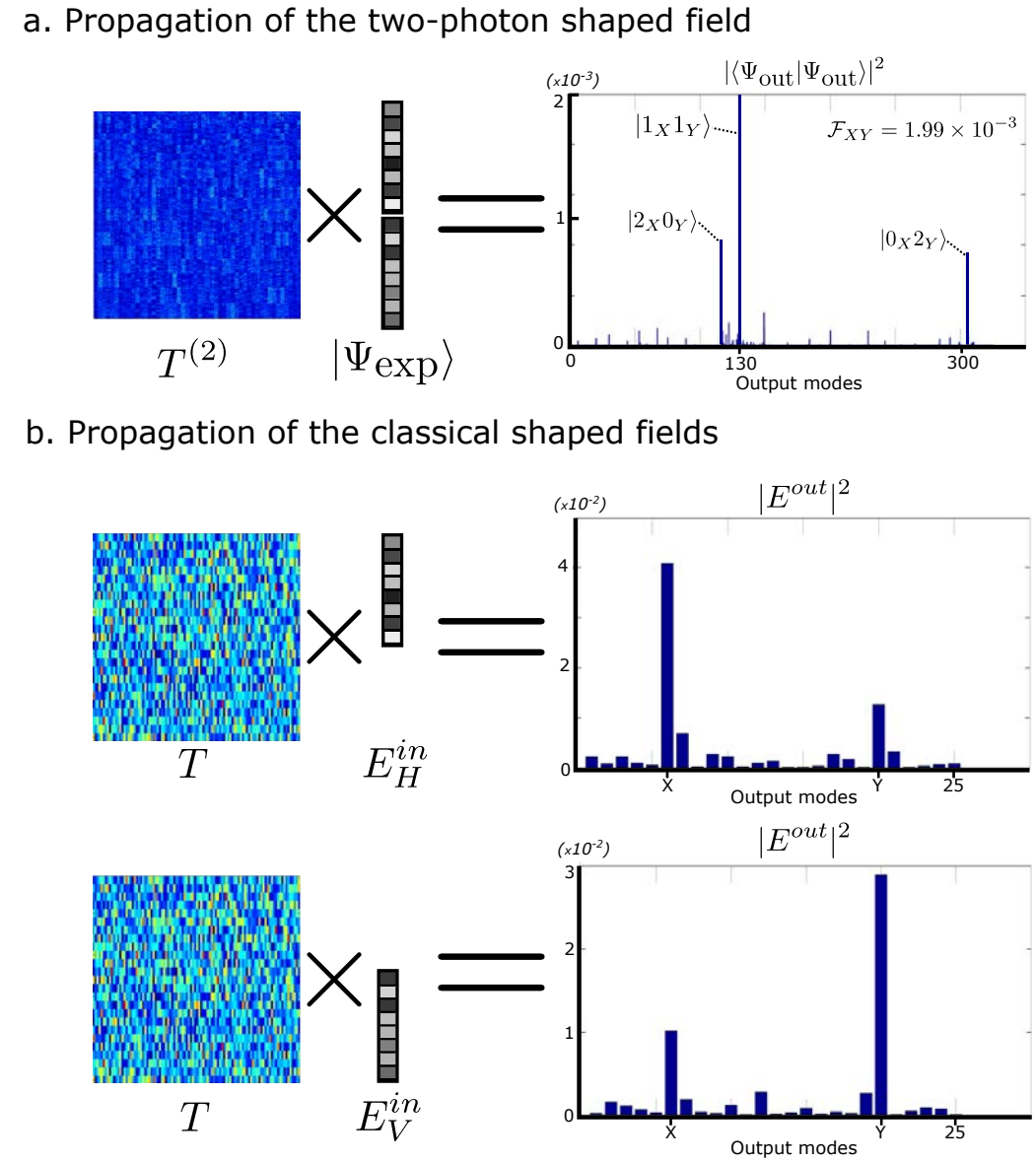

Figure 4.4: **Simulation of an analytical approach focusing process** The transmission matrix generated in this simulation is a 200×30 extracted from a 1000×1000 unitary random scattering matrix. The matrix is the same than the one used in Figure 4.3. **a.** The experimental input state calculated with the analytical procedure is re-propagated through the system and the corresponding two-photon speckle pattern is observed. Intensity of the targeted output mode $|1_X 1_Y\rangle$ is efficiently enhanced. $|2_X 0_Y\rangle$ and $|0_X 2_Y\rangle$ are also slightly optimized. The focusing fidelity is about $\mathcal{F}_{XY} \approx 1.99 \times 10^{-3}$. **c.** Classical speckles created by classical fields set alternatively on SLM V and SLM H are reconstructed. As expected, a simultaneous enhancement of X and Y modes with different weights is observed.

two-photon transmission matrix contains all the information relative to the propagation of photon-pairs through the system. This matrix takes into account classical and quantum interference effects and can be calculated directly from the classical transmission matrix. In consequence, once the TM has been retrieved using a classical source, the propagation of photon-pairs - and more generally of any non-classical state of light - can be predicted.

The second section of this chapter offers an extension the *scattering matrix approach*, a method originally developed to manipulate classical light propagation [80] and introduced in chapter 2, to non-classical light. After introducing the general idea behind the method, the theory focuses on the realistic case where each photon of the pairs is shaped independently. In this situation, we have developed two approaches that allow calculating the two-photon input field that focuses photon-pairs in coincidences between two targeted modes at the output.

The experimental constraints introduced here can be found in the optical setup described in chapter 5. In this experiment, photon-pairs are injected in a multimode fiber that acts as a multimode optical platform. A SLM shapes the two-photon field at the input and allows controlling photons propagation. We use the analytical approach developed here to focus photon-pairs in a targeted output mode of the MMF.

Chapter 5

Two-photon quantum walk in a multimode fiber

While focusing of single-photon states has been demonstrated [193, 127, 123], scaling to controlled multi-photon propagation is challenging due to the exceptionally high number of optical modes of a diffusive medium. Multimode fiber (MMF) provides a platform that delivers a sufficiently large number of modes to demonstrate a new regime of modal capacity for quantum light, but a small enough number to ensure that control is possible using techniques developed with classical light. Strong and complex mode mixing in the fiber arises from the interferences between a well-defined number of spatial modes sustained by the fiber. For instance, the MMF used in this experiment supports about 380 transverse spatial and polarization modes at 810nm. Moreover, the relevance of using MMFs is enhanced by the near lossless character of the light propagation. We present here the first implementation of a controlled two-photon quantum walk in a MMF. Some results of this study are reported in the letter [128].

In the first section of this chapter (5.1), we use the MMF as a passive linear multimode network to implement a two-photon quantum walk. We investigate here the properties of the walk through the measurement of a two-photon transmission matrix (TTM). The knowledge of this matrix allows retrieving information about the non-classical interference effects occurring in the fiber.
In a second part, we demonstrate our capacity to control photons propagation in the MMF. For this purpose, we use a similar strategy than the one employed in chapter 3. We first characterize our system by measuring its transmission matrix (TM) with a classical source (5.2). Then, we use the results reported in chapter 4 to calculate the TTM from the measured TM and exploit it to guide the photons through the fiber. In particular, we show how to focus photon-pairs into a targeted two-photon output mode of the medium by manipulating both classical and quantum interferences (5.3). A simplified scheme of the experiment is presented on Figure 5.1.

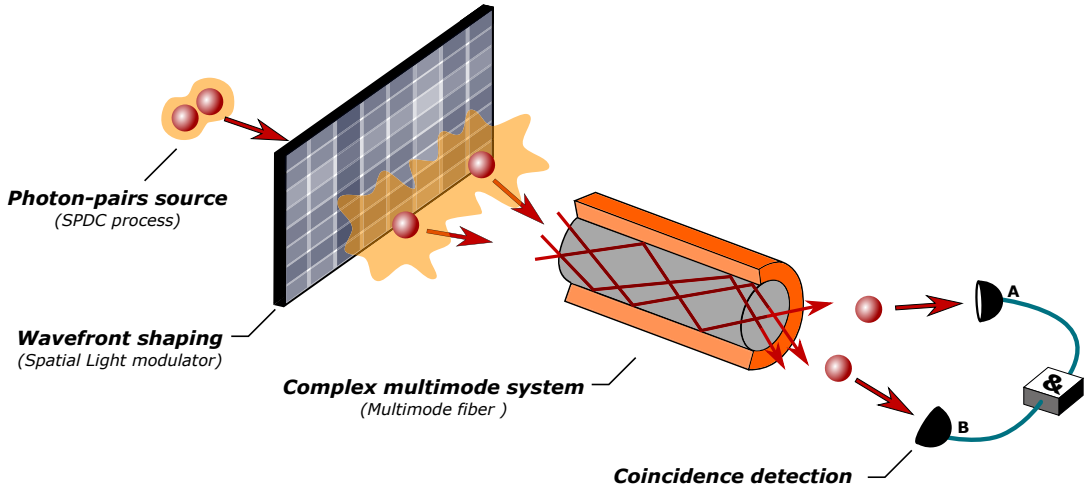

Figure 5.1: **Photon-pairs quantum walk in a multimode fiber**. Photon-pairs are generated using a SPDC process. They are distributed over all the input modes of the MMF using the SLM. After propagation, photons are collected at different output positions using polarization maintaining single-mode fibers (PMSMFs) and coincidence maps of speckle patterns can be measured.

5.1 Photon-pairs propagation in a multimode fiber

Photon-pairs injected in a MMF perform a two-photon quantum walk due to the coupling between modes. The probability for the photons to exit the fiber in certain modes is determined both by the classical propagation of each photon independently (each photon interferes with itself) and by their collective behavior (quantum interference effects). When coincidence measurements are performed between the different modes - or grains - of the direct speckle pattern, one can reconstruct a two-photon speckle pattern at the output [110, 116]. Contrary to the direct speckle pattern, the two-photon speckle pattern is sensitive to quantum interference effects.
If photons are distinguishable, they behave as uncorrelated particles and coincidence probability distribution is directly predicted from output statistics of each photon taken independently. More simply, the two-photon speckle is reconstructed by multiplying the direct speckle statistics of each photon.
However, if the photons are indistinguishable, quantum interference effects occur during their propagation and the two-photon speckle pattern changes. In this situation, the two-photon transmission matrix (TTM) is required to describe propagation of photon-pairs. This matrix takes into account both classical and quantum interference effects and allows predicting the coincidence statistics at the output for all possible arrangements of the photons at the input.

The notion of TTM is introduced theoretically in chapter 4. In this experiment, we show a direct measurement of the TTM of the fiber and demonstrate how this matrix can be used to retrieve information about the quantum walk performed by the photons.

For this purpose, we use the optical setup presented on Figure 2.5 in chapter 2 but replacing the classical source by a photon-pairs source.
In this section, we first briefly remind the properties of the photon-pairs source used in this experiment (5.1.1). Then, we explain how to reconstruct the TTM of the fiber (5.1.2). We also demonstrate in this part how this matrix can be used to analyze some properties of the walk, such as the quantum interference effects occurring in the MMF.

5.1.1 Photon-pairs source

The photon-pairs source used in this experiment is described at section 1.1.2 of chapter 1. The corresponding setup is represented on Figure 1.3 of chapter 1 and more details are also given in Appendix A. In this part, we simply remind some important characteristics of the source.
We generate photon-pairs by pumping a periodically poled potassium titanyl phosphate (PPKTP) crystal 50 mW continuous-wave laser diode at 405 nm. Photons are produced at around 810nm and are filtered using a 1nm narrowband filter centered at 810 nm. At the output of the crystal, photon-pairs are then spatially separated using a PBS and injected into two PMSFMs.
The relative path δ between the photons is controlled using a translation stage positioned on one of the arms. Due to their spectral properties, if δ is set to 0.4mm, the time delay between the photons is large enough to make them completely distinguishable. On the contrary, if δ is set to 0, there is no time delay between photons and they become indistinguishable [1]. They are subjected to quantum interference during their propagation, with a maximum interference visibility of 86% (see Appendix A for more details).
The PMSMFs are directly connected to the wavefront shaping setup. They ensure a good control over polarization and spatial properties of the photons before they reach the SLMs.

5.1.2 Experimental reconstruction of the two-photon transmission matrix

To perform this experiment, we adopt the experimental setup presented on Figure 2.5 in chapter 2 but we replace the classical source by the photon-pairs source. More precisely, one photon of the pair is injected in the MMF in the vertically polarized input (controlled by SLM V) and the other one in the horizontally polarized input (controlled by SLM H). The SLMs can then be programmed to distribute the photons over several spatial input modes of the MMF as depicted on Figure 5.2.a.
Direct speckle measurements made using the EMCCD camera presented on Figure 5.2.b show how each photon is delocalized over approximately 50 independent output speckle grains. Note that the overall intensity distribution is the incoherent sum of each individual photon intensity profile and is independent of the indistinguishability of the photons (see chapter 1 for more details).

1. One important challenge in this experiment is to determine precisely the position of the translation stage that makes photons perfectly indistinguishable during propagation in the MMF. This technical point is explained in Appendix D.

One element of the TTM is then reconstructed by measuring the coincidence rate between two output modes while the SLM excites specific modes at the input. In principle, the complete TTM could be recorded with this method by scanning all input and output modes. However, the weak intensity of the photon-pair source and the huge number of possible combinations impose to use very long acquisition times and only a small part of the TTM can be measured experimentally. In this experiment, we select therefore a small set of output and input modes to reconstruct a part of the TTM.

Two-photon matrix measurement

In the result discussed here, we only chose 2 positions for each fiber at the output and 4 spatial modes for each SLM at the input. In this configuration, we measure a part of the TTM with a size of 16×4.

At the output, intensity-correlations are measured by coincidence detection events between the two PMSMFs. The PMSMFs can be positioned at two different locations in the output image plane denoted $\{|X_1\rangle, |X_2\rangle\}$ and $\{|Y_1\rangle, |Y_2\rangle\}$ for fiber F1 and fiber F2 respectively. In this case, we scan the 4 two-photon output states of the form $\hat{a}^+_{|X_j\rangle}\hat{a}^+_{|Y'_j\rangle}|0\rangle$ with $j \in \{1,2\}$ and $j' \in \{1,2\}$. To simplify the notation, these output states are written $|X_jY'_j\rangle$ [2].
At the input, the SLMs scan 4 spatial modes for each photon denoted $\{|1V\rangle, |2V\rangle, |3V\rangle, |4V\rangle\}$ and $\{|1H\rangle, |2H\rangle, |3H\rangle, |4H\rangle\}$ for SLM H and SLM V respectively. We can then generate at the input 16 two-photon states of the form $\hat{a}^+_{|iH\rangle}\hat{a}^+_{|i'V\rangle}|0\rangle$ with $i \in [1,4]$ and $i' \in [1,4]$. To simplify this notation, an input state is written $|iHi'V\rangle$.
Although the indistinguishability can be continuously tuned by means of the delay line, we chose to explore the two extreme cases: TTM measurements are performed with either indistinguishable photons ($\delta = 0$) or distinguishable photons ($\delta = 0.4$mm). The measured matrices are presented on Figure 5.2.c.d.

While we only have access to the amplitude components of the matrix, we can still extract some relevant information about the walk performed by the photons. In particular, we observe some important changes in the coincidence rates of identical elements taken in the two different matrices. These differences represent a clear signature of two-photon quantum interferences occurring during photons propagation, as analogues of the Hong-Ou-Mandel effect [11]. The amount of quantum interferences that contributes to each element of the TTM is now studied quantitatively by calculating non-classical contrasts.

Quantitative analysis of quantum interferences

For each input-output configuration, we compare the elements of the TTM measured at $\delta = 0$ and $\delta = 0.4$mm presented on Figure 5.2c.d. by calculating a contrast.

2. This is just a notation and it *does not* correspond to a notation in the first quantization formalism. Using the first quantization formalism, this state would be written: $|X_jY'_j\rangle = \frac{1}{\sqrt{2}}(|X_j\rangle_1|X'_j\rangle_2 + |X'_j\rangle_1|X_j\rangle_2)$ where index 1 and 2 refer to each photon of the pair.

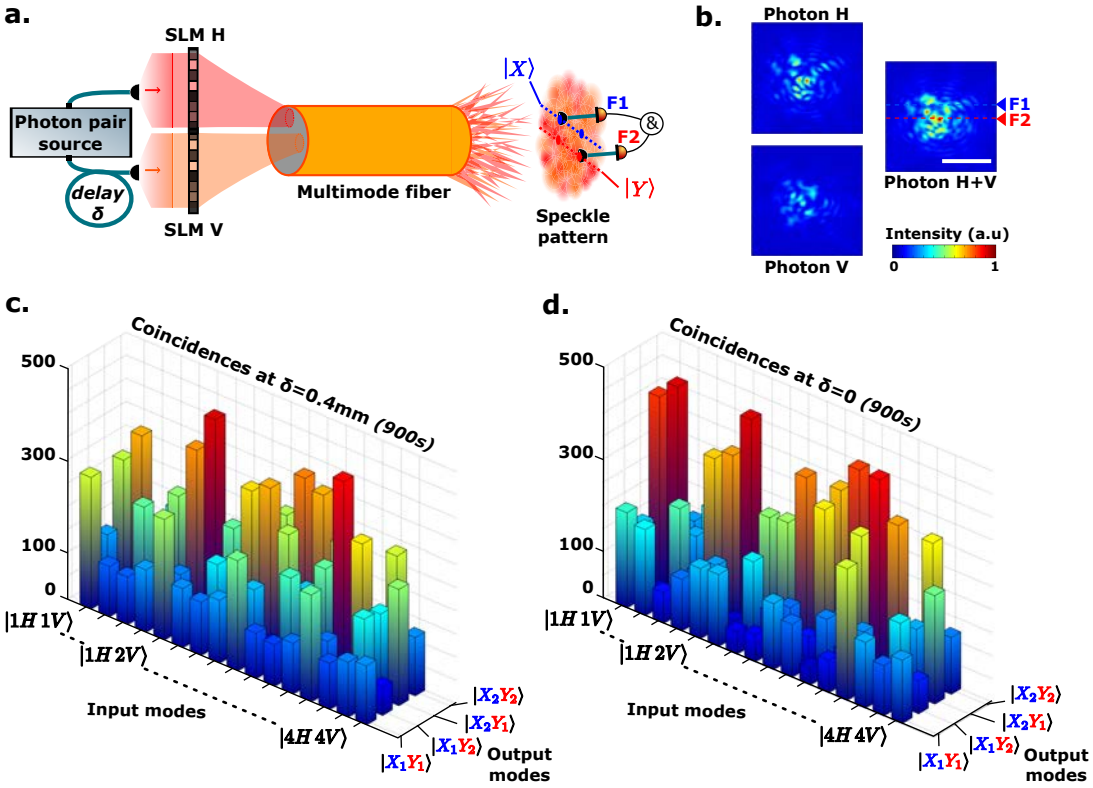

Figure 5.2: **Experimental reconstruction of a two-photon transmission matrix (a.)** Schematic of the experimental setup using a two-photon input state injected into two distinct input modes. **(b.)** Speckle patterns recorded with the EMCCD camera generated by photon H only, photon V only and both photons simultaneously. As expected, speckle H + V corresponds to the incoherent sum of each separate case. It contains about 50 independents speckle grains. Coincidence patterns **(c.)** and **(d.)** are determined from coincidence measurements between Fiber F1 and Fiber F2 for each mode of a set of 16 two-photon input states programmed by the SLMs. These 16 input modes are denoted $|iHi'V\rangle$ with $i \in [1,4]$ and $i' \in [1,4]$. F1 and F2 scan four output coincidence modes denoted $|X_jY'_j\rangle$ with $j \in \{1,2\}$ and $j' \in \{1,2\}$. The 16×4 coincidence matrix measured represents a subpart of the complete TTM. Differences observed in coincidence patterns measured with distinguishable ($\delta = 0.4$mm) or indistinguishable photons ($\delta = 0$) indicate that quantum interference occurs in the MMF. Data are acquired for 900s with a coincidence window of 2.5ns. The scale bar represents $25\mu m$ in the output plane of the multimode fiber. Note that some of these coefficients present strong uncertainties quantified in the statistical approach presented in Appendix D.

This contrast quantifies the contribution of quantum interference to the matrix coefficients. The contrast relative to input mode $|iHi'V\rangle$ and output mode $|X_jY'_j\rangle$ is estimated with the formula:

$$C_{ii'}^{jj'} = \frac{R_{ii'}^{jj'}(\delta = 0) - R_{ii'}^{jj'}(\delta = 0.4mm)}{R_{ii'}^{jj'}(\delta = 0.4mm)} \tag{5.1.1}$$

where $R_{ii'}^{jj'}(\delta)$ is the coincidence rate of the two-photon output state $|X_jY'_j\rangle$ when $|iHi'V\rangle$ is programmed at the input and the path length difference is set to δ. We then calculate contrast values for all the matrix coefficients and reconstruct a matrix of contrasts on Figure 5.3. This matrix highlights the very rich quantum interference structure offered by the MMF. Moreover, some contrast values are larger than $|0.5|$ and thus confirm the quantum nature of the phenomenon.

The matrix measurements performed here for distinguishable and indistinguishable photons confirm that quantum coherence between the photons survives during propagation through the MMF. The TTM then provides all the information about photons propagation between the selected modes and can predict the evolution of any two-photon state injected at the input. Finally, we have shown here that a MMF can therefore be exploited as a high-dimensional multimode platform for multi-photon quantum walks.

Limitations of the method

The TTM measurement technique presented in the last section is not completely mature and some aspects still need to be improved. We describe in this part some of the most important weaknesses of our approach:

Phase components of the matrix coefficients First, the measurement method explained here does not give access to the phase components of the matrix coefficients. One possibility to solve this problem would be to implement a holographic method similar to the one used to measure the classical TM (part 2.2.2 of chapter 2). However, this would increase the number of required measurements and then extend the total acquisition time which is not suitable considering the limited stability of the MMF.

Significance of the measured data Second, we observe on the measurements reported on Figure 5.2 that, in spite of the very long acquisition times (900 seconds for each input-output mode), the number of coincidences measured on certain modes remains very small and are not statistically significant. For instance, the number of coincidences measured in the less intense mode is equal to 10. A statistical analysis of the data reported in Appendix D confirms that some measurements have very large uncertainties.

Size of the measured TTM Finally, the too small number of TTM coefficients measured in this experiment does not bring enough information to use the TTM for controlling photon-pairs (using for instance the method described in part 4.6 of chapter 4).

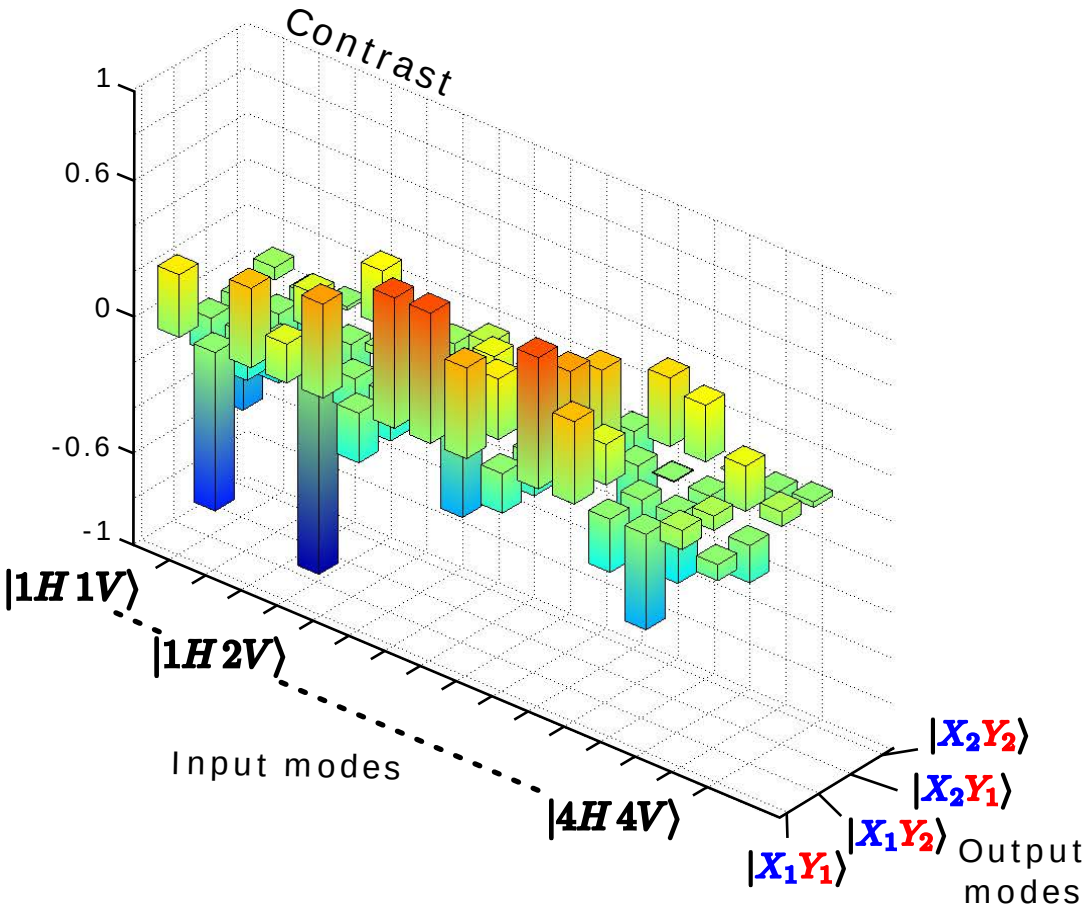

Figure 5.3: **Quantitative study of the quantum interference contributions.** Quantum interference effects occurring when photon-pairs propagate from one input to one output mode are quantified by calculating non-classical contrast values. The contrast is estimated using the formula: $C_{ii'}^{jj'} = (R_{ii'}^{jj'}(\delta = 0) - R_{ii'}^{jj'}(\delta = 0.4mm))/R_{ii'}^{jj'}(\delta = 0.4mm)$ where $R_{ij}^{jj'}(\delta)$ is the coincidence rate of the the two-photon output state $|X_j Y_j'\rangle$ when $|iHi'V\rangle$ is programmed at the input and the path length difference is set to δ. A matrix of contrast coefficients is then reconstructed. The distribution of these values highlights the very rich quantum interference structure offered by the MMF. In particular, some values are above the classical limit of $|0.5|$ and demonstrate the presence of a genuine quantum effect. Note that some of these coefficients present strong uncertainties quantified by a statistical approach presented in Appendix D.

Considering the experimental setup in its current form, our measurement technique does not allow measuring a TTM with enough precisions:

- to make quantitative predictions on the output probability distribution for a given two-photon input state,
- to control photon-pairs propagation in the MMF.

Some solutions could be to increase the intensity of the photon-pairs source as well as the stability of the MMF.

In chapter 4, we have demonstrated the possibility to calculate the TTM directly from the TM (part 4.3.2 of chapter 4) and then to use it to control photon-pairs propagation (part 4.7.3 of chapter 4). In the next sections of this chapter, we exploit these results using a similar approach than the one used to control single-photons in chapter 3: we first characterize the MMF by measuring its TM with classical light (5.2) and we then use its knowledge to control photon-pairs propagation (5.3).

5.2 Characterization of the MMF using a classical source

As we have seen in chapter 2, the TM describes light propagation in a complex system by taking into account classical interference effects. In chapter 3, we have shown that a TM measured with a classical source can be directly used to describe single-photon propagation, if both sources have the same properties. In the case of photon-pairs, the direct intensity speckle pattern is simply the incoherent sum of the speckles created by each photon and can thus also be predicted using the TM.
In the previous section, we have pointed out that the TM is also sufficient to describe any two-photon speckle pattern produced by distinguishable photons: the photons behave as uncorrelated particles and the coincidence speckle is just the product of the two direct speckles. However, the propagation of indistinguishable photon-pairs is not directly predictable because quantum interferences occur in the MMF. In this situation, we need to know the TTM of the medium.
A method to measure the TTM directly using a photon-pairs source has been previously described. In this section, we use an alternative approach: we first measure the TM of the system with a classical source, and then calculate the TTM from the measured TM. The TM measurement process used to characterize the MMF is totally described in section 2.2.4 of chapter 2 and can be done with a good accuracy in a reasonable time. In particular, the experimental setup used here is exactly the same that the one presented on Figure 2.5 in chapter 2.

In this section, we simply remind the important characteristics of the TM measurement process (5.2.2) and gives some details on the classical source used here (5.2.1). We then briefly explain and analyze the TTM reconstruction process (5.2.3).

5.2.1 Classical source

The classical light used to measure the TM comes from a Superluminescent Diode (SLED) centered at 810nm with a spectral bandwidth of 20nm. As shown on Figure 5.4,

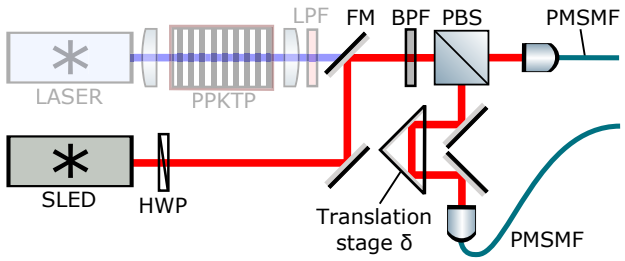

Figure 5.4: **Classical source configuration.** A Superluminescent Diode (SLED) centered at 810nm with a spectral bandwidth of 20nm is directly mounted on a photon-pairs source setup using a flipping mirror (FM). Light emitted is filtered using a 1nm bandpass filter (BPF) centered at 810nm. The field is then split and injected in two PMSMFs and sent towards the wavefront shaping setup using combination of an half wave plate (HWP) and a the polarizing beam splitter (PBS). PMSMFs ensure a good control over polarization and spatial properties. The relative path difference δ between the two arms can be adjusted using the translation stage.

the SLED is directly mounted on the photon-pair source setup [3]. This configuration has the strong advantage that we can easily switch between the classical and the photon-pairs source during the experiment, without needing to connect and disconnect SMFs. A narrowband filter (BPF) selects a 1nm band of the spectrum centered at 810nm which corresponds to a coherence length of about $L_c \approx 0.65\,\mu m$. The narrowband filter used here is the same than the one used to filter the photons when the source is used in the quantum source configuration, which enables a very good overlap between the two spectra.
Light is then split between two arms using a combination of a PBS and a HWP. The temporal coherence between the two arms is controlled by using a translation stage that adjusts the relative path difference δ. Light is finally injected into two PMSMFs that can be connected to the wavefront shaping setup. These PMSMFs ensure a good control over polarization and spatial properties.
As it has been pointed out in chapter 3, it is important to ensure that the classical light used to measure the TM is in the same optical mode than the quantum light. As shown on Figure 5.4, a very good overlap is certified here both by the use of a common spectral filter and the PMSMFs.

Note that the properties of the MMF and the narrow bandwidth of the light (1nm) ensure that temporal dispersion phenomenon is totally negligible: light propagating in the MMF can then be considered monochromatic. More details on the temporal dispersion are given in Appendix D.

3. The photon-pair source setup has been introduced at part 1.1.3 of chapter 1 and is more precisely described in part 5.1.1 of this chapter

5.2.2 TM measurement process

The experimental setup used to reconstruct the TM of the MMF is depicted on Figure 2.5 in chapter 2. All the details about the measurement process are given in section 2.2.4 of chapter 2. In this part, we provide the specific settings that we used in the experiment and give an example of a measured TM.
In this experiment, we use a 11-cm long graded index MMF with a core diameter of $50\,\mu m$. The TM denoted T is determined in the *Fourier basis* decomposed onto $N_V = 183$ vertical polarized and $N_H = 203$ horizontally polarized input modes. Output modes are collected simultaneously by the camera pixels and by two PMSMFs. Figure 5.5.a shows amplitude components of a TM measured between the $N = 386$ ($N = N_V + N_H$) input modes and 80 camera pixels. We observe that this matrix is very sparse. This is mainly due to our choice of the input basis [4].

Once the TM has been measured with the classical source, we directly calculate the TTM of the fiber.

5.2.3 Two-photon transmission matrix reconstruction

The method to calculate the TTM from the TM is described in section 4.3 of chapter 4. In this part, we give an example of a reconstructed TTM and analyze the errors introduced in the process.

Two-photon matrix calculation

Figure 5.5.b shows the TTM calculated from the TM displayed on Figure 5.5.b. We only represent here its amplitude components. This TTM contains complex coefficients linking $N_2 = 74691 \approx 386^2/2$ two-photon input modes to $M_2 = 3321 \approx 80^2/2$ coincidence output modes.

This TTM predicts propagation of indistinguishable photon-pairs through the MMF. From an experimental point of view, this calculation method is very convenient: acquisition of the TM takes about 10 minutes and the numerical calculation of the TTM is performed very quickly with a normal computer. After this calculation step, we can make some additional corrections to adapt more precisely the TTM to our experimental constraints. These corrections are detailed bellow.

Corrections to the calculated TTM

To calculate the TTM, we use the method described in section 4.3 of chapter 4. However, this approach assumes two important points that are not necessary verified in a real experimental setup:

1. Photons-pair are perfectly indistinguishable
2. The contribution of the two-photon reference speckle pattern - produced by photons reflected by the reference parts of each SLMs - is negligible

4. More details on the mixing process and on the TM of a MMF are also given in part 3.4.1 of chapter 3

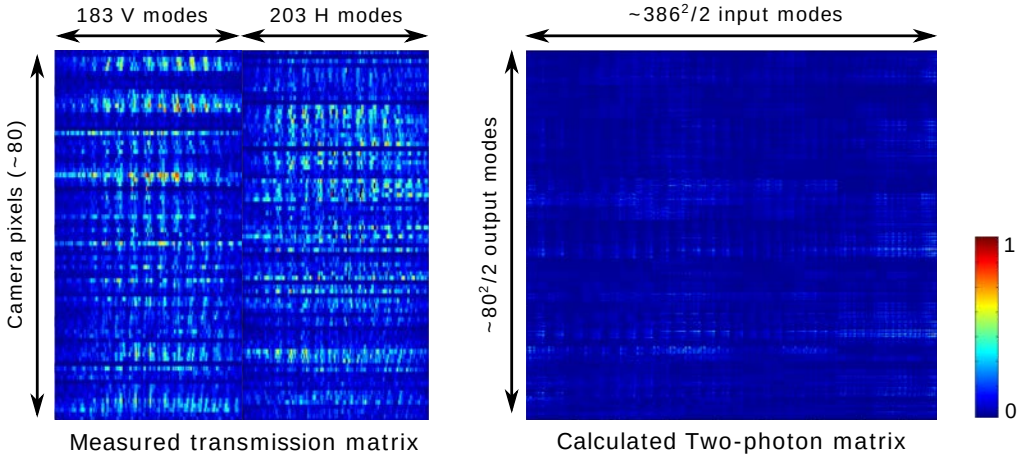

Figure 5.5: **Measured transmission matrix and calculated two-photon matrix** TM measured between $N = 386$ ($N_V = 183$ and $N_H = 203$) input modes and 80 camera pixels. Its associated two-photon matrix has a size of approximately $80^2/2 \times 386^2/2$.

In this part, we estimate the proportion of errors introduced in the TTM by these experimental effects and also provide solutions to correct them accordingly:

Partial indistinguishability The degree of indistinguishability of the photons can be precisely estimated by performing an Hong-Ou-Mandel experiment [11] on the source. In our experiment, the indistinguishably of photon-pairs is about 86%(see Appendix A). The maximum relative error introduced by the partial indistinguishability of the photons can then be estimated to be about $\sqrt{14} \approx 4\%$.
To take into account these experimental variations, we can use the theoretical approach described in part 4.2.2 of chapter 4. This approach allows correcting any two-photon speckle predicted by the calculated TTM by considering the degree of indistinguishability of the photons.

Two-photon reference speckle pattern The proportion of photons reflected by the reference part of each SLM (SLM H and SLM V) creates a reference two photon speckle pattern at the output. In our experiment, the proportion of light contained in each reference part is about 25%. In consequence, the two-photon reference speckle pattern represents a mean contribution of about 10% to the total coincidence speckle intensity.
The measurements performed on the classical reference speckles (intensities and relative phase) during the TM measurement process (described in part 2.2.4 of chapter 2) can be used to calculate the two-photon reference speckle pattern. Once the two-photon reference speckle pattern is known, we can correct in principle all the predictions given by the calculated TTM.

Experimental noise introduced in the TM Most of the errors existing in the TTM are due to experimental noise originally introduced in the TM during the measurement process. In particular, the holographic measurements performed to reconstruct the output fields associated to each input mode are very sensitive to intensity fluctuations. Noise is then introduced both in the phase and amplitude components of the matrix. To quantify this noise, we compare some speckles measured directly with the camera to the speckles predicted by a reconstructed TM. We find correlations oscillating between 85% and 90%. These error are then doubled in the TTM because we have to consider coincidence detections.
One possibility proposed to reduce the amount of noise introduced in the TM measurement would be to use more than 4 phases during the phase-stepping holographic processes or use more advanced calibration techniques such as off axis holography or phase retrieval [217, 218].

A good way to evaluate the impact of these corrections and noises would be to compare some predictions of the calculated TTM with real two-photon speckle measurements. However, as we have seen in the previous section, measurements of two-photon speckle pattern are very inaccurate because of the very weak intensity of the photon-pairs source. In consequence, it is for the moment not possible to study the impact of these corrections, but we believe that the method consisting in calculating the TTM from the measured TM is much faster, convenient and precise than the direct two-photon reconstruction technique. In particular, we can use the knowledge of the measured TM and the calculated TTM to control photon-pairs propagation through the MMF.

5.3 Controlling photon-pairs propagation through a MMF

The light propagation control method proposed in [80] and presented in chapter 2 has been theoretically extended to the control of photon-pairs in chapter 4. The SLMs can now be programmed to shape the input photon-pairs to obtain a specific photons distribution at the output. In this experiment, we exploit the measured TM and the calculated TTM to focus photon-pairs in an arbitrary two-photon output mode of the system.

In the first part of this section (5.3.1), we adapt the analytical approach developed in part 4.7 of chapter 4 to control photon-pairs propagation in our experimental configuration. We demonstrate that this method can be used to deterministically focus photon-pairs into a specific output mode of the MMF.
In the second part (5.3.2), this approach is slightly modified to characterize the contribution of quantum and classical interferences to the focusing process. We show in particular that wavefront shaping methods enable the deterministic control of quantum interferences occurring in the MMF.

5.3.1 Focusing photon-pairs using the analytical approach

In this particular experiment, the TM of the MMF has been measured using $N_H = 180$ modes and $N_V = 190$ modes. During the measurement process, the PMSMFs F1 and F2 are positioned at two output spatial modes denoted for simplicity $|X\rangle$ and $|Y\rangle$. Following the analytical approach described in part 4.7 of chapter 4, we use the knowledge of matrices T_H and T_V to determine the SLM pattern that optimize coincidences between these two output modes. However, before using this approach, we need to ensure that all these hypotheses are valid.

Validation of the hypotheses

The hypothesis 1 introduced in part 4.4.1 of chapter 4 stipulates that the coefficients of the TM are the realizations of independent complex variables. While this assumption is generally well-verified when working with a layer of paint due to the complexity of the scattering process [80, 215], a MMF has not the same structure and therefore not the same matrix properties. As it has been recently studied in detail by M.Ploschner and coworkers [147], MMFs are not really unpredictable complex systems: apart from the cases where the MMF is strongly bended or twisted, the TM of a MMF is not a random matrix [5]. Because the MMF used in our experiment has similar properties than the one studied in [147], we can not really consider that the hypothesis 1 is valid in our system.

Nevertheless, if we look more precisely at the role played by hypothesis 1 in the analytical approach presented in chapter 4, we observe that this hypothesis is sufficient but not necessary. By following the calculations performed in part 4.4.1 of chapter 4, we see that this hypothesis is first used to decompose $T_V \times T_V^+$ or $T_H \times T_H^+$ under the general form:

$$T \times T^+ \propto \mathbb{1} + \mu H \tag{5.3.1}$$

with $\mu = 1/\sqrt{N}$. Then, this result allows neglecting the term proportional to $1/N$ compared to the term in $1/\sqrt{N}$ in equation 4.7.27 of part 4.7.3 using the fact that $N \gg 1$. In fact, the condition $\mu \ll 1$ would be enough to simplify the calculations in the same way and we do not need to ensure the strong condition $\mu = 1/\sqrt{N}$.
The condition $\mu \ll 1$ can be verified in practice by calculating the products $T_V \times T_V^+$ or $T_H \times T_H^+$ and comparing amplitudes of the diagonal coefficients to those of off-diagonal coefficients.

The products $T_H \times T_H^+$ and $T_V \times T_V^+$ are represented on Figure 5.6a. We observe that the diagonal coefficients are much stronger than the off-diagonal coefficients, which ensures the possibility to use our analytical approach. We estimate the average values of μ for each product of about 10 for T_H and 20 for T_V. The product $T^{(2)} \times T^{(2)+}$ is also calculated on Figure 5.6b. and contains strong diagonal values as it is expected from theory (part 4.4.3 of chapter 4).

5. More information of the mixing process in a MMFs can be found at part 3.4.1 of chapter 3.

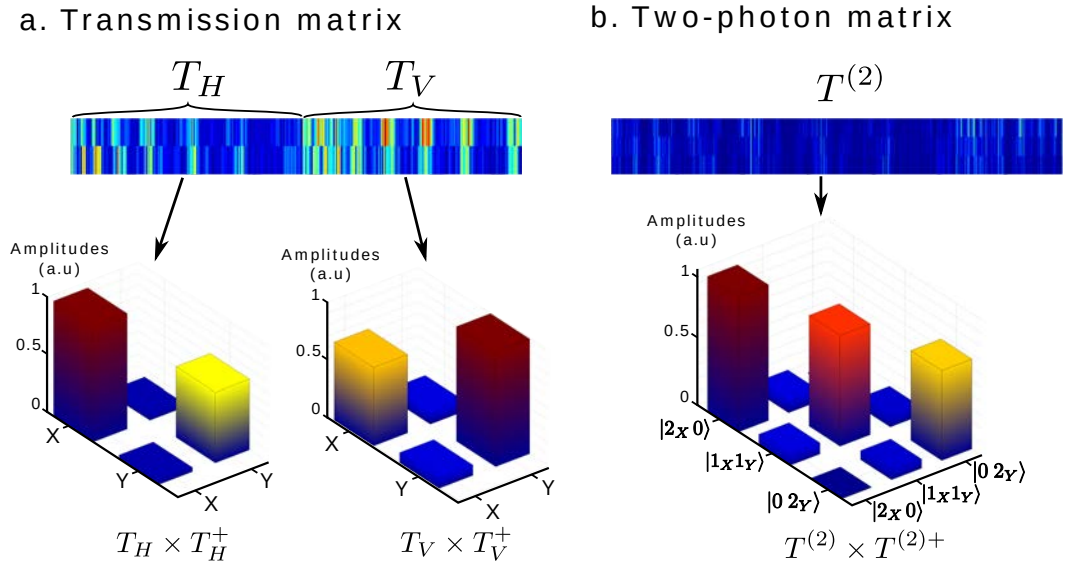

Figure 5.6: **TM and TTM matricial products**. **(a).** The 2×370 transmission matrix is composed of the two submatrices T_H (2×180) and T_V (2×190). The product $T_H \times T_H^+$ ($T_V \times T_V^+$) shows diagonal coefficients larger than off-diagonal coefficients with an average ratio of 9.6 (22). **(b).** The two-photon transmission matrix calculated from the TM has a size of 3×68635. As expected theoretically, the $T^{(2)} \times T^{(2)+}$ shows also strong diagonal values (average ratio of 16).

Analytical solution

We consider that the values of μ are low enough to use the analytical approach. Using the step-by-step practical method proposed in part 4.7.4 of chapter 2, we find the angular parameters:

$$\phi = \phi' = 0 \tag{5.3.2}$$
$$\theta = \theta' = 1.55 \approx \pi/2 \tag{5.3.3}$$

Using the notations of 4.7.3, an experimental state optimizing the coincidence rate in our experiment takes the simple form:

$$|\Psi_{\text{exp}}(\pi/2, \pi/2, 0, 0)\rangle = \hat{f}_Y^{V+} \hat{f}_X^{H+} |0\rangle \tag{5.3.4}$$

This experimental input state represents the simple case where each photon of the pair is focused into a different targeted mode.

In our experimental configuration, the TM has been measured in the *Fourier* basis at the input. A basis change matrix denoted $P_{\boldsymbol{k}\to\mathcal{C}}$ is then used to express the focusing state into the X-Y *canonical* basis:

$$P_{\boldsymbol{k}\to\mathcal{C}} \times |\Psi_{\text{exp}}\rangle = |\Psi_{\text{exp}}\rangle_C \tag{5.3.5}$$

The phase pattern associated to $|\Psi_{\text{exp}}\rangle_C$ is finally calculated and can be directly programmed on the SLM.

Experimental results

At this step of the experiment, the photon-pairs source has taken the place of the classical source, the relative path delay δ is reduced to zero and $|\Psi_{\text{exp}}\rangle_C$ is programmed on the SLM. Intensity of 25 two-photon modes is reconstructed at the output by measuring coincidences between 5×5 positions selected by fibers F1 and F2. Each mode is acquired during 900s.

The focusing configuration associated to equation 5.3.4 is represented on Figure 5.7.a: the SLM directs photon H in output mode $|X\rangle$ and independently photon V in output mode $|Y\rangle$. The camera images (Figure 5.7.b) show localization of the foci at the two targeted positions. The coincidence pattern (Figure 5.7.c.1) now exhibits a pronounced spike of coincidences between these two modes: we have optimized the state $\hat{a}^+_{|X\rangle}\hat{a}^+_{|Y\rangle}|0\rangle$ at the output. The strong enhancement ratio measured (about 150 times higher than the background) confirms the success of the focusing process.
Since each photon is directed independently to a different output, we do not observe significant changes in the coincidences rate when the relative path delay δ becomes larger (Figure 5.7c1.c2). This result demonstrates that quantum interferences do not contribute to the focusing process.

Even if it is not the case here, the analytical approach could also lead to configurations where $\theta \neq \pi/2$. In these cases, quantum interferences can participate in the focusing process.
In the next part of this experiment, we decide to arbitrary set the angular parameter θ to the value $\pi/4$. We will see that the coincidence rate of the targeted mode remains enhanced but it is less intense than in the previous case. However, this different focusing configuration allows us to study and control the quantum interferences that contribute to the focusing process.

5.3.2 Deterministic manipulation of the quantum interferences

The angular parameter θ is now set to the value $\theta = \pi/4$. Using the notations of 4.7.3, the corresponding experimental state takes the form:

$$|\Psi_{\text{exp}}(\phi, \phi')\rangle = \frac{1}{2}\left(\hat{f}_X^{V+} + e^{i\phi}\hat{f}_Y^{V+}\right)\left(\hat{f}_X^{H+} + e^{i\phi}\hat{f}_Y^{H+}\right)|0\rangle \tag{5.3.6}$$

Similarly to the approach described in the previous section, we shape the input field by first performing the change of basis $|\Psi_{\text{exp}}(\phi, \phi')\rangle \mapsto |\Psi_{\text{exp}}(\phi, \phi')\rangle_C$ and then programming the phase component of $|\Psi_{\text{exp}}(\phi, \phi')\rangle_C$ on the SLM. The parameters ϕ and ϕ' involved in equation 5.3.6 will be set to certain values that will be specified in the following parts.

In this part, we demonstrate that quantum interferences strongly contribute to the

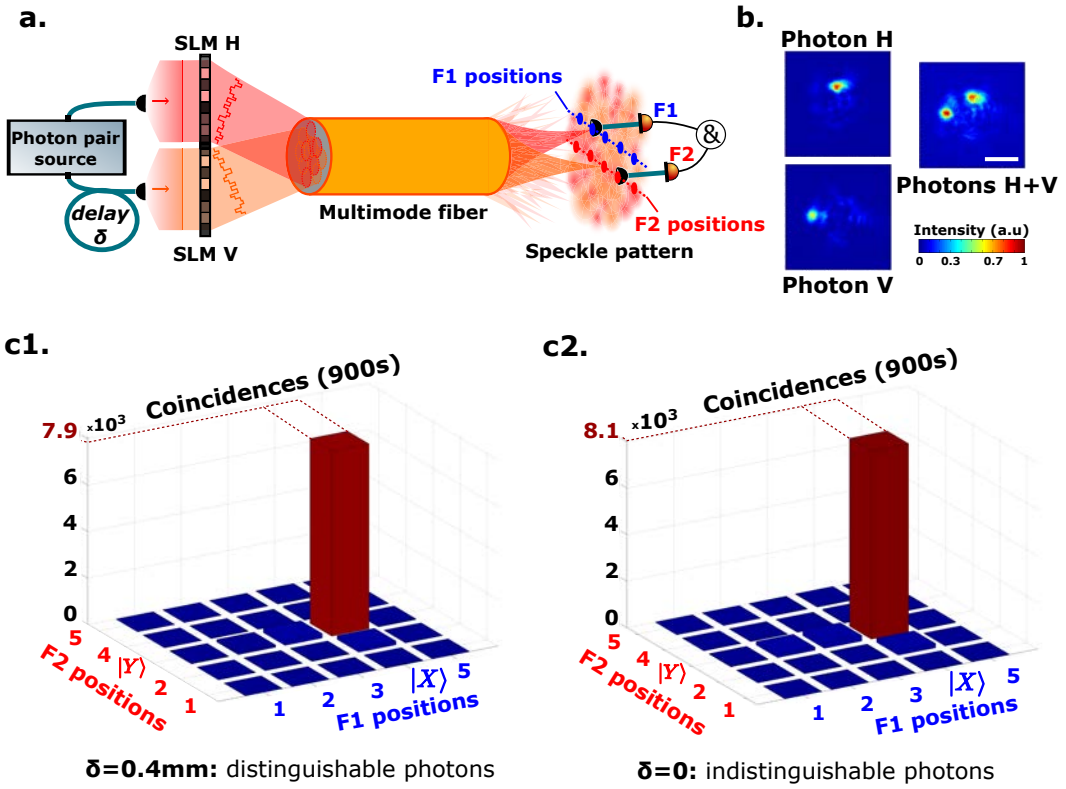

Figure 5.7: **Focusing photon-pairs using the analytical approach** The focusing configuration **(a.)** directs photon H to output mode $|X\rangle$ of F1 and photon V to output mode $|Y\rangle$ of F2. This is shown on the direct images measured using the EMCCD camera **(b.)**. Coincidence speckle patterns **(c.)** are measured for 25 coincidence output modes. Coincidence rate in the targeted two-photon mode $\hat{a}^+_{|X\rangle}\hat{a}^+_{|Y\rangle}|0\rangle$ is about 150 times higher than the background, for both distinguishable and indistinguishable photons. Data are acquired for 900s with a coincidence window of 2.5ns. The scale bar represents $25\mu m$ in the output plane of the multimode fiber.

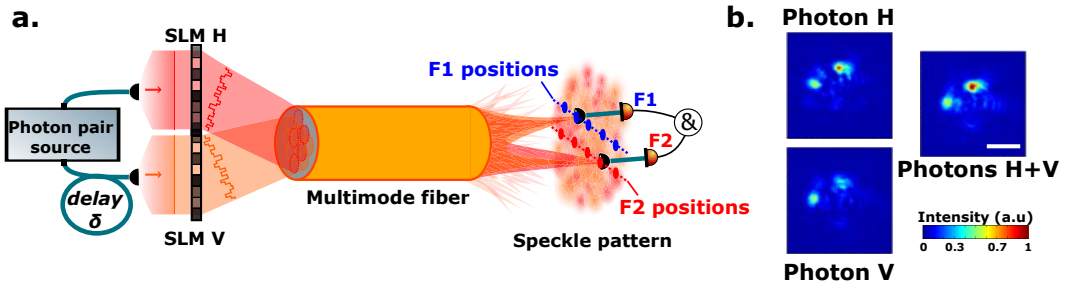

Figure 5.8: **Two photons focused onto a superposition of two output modes (a.)** The experimental configuration corresponds to a photon reflected by SLM H being sent in a superposition of output modes $|X\rangle$ and $|Y\rangle$ with a relative phase ϕ and a photon reflected by SLM V being directed to a superposition of the same output modes with a relative phase ϕ'. **(b.)** Direct images measured with the EMCCD confirm that both photons are directed to the two output modes .

coincidence intensity of the targeted mode when θ is set to $\pi/4$, but also that the settings of ϕ and ϕ' play an important role in the focusing process.

Constructive and destructive quantum interference effects

When θ is fixed to $\pi/4$, each photon is now delivered onto a superposition of two output modes: SLM H is programmed to direct photon H in a superposition of output modes $|X\rangle$ and $|Y\rangle$, and SLM V is also programmed to direct photon V in a superposition of the same output modes. The corresponding experimental configuration is displayed on Figure 5.8a. The speckle images acquired with the camera (Figure 5.8b) confirm that each photon is delocalized on the two targeted modes.

In this experiment, we first set the angular parameters ϕ and ϕ' to the values $(\phi, \phi') = (0, 0)$. Figure 5.9a shows the resulting coincidence patterns.
The strong coincidence rates visible on Figure 5.9.a1 and a2 confirm that we still focus the photon-pairs in the targeted output state. However, the enhancement is much higher when the delay δ is reduced to zero: this is due to a constructive contribution of quantum interference to the focusing process (Figure 5.9.a2). On the contrary, if δ is set to 0.4mm, photons are distinguishable and the optimized coincidence rate is lower (Figure 5.9.a1). If we analyze more precisely the result of Figure 5.9.a2, we find that the coincidence rate in the indistinguishable case is just 24% lower that the result obtained by using the analytical approach presented on Figure 5.7.c2. This means that constructive quantum interference effects almost compensate the loss of coincidence due to the distribution of the photon intensities between two modes.
Phase parameters are then set to $(\phi, \phi') = (0, \pi)$. As drawn on Figure 5.9b1, the optimized intensity measured in the distinguishable case ($\delta = 0.4$mm) is very similar to the one observed in the previous case. However, the coincidence rate is now decreased by 76% when the relative path delay is reduced to zero (indistinguishable photons). In this case, quantum interferences are destructive and the coincidence focusing effect

is lost.

These results demonstrate that quantum interference can also strongly contribute to the focusing process. In particular, ϕ and ϕ' are very important parameters to address this contribution. In the next part, we demonstrate that a complete control over these parameters allows deterministic manipulation of quantum interference occurring in the MMF.

Deterministic control of quantum interference

As demonstrated previously, some specific phase settings can make quantum interference either constructive or destructive. These settings have important consequence on the resulting coincidence rates. More generally, we demonstrate here that these quantum interference effects can be manipulated deterministically by using a larger set of parameters ϕ and ϕ'.
In this section, we investigate quantitatively the role played by quantum interferences (constructive or destructive) by calculating non-classical contrast values (equation 5.1.1) of the targeted output mode for different settings ϕ and ϕ'.

Complete control over quantum interference between the two photons is presented in Figure 5.10.a. In this experiment, non-classical contrast measurements are performed in the optimized output mode $\hat{a}^+_{|X\rangle}\hat{a}^+_{|Y\rangle}|0\rangle$ for 64 different relative phases settings (ϕ, ϕ'). Photon-pairs interfere constructively, leading to a photon bunching effect, when $\phi = \phi'$, and destructively when $\phi = \phi' \pm \pi$. Contrasts values vary between a maximum of 0.81 and a minimum of -0.76 [6].
To better view the quantum interferences effect, we also measure three HOM-like plots (Figure 5.10.b) for three specific phase settings $(\phi, \phi') \in \{(0,0), (0,\pi), (0,\pi/2)\}$ by scanning the path length difference δ between -0.4mm and 0.4mm. These plots display respectively a peak with a contrast of $+0.74$(green), a dip with a contrast of -0.76 (red), and flat line with a contrast of 0.06 (blue).
In this experiment, we demonstrate the possibility to deterministically control the contribution of quantum interference to the focusing process. This indeed demonstrates the capacity of our system to distribute both photons into two arbitrary output states of the system with a complete control over the coupling parameters, including phase.

The scattering matrix approach, initially developed to manipulate classical interference effects, has been extended in this work to the control of quantum interferences. This deterministic manipulation offers a complete control over the coupling parameters between the different targeted modes. In particular, any output two-photon state can be prepared in a well-controlled superposition of the two targeted output modes.

6. Statistical analysis of the data are given in Appendix D

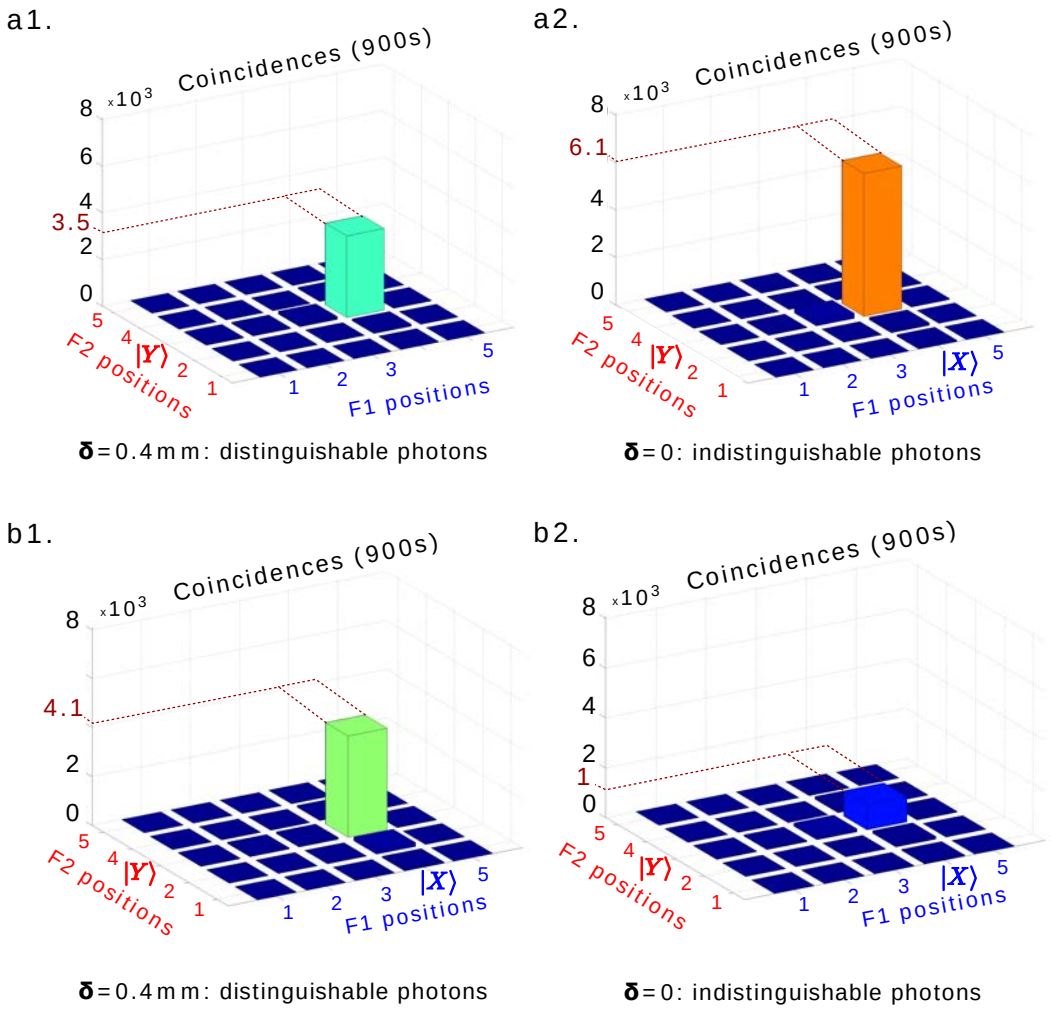

Figure 5.9: **Destructive and constructive quantum interferences (a1.)** and **(a2.)** When the phase are set to $\phi = \phi' = 0$, quantum interference enhance the intensity of the two photon state $\hat{a}^+_{|X\rangle}\hat{a}^+_{|Y\rangle}|0\rangle$ when the relative path delay is reduced to zero. Photons quantum interfere constructively. **(b1.)** and **(b2.)**:If phase parameters are set to $(\phi, \phi') = (0, \pi)$, quantum interferences become destructive and the focusing effect is lost when $\delta = 0$. Data are acquired for 900s with a coincidence window of 2.5ns. The scale bar represents $25\mu m$ in the output plane of the multimode fiber.

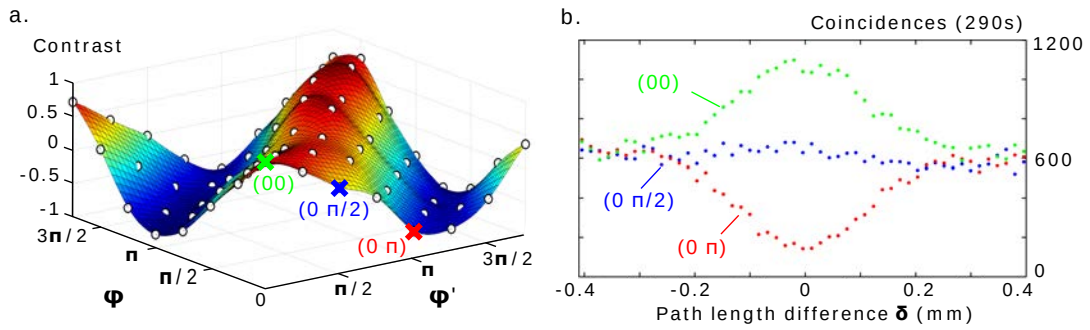

Figure 5.10: **Deterministic control of quantum interferences (a)** Contrast values measured with $8 \times 8 = 64$ phase settings. A non-classical interference contrast is defined as $C = (R(\delta = 0) - R(\delta = 0.4mm))/R(\delta = 0.4mm)$ where $R(\delta)$ is the coincidence rate of the targeted two-photon output mode $\hat{a}^+_{|X\rangle}\hat{a}^+_{|Y\rangle}|0\rangle$ when the path length difference is set to δ. Regions with positive contrast values are associated to constructive quantum interference effects and negative regions to destructive interference effects. **(b)** HOM-like plots reconstructed for three phase settings $(\alpha) : (\phi = 0, \phi' = 0)$, $(\beta) : (\phi = 0, \phi' = \pi/2)$ and $(\gamma) : (\phi = 0, \phi' = \pi)$, as a function of the path length difference between input photons δ. Contrast values of $+0.74$ (green dots), 0.06 (blue dots) and -0.76 (red dots) can easily be measured on the curves. Data are acquired for 290s with a coincidence window of 2.5ns.

5.4 Conclusion

On the one hand, these results show the strong potential of using MMF as a multimode optical platform to implement quantum walk of photons. Low losses, stability and scalability of this device hold promises for realization of quantum walks in regimes where classical verification becomes challenging [83]. We demonstrate the possibility to characterize photon-pairs propagation through this system by measuring its TTM. On the other hand, this matrix can then be combined with wavefront shaping methods to focus deterministically indistinguishable photon-pairs in an arbitrary set of selected output coincidence modes. These results show that this system can be turned into a programmable multimode optical network [125, 124], establishing multimode fibers as a high-dimensional and reconfigurable platform for multi-photon quantum walks.
In particular, we believe that the concept of the TTM, introduced for the first time in this work, bridges a gap between the two communities of quantum optics and complex media and paves the way for the development of new applications and fundamental studies in quantum information processing.

General conclusion

If electrons were at the heart of some of the greatest discoveries of the 20^{th} century, photons could play a major role in the scientific community in the 21^{th} century [219]. Light is not only an ideal medium to transmit information, but also a very interesting physical system to process it [17]. In this respect, quantum optics has recently emerged as a higly promising domain for the development of new applications that can surpass the performances of currently available systems [83]. Compare to other quantum systems using atoms or ions [220, 221], light has the strong advantage to deal with photons, which are particles that do not interact between them and exhibit quantum features at room temperature [222]. However, one important step that need to be achieved before replacing all the electronic devices with integrated optical systems, consist in making the manipulation of light at the nanoscale easier.
The study of light propagation in disordered systems has led the development of new methods [122, 80] to manipulate light propagation in a complex regime. These investigations have also contributed to improve light manipulation techniques, but not at the same scale and with the same aims than the works dedicated directly to information processing. In particular, most of these studies simply consider disordered media as obstacles to light propagation. For example, scattering in biological tissues limits the capabilities of light-based imaging techniques, some techniques are thus developed to overcome these effects and recover images of the structures [223]. However, only few teams have considered the strong potential of exploiting directly the mixing properties of these systems [224, 188]. In our work, we do not consider a complex system as an obstacle for light propagation, but on the contrary as a new optical platform to mix light in a very complex way at the nanoscale. Combined with quantum optics, these systems are very promising for quantum information processing.

In the work reported in this thesis, we have focused our attention on a specific class of computational model: the *photonic quantum walks* [61]. Using a combination of experimental techniques coming from the domains of quantum optics and complex media, we have investigated a novel solution to implement multi-photon quantum walks by using disordered systems as highly multimode optical platforms. Our study was conducted by performing two experiments demonstrating the possibility to implement and control single-photons and two-photon quantum walks in layers of paint and multimode fibers (MMFs).
First, we have studied the propagation of single-photons through a static scattering medium, here a layer of white paint (chapter 3). This experiment has demonstrated

that this medium can be used as a multimode optical platform to implement single-photon quantum walks. Moreover, we have proven that wavefront shaping methods - originally developed to control classical light propagation - can also be extended to the manipulation of single-photons.
In the second part of this work, we have demonstrated the possibility to implement a two-photon quantum walk in a MMF (chapter 5). We have proven that photon-pairs propagation can also be manipulated using a method derived from classical wavefront shaping methods. In particular, we have introduced the new concept of two-photon transmission matrix (TTM) which really bridges a gap between the two communities of quantum optics and complex media (chapter 4). Figure 5.11 gives a pictorial representation of the two-photon matrix.

We believe that this study represents a first step towards the realization of reconfigurable highly multimode optical network and paves the way for the next generation of quantum information processing photonic devices.

The long-term perspectives of our work have been frequently discussed throughout this manuscript. To conclude, we would like to discuss some short-term potential directions that we would like to follow in our future investigations:

Towards a more efficient control of the photons In light of some recent studies about light propagation in MMFs [147, 206], we believe that it is possible to substantially improve our light propagation control method in the MMF. This would enable a better control of the output state and would open for instance the possibility to focus efficiently on more than two modes.

Towards a more efficient characterization of the output state On the detection side, we are convinced that photonic lanterns [225, 226] could improve our system by offering simple and efficient interfacing of the MMF with a larger array of detectors. Another possibility would be the use of the EMCCD camera to directly detect spatial coincidences [227, 228, 229].

Towards more complex quantum states The complexity of a quantum walk and the performance of the algorithms based on it strongly rely on the number of photons propagating in the system. For instance, in the particular case of the boson sampling problem, it has been estimated in [83] that this problem would become intractable for classical computers if more than 20 photons are injected in about 400 modes. Generating more photons would then naturally enhance the relevance of our investigations. In addition, it has been demonstrated that entanglement is also an interesting property that can influence the photons propagation in a multimode system [110, 66, 112]. Our multimode systems could for instance be combined with high-dimentional entangled quantum sources [230, 231, 232].

Towards multi-dimentional quantum walks The use of broadband non-classical sources combined with recently developed spatio-temporal wavefront shaping techniques [157, 99, 203] could also provide additional temporal degrees of freedom to the

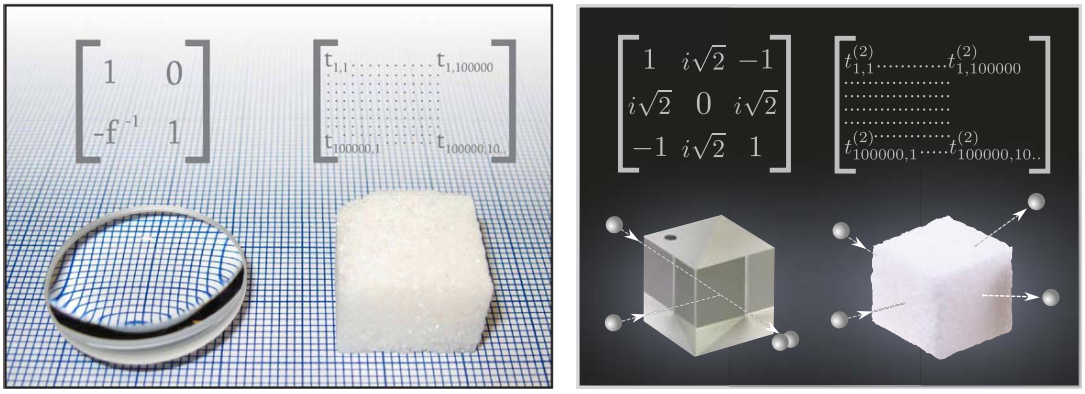

Figure 5.11: **Scattering matrix and two-photon scattering matrix of some photonic systems**. The image on the left displays the form of the scattering matrix for a simple converging lens and a cube of sugar (taken from [24]). These scattering matrices describe the propagation of light by taking into account all classical interference effects occurring in the medium. By using the same type of representation, the image on the right shows the two-photon matrix of a balanced beam-splitter. This matrix contains in particular a null element in the center that represents a destructive quantum interference effect which can be observed by performing an Hong-Ou-Mandel experiment [11]. The two-photon transmission matrix of a cube of sugar is also represented. These matrices describe the propagation of photon-pairs through the system by taking into account both classical and quantum interference effects.

walkers. The dimension of the walk can also be increased by measuring both polarization modes of the photons at the output [233]. In this respect, MMFs are very convenient optical platforms because their characteristics can be selected very precisely. This feature allows adapting them perfectly to the chosen control method and to the properties of the photons [147].

Appendix A

This appendix provides some additional information to chapter 1, chapter 4 and chapter 5.

A.1 Photon-pair source

The photon-pair source implemented in this thesis is detailed on Figure A.1.a. This source exploits a type-II Spontaneous Parametric Down Convertion (SPDC) process to produce pairs of frequency-degenerated photons [38, 39, 40, 41, 42].
The pump is a 25 mW continuous-wave laser diode at 405 nm central wavelength from Coherent (Model: Compass 405-25). The pump field is vertically polarized and focused into a $10 \times 1 \times 1\, mm^3$ periodically poled potassium titanyl phosphate (PPKTP) crystal placed in a oven to stabilize its temperature. The non-linear crystal and the oven are provided by Raicol Crystal. The focusing spot waist has been chosen about $20\,\mu m$ to optimize the generation process following the results reported in [41]. Because the spectral properties of the laser diode have deteriorated over time, we have implemented an external cavity in a Lithrow configuration to purify the pump spectrum [234].
This process produces crossed polarized photon-pairs by type II SPDC centered at 810nm in a direction collinear to the pump. The blue photons crossing the crystal are filtered out using a low-pass filter (LPF). Infrared photon pairs are then separated using a polarizing beam-splitter (PBS) and injected into two different polarization maintaining single mode fibers (PMSMFs) using microscope objectives (MO). The lens L2 and the MOs are chosen to collect photons generated in a volume characterized by a waist of $20\,\mu m$ to maximize the collection efficiency [41]. A translation stage positioned on one of the two arms allows adjusting the relative path delay δ between the photons.
Both photons are also filtered at the output of the crystal using a 1nm narrow band-pass filter (BPF) centered at 810nm with a minimum transmission of 55% (provided by Andover corporation), yielding a coincidence rate of up to 6×10^4 counts/s.

Photodetections are performed using 4 avalanche photodiodes (APDs) provided by Perkin Elmer with a detection efficiency of about 50% at 800nm and a dark count rate is about 400 counts/s (counting module SPCM-AQ4C-IO provided by Excelitas). The APDs are connected to a field -programmable gate array (FPGA) system to measure

coincidences within a time window of 2.5ns. The program used to drive the FPGA card was provided by J.Spring and the Ultrafast Quantum Optics and Optical Metrology group from Oxford University.

Indistinguishability of the photon-pairs is estimated by performing a Hong-Ou-Mandel (HOM) experiment [11]. Coincidences are measured at the output of a fibered beam-spliter (BS) while the relative path delay is scanned between -0.4mm and 0.4mm. The HOM-dip recorded on Figure A.1.b shows a quantum interference visibility of 86%. This visibility value is the criteria used to characterize the maximum indistinguishability degree of the photons-pairs.

A.2 Stability curves of a layer of paint and a multimode fiber

Stability of complex system can be characterized by measuring the decorrelation of speckle images under a constant illumination.
In this procedure, the system is illuminated with monochromatic light kept fixed during the whole experiment. A speckle pattern is recorded at the output with a camera. By correlating the images taken at time $t = 0$ and time t, we can follow the changes in conformations of the medium due to vibrations and temperature fluctuations. This method characterizes in the same time some other experimental instabilities, such as the spectral drift of the laser or the general stability of the optical setup.
Stability curves of a white paint layer and a multimode fiber (MMF) under are presented on Figure A.2. We observe that the MMF is much more stable than the layer of paint in our laboratory conditions.

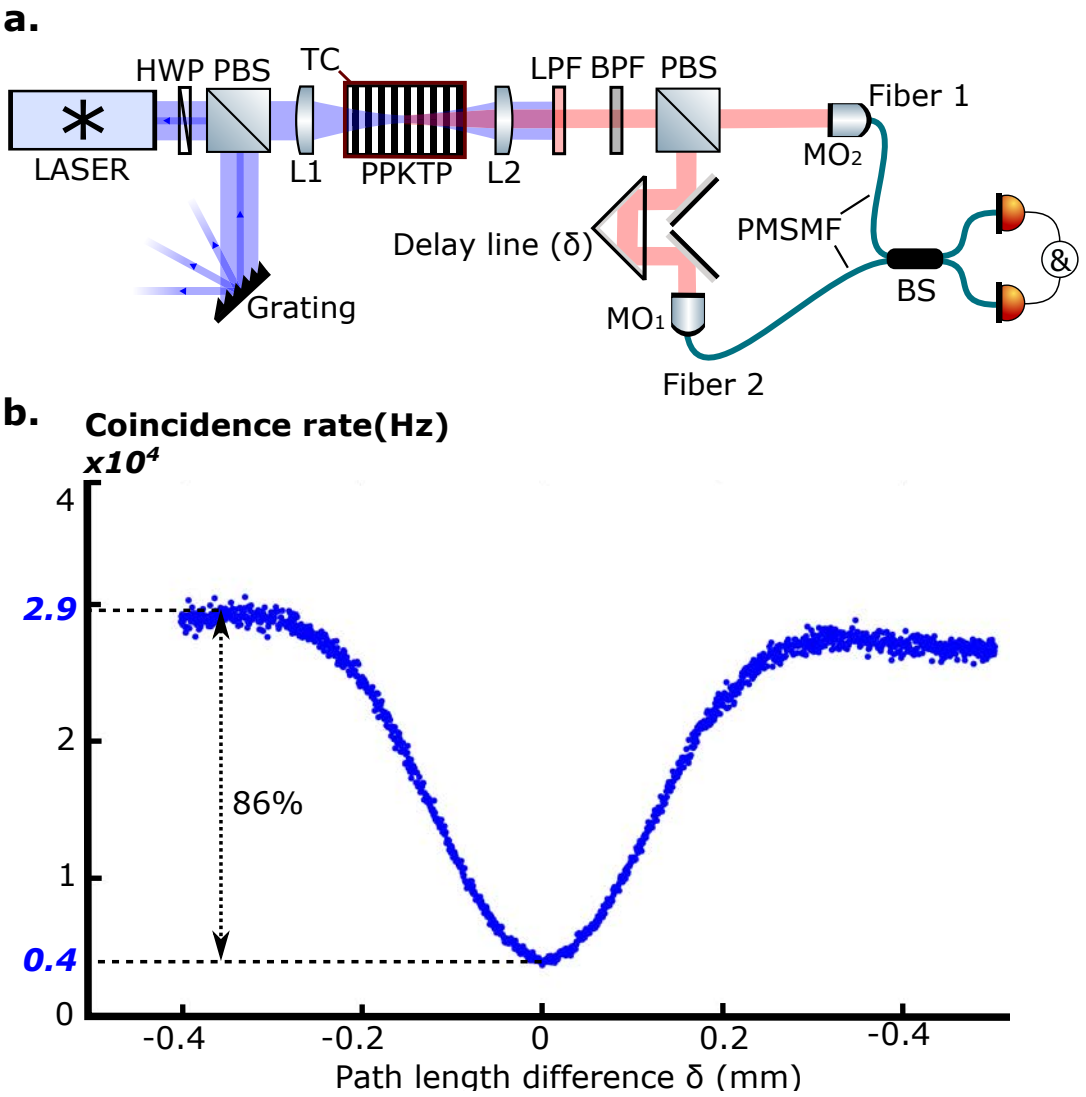

Figure A.1: **Characterization of the photon-pairs indistinguishability by Hong-Ou-Mandel (HOM) experiment. (a.)** Optical setup to generate photon-pairs and measure their indistinguishability degree. A 10 mm PPKTP crystal pumped with a 25 mW continuous-wave laser diode at 405 nm produces pairs of photons by a type-II Spontaneous Parametric Down Conversion (SPDC) process. Both photons are filtered using a 1nm bandpass filter centered at 810 nm (BPF) yielding a coincidence rate up to 6×10^4 counts/s and a coupling ratio around 9%. After separating them using a polarizing beam splitter (PBS), they are injected in a balanced beam splitter (BS). **(b.)** Hong-Ou-Mandel (HOM) plot showing a dip in the coincidences recorded by monitoring the path length difference δ between the photons. The visibility measured is about 86%.

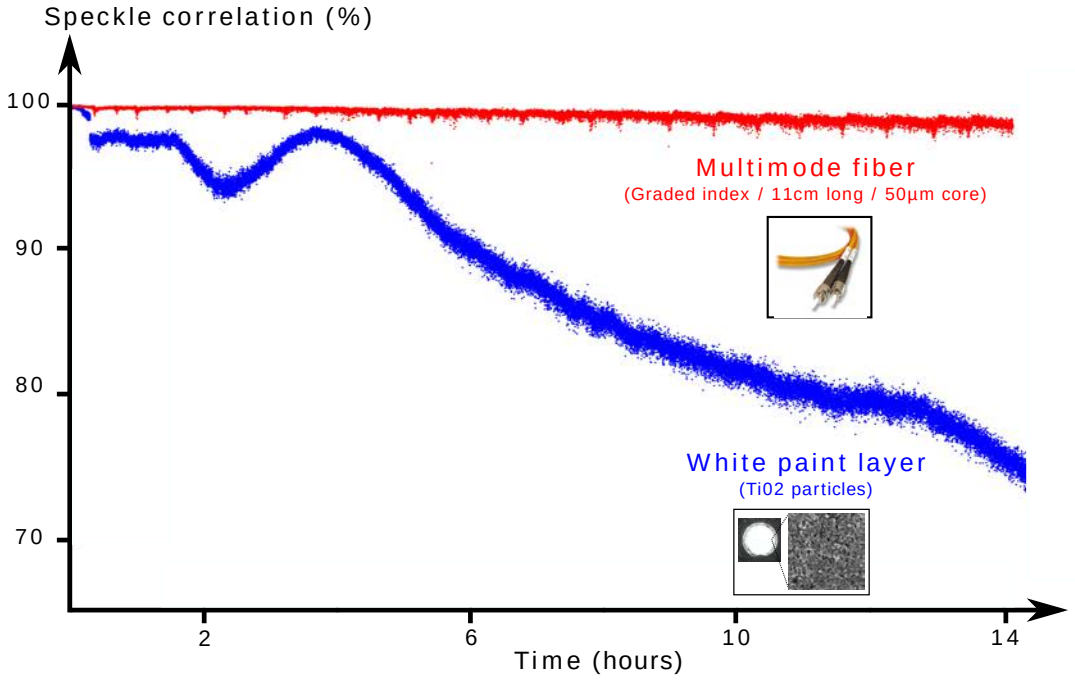

Figure A.2: **Stability curves of a white paint layer and a multimode fiber**. Time evolution curves of the stability of an optical system comprising a white paint layer (blue) and a multimode fiber (red) by measuring speckle decorrelation. The white paint layer is a thick layer of white paint composed of TiO_2 particles. The multimode fiber is a 11cm long graded index fiber with a $50\mu m$ core diameter. In both acquisitions, the correlation value at t is obtained by calculating the image correlation between a reference speckle image taken at $t = 0$ and the speckle image captured at t.

Appendix B

This appendix provides additional information to chapter 2.

B.1 Technical constraints of the SLM

Three other technical constraints introduced by the SLM need to be taken into account in the experiments performed in this thesis. These additional limitations are listed bellow:

1. After a command on the computer, the liquid crystal cells of the SLM take about 0.15s to rearrange and change the phase components of the field. This imposes that a waiting time of 0.15s has to be respected between two acquisitions if the SLM pattern changes.
2. The specific arrangement of the liquid crystals contained in SLM pixel is set by a local electric field. This technology makes use of oscillating electric fields rather than constant electric field to increase the precision and the reproducibility of the phase control. These fields oscillate at 120 Hz. In consequence, acquisition times of the detection devices (APD or CCD camera) have to be set larger than $1/120 \approx 10$ms to average over many field oscillations. In experiments conducted in this thesis, we use a minimum acquisition time of 0.05s to average over approximately 50 cycles.
3. The SLM can only shape the vertically polarized component of the field. In consequence, polarization of the incoming beam has to be vertical before to be reflected and shaped by the SLM.

B.2 Calibration of the *Fourier* basis

As presented on Figure 2.6 of chapter 2, each SLM pattern of the *Fourier* basis generates a focused spot on the input face of the MMF. Its position on the surface of the fiber is characterized by parameters r and α.
The present calibration allow determining a radius step denoted Δr, an angular step denoted $\Delta\alpha(r)$ and a maximal radius denoted r_m. These parameters will enable to select a subset of independent input modes within all the accessible (r,α) combinations.

Δr and $\Delta\alpha(r)$ define minimal steps separating two independent input mode and r_m defines the upper limit for r.

r_m calibration The maximal radius r_m is a value of r that generates a focused spot outside of the MMF aperture. In this situation, only the light reflected by the reference part of the SLM remains injected.
r_m can be determined experimentally. For this purpose, we measure speckle patterns at the output of the MMF while the focusing spot in scanned along the radial direction (increasing the value of r) with $\alpha = 0$.
We first calculate image correlations between a speckle created by a input spot positioned at r and a reference speckle taken at $r = 0$. The corresponding plot is represented in blue on Figure B.1.a.
We also determine the total transmitted intensity for each speckle pattern measured. The corresponding plot is represented in red on FigureB.1.a.
We observe that the intensity plot (red) shows a strong extinction when the r parameter is set larger than approximately $25\,\mu m$, which corresponds to the radius of the fiber. The remaining intensity corresponds to the speckle pattern created by the reference part of the SLM. This reference speckle pattern is created by light reflected by a flat reference part of the SLM (surrounding the control part) and is then injected through the middle ($r = 0$, $\alpha = 0$) of the MMF aperture. In consequence, the speckle generated by the control zone set to ($r = 0$, $\alpha = 0$) and the reference speckle pattern are very similar. This similarity explains why the correlation value (blue) comes back to a value close to one when r reaches the limit of the MMF aperture ($|r| > 25\,\mu m$). Using these calibration plots, we determined $r_m \approx 30\,\mu m$.

Δr and $\Delta\alpha(r)$ calibration In the second step of the calibration process, we determine the values of Δr and $\Delta\alpha(r)$. These quantities represent respectively minima radius and angular steps that discriminate two independant input modes. They can be characterized experimentally:

- Δr is directly estimated from the correlation curve presented on Figure B.1.a by taking the value of the radius when the correlation reaches 0.5.
- $\Delta\alpha(r_k)$ is estimated by measuring speckle correlation when α is scanned from $-\pi/2$ to $\pi/2$ for all possible radii $r_k = k \times \Delta r < r_m$. Figure B.1.b. shows examples of angular correlation curves measured for three values of $r = \{6, 12, 21\}\,\mu m$.

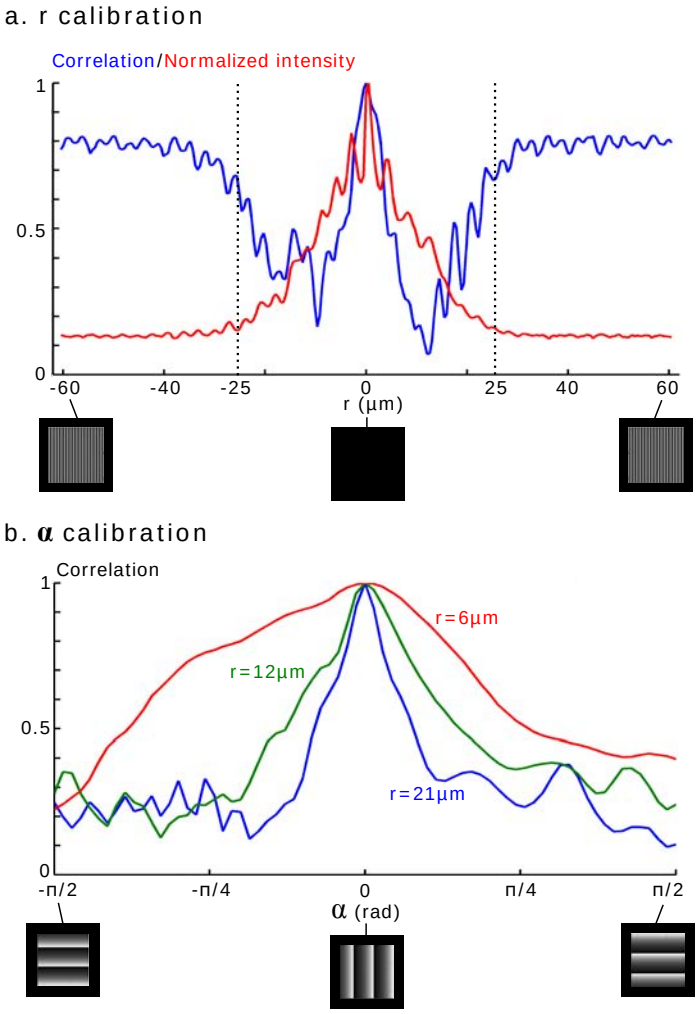

Figure B.1: **Calibration of the *Fourier* basis**. **(a.)** Normalized total transmitted intensity (red) and speckle correlation (blue) plots after light propagation through a $50\,\mu m$ core diameter graded index MMF when r is scanned between $-60\,\mu m$ and $-60\,\mu m$ and $\alpha = 0$. Vertical dashed line at $25\,\mu m$ define the radius of the MMF aperture. The correlation curve (blue) goes back to a value close to one when r reaches the border of the MMF because the reference speckle pattern and speckle pattern generated by the control part at $r = 0$ are very similar. Values of $r_m \approx 30\,\mu m$ and $\Delta r \approx 6\,\mu m$ are determined from these plots. SLM patterns that correspond to some specific values of r are displayed bellow the figure. **(b.)** Speckle correlation plot when α is scanned from $-\pi/2$ to $\pi/2$ with three different radius values $r = 6\,\mu m$ (red), $r = 12\,\mu m$ (green) and $r = 21\,\mu m$ (blue). $\Delta\alpha(r_k)$ are estimated from the tree curves as the angular value when correlation equals 0.5. SLM patterns that correspond to some specific values of α for $r = 6\,\mu m$ are displayed bellow the figure.

Appendix C

This appendix provides additional information to chapter 3.

C.1 Reduced density matrix and concurrence measurement

At the end of chapter 3, we use a method based on partial quantum state tomography to detect single-photon entanglement. We first reconstruct a reduced density matrix that corresponds to a projection of the full density matrix into a subspace with not more than one photon by mode. The presence of entanglement is then inferred from an entanglement measure computed using some elements of this matrix [175, 176, 235].

In our experiment, a single-photon is focused into two targeted modes A and B simultaneously with a controlled relative phase ϕ. These modes are selected using single mode fibers (SMFs) which filter out different spatial modes. These SMFs are connected to APDs and we then consider that all detector clicks arise only from modes A and B. We also assume that our system does not contain more than two photons populating the modes A and B in total. The density matrix $\hat{\rho}$ takes the general form:

$$\hat{\rho} = \sum_{i,j,i'j' \leq 2} P_{iji'j'} |ij\rangle\langle i'j'| \tag{C.1.1}$$

where $|ij\rangle$ is a state representing $i \leq 2$ photon in mode A and $j \leq 2$ in mode B and $P_{iji'j'}$ is a coefficient of $\hat{\rho}$ associated to $|ij\rangle\langle i'j'|$.
We also assume that all off-diagonal elements of the matrix between states with different numbers of photons vanish. This assumption is discussed in the supplementary document of [175]. The resulting density matrix is simplified to:

$$\hat{\rho} = \begin{bmatrix} P_{00} & 0 & 0 & 0 & 0 & 0 \\ 0 & P_{01} & d & 0 & 0 & 0 \\ 0 & d^* & P_{10} & 0 & 0 & 0 \\ 0 & 0 & 0 & P_{11} & e & f \\ 0 & 0 & 0 & e^* & P_{02} & g \\ 0 & 0 & 0 & f^* & g^* & P_{20} \end{bmatrix} \tag{C.1.2}$$

In this study, we are only interested in a subpart of $\hat{\rho}$ that constitutes the reduced density matrix $\hat{\rho}_r$:

$$\hat{\rho}_r = \begin{bmatrix} P_{00} & 0 & 0 & 0 \\ 0 & P_{01} & d & 0 \\ 0 & d^* & P_{10} & 0 \\ 0 & 0 & 0 & P_{11} \end{bmatrix} \tag{C.1.3}$$

This reduced matrix contains enough information to estimate a lower bound of the concurrence and then demonstrate that the single-photon state is entangled. We now explain with more details how to measure the elements of the reduced density matrix.

C.1.1 Measurements of the elements of $\hat{\rho}_r$

In this section, we explain how to measure the elements of $\hat{\rho}_r$. For this purpose, we first introduce some notations that will be useful in the future calculations and then describe the links between the elements of the matrix and the measurements that we can perform on our system.

Measurement operators

We assume that there are only two possible outcomes of a photodetection measurement performed by an APD: no click or a certain nonzero number of clicks. A photodector measuring photons in mode A performs then a positive operator valued measure (POVM) of the form:

$$\hat{\Pi}_0^A = \sum_{n\geq 0} (-1)^n \frac{\hat{a}_A^{+n} \hat{a}_A^n}{n!} \tag{C.1.4}$$

$$\hat{\Pi}_1^A = \mathbb{1} - \hat{\Pi}_0 \tag{C.1.5}$$

where $\hat{a}_A$ is an annihilation operator in mode A.
A coincidence measurement performed between A and B is represented by the operator:

$$\hat{\Pi}_{kk'}^{AB} = \hat{\Pi}_k^A \otimes \hat{\Pi}_{k'}^B \tag{C.1.6}$$

where $k \in \{0,1\}$ ($k' \in \{0,1\}$).
To simplify the future calculations, we highlight three important relationships between these operators:

$$\hat{\Pi}_{10}^{AB} = \hat{\Pi}_1^A \otimes \mathbb{1}^B - \hat{\Pi}_1^A \otimes \hat{\Pi}_1^B \tag{C.1.7}$$

$$\hat{\Pi}_{01}^{AB} = \mathbb{1}^A \otimes \hat{\Pi}_1^B - \hat{\Pi}_1^A \otimes \hat{\Pi}_1^B \tag{C.1.8}$$

$$\hat{\Pi}_{00}^{AB} = \mathbb{1}^A \otimes \mathbb{1}^B - \hat{\Pi}_{01}^{AB} - \hat{\Pi}_{10}^{AB} - \hat{\Pi}_{11}^{AB} \tag{C.1.9}$$

Experimental measurements

Because we use an heralded single-photon source our system (chapter 3), three APDs are involved in the measurement processes: two APDs are used to detect photons in modes A and B and a third APD denoted T detects the other photon generated by the source used as a trigger. These APDs do not estimate directly the probability values but only return a number of clicks within a certain time window (2.5ns with our system).
In our system, we assume that the maximum number of single-photons that can be detected after the medium is given by the number of click returned by the trigger detector T. We then define the probability to measure a photon at the output of the medium for instance in mode A as the number of photon measured in coincidence with T (denoted N_{AT}) divided by the total number of photons measured by T (denoted N_T). As a consequence, we are only able to perform three types of operations with our experimental setup:

$$\mathrm{Tr}(\hat{\rho}\hat{\Pi}_1^A \otimes \mathbb{1}^B) = \frac{N_{AT}}{N_T} \tag{C.1.10}$$

$$\mathrm{Tr}(\hat{\rho}\mathbb{1}^A \otimes \hat{\Pi}_1^B) = \frac{N_{BT}}{N_T} \tag{C.1.11}$$

$$\mathrm{Tr}(\hat{\rho}\hat{\Pi}_1^A \otimes \hat{\Pi}_1^B) = \frac{N_{ABT}}{N_T} \tag{C.1.12}$$

where N_{XY} is the number of coincidences between the detectors X and Y, N_{XYZ} the number of triple coincidences between X, Y and Z, and N_T the number of single clicks detected by T during a certain time.

Diagonal elements Diagonal elements of $\hat{\rho}_r$ are P_{00},P_{01} and P_{10}. P_{00} can be calculated by making the measurement $\hat{\Pi}_{00}^{AB}$:

$$\begin{aligned} P_{00} &= \mathrm{Tr}(\hat{\rho}\hat{\Pi}_{00}^{AB}) \\ &= \mathrm{Tr}(\mathbb{1}^A \otimes \mathbb{1}^B - \hat{\Pi}_{01}^{AB} - \hat{\Pi}_{10}^{AB} - \hat{\Pi}_{11}^{AB}) \\ &= \frac{N_T - N_{AT} - N_{BT} + N_{ABT}}{N_T} \end{aligned} \tag{C.1.13}$$

This expression has been simplified using the results of equations C.1.9.
The measurements $\hat{\Pi}_{01}^{AB}$ and $\hat{\Pi}_{10}^{AB}$ performed on $\hat{\rho}$ lead to:

$$\begin{aligned} \mathrm{Tr}(\hat{\rho}\hat{\Pi}_{10}^{AB}) &= \mathrm{Tr}(\hat{\Pi}_1^A \otimes \mathbb{1}^B - \hat{\Pi}_1^A \otimes \hat{\Pi}_1^B) \\ P_{10} + P_{20} &= \frac{N_{AT} - N_{ABT}}{N_T} \end{aligned} \tag{C.1.14}$$

and

$$\begin{aligned} \mathrm{Tr}(\hat{\rho}\hat{\Pi}_{01}^{AB}) &= \mathrm{Tr}(\mathbb{1}^A \otimes \hat{\Pi}_1^B - \hat{\Pi}_1^A \otimes \hat{\Pi}_1^B) \\ P_{01} + P_{02} &= \frac{N_{BT} - N_{ABT}}{N_T} \end{aligned} \tag{C.1.15}$$

In our experiment, we can safely assume that $P_{10} \gg P_{20}$ and $P_{01} \gg P_{02}$. In this case, the previous expressions can be simplifies in:

$$P_{10} \approx \frac{N_{AT} - N_{ABT}}{N_T} \tag{C.1.16}$$

$$P_{01} \approx \frac{N_{BT} - N_{ABT}}{N_T} \tag{C.1.17}$$

$$\tag{C.1.18}$$

Off-diagonal elements The off-diagonal element d is measured by interfering the two modes A and B on a balanced beam-splitter (BS). The corresponding transformation rules for the photonic operators are:

$$\hat{a}_A^+ \rightarrow \frac{1}{\sqrt{2}}(\hat{a}_{A'}^+ + \hat{a}_{B'}^+)e^{i\phi} \tag{C.1.19}$$

$$\hat{a}_B^+ \rightarrow \frac{1}{\sqrt{2}}(\hat{a}_{A'}^+ + \hat{a}_{B'}^+) \tag{C.1.20}$$

where A' and B' denote the two outputs of the BS and ϕ the relative phase between the two input modes A and B. The density matrix $\hat{\rho}$ is transformed into the matrix $\hat{\rho}'$.
We define the quantity V_ϕ as:

$$V_\phi = \frac{|\mathrm{Tr}\left(\hat{\rho}(\hat{\Pi}_1^A \otimes \mathbb{1}^B - \mathbb{1}^B \otimes \hat{\Pi}_1^B)\right)|}{\mathrm{Tr}\left(\hat{\rho}(\hat{\Pi}_1^A \otimes \mathbb{1}^B + \mathbb{1}^B \otimes \hat{\Pi}_1^B)\right)} \tag{C.1.21}$$

The maximum value of V_ϕ denoted V_m defines the visibility (or the contrast) of the interference phenomenon. It can be estimated experimentally using the formula $V_m = |M - m|/(M + m)$ where M is the maximum value and m the minimum value of $N_{A'T}/N_T$ and $N_{B'T}/N_T$ when the relative phase ϕ is driven between 0 and 2π.
Because the probability of having two photons in the scattering medium is very weak in our experiment, we can use the following approximations: $P_{02}, P_{20}, |e|, |f|, |g| \ll P_{11} \ll P_{01}, P_{10}$ (supplementary document of [175]). We can then express V_ϕ as a function of the elements of $\hat{\rho}$:

$$V_\phi \approx \frac{2|d|\sin(\phi + \phi_0)}{P_{01} + P_{10}} \tag{C.1.22}$$

where $\phi_0 = \arg(d)$. Amplitude of the off-diagonal element $|d|$ takes then the form:

$$|d| \approx \frac{P_{01} + P_{10}}{2} V_m \tag{C.1.23}$$

$|d|$ is therefore estimated from the values of P_{01} and P_{10} (previous paragraph) and from the value of the interference visibility V_m that can be experimentally measured by connecting both outputs on a BS and changing the relative phase over 2π radians.

C.1.2 Concurrence measurement

The level of entanglement in the measured state has a lower bound given by the concurrence [175, 176, 235]. The concurrence denoted C is a monotonic measure of bipartite entanglement that is zero for any separable state and positive for entangled state. Value of C is estimated from elements of the reduced density matrix through the equation:

$$C = \max(2|d| - 2\sqrt{P_{00}P_{11}}, 0) \tag{C.1.24}$$

This formula provides a strict lower bound to the entanglement.

C.2 Statistical data analysis of data presented in Chapter 3

As detailed in the previous section, the number of triple coincidences events between A, B and T allow calculating the value of P_{11}. However, in the experiment conducted in part 3.3.3 of chapter 3, these events are very rare and the value N_{ABT} remains very low compare to the total number of events N_T. As shown in equation C.1.24, the value of the concurrence is strongly sensitive to the number of triple events measured during a given acquisition time. To determine our confidence in concluding that the concurrence is positive, we analyze the relevance of our data using a Bayesian approach [236, 237, 238, 239].
Rare events can be modeled by a Poissonian distribution. The probability of an observation X is then simply given by:

$$P_\mu(X|\mu) = \frac{\mu^X e^{-\mu}}{X!} \tag{C.2.1}$$

where μ is the parameter (variance and mean value) of the Poissonian distribution. In our experiment, while P_{11} is very difficult to evaluate because of the small number of N_{ABT}, the values of P_{00} and d can be estimated with a good precision. These values are then injected into equation C.1.24 to estimate N^0_{ABT}. N^0_{ABT} is the minimum number of triple events required to set the concurrence to a negative value. Then, by considering the real number of triple coincidences measured N_{ABT}, we can estimate the likelihood that this number of events has been generated from a statistical process following a Poissonian distribution of parameter N^0_{ABT}. This likelihood gives the level of confidence that the concurrence measured is positive.
The results presented in part 3.3.3 of chapter 3 have been acquired during 1 hour. The maximum value allowed in order that the concurrence is positive is calculated to be $N^0_{ABT} = 11$ and we have registered $N_{ABT} = 1$. Therefore we have found confidence level of 99% that the measured concurrence is positive. Using equation C.1.24, the value of the concurrence equals $C = 4.6 \times 10^5$. As presented on Figure 3.5 of chapter3, we also determined the error bars associated to the quantities $P_{00}, P_{01}, P_{10}, d, V$ by calculating their standard deviations.

Appendix D

This appendix provides additional information to chapter 5.

D.1 Spectral dispersion in a MMF

When polychromatic light propagates in optical waveguides, spectral dispersion influences the temporal evolution and has three primary origins: chromatic dispersion, group velocity dispersion and modal dispersion. Working with a multimode fibre (MMF), modal dispersion is the main contributing source of dispersion [240]. It describes the phenomenon in which the different modes supported in a MMF experience different delays along the propagation because of the different paths that they follow. This type of dispersion leads to the broadening of the initial temporal profile of the input light. While we do not control the temporal degree of freedom in this experiment [157, 99], characteristics of the MMF have been chosen to have negligible spectral dispersion considering the 1 nm bandwidth of the photons.
In the experiment described in part 5.2 of chapter 5, we use a graded-index MMF with a core diameter of $50\,\mu m$ and a total length of 11 cm. The fiber dispersion can be characterized using the setup in Figure D.1.a. The photon-pair source is replaced by a superluminescent diode (SLED) filtered using the same 1 nm bandpass filter. Part of the light entering the MMF after refection on SLM H creates an output speckle (Speckle A) that can interfere with the speckle created by the part of the light reflected by SLM V (Speckle B). Interference appears only if the path length difference δ between the two parts is close to $\delta = 0$. By choosing an output position (speckle grain) where both speckles have the same intensity, interference fringes recorded on Figure D.1.b using the 11 cm long MMF shows a contrast value close to unity, indicating that the fiber dispersion is then negligible. As a comparative example, dispersion is clearly visible with a 3nm bandpass filter on Figure D.1.c showing an interference pattern recorded using the 1 m long graded index MMF with a core diameter of $62.5\,\mu m$. This pattern has a contrast value of 65%, far from unity, corresponding to significant temporal distortion.

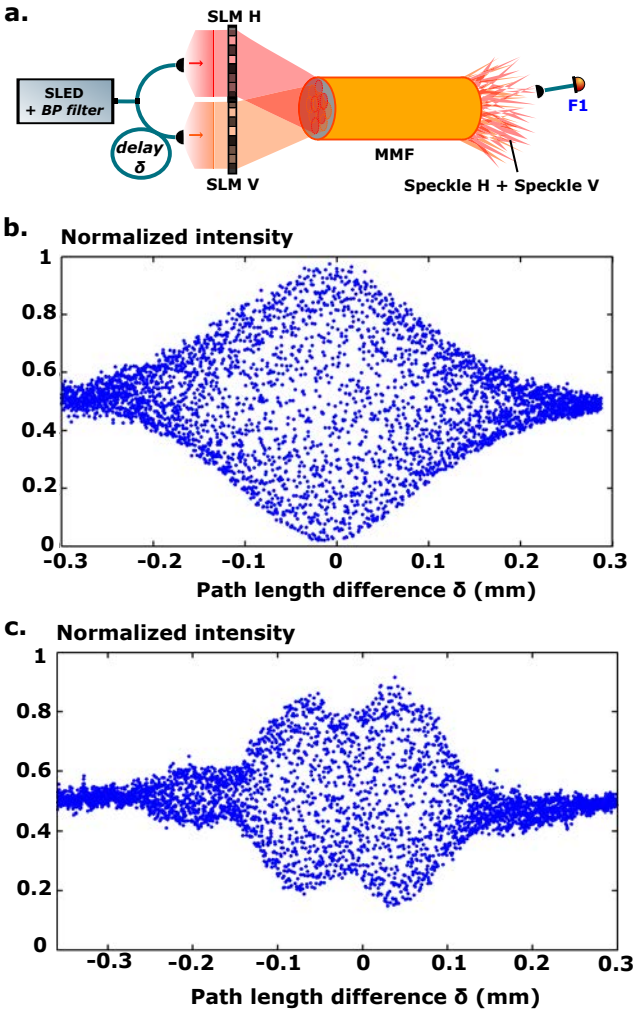

Figure D.1: **Dispersion characterization through the MMF. (a.)** represents the experimental configuration used to characterize the dispersion in the MMF. Light coming from the SLED is filtered out and split in two parts. Each part is injected into the MMF using SLM H or SLM V. Combination of the two corresponding speckles created after propagation in the MMF are measured at a specific output position using fiber F1 and interference fringes are recorded by monitoring the path length difference δ. Interferences pattern measured with a 11cm long graded-index MMF with a core diameter of $50\mu m$ **(b.)** and a SLED filtered with a 1nm bandpass filter permits to extract a contrast value about 95%. Temporal dispersion is then negligible. As a comparative example, interferences fringes recorded using a 1m long graded-index MMF with a core diameter of $62.5\mu m$ **(c.)** and a SLED filtered with a 3nm bandpass presents a strong temporal distortion and a contrast reduced to 65%.

D.2 Method to find the zero delay optical path difference

To observe quantum interferences with photon-pairs in the MMF, we need to reduce the relative optical path delay δ between photons to zero. In practice, this consists in finding the position of the translation stage (visible on Figure 5.4 of chapter 5) that corresponds to a relative optical path delay equal to 0 for the photons.

Calibrating of the optical path delay for the SLED is easily performed using the experimental configuration presented on Figure D.1.a. We observe interferences fringes by moving the translation stage between the two inputs and determines directly the position where the contrast is maximum (Figure D.1.b). This position is denoted L_{SLED}.
However, the position of the translation stage that cancels the optical path delay is slightly different when using photon-pairs. This difference denoted Δ is due to the birefringence of the crystal. Because photon-pairs are generated in the center of the crystal with different polarizations (see Appendix A for more details), they have to propagate through its half and then exit with a certain relative path delay denoted Δ. On the contrary, we observe on Figure 5.4 of chapter 5 that the classical source does not propagate through the crystal. The delay Δ_{dis} is then is not taken into account when observing classical interference effect.

The relative path delay Δ_{dis} is determined in two steps. First, we directly inject the photons of the pair into a beam-splitter. By performing an Hong-Ou-Mandel experiment, we measure the position of the translation stage that corresponds to a relative optical path delay reduced to zero (dip of the HOM). The position is denoted L_{HOM}. Second, we replace the photon-pair source by the SLED using the optical setup presented on Figure 5.4 of chapter 5. By driving the relative path delay using the translation stage, we observe interference fringes and determine the position of the translation stage where the interference contrast is maximum. This position is denoted L_{cla}. Then, the delay Δ_{dis} is estimated by subtracting these two position values: $\Delta_{dis} = L_{HOM} - L_{cla}$.

Finally, we estimate the position of the translation stage that corresponds to a relative optical path delay reduced to zero for photon-pairs (denoted L_{QS}) by compensating the value of L_{SLED}:

$$L_{QS} = L_{SLED} + \Delta \tag{D.2.1}$$

Note that L_{QS} could also be estimated experimentally by scanning the translation stage when measuring coincidences at the output of the MMF. However, this experiment would require very long acquisitions times due to the very weak intensity of the source. It is then more convenient to use classical light to directly calibrate the position of the translation stage.

D.3 Statistical data analysis of data presented in Chapter 5

Measurements realized in our study require long acquisition time and therefore long-term stability of the system. Due to temperature fluctuations and mechanical vibrations, conformation of the MMF evolves with time and the speckle pattern changes. Stability of the MMF is monitored during the measurement process by correlating the output speckle pattern at regular time intervals. In all results presented here, a lower limit for the correlation of 85% has been observed.
We conduct a statistical analysis of our data to assess the error on the measured contrast [241, 242]. Poisson statistics (mean value and standard deviation denoted respectively μ and σ) is an appropriate model for our counting experiment. Considering the high number of measurements $N_m = 90$, this distribution can be approximated by a Gaussian. The estimators associated with μ and σ are respectively denoted $\bar{\mu}$ and $\bar{\sigma}$. Experimental values divided by the number of measurements N_m represent a direct estimation of μ. The standard deviation of this estimator, which corresponds to its 85% confidence interval, is given by:

$$\sigma_{\bar{\mu}} = \frac{\bar{\sigma}}{N_m} \tag{D.3.1}$$

$\bar{\sigma}$ is calculated from experimental data as $\bar{\sigma}^2 = 1/N \sum_{i=1}^{N} (X_i - \bar{\mu})^2$ where X_i is the number of coincidences measured during the i^{th} measurement. Data presented in the manuscript have been analyzed with this statistical tool.

Coincidence matrices of Figure 5.2.c and d Figure D.2 represents the relative standard deviations associated with measurements of Figure 5.2c and d of chapter 5. While a limited number of coincidence measurements present a high uncertainty value, due to their low intensity, the average error values for matrices measured with distinguishable and indistinguishable photons are below 10%.

Contrast matrix of Figure 5.3 Figure D.3 represents the standard deviations associated with measurements of Figure 5.3 of chapter 5. The average standard deviation on the non-classical contrast matrix is about ± 0.22. Data acquired are then sufficiently relevant to conclude that non-classical interference occurs in the MMF during photon propagation.

Focusing processes of Figure 5.7 c1 and c2 and Figure 5.9 Table D.1 represents data analysis of the experimental values relative to the targeted focusing state represented in Fig.3. In particular, non-classical contrasts associated with each focusing configuration (respectively 0.017, 0.72 and -0.75) show small errors (respectively ± 0.035, ± 0.07 and ± 0.1). The role played by non-classical interference in the focusing process is clear.

Associated Figures	Data type	Measurement value	Standard deviations
Focusing processes of Figure 5.7 c1 and c2	Coincidences with distinguishable photons in 900s (Figure 5.7.c1)	7949	2.1%
	Coincidences with indistinguishable photons in 900s (Figure 5.7.c2)	8088	1.3%
	Non-classical contrast	0.017	± 0.035
Focusing processes of Figure 5.9 a1 and a2	Coincidences with distinguishable photons in 900s (Figure 5.9.a1)	3491	2.3%
	Coincidences with indistinguishable photons in 900s (Figure 5.9.a2)	6038	1.8 %
	Non-classical contrast	0.73	± 0.07
Focusing processes of Figure 5.9 b1 and b2	Coincidences with distinguishable photons in 900s (Figure 5.9.b1)	4135	1.9%
	Coincidences with indistinguishable photons in 900s (Figure 5.9.b2)	1029	3.8 %
	Non-classical contrast	-0.75	± 0.1

Table D.1: **Statistical analysis of experimental data presented on Figure 5.7 c1 and c2 and on Figure 5.9.** Coincidences and non-classical contrast relative to the targeted output focusing mode show a very good confidence in the results. In particular, non-classical contrasts associated to each focusing configuration (respectively 0.017, 0.72 and -0.75) present very small relative errors (respectively ± 0.035, ± 0.07 and ± 0.1).

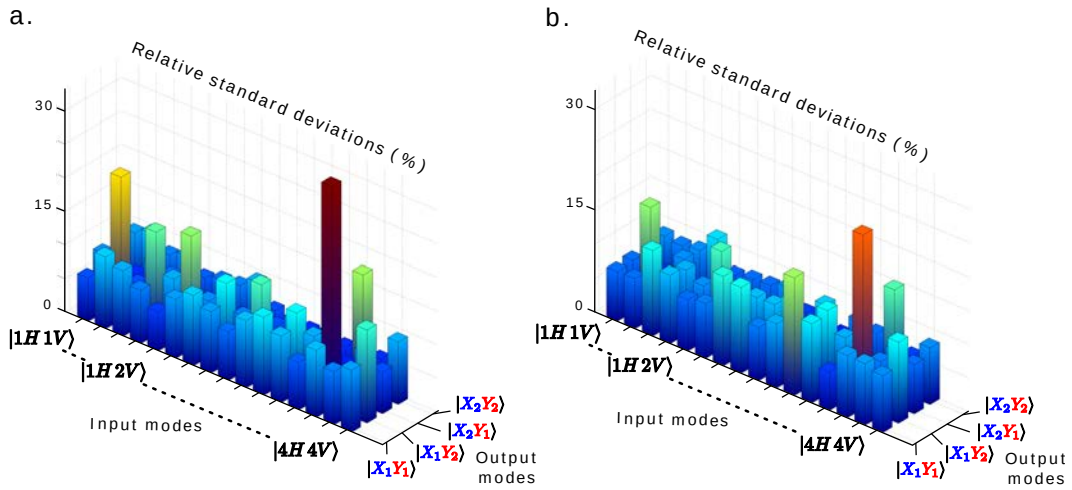

Figure D.2: **Standard deviations associated to data represented on Figure 5.2. (a.)** Relative standard deviation associated to the matrix values measured with distinguishable photons. The average error value over the matrix is equal to 8.8%. **(b.)** Relative standard deviation associated to the matrix values measured with indistinguishable photons. The average error value over the matrix is equal to 8.9%.

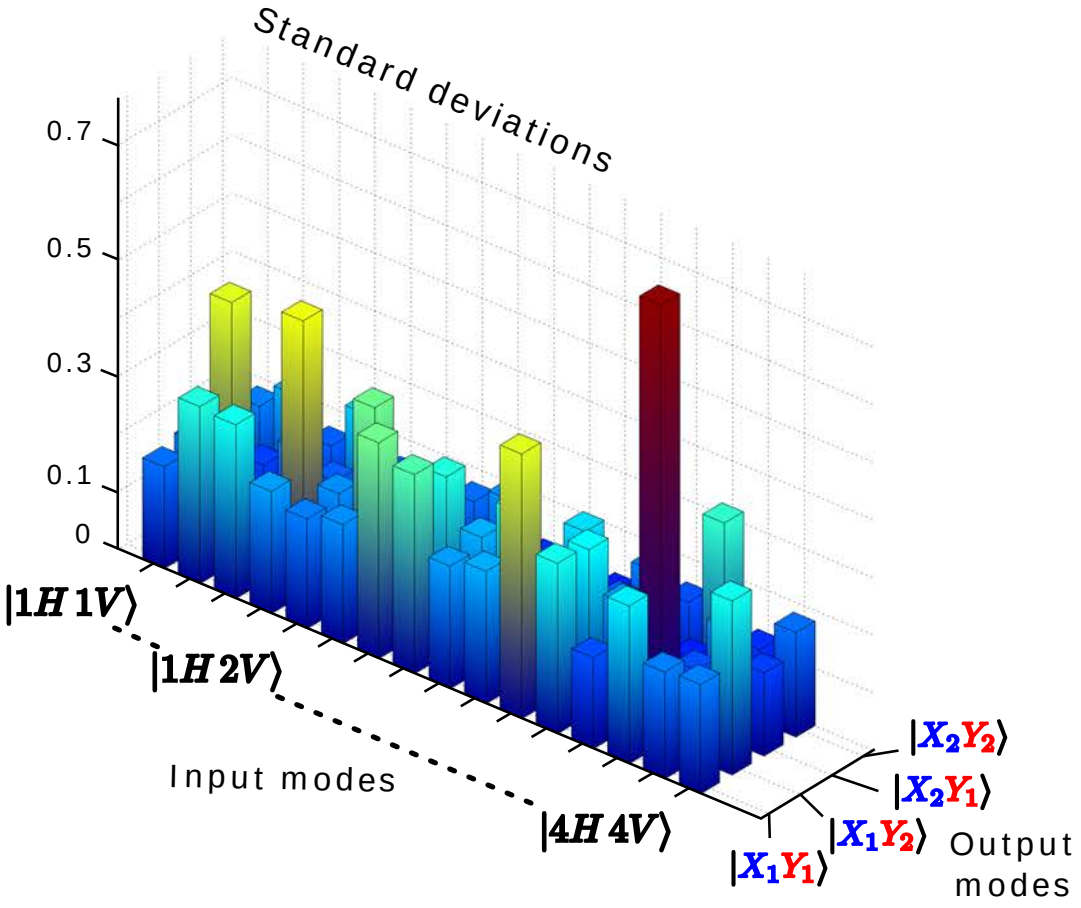

Figure D.3: **Standard deviations associated to data represented on Figure 5.2 of chapter 5.** Standard deviations associated to the non-classical contrast matrix. The average error value over the matrix is about 0.22.

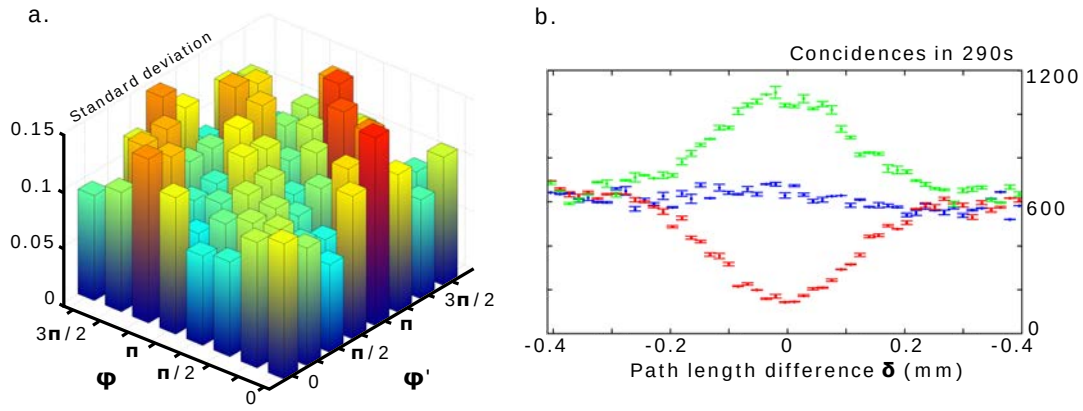

Figure D.4: **Statistical analysis of experimental data presented on Figure 5.10.** **(a)** Standard deviation of contrast matrix measured with $8 \times 8 = 64$ phase settings (Figure 5.10.a). **(b)** Contrast values and corresponding error bars for three phase settings as a function of the path length difference between input photons δ (Figure 5.10.b).

Control of quantum interferences presented on Figure 5.10 Statistical data analysis of Figure 5.10 is represented in Figure D.4. The average error on the contrast matrix reconstructed with 8×8 different phase settings (Figure D.4.a) is around ± 0.11. Error values registered on the scans realized with three different phase settings (Figure D.4.b) are below 5%.

Bibliography

[1] M. Born and E. Wolf, *Principles of optics: electromagnetic theory of propagation, interference and diffraction of light* (Cambridge university press, 1999).

[2] M. Planck, "Ueber das Gesetz der Energieverteilung im Normalspectrum," Ann. Phys. **309**, 553–563 (1901).

[3] A. Einstein, "Über einen die Erzeugung und Verwandlung des Lichtes betreffenden heuristischen Gesichtspunkt," Ann. Phys. **322**, 132–148 (1905).

[4] G. N. Lewis, "The conservation of photons," Nature **118**, 874–875 (1926).

[5] G. I. Taylor, "Interference fringes with feeble light," in "Proceedings of the Cambridge Philosophical Society," , vol. 15 (1909), vol. 15, pp. 114–115.

[6] R. H. Brown and R. Q. Twiss, "A test of a new type of stellar interferometer on Sirius," Nature **178**, 1046–1048 (1956).

[7] R. J. Glauber, "The quantum theory of optical coherence," Physical Review **130**, 2529 (1963).

[8] H. J. Kimble, M. Dagenais, and L. Mandel, "Photon Antibunching in Resonance Fluorescence," Phys. Rev. Lett. **39**, 691–695 (1977).

[9] A. Aspect, P. Grangier, and G. Roger, "Experimental realization of Einstein-Podolsky-Rosen-Bohm Gedankenexperiment: a new violation of Bell's inequalities," Physical review letters **49**, 91 (1982).

[10] J.-W. Pan, D. Bouwmeester, M. Daniell, H. Weinfurter, and A. Zeilinger, "Experimental test of quantum nonlocality in three-photon Greenberger–Horne–Zeilinger entanglement," Nature **403**, 515–519 (2000).

[11] C. Hong, Z. Ou, and L. Mandel, "Measurement of subpicosecond time intervals between two photons by interference," Phys. Rev. Lett. **59**, 2044–2046 (1987).

[12] J. S. Bell, *On the Einstein Podolsky Rosen paradox* (1964).

[13] D. Bouwmeester, J.-W. Pan, K. Mattle, M. Eibl, H. Weinfurter, and A. Zeilinger, "Experimental quantum teleportation," Nature **390**, 575–579 (1997).

[14] M. Ringbauer, B. Duffus, C. Branciard, E. G. Cavalcanti, A. G. White, and A. Fedrizzi, "Measurements on the reality of the wavefunction," Nat Phys **11**, 249–254 (2015).

[15] H.-A. Bachor and T. C. Ralph, *A guide to experiments in quantum optics* (Wiley, 2004).

[16] A. Zeilinger, G. Weihs, T. Jennewein, and M. Aspelmeyer, "Happy centenary, photon," Nature **433**, 230–238 (2005).

[17] I. A. Walmsley, "Quantum optics: Science and technology in a new light," Science **348**, 525–530 (2015).

[18] P. Kok, W. J. Munro, K. Nemoto, T. C. Ralph, J. P. Dowling, and G. J. Milburn, "Linear optical quantum computing with photonic qubits," Rev. Mod. Phys. **79**, 135–174 (2007).

[19] A. Ambainis, "Quantum walk algorithm for element distinctness," SIAM Journal on Computing **37**, 210–239 (2007).

[20] E. Farhi, J. Goldstone, and S. Gutmann, "A Quantum Algorithm for the Hamiltonian NAND Tree," Theory OF Computing **4**, 169–190 (2008).

[21] V. Potoček, A. Gábris, T. Kiss, and I. Jex, "Optimized quantum random-walk search algorithms on the hypercube," Phys. Rev. A **79**, 012325 (2009).

[22] A. M. Childs, "Universal Computation by Quantum Walk," Phys. Rev. Lett. **102**, 180501 (2009).

[23] A. M. Childs, D. Gosset, and Z. Webb, "Universal Computation by Multiparticle Quantum Walk," Science **339**, 791–794 (2013).

[24] E. G. van Putten and A. P. Mosk, "The information age in optics: Measuring the transmission matrix," Physics **3**, 22 (2010).

[25] J. R. Ott, N. A. Mortensen, and P. Lodahl, "Quantum Interference and Entanglement Induced by Multiple Scattering of Light," Phys. Rev. Lett. **105**, 090501 (2010).

[26] T. C. Ralph, "Quantum computation: Boson sampling on a chip," Nature Photonics **7**, 514–515 (2013).

[27] D. F. Walls, "Squeezed states of light," Nature **306**, 141–146 (1983).

[28] A. Kuhn, M. Hennrich, and G. Rempe, "Deterministic Single-Photon Source for Distributed Quantum Networking," Phys. Rev. Lett. **89**, 067901 (2002).

[29] P. Michler, A. Kiraz, C. Becher, W. V. Schoenfeld, P. M. Petroff, L. Zhang, E. Hu, and A. Imamoglu, "A Quantum Dot Single-Photon Turnstile Device," Science **290**, 2282–2285 (2000).

[30] R. Brouri, A. Beveratos, J.-P. Poizat, and P. Grangier, "Photon antibunching in the fluorescence of individual color centers in diamond," Optics Letters **25**, 1294 (2000).

[31] C. Kurtsiefer, S. Mayer, P. Zarda, and H. Weinfurter, "Stable Solid-State Source of Single Photons," Phys. Rev. Lett. **85**, 290–293 (2000).

[32] C. W. Chou, S. V. Polyakov, A. Kuzmich, and H. J. Kimble, "Single-Photon Generation from Stored Excitation in an Atomic Ensemble," Phys. Rev. Lett. **92**, 213601 (2004).

[33] D. C. Burnham and D. L. Weinberg, "Observation of Simultaneity in Parametric Production of Optical Photon Pairs," Phys. Rev. Lett. **25**, 84–87 (1970).

[34] Y. H. Shih and C. O. Alley, "New Type of Einstein-Podolsky-Rosen-Bohm Experiment Using Pairs of Light Quanta Produced by Optical Parametric Down Conversion," Phys. Rev. Lett. **61**, 2921–2924 (1988).

[35] R. Ghosh and L. Mandel, "Observation of nonclassical effects in the interference of two photons," Phys. Rev. Lett. **59**, 1903–1905 (1987).

[36] P. G. Kwiat, E. Waks, A. G. White, I. Appelbaum, and P. H. Eberhard, "Ultra-bright source of polarization-entangled photons," Phys. Rev. A **60**, R773–R776 (1999).

[37] S. Takeuchi, "Beamlike twin-photon generation by use of type II parametric downconversion," Optics Letters **26**, 843 (2001).

[38] W. P. Grice and I. A. Walmsley, "Spectral information and distinguishability in type-II down-conversion with a broadband pump," Physical Review A **56**, 1627 (1997).

[39] C. E. Kuklewicz, M. Fiorentino, G. Messin, F. N. C. Wong, and J. H. Shapiro, "High-flux source of polarization-entangled photons from a periodically poled ${\mathrm{KTiOPO}}_{4}$ parametric down-converter," Phys. Rev. A **69**, 013807 (2004).

[40] A. Fedrizzi, T. Herbst, A. Poppe, T. Jennewein, and A. Zeilinger, "A wavelength-tunable fiber-coupled source of narrowband entangled photons," Optics Express **15**, 15377–15386 (2007).

[41] A. Fedrizzi, T. Herbst, M. Aspelmeyer, M. Barbieri, T. Jennewein, and A. Zeilinger, "Anti-symmetrization reveals hidden entanglement," New J. Phys. **11**, 103052 (2009).

[42] F. Steinlechner, P. Trojek, M. Jofre, H. Weier, D. Perez, T. Jennewein, R. Ursin, J. Rarity, M. W. Mitchell, J. P. Torres, H. Weinfurter, and V. Pruneri, "A high-brightness source of polarization-entangled photons optimized for applications in free space," Optics Express **20**, 9640 (2012).

[43] A. B. U'Ren, C. Silberhorn, K. Banaszek, and I. A. Walmsley, "Efficient Conditional Preparation of High-Fidelity Single Photon States for Fiber-Optic Quantum Networks," Phys. Rev. Lett. **93**, 093601 (2004).

[44] J. G. Rarity and P. R. Tapster, "Experimental violation of Bell's inequality based on phase and momentum," Phys. Rev. Lett. **64**, 2495–2498 (1990).

[45] P. J. Mosley, "Generation of heralded single photons in pure quantum states," Ph.D. thesis, University of Oxford (2007).

[46] P. Grangier, G. Roger, and A. Aspect, "Experimental evidence for a photon anti-correlation effect on a beam splitter: a new light on single-photon interferences," EPL (Europhysics Letters) **1**, 173 (1986).

[47] L. Mandel, "Quantum effects in one-photon and two-photon interference," Rev. Mod. Phys. **71**, S274–S282 (1999).

[48] E. Knill, R. Laflamme, and G. J. Milburn, "A scheme for efficient quantum computation with linear optics," Nature **409**, 46–52 (2001).

[49] de Broglie and L. d. Broglie, "Wave mechanics and the atomic structure of matter and radiationLa mécanique ondulatoire et la structure atomique de la matière et du rayonnement," Journal de Physique et le Radium **8**, 17 (1927).

[50] J. Liu, Y. Zhou, W. Wang, R.-f. Liu, K. He, F.-l. Li, and Z. Xu, "Spatial second-order interference of pseudothermal light in a Hong-Ou-Mandel interferometer," Optics Express **21**, 19209 (2013).

[51] H. Chen, T. Peng, S. Karmakar, Z. Xie, and Y. Shih, "Observation of anticorrelation in incoherent thermal light fields," Phys. Rev. A **84**, 033835 (2011).

[52] J. H. Shapiro and E. Lantz, "Comment on "Observation of anticorrelation in incoherent thermal light fields"," arXiv:1110.5691 [quant-ph] (2011). ArXiv: 1110.5691.

[53] H. Fearn and R. Loudon, "Theory of two-photon interference," J. Opt. Soc. Am. B **6**, 917–927 (1989).

[54] A. V. Belinsky and D. N. Klyshko, "Two-photon wave packets," Laser Physics **4**, 663–689 (1994).

[55] P.-G. De Gennes, *Scaling concepts in polymer physics* (Cornell university press, 1979).

[56] N. G. V. Kampen, *Stochastic Processes in Physics and Chemistry* (Elsevier, 1992).

[57] N. S. Goel and N. Richter-Dyn, *Stochastic models in biology* (Elsevier, 2013).

[58] G. H. Weiss, *Aspects and applications of the random walk*, Random Materials and Processes (North-Holland Publishing Co., Amsterdam, 1994).

[59] J. Y. Campbell, A. W.-C. Lo, A. C. MacKinlay, and others, *The econometrics of financial markets*, vol. 2 (princeton University press Princeton, NJ, 1997).

[60] M. Doi and S. F. Edwards, *The theory of polymer dynamics*, vol. 73 (oxford university press, 1988).

[61] R. Portugal, *Quantum walks and search algorithms* (Springer Science & Business Media, 2013).

[62] J. K. Gamble, M. Friesen, D. Zhou, R. Joynt, and S. N. Coppersmith, "Two-particle quantum walks applied to the graph isomorphism problem," Phys. Rev. A **81**, 052313 (2010).

[63] P. P. Rohde, A. Schreiber, M. Štefaňák, I. Jex, and C. Silberhorn, "Multi-walker discrete time quantum walks on arbitrary graphs, their properties and their photonic implementation," New J. Phys. **13**, 013001 (2011).

[64] M. Karski, L. Förster, J.-M. Choi, A. Steffen, W. Alt, D. Meschede, and A. Widera, "Quantum Walk in Position Space with Single Optically Trapped Atoms," Science **325**, 174–177 (2009).

[65] J. Du, H. Li, X. Xu, M. Shi, J. Wu, X. Zhou, and R. Han, "Experimental implementation of the quantum random-walk algorithm," Phys. Rev. A **67**, 042316 (2003).

[66] L. Sansoni, F. Sciarrino, G. Vallone, P. Mataloni, A. Crespi, R. Ramponi, and R. Osellame, "Two-Particle Bosonic-Fermionic Quantum Walk via Integrated Photonics," Phys. Rev. Lett. **108**, 010502 (2012).

[67] Z. Zhao, J. Du, H. Li, T. Yang, Z.-B. Chen, and J.-W. Pan, "Implement Quantum Random Walks with Linear Optics Elements," arXiv:quant-ph/0212149 (2002). ArXiv: quant-ph/0212149.

[68] B. Do, M. L. Stohler, S. Balasubramanian, D. S. Elliott, C. Eash, E. Fischbach, M. A. Fischbach, A. Mills, and B. Zwickl, "Experimental realization of a quantum quincunx by use of linear optical elements," Journal of the Optical Society of America B **22**, 499 (2005).

[69] F. Galton, "Typical laws of heredity," Nature **15**, 492–5 (1877).

[70] A. Politi, M. J. Cryan, J. G. Rarity, S. Yu, and J. L. O'Brien, "Silica-on-Silicon Waveguide Quantum Circuits," Science **320**, 646–649 (2008).

[71] A. Schreiber, A. Gábris, P. P. Rohde, K. Laiho, M. Štefaňák, V. Potoček, C. Hamilton, I. Jex, and C. Silberhorn, "A 2d Quantum Walk Simulation of Two-Particle Dynamics," Science **336**, 55–58 (2012).

[72] A. Crespi, R. Osellame, R. Ramponi, V. Giovannetti, R. Fazio, L. Sansoni, F. De Nicola, F. Sciarrino, and P. Mataloni, "Anderson localization of entangled photons in an integrated quantum walk," Nature Photonics **7**, 322–328 (2013).

[73] M. A. Broome, A. Fedrizzi, S. Rahimi-Keshari, J. Dove, S. Aaronson, T. C. Ralph, and A. G. White, "Photonic Boson Sampling in a Tunable Circuit," Science **339**, 794–798 (2013).

[74] J. B. Spring, B. J. Metcalf, P. C. Humphreys, W. S. Kolthammer, X.-M. Jin, M. Barbieri, A. Datta, N. Thomas-Peter, N. K. Langford, D. Kundys, J. C. Gates, B. J. Smith, P. G. R. Smith, and I. A. Walmsley, "Boson Sampling on a Photonic Chip," Science **339**, 798–801 (2013).

[75] A. Crespi, R. Osellame, R. Ramponi, D. J. Brod, E. F. Galvão, N. Spagnolo, C. Vitelli, E. Maiorino, P. Mataloni, and F. Sciarrino, "Integrated multimode interferometers with arbitrary designs for photonic boson sampling," Nature Photonics **7**, 545–549 (2013).

[76] M. Tillmann, B. Dakić, R. Heilmann, S. Nolte, A. Szameit, and P. Walther, "Experimental boson sampling," Nature Photonics **7**, 540–544 (2013).

[77] M. Reck, A. Zeilinger, H. J. Bernstein, and P. Bertani, "Experimental realization of any discrete unitary operator," Physical Review Letters **73**, 58 (1994).

[78] S. Rahimi-Keshari, M. A. Broome, R. Fickler, A. Fedrizzi, T. C. Ralph, and A. G. White, "Direct characterization of linear-optical networks," Optics express **21**, 13450–13458 (2013).

[79] A. Laing and J. L. O'Brien, "Super-stable tomography of any linear optical device," arXiv preprint arXiv:1208.2868 (2012).

[80] S. M. Popoff, G. Lerosey, R. Carminati, M. Fink, A. C. Boccara, and S. Gigan, "Measuring the transmission matrix in optics: an approach to the study and control of light propagation in disordered media," Physical review letters **104**, 100601 (2010).

[81] H. Jeong, M. Paternostro, and M. S. Kim, "Simulation of quantum random walks using the interference of a classical field," Phys. Rev. A **69**, 012310 (2004).

[82] K. Mattle, "Non classical statistics at multiport beam splitter," Applied Physics B **60**, S111–S117 (1994).

[83] S. Aaronson and A. Arkhipov, "The computational complexity of linear optics," (ACM Press, 2011), p. 333.

[84] S. Scheel, "Permanents in linear optical networks," arXiv:quant-ph/0406127 (2004). ArXiv: quant-ph/0406127.

[85] H. J. Ryser, *Combinatorial mathematics* (Mathematical Association of America; distributed by Wiley [New York, 1963).

[86] N. Spagnolo, C. Vitelli, M. Bentivegna, D. J. Brod, A. Crespi, F. Flamini, S. Giacomini, G. Milani, R. Ramponi, P. Mataloni, R. Osellame, E. F. Galvão, and F. Sciarrino, "Experimental validation of photonic boson sampling," Nat Photon **8**, 615–620 (2014).

[87] M. C. Tichy, "Interference of identical particles from entanglement to boson-sampling," Journal of Physics B: Atomic, Molecular and Optical Physics **47**, 103001 (2014).

[88] P. P. Rohde, "Optical quantum computing with photons of arbitrarily low fidelity and purity," Phys. Rev. A **86**, 052321 (2012).

[89] P. P. Rohde and T. C. Ralph, "Error tolerance of the boson-sampling model for linear optics quantum computing," Physical Review A **85** (2012).

[90] V. S. Shchesnovich, "Sufficient condition for the mode mismatch of single photons for scalability of the boson-sampling computer," Phys. Rev. A **89**, 022333 (2014).

[91] L. K. Grover, "A Fast Quantum Mechanical Algorithm for Database Search," in "Proceedings of the Twenty-eighth Annual ACM Symposium on Theory of Computing," (ACM, New York, NY, USA, 1996), STOC '96, pp. 212–219.

[92] P. Shor, "Polynomial-Time Algorithms for Prime Factorization and Discrete Logarithms on a Quantum Computer," SIAM J. Comput. **26**, 1484–1509 (1997).

[93] M. A. Nielsen, "Optical Quantum Computation Using Cluster States," Phys. Rev. Lett. **93**, 040503 (2004).

[94] D. E. Browne and T. Rudolph, "Resource-Efficient Linear Optical Quantum Computation," Phys. Rev. Lett. **95**, 010501 (2005).

[95] M. A. Nielsen and I. L. Chuang, *Quantum Computation and Quantum Information: 10th Anniversary Edition* (Cambridge University Press, 2010).

[96] K. Lemr, A. Černoch, J. Soubusta, and M. Dušek, "Entangling efficiency of linear-optical quantum gates," Phys. Rev. A **86**, 032321 (2012).

[97] G. Mie, "Beiträge zur Optik trüber Medien, speziell kolloidaler Metallösungen," Ann. Phys. **330**, 377–445 (1908).

[98] M. C. W. van Rossum and T. M. Nieuwenhuizen, "Multiple scattering of classical waves: microscopy, mesoscopy, and diffusion," Rev. Mod. Phys. **71**, 313–371 (1999).

[99] D. Andreoli, G. Volpe, S. Popoff, O. Katz, S. Grésillon, and S. Gigan, "Deterministic control of broadband light through a multiply scattering medium via the multispectral transmission matrix," Scientific Reports **5**, 10347 (2015).

[100] N. Curry, P. Bondareff, M. Leclercq, N. F. van Hulst, R. Sapienza, S. Gigan, and S. Grésillon, "Direct determination of diffusion properties of random media from speckle contrast," Optics Letters **36**, 3332 (2011).

[101] O. Katz, E. Small, Y. Bromberg, and Y. Silberberg, "Focusing and compression of ultrashort pulses through scattering media," Nat Photon **5**, 372–377 (2011).

[102] B. Redding and H. Cao, "Using a multimode fiber as a high-resolution, low-loss spectrometer," Opt. Lett., OL **37**, 3384–3386 (2012).

[103] I. Papadopoulos and D. P. (Ingenieur), *Dynamic Control of Light Transmission Through Multimode Fibers* (EPFL, 2014).

[104] M. Patra, "On quantum optics of random media," Ph.D. thesis, Ph. D. thesis, University of Leiden (2000).

[105] M. Patra and C. W. J. Beenakker, "Propagation of squeezed radiation through amplifying or absorbing random media," Phys. Rev. A **61**, 063805 (2000).

[106] S. E. Skipetrov, "Quantum theory of dynamic multiple light scattering in fluctuating disordered media," Physical Review A **75**, 053808 (2007).

[107] P. Lodahl, A. P. Mosk, and A. Lagendijk, "Spatial quantum correlations in multiple scattered light," Physical review letters **95**, 173901 (2005).

[108] P. Lodahl and A. Lagendijk, "Transport of quantum noise through random media," Physical review letters **94**, 153905 (2005).

[109] A. Aiello, G. Puentes, and J. P. Woerdman, "Linear optics and quantum maps," Phys. Rev. A **76**, 032323 (2007).

[110] C. Beenakker, J. Venderbos, and M. van Exter, "Two-Photon Speckle as a Probe of Multi-Dimensional Entanglement," Physical Review Letters **102** (2009).

[111] M. Candé and S. E. Skipetrov, "Quantum versus classical effects in two-photon speckle patterns," Physical Review A **87**, 013846 (2013).

[112] M. Candé, A. Goetschy, and S. E. Skipetrov, "Transmission of quantum entanglement through a random medium," arXiv preprint arXiv:1406.7202 (2014).

[113] S. Smolka, A. Huck, U. L. Andersen, A. Lagendijk, and P. Lodahl, "Observation of Spatial Quantum Correlations Induced by Multiple Scattering of Nonclassical Light," Phys. Rev. Lett. **102**, 193901 (2009).

[114] G. Puentes, A. Aiello, D. Voigt, and J. P. Woerdman, "Entangled mixed-state generation by twin-photon scattering," Phys. Rev. A **75**, 032319 (2007).

[115] G. Puentes and F. d. W. e. Natuurwetenschappen, "Classical and quantum scattering in optical systems," (2007).

[116] W. H. Peeters, J. J. D. Moerman, and M. P. van Exter, "Observation of Two-Photon Speckle Patterns," Physical Review Letters **104** (2010).

[117] W. H. Peeters, *Two-photon interference* (s.n.], S.l., 2010).

[118] M. P. van Exter, J. Woudenberg, H. Di Lorenzo Pires, and W. H. Peeters, "Bosonic, fermionic, and anyonic symmetry in two-photon random scattering," Phys. Rev. A **85**, 033823 (2012).

[119] H. Pires, *Spatial coherence and entanglement of light* (s.n.], S.l., 2011).

[120] H. Di Lorenzo Pires, J. Woudenberg, and M. P. van Exter, "Statistical properties of two-photon speckles," Phys. Rev. A **85**, 033807 (2012).

[121] A. P. Mosk, A. Lagendijk, G. Lerosey, and M. Fink, "Controlling waves in space and time for imaging and focusing in complex media," Nature photonics **6**, 283–292 (2012).

[122] I. M. Vellekoop and A. P. Mosk, "Focusing coherent light through opaque strongly scattering media," Optics letters **32**, 2309–2311 (2007).

[123] T. J. Huisman, S. R. Huisman, A. P. Mosk, and P. W. H. Pinkse, "Controlling single-photon Fock-state propagation through opaque scattering media," Appl. Phys. B **116**, 603–607 (2014).

[124] S. R. Huisman, T. J. Huisman, T. A. Wolterink, A. P. Mosk, and P. W. Pinkse, "Programmable multiport optical circuits in opaque scattering materials," arXiv preprint arXiv:1408.1856 (2014).

[125] S. R. Huisman, T. J. Huisman, S. A. Goorden, A. P. Mosk, and P. W. H. Pinkse, "Programming balanced optical beam splitters in white paint," Optics Express **22**, 8320 (2014).

[126] S. Popoff, G. Lerosey, M. Fink, A. C. Boccara, and S. Gigan, "Image transmission through an opaque material," Nature Communications **1**, 81 (2010).

[127] H. Defienne, M. Barbieri, B. Chalopin, B. Chatel, I. A. Walmsley, B. J. Smith, and S. Gigan, "Nonclassical light manipulation in a multiple-scattering medium," Opt. Lett. **39**, 6090–6093 (2014).

[128] H. Defienne, M. Barbieri, I. A. Walmsley, B. J. Smith, and S. Gigan, "Control of two-photon quantum walk in a complex multimode system by wavefront shaping," arXiv:1504.03178 [physics, physics:quant-ph] (2015). ArXiv: 1504.03178.

[129] V. Ntziachristos, "Going deeper than microscopy: the optical imaging frontier in biology," Nat Meth **7**, 603–614 (2010).

[130] Z. Merali, "Optics: Super vision," Nature **518**, 158–160 (2015).

[131] "Deciphering speckle," Nat Photon **8**, 808–808 (2014).

[132] D. Psaltis and I. N. Papadopoulos, "Imaging: The fog clears," Nature **491**, 197–198 (2012).

[133] J. Bertolotti, E. G. van Putten, C. Blum, A. Lagendijk, W. L. Vos, and A. P. Mosk, "Non-invasive imaging through opaque scattering layers," Nature **491**, 232–234 (2012).

[134] O. Katz, P. Heidmann, M. Fink, and S. Gigan, "Non-invasive single-shot imaging through scattering layers and around corners via speckle correlations," Nature Photonics **8**, 784–790 (2014).

[135] C. F. Bohren and D. R. Huffman, *Absorption and Scattering of Light by Small Particles* (John Wiley & Sons, 2008).

[136] J. W. Goodman, *Speckle Phenomena in Optics: Theory and Applications* (Roberts and Company Publishers, 2007).

[137] C. Maurer, A. Jesacher, S. Bernet, and M. Ritsch-Marte, "What spatial light modulators can do for optical microscopy," Laser & Photon. Rev. **5**, 81–101 (2011).

[138] I. M. Vellekoop and A. P. Mosk, "Phase control algorithms for focusing light through turbid media," Optics Communications **281**, 3071–3080 (2008).

[139] D. B. Conkey, A. N. Brown, A. M. Caravaca-Aguirre, and R. Piestun, "Genetic algorithm optimization for focusing through turbid media in noisy environments," Optics Express **20**, 4840 (2012).

[140] Z. Yaqoob, D. Psaltis, M. S. Feld, and C. Yang, "Optical phase conjugation for turbidity suppression in biological samples," Nat Photon **2**, 110–115 (2008).

[141] F. Kong, R. H. Silverman, L. Liu, P. V. Chitnis, K. K. Lee, and Y. C. Chen, "Photoacoustic-guided convergence of light through optically diffusive media," Optics Letters **36**, 2053 (2011).

[142] T. Chaigne, J. Gateau, O. Katz, C. Boccara, S. Gigan, and E. Bossy, "Improving photoacoustic-guided optical focusing in scattering media by spectrally filtered detection," Optics Letters **39**, 6054 (2014).

[143] R. Grange, T. Lanvin, C.-L. Hsieh, Y. Pu, and D. Psaltis, "Imaging with second-harmonic radiation probes in living tissue," Biomedical Optics Express **2**, 2532 (2011).

[144] S. M. Popoff, G. Lerosey, M. Fink, A. C. Boccara, and S. Gigan, "Controlling light through optical disordered media: transmission matrix approach," New J. Phys. **13**, 123021 (2011).

[145] M. Åbom, "Measurement of the scattering-matrix of acoustical two-ports," Mechanical Systems and Signal Processing **5**, 89–104 (1991).

[146] J. Carpenter and T. D. Wilkinson, "Characterization of multimode fiber by selective mode excitation," Journal of lightwave technology **30**, 1386–1392 (2012).

[147] M. Plöschner, T. Tyc, and T. Čižmár, "Seeing through chaos in multimode fibres," Nat Photon **9**, 529–535 (2015).

[148] T. Chaigne, O. Katz, A. C. Boccara, M. Fink, E. Bossy, and S. Gigan, "Controlling light in scattering media non-invasively using the photoacoustic transmission matrix," Nat Photon **8**, 58–64 (2014).

[149] A. Aubry and A. Derode, "Random Matrix Theory Applied to Acoustic Backscattering and Imaging In Complex Media," Phys. Rev. Lett. **102**, 084301 (2009).

[150] S. Kang, S. Jeong, W. Choi, H. Ko, T. D. Yang, J. H. Joo, J.-S. Lee, Y.-S. Lim, Q.-H. Park, and W. Choi, "Imaging deep within a scattering medium using collective accumulation of single-scattered waves," Nat Photon **9**, 253–258 (2015).

[151] S. E. Skipetrov and A. Goetschy, "Eigenvalue distributions of large Euclidean random matrices for waves in random media," Journal of Physics A-Mathematical and Theoretical **44**, 065102 (2011).

[152] R. Penrose, "A generalized inverse for matrices," in "Mathematical proceedings of the Cambridge philosophical society," , vol. 51 (Cambridge Univ Press, 1955), vol. 51, pp. 406–413.

[153] T. A, "Solution of Incorrectly Formulated Problems and the Regularization Method," Soviet Math. Dokl. **5**, 1035/1038 (1963).

[154] C. Prada and M. Fink, "Eigenmodes of the time reversal operator: A solution to selective focusing in multiple-target media," Wave motion **20**, 151–163 (1994).

[155] A. Derode, A. Tourin, and M. Fink, "Time reversal versus phase conjugation in a multiple scattering environment," Ultrasonics **40**, 275–280 (2002).

[156] M. Kim, W. Choi, Y. Choi, C. Yoon, and W. Choi, "Transmission matrix of a scattering medium and its applications in biophotonics," Optics Express **23**, 12648 (2015).

[157] J. Aulbach, B. Gjonaj, P. M. Johnson, A. P. Mosk, and A. Lagendijk, "Control of Light Transmission through Opaque Scattering Media in Space and Time," Physical Review Letters **106** (2011).

[158] M. Mohseni, P. Rebentrost, S. Lloyd, and A. Aspuru-Guzik, "Environment-assisted quantum walks in photosynthetic energy transfer," The Journal of Chemical Physics **129**, 174106 (2008).

[159] J. Klafter and R. Silbey, "Derivation of the Continuous-Time Random-Walk Equation," Phys. Rev. Lett. **44**, 55–58 (1980).

[160] A. M. Childs and J. Goldstone, "Spatial search by quantum walk," Phys. Rev. A **70**, 022314 (2004).

[161] N. Shenvi, J. Kempe, and K. B. Whaley, "Quantum random-walk search algorithm," Phys. Rev. A **67**, 052307 (2003).

[162] A. M. Childs and J. M. Eisenberg, "Quantum algorithms for subset finding," arXiv:quant-ph/0311038 (2003). ArXiv: quant-ph/0311038.

[163] B. Reichardt and R. Spalek, "Span-Program-Based Quantum Algorithm for Evaluating Formulas." Theory of Computing **8**, 291–319 (2012).

[164] P. Shadbolt, *Complexity and Control in Quantum Photonics* (Springer, 2015).

[165] Y. Lahini, Y. Bromberg, D. N. Christodoulides, and Y. Silberberg, "Quantum Correlations in Two-Particle Anderson Localization," Phys. Rev. Lett. **105**, 163905 (2010).

[166] Y. Gilead, M. Verbin, and Y. Silberberg, "Ensemble-Averaged Quantum Correlations between Path-Entangled Photons Undergoing Anderson Localization," Phys. Rev. Lett. **115**, 133602 (2015).

[167] J. Sun, E. Timurdogan, A. Yaacobi, E. S. Hosseini, and M. R. Watts, "Large-scale nanophotonic phased array," Nature **493**, 195–199 (2013).

[168] J. Carolan, C. Harrold, C. Sparrow, E. Martín-López, N. J. Russell, J. W. Silverstone, P. J. Shadbolt, N. Matsuda, M. Oguma, M. Itoh, G. D. Marshall, M. G. Thompson, J. C. F. Matthews, T. Hashimoto, J. L. O'Brien, and A. Laing, "Universal linear optics," Science **349**, 711–716 (2015).

[169] S.-M. Reijn, F. A. Pinheiro, D. Geskus, and N. U. Wetter, "Enabling focusing around the corner in multiple scattering media," Applied Optics **54**, 7740 (2015).

[170] P. Sebbah, ed., *Waves and Imaging through Complex Media* (Springer Netherlands, Dordrecht, 2001).

[171] J. Wang and A. Z. Genack, "Transport through modes in random media," Nature **471**, 345–348 (2011).

[172] S. V. Gaponenko, *Introduction to Nanophotonics* (Cambridge University Press, 2010).

[173] R. D. Skocypec and R. O. Buckius, "Photon path length distributions for an isotropically scattering planar medium," Journal of Quantitative Spectroscopy and Radiative Transfer **28**, 425–439 (1982).

[174] H. C. Hulst and H. C. v. d. Hulst, *Light Scattering by Small Particles* (Courier Corporation, 1957).

[175] C. W. Chou, H. de Riedmatten, D. Felinto, S. V. Polyakov, S. J. van Enk, and H. J. Kimble, "Measurement-induced entanglement for excitation stored in remote atomic ensembles," Nature **438**, 828–832 (2005).

[176] K. C. Lee, M. R. Sprague, B. J. Sussman, J. Nunn, N. K. Langford, X.-M. Jin, T. Champion, P. Michelberger, K. F. Reim, D. England, D. Jaksch, and I. A. Walmsley, "Entangling Macroscopic Diamonds at Room Temperature," Science **334**, 1253–1256 (2011).

[177] W. Dür, G. Vidal, and J. I. Cirac, "Three qubits can be entangled in two inequivalent ways," Physical Review A **62**, 062314 (2000).

[178] H. Häffner, W. Hänsel, C. F. Roos, J. Benhelm, D. Chek-al kar, M. Chwalla, T. Körber, U. D. Rapol, M. Riebe, P. O. Schmidt, C. Becher, O. Gühne, W. Dür, and R. Blatt, "Scalable multiparticle entanglement of trapped ions," Nature **438**, 643–646 (2005).

[179] M. Gräfe, R. Heilmann, A. Perez-Leija, R. Keil, F. Dreisow, M. Heinrich, H. Moya-Cessa, S. Nolte, D. N. Christodoulides, and A. Szameit, "On-chip generation of high-order single-photon W-states," Nat Photon **8**, 791–795 (2014).

[180] S. J. van Enk, "Single-particle entanglement," Phys. Rev. A **72**, 064306 (2005).

[181] M. Fuwa, S. Takeda, M. Zwierz, H. M. Wiseman, and A. Furusawa, "Experimental proof of nonlocal wavefunction collapse for a single particle using homodyne measurements," Nat Commun **6**, 6665 (2015).

[182] P. Lougovski, S. J. v. Enk, K. S. Choi, S. B. Papp, H. Deng, and H. J. Kimble, "Verifying multipartite mode entanglement of W states," New Journal of Physics **11**, 063029 (2009).

[183] A. Peruzzo, M. Lobino, J. C. F. Matthews, N. Matsuda, A. Politi, K. Poulios, X.-Q. Zhou, Y. Lahini, N. Ismail, K. Wörhoff, Y. Bromberg, Y. Silberberg, M. G. Thompson, and J. L. OBrien, "Quantum Walks of Correlated Photons," Science **329**, 1500–1503 (2010).

[184] Bates, *Optical Switching and Networking Handbook* (Mcgraw-hill, 2001).

[185] G. P. Agrawal, *Fiber-Optic Communication Systems* (John Wiley & Sons, 2012).

[186] A. W. Snyder and J. Love, *Optical Waveguide Theory* (Springer Science & Business Media, 2012).

[187] S. Berdagué and P. Facq, "Mode division multiplexing in optical fibers," Appl. Opt., AO **21**, 1950–1955 (1982).

[188] D. J. Richardson, J. M. Fini, and L. E. Nelson, "Space-division multiplexing in optical fibres," Nat Photon **7**, 354–362 (2013).

[189] R. D. Leonardo and S. Bianchi, "Hologram transmission through multi-mode optical fibers," Opt. Express, OE **19**, 247–254 (2011).

[190] S. Bianchi and R. D. Leonardo, "A multi-mode fiber probe for holographic micromanipulation and microscopy," Lab Chip **12**, 635–639 (2012).

[191] T. Čižmár and K. Dholakia, "Exploiting multimode waveguides for pure fibre-based imaging," Nat Commun **3**, 1027 (2012).

[192] I. N. Papadopoulos, O. Simandoux, S. Farahi, J. P. Huignard, E. Bossy, D. Psaltis, and C. Moser, "Optical-resolution photoacoustic microscopy by use of a multimode fiber," Applied Physics Letters **102**, 211106 (2013).

[193] J. Carpenter, C. Xiong, M. J. Collins, J. Li, T. F. Krauss, B. J. Eggleton, A. S. Clark, and J. Schröder, "Mode multiplexed single-photon and classical channels in a few-mode fiber," Opt. Express **21**, 28794–28800 (2013).

[194] T. Čižmár and K. Dholakia, "Shaping the light transmission through a multimode optical fibre: complex transformation analysis and applications in biophotonics," Opt. Express, OE **19**, 18871–18884 (2011).

[195] A. M. Caravaca-Aguirre, E. Niv, D. B. Conkey, and R. Piestun, "Real-time resilient focusing through a bending multimode fiber," Opt. Express, OE **21**, 12881–12887 (2013).

[196] I. N. Papadopoulos, S. Farahi, C. Moser, and D. Psaltis, "Focusing and scanning light through a multimode optical fiber using digital phase conjugation," Opt. Express, OE **20**, 10583–10590 (2012).

[197] Y. Choi, C. Yoon, M. Kim, T. D. Yang, C. Fang-Yen, R. R. Dasari, K. J. Lee, and W. Choi, "Scanner-Free and Wide-Field Endoscopic Imaging by Using a Single Multimode Optical Fiber," Phys. Rev. Lett. **109**, 203901 (2012).

[198] I. N. Papadopoulos, S. Farahi, C. Moser, and D. Psaltis, "High-resolution, lensless endoscope based on digital scanning through a multimode optical fiber," Biomed. Opt. Express, BOE **4**, 260–270 (2013).

[199] E. E. Morales-Delgado, S. Farahi, I. N. Papadopoulos, D. Psaltis, and C. Moser, "Delivery of focused short pulses through a multimode fiber," Opt. Express, OE **23**, 9109–9120 (2015).

[200] B. Redding, S. M. Popoff, and H. Cao, "All-fiber spectrometer based on speckle pattern reconstruction," Opt. Express, OE **21**, 6584–6600 (2013).

[201] J. Carpenter, B. J. Eggleton, and J. Schröder, "110x110 optical mode transfer matrix inversion," Opt. Express, OE **22**, 96–101 (2014).

[202] G. Milione, D. A. Nolan, and R. R. Alfano, "Determining principal modes in a multimode optical fiber using the mode dependent signal delay method," J. Opt. Soc. Am. B, JOSAB **32**, 143–149 (2015).

[203] J. Carpenter, B. J. Eggleton, and J. Schröder, "Observation of Eisenbud–Wigner–Smith states as principal modes in multimode fibre," Nat Photon **advance online publication** (2015).

[204] S. Rosen, D. Gilboa, O. Katz, and Y. Silberberg, "Focusing and Scanning through Flexible Multimode Fibers without Access to the Distal End," arXiv:1506.08586 [physics] (2015). ArXiv: 1506.08586.

[205] L. V. Amitonova, A. P. Mosk, and P. W. H. Pinkse, "The rotational memory effect of a multimode fiber," arXiv:1506.07960 [physics] (2015). ArXiv: 1506.07960.

[206] D. Loterie, S. Farahi, I. Papadopoulos, A. Goy, D. Psaltis, and C. Moser, "Digital confocal microscopy through a multimode fiber," Optics Express **23**, 23845 (2015).

[207] Y. Bromberg, B. Redding, S. M. Popoff, and H. Cao, "Control of coherent backscattering by breaking optical reciprocity," arXiv:1505.01507 [physics, physics:quant-ph] (2015). ArXiv: 1505.01507.

[208] D. Branning, W. P. Grice, R. Erdmann, and I. A. Walmsley, "Engineering the Indistinguishability and Entanglement of two Photons," Physical Review Letters **83**, 955 (1999).

[209] D. Branning, W. Grice, R. Erdmann, and I. A. Walmsley, "Interferometric technique for engineering indistinguishability and entanglement of photon pairs," Physical Review A **62**, 013814 (2000).

[210] H. d. Riedmatten, I. Marcikic, W. Tittel, H. Zbinden, and N. Gisin, "Quantum interference with photon pairs created in spatially separated sources," Phys. Rev. A **67**, 022301 (2003).

[211] Y.-H. Kim and W. P. Grice, "Quantum interference with distinguishable photons through indistinguishable pathways," JOSA B **22**, 493–498 (2005).

[212] V. S. Shchesnovich, "Partial indistinguishability theory for multiphoton experiments in multiport devices," Phys. Rev. A **91**, 013844 (2015).

[213] R. A. Campos, B. E. A. Saleh, and M. C. Teich, "Quantum-mechanical lossless beam splitter: SU(2) symmetry and photon statistics," Phys. Rev. A **40**, 1371–1384 (1989).

[214] A. Z. G. Weihs, "Photon statistics at beam-splitters: an essential tool in quantum information and teleportation," Tech. rep., Wiley (2001).

[215] A. Goetschy and A. D. Stone, "Filtering random matrices: The effect of incomplete channel control in multiple scattering," Physical review letters **111**, 063901 (2013).

[216] V. A. Marčenko and L. A. Pastur, "DISTRIBUTION OF EIGENVALUES FOR SOME SETS OF RANDOM MATRICES," Mathematics of the USSR-Sbornik **1**, 457–483 (1967).

[217] E. N. Leith and J. Upatnieks, "Reconstructed Wavefronts and Communication Theory," Journal of the Optical Society of America **52**, 1123 (1962).

[218] J. R. Fienup, "Phase retrieval algorithms: a comparison," Applied Optics **21**, 2758 (1982).

[219] "International Year of Light - Home," .

[220] L. M. K. Vandersypen, M. Steffen, G. Breyta, C. S. Yannoni, M. H. Sherwood, and I. L. Chuang, "Experimental realization of Shor's quantum factoring algorithm using nuclear magnetic resonance," Nature **414**, 883–887 (2001).

[221] D. Stick, W. K. Hensinger, S. Olmschenk, M. J. Madsen, K. Schwab, and C. Monroe, "Ion trap in a semiconductor chip," Nat Phys **2**, 36–39 (2006).

[222] A. Politi, J. C. F. Matthews, and J. L. O'Brien, "Shor's Quantum Factoring Algorithm on a Photonic Chip," Science **325**, 1221–1221 (2009).

[223] J.-H. Park, W. Sun, and M. Cui, "High-resolution in vivo imaging of mouse brain through the intact skull," PNAS **112**, 9236–9241 (2015).

[224] S. A. Goorden, M. Horstmann, A. P. Mosk, B. Škorić, and P. W. H. Pinkse, "Quantum-secure authentication of a physical unclonable key," Optica **1**, 421 (2014).

[225] D. Noordegraaf, P. M. Skovgaard, M. D. Nielsen, and J. Bland-Hawthorn, "Efficient multi-mode to single-mode coupling in a photonic lantern," Optics Express **17**, 1988–1994 (2009).

[226] S. G. Leon-Saval, A. Argyros, and J. Bland-Hawthorn, "Photonic lanterns: a study of light propagation in multimode to single-mode converters," Optics Express **18**, 8430–8439 (2010).

[227] J.-L. Blanchet, F. Devaux, L. Furfaro, and E. Lantz, "Purely spatial coincidences of twin photons in parametric spontaneous down-conversion," Phys. Rev. A **81**, 043825 (2010).

[228] P.-A. Moreau, J. Mougin-Sisini, F. Devaux, and E. Lantz, "Realization of the purely spatial Einstein-Podolsky-Rosen paradox in full-field images of spontaneous parametric down-conversion," Phys. Rev. A **86**, 010101 (2012).

[229] P.-A. Moreau, F. Devaux, and E. Lantz, "Einstein-Podolsky-Rosen Paradox in Twin Images," Phys. Rev. Lett. **113**, 160401 (2014).

[230] R. Fickler, R. Lapkiewicz, W. N. Plick, M. Krenn, C. Schaeff, S. Ramelow, and A. Zeilinger, "Quantum entanglement of high angular momenta," Science **338**, 640–643 (2012).

[231] M. Krenn, M. Huber, R. Fickler, R. Lapkiewicz, S. Ramelow, and A. Zeilinger, "Generation and confirmation of a (100$\times$ 100)-dimensional entangled quantum system," Proceedings of the National Academy of Sciences **111**, 6243–6247 (2014).

[232] M. Malik, M. Erhard, M. Huber, M. Krenn, R. Fickler, and A. Zeilinger, "Multi-photon entanglement in high dimensions," arXiv preprint arXiv:1509.02561 (2015).

[233] Y. Guan, O. Katz, E. Small, J. Zhou, and Y. Silberberg, "Polarization control of multiply scattered light through random media by wavefront shaping," Optics Letters **37**, 4663 (2012).

[234] C. J. Hawthorn, K. P. Weber, and R. E. Scholten, "Littrow configuration tunable external cavity diode laser with fixed direction output beam," Review of Scientific Instruments **72**, 4477–4479 (2001).

[235] W. K. Wootters, "Entanglement of Formation of an Arbitrary State of Two Qubits," Phys. Rev. Lett. **80**, 2245–2248 (1998).

[236] J. Berger and others, "The case for objective Bayesian analysis," Bayesian analysis **1**, 385–402 (2006).

[237] L. Demortier, "Objective Bayesian upper limits for Poisson processes," CDF5928 (2005).

[238] S. E. Fienberg and others, "Does it make sense to be an" objective Bayesian"?(comment on articles by Berger and by Goldstein)," Bayesian Analysis **1**, 429–432 (2006).

[239] M. Goldstein and others, "Subjective Bayesian analysis: principles and practice," Bayesian Analysis **1**, 403–420 (2006).

[240] P. Hlubina, "Spectral and Dispersion Analysis of Laser Sources and Multimode Fibres Via the Statistics of the Intensity Pattern," Journal of Modern Optics **41**, 1001–1014 (1994).

[241] W. J. Dixon, F. J. Massey, and others, *Introduction to statistical analysis*, vol. 344 (McGraw-Hill New York, 1969).

[242] R. L. Mason, R. F. Gunst, and J. L. Hess, *Statistical design and analysis of experiments: with applications to engineering and science*, vol. 474 (John Wiley & Sons, 2003).

Hugo DEFIENNE **2 Décembre 2015**

Sujet : Quantum walks of photons in disordered media

Résumé : Dans ce travail, nous nous interessons à la propagation d'états non-classiques de la lumière à travers des milieux désordonnés, comme les couches de peinture ou les fibres multimodes. Ces milieux sont généralement considérés comme des obstacles à la propagation de la lumière: par exemple, la diffusion de la lumière dans les tissus biologiques diminue considérablement les capacités des systèmes d'imagerie optique. C'est donc un phénomène duquel on souhaite généralement s'affranchir. Au contraire, dans notre étude nous exploitons ce désordre et utilisons ces milieux comme des "mélangeurs" de lumière. La lumière qui y pénètre est fortement diffusée et ses propriétés spectrales, spatiales et de polarisation sont complètement redistribuées. Cette redistribution est associé a un phénomène de propagation d'onde et d'interférence complexe qui est donc déterministe. Nous pouvons alors utiliser des méthodes de manipulation de front d'onde pour étudier ou contrôler ce mélange. Associés à des états non-classiques, ces systèmes permettent de réaliser des marches aléatoires quantiques dans des environnements bien plus complexes que ceux qui existent actuellement, par exemple utilisant des plateformes optiques intégrés. Au cours de ma thèse, j'ai utilisé les méthodes de contrôle de front d'onde pour étudier et manipuler ces marches aléatoires quantiques. Nous avons notamment montré qu'il est possible de guider les photons en manipulant les interférences classiques et quantiques. Ce travail nous a permis d'étudier de nouveaux aspects de la physique des milieux complexes, mais aussi d'explorer un nouveau type de plateformes pour marches aléatoires quantiques qui pourraient jouer un rôle important dans le développement des nouvelles applications pour traitement de l'information quantique.

Mots clés :

Subject :

Résumé : Light is not only an ideal medium to transmit information, but also a very interesting physical system to process it. In this respect, quantum optics has recently emerged as a highly promising domain for the development of new computing applications that can surpass the performances of currently available systems. In this respect, quantum walk of photons has recently emerged as a very powerful model for quantum information science, and integrated photonic devices have proven a versatile architecture for their implementation. While these waveguide structures allow only near-neighbor coupling between up to a few tens of modes, complex linear systems, such as white paint layer or multimode fiber, enable to couple efficiently a huge numbers of optical modes. Unstable and lossy, these systems have always been considered unpractical for quantum optics experiments. Wavefront shaping methods, developed in the last decade to control light propagating in

complex media, allow moving beyond these limitations and make them exploitable with non-classical light. In our work, we demonstrate the implementation of quantum walks in a layer of paint and a multimode fiber using single-photons and photon-pairs. For this purpose, we extend wavefront shaping methods, originally developed to control classical light propagation in complex media, to non-classical light. This capability to manipulate photons allows building new controllable highly multimode optical platforms. Such systems pave the way for the next generation of quantum information processing devices.

Keywords :